Investigations of Anomalous Earthquakes at Active Volcanoes

Ashley Elizabeth Shuler

Submitted in partial fulfillment of the
requirements for the degree of
Doctor of Philosophy
in the Graduate School of Arts and Sciences

COLUMBIA UNIVERSITY

2012

ABSTRACT

Investigations of Anomalous Earthquakes at Active Volcanoes

Ashley Elizabeth Shuler

This dissertation investigates the link between volcanic unrest and the occurrence of moderate-to-large earthquakes with a specific type of focal mechanism. Vertical compensated-linear-vector-dipole (vertical-CLVD) earthquakes have vertical pressure or tension axes and seismic radiation patterns that are inconsistent with the double-couple model of slip on a planar fault. Prior to this work, moderate-to-large vertical-CLVD earthquakes were known to be geographically associated with volcanic centers, and vertical-CLVD earthquakes were linked to a tsunami in the Izu-Bonin volcanic arc and a subglacial fissure eruption in Iceland. Vertical-CLVD earthquakes are some of the largest and most anomalous earthquakes to occur in volcanic systems, yet their physical mechanisms remain controversial largely due to the small number of observations.

Five vertical-CLVD earthquakes with vertical pressure axes are identified near Nyiragongo volcano in the Democratic Republic of the Congo. Three earthquakes occur within days of a fissure eruption at Nyiragongo, and two occur several years later in association with the refilling of the lava lake in the summit crater of the volcano. Detailed study of these events shows that the earthquakes have slower source processes than tectonic earthquakes with similar magnitudes and locations. All five earthquakes are interpreted as resulting from slip on inward-dipping ring-fault structures located above deflating shallow magma chambers. The Nyiragongo study supports the interpretation that vertical-CLVD earthquakes may be causally related to dynamic physical processes occurring inside the edifices or magmatic plumbing systems of active volcanoes.

Two seismicity catalogs from the Global Centroid Moment Tensor (CMT) Project are used to search for further examples of shallow earthquakes with robust vertical-CLVD focal mechanisms. CMT solutions for approximately 400 target earthquakes are calculated and 86 vertical-CLVD earthquakes are identified near active volcanoes. Together with the Nyiragongo study, this work increases the number of well-studied vertical-CLVD earthquakes from 14 to 101. Vertical-CLVD earthquakes have focal depths in the upper ~10 km of the Earth's crust, and ~80% have centroid locations within 30 km of an active volcanic center. Vertical-CLVD earthquakes are observed near several different types of volcanoes in a variety of geographic and tectonic settings, but most vertical-CLVD earthquakes are observed near basaltic-to-andesitic stratovolcanoes and submarine volcanoes in subduction zones. Vertical-CLVD earthquakes are linked to tsunamis, volcanic earthquake swarms, effusive and explosive eruptions, and caldera collapse, and approximately 70% are associated with documented volcanic eruptions or episodes of volcanic unrest. Those events with vertical pressure axes typically occur after volcanic eruptions initiate, whereas events with vertical tension axes commonly occur before the start of volcanic unrest. Both types of vertical-CLVD earthquakes have longer source durations than tectonic earthquakes of the same magnitude.

The isotropic and pure vertical-CLVD components of the moment tensor cannot be independently resolved using our long-period seismic dataset. As a result, several physical mechanisms can explain the retrieved deviatoric vertical-CLVD moment tensors, including dip-slip motion on ring faults, volume exchange between two reservoirs, the opening and closing of tensile cracks, and volumetric sources. An evaluation of these mechanisms is performed using constraints obtained from detailed studies of individual vertical-CLVD earthquakes. Although no single physical mechanism can explain all of the characteristics of vertical-CLVD earthquakes, a

ring-faulting model consisting of slip on inward- or outward-dipping ring faults triggered by the inflation or deflation of a shallow magma chamber can account for their seismic radiation patterns and source durations, as well as their temporal relationships with volcanic unrest. The observation that most vertical-CLVD earthquakes are associated with volcanoes with caldera structures supports this interpretation.

Table of Contents

List of Figures ii

List of Tables ..... *iv*

Acknowledgements ..... *v*

Dedication ..... *vii*

Introduction 1

Chapter 1: *Anomalous earthquakes associated with Nyiragongo volcano: Observations and potential mechanisms* 7

Chapter 2: *Global observation of vertical-CLVD earthquakes at active volcanoes* 42

Chapter 3: *Physical mechanisms for vertical-CLVD earthquakes at active volcanoes* 106

Concluding Remarks 162

References 169

Appendix A: *Supplementary Information for Chapter 2* 195

Appendix B: *Earthquake source parameters for the 2010 western Gulf of Aden rifting episode* 219

Appendix C: *Supplementary Information for Appendix B* 254

List of Figures

Chapter 1: *Anomalous earthquakes associated with Nyiragongo volcano: Observations and potential mechanisms*

Figure 1.1. Shaded relief map of the Virunga Volcanic Complex 9
Figure 1.2. Temporal distribution of seismicity associated with the 2002 eruption of Nyiragongo Volcano 14
Figure 1.3. Surface-wave detection method 18
Figure 1.4. Example record section 19
Figure 1.5. Unfiltered seismograms 21
Figure 1.6. Frequency spectra 22
Figure 1.7. Spectrograms 23
Figure 1.8. Comparison of observed and synthetic seismograms 27
Figure 1.9. Focal mechanisms for newly detected earthquakes 29
Figure 1.10. Schematic diagram of ring-faulting mechanisms 39

Chapter 2: *Global observation of vertical-CLVD earthquakes at active volcanoes*

Figure 2.1. Criteria for the two types of vertical-CLVD earthquakes 46
Figure 2.2. Map of recently active volcanoes and target earthquakes 51
Figure 2.3. Focal mechanisms for all target earthquakes 58
Figure 2.4. Comparison between original and recalculated CMT solutions 61
Figure 2.5. Map of focal mechanisms for vertical-CLVD earthquakes from the Global CMT catalog 63
Figure 2.6. Map of focal mechanisms for vertical-CLVD earthquakes from the Surface Wave catalog 64
Figure 2.7. Map of focal mechanisms for vertical-CLVD earthquakes at Miyakejima Volcano 65
Figure 2.8. Teleseismic body-wave modeling 70
Figure 2.9. Map of focal mechanisms for vertical-CLVD earthquakes at Vailulu'u volcano 78
Figure 2.10. Temporal relationships between vertical-CLVD earthquakes and volcanic unrest 103

Chapter 3: *Physical mechanisms for vertical-CLVD earthquakes at active volcanoes*

Figure 3.1. Map of 101 vertical-CLVD earthquakes 109
Figure 3.2. Teleseismic body-wave modeling 117
Figure 3.3. Scalar moment vs. source duration for vertical-CLVD earthquakes 120
Figure 3.4. Magnitude distributions of vertical-CLVD earthquakes by source catalog 123
Figure 3.5. Examination of covariance matrix 127
Figure 3.6. Full moment-tensor solutions for vertical-CLVD earthquakes 129
Figure 3.7. Schematic diagram for ring faults 133
Figure 3.8. Effect of ring fault dip angle and arc angle of rupture on source parameters of vertical-CLVD earthquakes 137

Figure 3.9. Effects of ring-fault orientation and direction of relative motion on composite moment tensors for ring-faulting earthquakes 139
Figure 3.10. Results of inverting source parameters for vertical-CLVD earthquakes for ring fault dip and arc angles..... 141
Figure 3.11. Comparison between the measured fault scarp and focal mechanism for the vertical-CLVD earthquakes resulting from a trapdoor-faulting event at Sierra Negra in 2005 144

Appendix B*: Earthquake source parameters for the 2010 western Gulf of Aden rifting episode*
Figure B1. Map of the western Gulf of Aden and surroundings..... 221
Figure B2. Map of the centroid locations 225
Figure B3. Cumulative seismic moment and temporal distribution of earthquakes by magnitude 226
Figure B4. Map of focal mechanisms for western Gulf of Aden..... 230
Figure B5. Lateral propagation of seismicity..... 232
Figure B6. Tension axes 233
Figure B7. Teleseismic body-wave modeling..... 235

List of Tables

Chapter 1*: Anomalous earthquakes associated with Nyiragongo volcano: Observations and potential mechanisms*

Table 1.1. Dates, times and magnitudes of newly detected earthquakes at Nyiragongo volcano 10

Table 1.2. Source parameters for newly detected earthquakes at Nyiragongo volcano 26

Chapter 2*: Global observation of vertical-CLVD earthquakes at active volcanoes*

Table 2.1. Source parameters for shallow vertical-CLVD earthquakes located near recently active volcanoes 66

Table 2.2. Volcanoes located near shallow vertical-CLVD earthquakes 72

Chapter 3*: Physical mechanisms for vertical-CLVD earthquakes at active volcanoes*

Table 3.1. Results of broadband body-wave modeling 119

Appendix A: *Supplementary Information for Chapter 2*

Table A1. CMT solutions for target earthquakes from the Global CMT catalog 199

Table A2. Principal axes and best-double-couple parameters for target earthquakes from the Global CMT catalog 202

Table A3. CMT solutions for Category 1 target earthquakes from the Surface Wave catalog 205

Table A4. Principal axes and best-double-couple parameters for Category 1 target earthquakes from the Surface Wave catalog 207

Table A5. CMT solutions for Category 2 target earthquakes from the Surface Wave catalog 209

Table A6. Principal axes and best-double-couple parameters for Category 2 target earthquakes from the Surface Wave catalog 212

Table A7. CMT solutions for vertical-CLVD earthquakes 215

Table A8. Principal axes and best-double-couple parameters for vertical-CLVD earthquakes 217

Appendix B*: Earthquake source parameters for the 2010 western Gulf of Aden rifting episode*

Table B1. Focal-depth estimates determined by broadband analysis 235

Appendix C*: Supplementary Information for Appendix B*

Table C1. CMT solutions for western Gulf of Aden earthquakes 257

Table C2. Principal axes and best-double-couple parameters for western Gulf of Aden earthquakes 260

Acknowledgements

I am deeply grateful to my advisors, Göran Ekström and Meredith Nettles, for their generous support and constructive ideas. Thank you for encouraging me to pursue a wide variety of research topics, even when they were completely unrelated to my dissertation. You have provided excellent examples of what it means to be a successful and productive seismologist. Thank you to the remaining members of my thesis committee, James Gaherty, Bill Menke, and Cindy Ebinger, for your time and consideration. Cindy, thank you for your support and enthusiasm, and for introducing me to many new colleagues in the East African Rift community. Thank you also to Christopher Bean, Manahloh Belachew, Bill Chadwick, Nicholas d'Oreye, Eoghan Holohan, Gareth O'Brien, Steve Saunders, and Dario Tedesco for helpful conversations.

Thank you to the members of the 2008 and 2009 PIRE teams, especially Michael West, Jeff Freymueller, Pavel Izbekov, Helena Buurman, Ronni Grapenthin, Taryn Lopez, Theresa Kayzar, Alex Nikulin, Owen Neill, Richard Sanderson, Agathe Schmid, and our Russian colleagues, Sergey Ushakov, Sergey Senyukov, Sergey Serovetnikov, Sasha Belousov, and Marina Belousova. Some of my fondest memories are of the times we spent exploring volcanoes in Kamchatka. Thank you to also to Vadim Levin for your support and encouragement, and for reminding me to achieve a work-life balance.

Thank you to Jennifer Arbuszewski, Adrienne Block, Antonio Buono, Janet Fang, Jennifer Levy-Varon, and Danielle Sumy, my closest friends at Lamont-Doherty Earth Observatory. Thank you for sharing many fun experiences with me over the past six years, and for supporting and

encouraging me intellectually and personally. Thank you also to the many current and past Lamonters who helped me with my research in one way or another, especially Roger Buck, Colleen Dalton, Anna Foster, Vala Hjörleifsdóttir, Ben Holtzman, Howie Koss, Philipp Ruprecht, Donna Shillington, and Liz Starin, as well as my summer intern, Siobhan Campbell.

Above all else, I am grateful to my family for their love, patience, and support during this arduous process. Thank you to my husband, Jeremy Estey, for keeping me calm when I am feeling overwhelmed, and for always encouraging me to push forward. Thank you for being such a devoted and loving partner. I acknowledge and appreciate the personal sacrifices you have made so I can achieve my dreams. Thank you to my parents, Russell and Fran Shuler, for telling me that you are proud of me in every conversation. Thank you for always being excited about whatever I am doing. Mom, I would never have made it here if you had not shared your rock collection with me when I was a little girl. Thank you also to my grandmother, Sara Gibson, my uncle, Barry Shuler, and my mother-in-law, Sharlene Estey.

As a graduate student, I have been funded by Columbia University, a National Science Foundation Graduate Research Fellowship, NSF Grants EAR-0639963 and EAR-0944055, and a Geological Society of America Research Grant. I have also received travel funding from IAVCEI, UNAVCO, and an NSF PIRE Grant awarded to the University of Alaska Fairbanks.

Two chapters in this dissertation were previously published in *Journal of Volcanology and Geothermal Research* and *Geophysical Journal International*, and are reprinted here with permission granted by Elsevier Limited and John Wiley and Sons.

Dedication

For my husband, Jeremy, with endless love and appreciation.

Introduction

Understanding how magma ascends through the crust and erupts on the surface is one of the fundamental challenges of earth science. Along the mid-ocean ridge system, submarine volcanoes create new oceanic crust, and in continental rifts, island arcs, and convergent margins, as well as above mantle plumes, thousands of subaerial volcanoes create dramatic landscapes and produce fertile soils and rich mineral deposits. Volcanoes shape the surface of our planet, and in doing so, threaten the safety and livelihoods of millions of people. Volcanic hazards such as lava and pyroclastic flows, lahars, landslides, ash fall, and toxic gases endanger settlements and infrastructure in the vicinity of active volcanoes, and hazards such as ash dispersal in the atmosphere and climate change can affect the global population.

One of the most reliable techniques for monitoring active volcanoes is volcano seismology. Volcanic earthquakes are generated by a wide variety of processes including brittle fracture, fluid flow, mass transport and explosions [*Chouet,* 2003; *McNutt,* 2005; *Kumagai*, 2009; *Zobin,* 2011]. By observing, analyzing, and interpreting volcanic earthquakes, we can learn about dynamic processes occurring inside the edifices and magmatic plumbing systems of active volcanoes. Most volcanic earthquakes are small, and can only be observed by seismometers deployed close to the source region. However, on rare occasions, volcanic earthquakes are large enough to be detected globally. Often the largest volcanic earthquakes have unusual source properties and are linked to magmatic intrusions or volcanic eruptions [*Filson et al*., 1973; *Francis*, 1974; *Kanamori et al*., 1993; *Nettles and Ekström*, 1998; *Dreger et al*., 2000; *Kumagai et al*., 2001; *Minson et al*., 2007].

Some of the largest and most anomalous earthquakes to occur near volcanoes are the 1984 M_W 5.6 Tori Shima earthquake, which occurred near a large submarine volcano in the Izu-Bonin volcanic arc [*Kanamori et al.,* 1993], and the series of ten $5.1 \leq M_W \leq 5.6$ earthquakes that took place near Bárdarbunga volcano in Iceland between 1976 and 1996 [*Nettles and Ekström*, 1998]. These earthquakes have dominant vertical tension axes and moment tensors with large compensated-linear-vector-dipole (CLVD) components [*Knopoff and Randall*, 1970]. In addition to having anomalous seismic radiation patterns, these vertical-CLVD earthquakes are linked to volcanic activity. The Tori Shima earthquake produced a disproportionately large tsunami [*Satake and Kanamori*, 1991], and the final Bárdarbunga earthquake occurred only days before a large subglacial fissure eruption [*Nettles and Ekström,* 1998].

Moderate-to-large earthquakes with focal mechanisms similar to the Tori Shima and Bárdarbunga events occur most frequently near volcanic centers [*Ekström,* 1994]. However, these earthquakes are rare, and prior to this dissertation, only 14 vertical-CLVD earthquakes near volcanoes had been studied [*Kanamori et al.,* 1993; *Ekström,* 1994; *Nettles and Ekström*, 1998]. The azimuthally symmetric seismic radiation patterns of these earthquakes cannot be explained by the double-couple model for shear failure on planar faults, and suggested physical mechanisms include magma and/or fluid injection [*Kanamori et al., 1993; Konstantinou et al*., 2003; *Tkalčić et al*., 2009] and slip on volcanic ring-fault structures [*Ekström*, 1994; *Nettles and Ekström*, 1998]. Due to the small number of observations, the links between the occurrence of vertical-CLVD earthquakes and volcanic deformation processes remain controversial and poorly understood.

In this dissertation, we use global seismic data to investigate the relationship between shallow, moderate-to-large vertical-CLVD earthquakes and volcanic unrest. In addition to examining vertical-CLVD earthquakes with dominant vertical tension axes, such as the Tori Shima and Bárdarbunga events, we also consider vertical-CLVD earthquakes with dominant pressure axes. This work begins with a case study of five vertical-CLVD earthquakes at a single volcano, after which we perform a systematic global search for vertical-CLVD earthquakes located near volcanoes with known eruptions in the last ~100 years.

We identify vertical-CLVD earthquakes and describe their source properties by calculating centroid-moment-tensor (CMT) solutions [*Dziewonski et al.,* 1981; *Arvidsson and Ekström,* 1998; *Ekström et al.,* 2012], modeling teleseismic body waves [*Ekström,* 1989], and examining frequency spectra. We document in detail how vertical-CLVD earthquakes are related spatially and temporally to episodes of unrest at nearby volcanoes, and evaluate a variety of potential physical mechanisms for producing these earthquakes. This work increases the number of well-studied vertical-CLVD earthquakes located near volcanoes from 14 to 101 and greatly improves our understanding of how these earthquakes are linked to large-scale magma migration and volcanic eruptions.

In Chapter 1, we investigate a series of five $4.6 \leq M_W \leq 5.3$ vertical-CLVD earthquakes that took place near Nyiragongo volcano in the Democratic Republic of the Congo between 2002 and 2005. These earthquakes are missing from standard global-seismicity catalogs, and were only detected using intermediate-period surface waves [*Ekström,* 2006]. The first three earthquakes

occurred days after a large-scale fissure eruption at Nyiragongo, and the final two earthquakes occurred a few years later, as the lava lake in the summit crater of the volcano began to refill. We present CMT solutions for these earthquakes and compare the frequency content of their seismic radiation with that of tectonic earthquakes with similar magnitudes and locations. We explain our observations using a volcano-tectonic mechanism, in which the earthquakes are generated by the collapse of the roof of a shallow magma chamber. This work was published in *Journal of Volcanology and Geothermal Research* [*Shuler and Ekström*, 2009].

In Chapter 2, we perform a systematic global search for additional examples of vertical-CLVD earthquakes near active volcanoes. We select approximately 400 target earthquakes from the Global CMT catalog, and a catalog of earthquakes detected using surface waves [*Ekström,* 2006]. We recalculate CMT solutions for vertical-CLVD earthquakes in the Global CMT catalog using additional data and updated methodology, and present the first CMT solutions for target earthquakes from the Surface Wave Catalog. In total, we identify 86 shallow vertical-CLVD earthquakes with magnitudes $4.3 \leq M_W \leq 5.8$ located near active volcanoes. We examine the tectonic settings where these earthquakes occur and search for trends regarding volcano type. Approximately 70% of the vertical-CLVD earthquakes are associated with reported volcanic unrest, and we document these episodes in detail in order to shed light on the relationships between the earthquakes and dynamic volcanic processes. This work has been submitted to *Journal of Geophysical Research – Solid Earth.*

In Chapter 3, we further investigate our dataset of vertical-CLVD earthquakes. We build on our work from Chapters 1 and 2, and perform additional analyses in order to gain insight into the

physical mechanisms that produce vertical-CLVD earthquakes. We model the teleseismic body waves and examine the frequency contents of vertical-CLVD earthquakes. Although vertical-CLVD earthquakes are defined by the properties of their deviatoric moment tensors, we also explore the possibility that these earthquakes may have non-zero isotropic components caused by net volume changes. We quantify the tradeoff between the isotropic and pure vertical-CLVD components of the moment tensor for our dataset by examining covariance matrices. We calculate full moment-tensor solutions and identify a range of physical mechanisms that can explain the anomalous seismic radiation patterns of vertical-CLVD earthquakes. Using our observations of vertical-CLVD earthquakes, we evaluate a range of potential mechanisms including slip on ring-fault structures, volume exchange between two reservoirs, opening and closing tensile cracks and volumetric sources. This work has been submitted to *Journal of Geophysical Research – Solid Earth* as a companion paper to the work presented in Chapter 2.

We provide a summary of the major findings from this dissertation and discuss several remaining questions regarding vertical-CLVD earthquakes in the Concluding Remarks section.

In Appendix B, we present the results of a study published in *Geophysical Journal International* [*Shuler and Nettles*, 2012]. The subject of this paper is not vertical-CLVD earthquakes at active volcanoes, but rather an intense swarm of earthquakes that took place in the western Gulf of Aden beginning on 14 November 2010. This swarm occurred on an ~80-km-long segment of the Aden Ridge that is evolving from a continental rift into a mid-ocean ridge. Previously, this section of the ridge was characterized by low levels of seismicity and a lack of recent volcanism on the seafloor. We present CMT solutions for 110 earthquakes with magnitudes $4.5 \leq M_W \leq 5.5$

that occurred between November 2010 and April 2011, and model the body waves for four of the largest earthquakes. We interpret the source parameters for this sequence in light of the slow spreading rate and oblique style of rifting occurring along the nascent Aden Ridge. Based on the similarities between this sequence and dike-induced rifting episodes in continental and oceanic settings, we conclude that the swarm was caused by laterally propagating dike intrusions that accommodated several meters of opening. The rifting episode demonstrates the westward propagation of active seafloor spreading into this section of the Gulf of Aden.

Chapter 1

Anomalous earthquakes associated with Nyiragongo volcano: Observations and potential mechanisms

A slightly modified version of this work has been published as:
Shuler, A., and G. Ekström (2009), Anomalous earthquakes associated with Nyiragongo volcano: Observations and potential mechanisms, *J. Volcanol. Geotherm. Res., 181*(3-4), 219-230, doi:10.1016/j.jvolgeores.2009.01.011.

Abstract

A series of five unusual earthquakes ($4.6 \leq M_W \leq 5.3$) took place near Nyiragongo volcano (D. R. Congo) in the Western Rift Valley of the East African Rift. Despite their moderate size, these earthquakes are missing from global seismicity catalogs, and were only recently located using long-period surface waves primarily recorded on the Global Seismographic Network. Three earthquakes occurred in the week following the January 2002 eruption of Nyiragongo, but the final two earthquakes, which occurred in 2003 and 2005, are not linked to a major eruption at either Nyiragongo or its neighboring volcano, Nyamuragira. Several common techniques were used to investigate the characteristics of these seismic sources in the context of the volcanic activity in the region. Compared to local earthquakes reported in global seismicity catalogs, the newly detected events are depleted in frequencies above 0.1 Hz, and their frequency contents suggest that they are slow earthquakes. Each of the newly detected earthquakes was modeled by a series of forces and by a centroid-moment tensor. A deviatoric moment tensor was shown to provide a better fit to the data. The newly detected earthquakes are highly non-double-couple in nature, each having a large compensated-linear-vector-dipole component of the moment tensor. Drawing on models based on similar observations from other active volcanoes, we propose that the earthquakes are caused by slip on non-planar faults located beneath the volcano. We suggest a mechanism in which the newly detected earthquakes are generated by the collapse of the roof

of a shallow magma chamber along inward-dipping, cone-shaped ring faults. Diking events, which result in magma evacuation from shallow magma chambers, could trigger such earthquakes. Our results provide new constraints on the dynamics of the poorly understood magma system beneath Nyiragongo, an active volcano that is a significant threat to life and property.

1.1. Introduction

The Virunga Volcanic Complex consists of eight volcanoes aligned in an east-west configuration, nearly perpendicular to the axis of the Western Rift Valley of the East African Rift (Figure 1.1). Of these, only Nyiragongo and Nyamuragira are active today. While Nyamuragira remains one of Africa's most active volcanoes with regular eruptions every few years, Nyiragongo has been the subject of numerous studies for decades. Nyiragongo is renowned for containing a semi-permanent lava lake in its summit crater, a feature shared by fewer than a dozen volcanoes worldwide.

In 1977, this lava lake was completely drained in a matter of minutes during a lateral eruption [*Durieux*, 2002/2003b]. The lava lake began to refill in 1982, and existed at varying levels inside the summit crater until it was emptied once again during the catastrophic eruption on 17 January 2002. This eruption was characterized by fast-moving lava flows that destroyed roughly 15% of Goma, a city of more than half a million people on the banks of Lake Kivu in the Democratic Republic of the Congo [*Komorowski et al.,* 2002/2003]. The lava lake reappeared in late 2002, and since then, eruptive activity characterized by intermittent lava fountaining has remained confined to the summit crater.

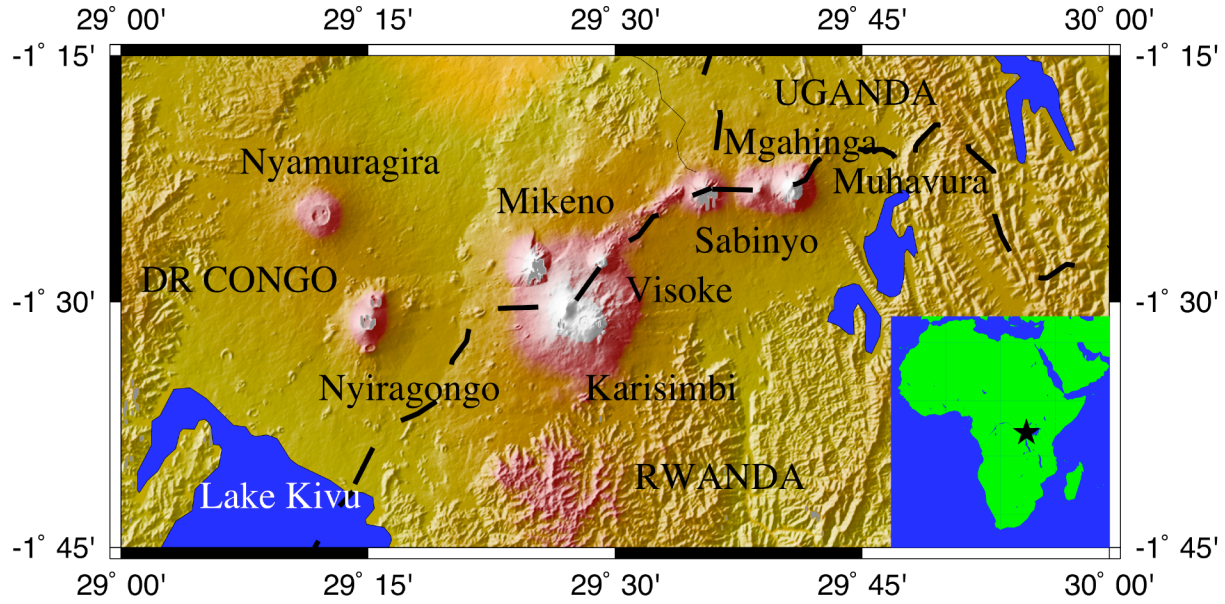

Figure 1.1. Shaded relief map of the Virunga Volcanic Complex. Eight volcanoes are aligned roughly perpendicular to the rift axis. Of these, only Nyiragongo and Nyamuragira are still active. The dashed lines indicate political boundaries. Topography is from the Shuttle Radar Topography Mission (SRTM).

Between 2002 and 2005, five unusual earthquakes ($4.6 \leq M_W \leq 5.3$) occurred near Nyiragongo volcano (Table 1.1). Three earthquakes occurred within one week of the January 2002 eruption, and the final two earthquakes occurred in 2003 and 2005 and are not linked to a significant eruption at either Nyiragongo or its neighboring volcano, Nyamuragira. Although these shallow earthquakes are of moderate size, they went unrecorded in global seismicity catalogs, which routinely contain information concerning events of lesser magnitudes [*Woessner and Wiemer*, 2005]. New techniques involving detailed analysis of long-period surface wave data primarily from the Global Seismographic Network (GSN) allowed these events to be located, however. In this chapter, we investigate the characteristics of these newly detected events. We present our findings in the context of the eruptive history of the volcano, and evaluate a number of potential

physical mechanisms to explain these anomalous earthquakes. Ultimately, we work towards constraining the geometry and dynamics of the magma system beneath Nyiragongo volcano for future mitigation purposes.

Event	Date	Origin Time (UTC)	M_W
1	1/21/2002	21:10:32	5.3
2	1/22/2002	5:41:44	5.3
3	1/22/2002	14:22:56	4.6
4	5/17/2003	11:46:24	4.6
5	4/15/2005	20:35:36	4.7

Table 1.1. Newly Detected Events. The origin time is determined by the maximum of the peak in the stacked waveforms when there is a 0.25-degree grid of target locations. The values of M_W are from the CMT inversions.

1.2. Background

1.2.1. Regional Setting

Nyiragongo and Nyamuragira are located in the Kivu Rift Basin, which is one of a series of extensional basins that comprise the Western Rift Valley. While Nyamuragira (elevation of 3058 m) is a symmetrical shield volcano, Nyiragongo (3470 m) is a stratovolcano that extends roughly 2 km above the elevation of Lake Kivu. As these volcanoes are located in the axis of one of the world's largest continental rifts, they are sensitive to regional tectonics. In general, volcanism at Nyiragongo and Nyamuragira is believed to be directly related to the opening of the Western Rift Valley, and the creation of a new plate boundary there [*Kasahara et al.,* 1992]. The volcanoes are located in accommodation zones where deep faults presumably reach magmatic reservoirs [*Ebinger and Furman*, 2002/2003]. The 2002 eruption of Nyiragongo is interpreted as being synchronous with fracturing and fault slip in the rift valley, and it has been suggested that a significant rifting event in the Nyiragongo-Lake Kivu area fractured the edifice of Nyiragongo,

leading to a massive fissure eruption that emptied magma stored in the upper conduit and lava lake [*Komorowski et al.*, 2002/2003; *Tedesco et al*., 2007].

1.2.2. January 2002 Eruption of Nyiragongo

Although more complete descriptions of the 17 January 2002 eruption of Nyiragongo can be found in a number of references [*Allard et al*., 2002; *Komorowski et al*., 2002/2003; *Tedesco et al*., 2007], we provide a short description of key features here.

Eruption Overview

A number of precursory signals were observed in the weeks and months leading up to the 17 January 2002 eruption of Nyiragongo. These signals included fracturing and fumarolic activity on the southern slopes of the volcano and escalating seismicity beginning on 4 January. Volcanic long-period earthquakes increased in both magnitude and frequency prior to the eruption. These were often followed by several minutes of volcanic tremor, indicating that magma was moving at depth [*Kavotha et al.,* 2002/2003].

The eruption started on the morning of 17 January, when the extensive fracture system of the 1977 eruption reopened on the southern flank of the volcano. The initial fractures ruptured the edifice of the volcano, triggering the eruption of highly fluid, largely degassed magma that had been stored in the lava lake and upper conduit since a period of vigorous lava-lake activity in 1994-1995. An eruptive plume did not develop until 25-45 min after the start of the eruption [*Carn*, 2002/2003]. This is taken to indicate that the eruption was not caused by gas overpressure

in the shallow magma chamber, but was instead a result of fracturing caused by a regional rifting event.

Over the next few hours, additional north-south-trending parallel fractures opened, and a series of grabens propagated downwards from the base of the volcano towards the city of Goma. This extensive system of radial fractures propagated for a distance of 20 km from the top of the volcano, significantly further than the fracture system of the 1977 eruption [*Allard et al*., 2002]. The later fractures, which erupted gas-rich magma in forceful lava fountains, are believed to have been caused by magma ascent resulting from depressurization of the shallow magmatic system caused by the initial fracturing of the volcanic edifice [*Tedesco et al*., 2007]. Lava flows from these later fractures inundated the city of Goma, dividing it in two. It is estimated that between 14 and 34 million cubic meters of lava were erupted over a period of 12 hours or less during the January 2002 eruption [*Tedesco et al*., 2007]. Lava continued to flow towards Lake Kivu for several days following the end of the eruption.

Crater Collapse

Although the eruption on 17 January drained magma from the lava lake and upper conduit, the surface of the lava lake, which had been solidified since 1995, did not collapse. A helicopter flight over the summit of the volcano confirmed that the solidified lava lake floor was still in place on 21 January. The surface, however, was cut by a series of concentric fractures and fumaroles [*Smithsonian Institution*, 2002; *Tedesco et al*., 2007]. The weakened lava-lake surface, along with several solidified terraces, evidently collapsed during the night of 22 January. The start of the collapse was marked by a series of felt earthquakes, and was followed by four hours

of continuous seismic tremor and ashfall over the immediate area [*Komorowski et al.*, 2002/2003]. The intense tremor is attributed to phreatomagmatic explosions caused by the interaction of groundwater with the high-temperature volcanic material below. Despite the occurrence of these explosions, no significant emissions of sulfur dioxide were observed in association with the collapse, indicating that negligible magma was degassed during this process [*Carn*, 2002/2003]. A flight over Nyiragongo on 24 January revealed that the previously flat solidified lava-lake surface, which had persisted at an elevation of 280 m beneath the rim of the volcano since 1995, had collapsed to form an inverted conical crater with a maximum depth of approximately 900 m [*Tedesco et al.*, 2007].

Post-Eruption Seismicity

One of the most striking features of the 2002 eruption was the intense seismic activity that followed. Approximately 100 tectonic earthquakes ($M > 3.5$) were located in the region within five days of the eruption [*Tedesco et al.*, 2007]. The number of located earthquakes increased following the eruption, and although seismicity levels declined with time, they remained anomalously high for several weeks following the eruption.

Figure 1.2 shows the temporal distributions of the newly located earthquakes as well as earthquakes described in the National Earthquake Information Center (NEIC) catalog from 16 to 25 January 2002. All of these earthquakes occurred between the beginning of the eruption and the collapse of the summit crater. The number of earthquakes occurring each day increased from 17 to 22 January, reaching a maximum on the same day that the crater collapsed. No earthquakes were located near Nyiragongo in the 13 days leading up to the eruption, or in the 8 days

following the crater collapse. This pattern is very unusual, as seismicity typically decreases rapidly after an eruption removes local stresses [*Zobin*, 2003]. The duration and intensity of the post-eruption seismicity cannot be explained by ground compaction and lava drainage alone, and is believed to be one of the chief pieces of evidence that a local rifting event caused the 2002 eruption [*Komorowski et al*., 2002/2003].

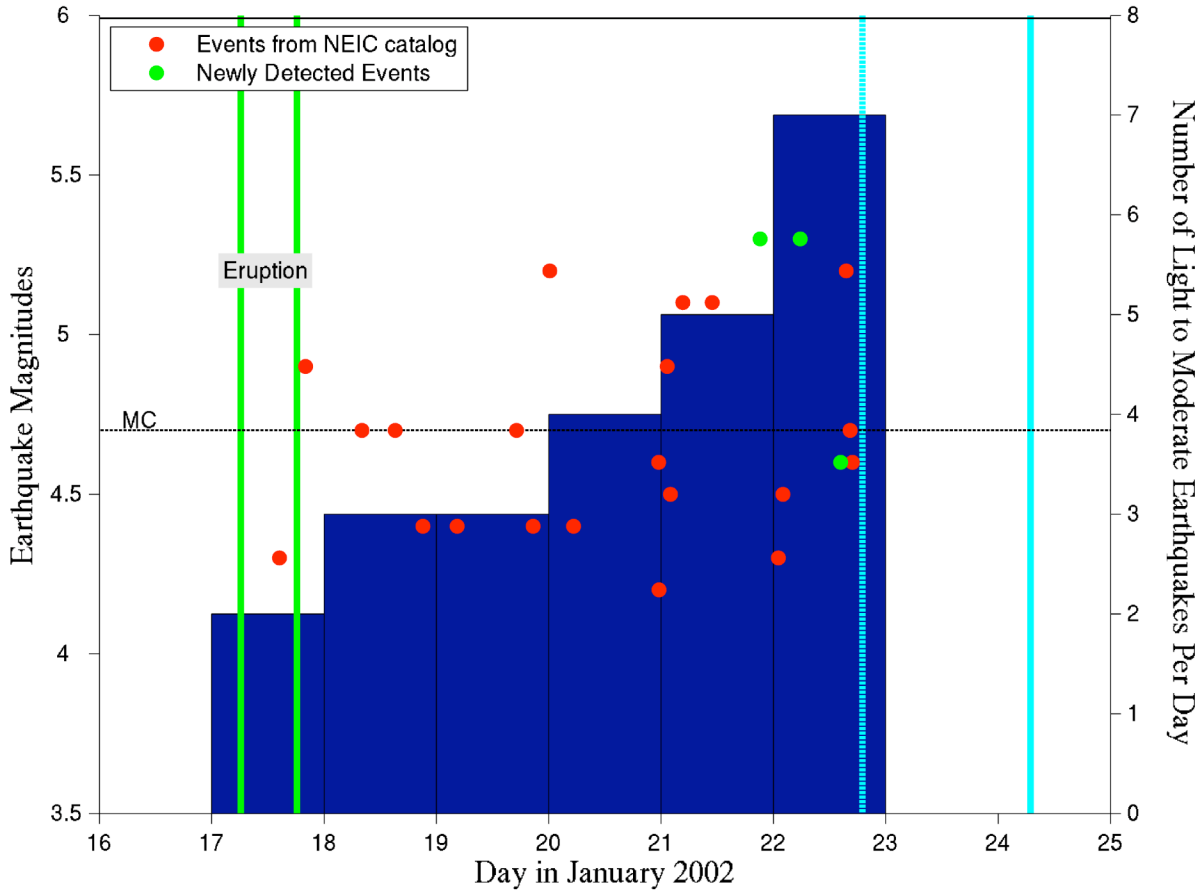

Figure 1.2. Temporal distribution of seismicity associated with the 2002 eruption of Nyiragongo. The red dots denote earthquakes described in the NEIC catalog, and the green dots denote the newly detected events. The magnitude of completeness, MC, was calculated by assuming standard Gutenberg-Richter relationships for seismicity within a 100-kilometer radius of Nyiragongo as described in the NEIC catalog. The blue bars in the background show the number of earthquakes that occurred each day. The two green lines indicate the beginning and end of the eruption. The first blue line indicates when the collapse of the summit crater is assumed to have taken place from seismic observations and local reports. The last blue line indicates when the crater collapse was confirmed by a helicopter survey. Times are UTC.

The spatial distribution of the earthquakes was also quite atypical. The majority of long-period events were located in the Nyamuragira area, northwest of Nyiragongo [*Kavotha et al*., 2002/2003]. These are attributed to inflation of Nyamuragira's magma chamber prior to its eruption in the summer of 2002. The majority of short-period events, however, were located south of Nyiragongo, in the area between the volcano and Lake Kivu. These events occur in roughly the same location as the majority of fractures and fissures produced in the eruption. This same area also experienced significant subsidence following the eruption, up to ~80 cm in some areas [*Tedesco et al*., 2007]. Modeling of radar interferograms suggests that the rift valley experienced deformation related to a period of horizontal extension, which lasted no longer than one month following the eruption [*Poland and Lu*, 2004]. These observations further support the hypothesis that the eruption was caused by a regional rifting event, which most likely involved continued injection of dikes below the rift graben for several days after the eruption. We investigate the relationship between the collapse of the summit crater and the cessation of seismicity later in this chapter.

1.2.3. Nyiragongo's Post-Eruption Activity (2002-2005)

The presence of the lava lake in Nyiragongo's summit crater enables changes in the dynamics of the magmatic system to be discerned. Decades of observations of the lava lake indicate that Nyiragongo has experienced several cycles of crater collapse followed by refilling of the lava lake and finally lateral eruptions [*Durieux*, 2002/2003]. Following a period of vigorous activity in 1994-1995, the surface of the lava lake began to crust over, forming a solid layer that remained in place until 2002. The presence of this layer indicates that the system remained rather stable, and was not significantly recharged during this period.

After the January 2002 eruption and subsequent collapse of the summit crater, lava fountaining reappeared in the crater in the summer of 2002. This activity was intense at times, sending volcanic material several hundred meters into the air and generating dense ash plumes [*Smithsonian Institution*, 2003]. The refilling of the lava lake coincided with a period of intense degassing confirmed by the satellite measurement of sulfur dioxide emissions [*Carn,* 2002/2003]. The days of peak emissions were accompanied by long-period earthquakes attributed to magma migration [*Smithsonian Institution*, 2003]. The fourth event in this study occurred during this period of especially vigorous degassing as the lava lake was recharged from a deeper source [*Carn*, 2002/2003].

Following this period of intense degassing, Nyiragongo entered a phase of steady-state convection marked by a decrease in sulfur dioxide emission concentrations [*Sawyer et al*., 2008]. The fifth newly detected event occurred during this relatively calm period, when the lava lake was not convecting vigorously. The final two earthquakes occurred during periods of greatly contrasting degassing activity, and therefore seem essentially unrelated to shallow magmatic processes. These observations suggest a deeper source for these events. Interferograms provide no evidence of significant surface deformation associated with the final two earthquakes [*Poland*, 2008, personal communication], and no local earthquakes are reported in the NEIC catalog.

1.3. Seismic Observations

1.3.1. Method of Detection

Global seismicity catalogs, such as the bulletins of the International Seismological Centre (ISC) and the NEIC, contain earthquakes that are detected and located using the arrival times of short-period body-wave phases. While this method is appropriate for most earthquakes, seismic sources that are deficient in high-frequency energy may go undetected. The five earthquakes in our study were located using the method of *Ekström* [2006], which detects events using long-period (35-150 s) surface-wave data. This method uses vertical-component data collected from the GSN and a global grid of target locations. For each target location, a surface-wave propagation operator is deconvolved from the seismograms from each station to remove effects such as dispersion and geometric spreading. The envelopes of these signals are cross-correlated with a theoretical source-pulse shape to determine the likelihood that a seismic event occurred at a given place and time. Envelopes are stacked to improve visualization (Figure 1.3).

The application of the method of *Ekström* [2006] to seismic data from 1991-2006 has resulted in the location of over 1700 seismic events that are not described in the NEIC or ISC catalogs [*Ekström*, 2007, personal communication]. Many of the newly detected seismic events have anomalous source characteristics, and some have been shown to be associated with newly observed or unusual seismogenic processes. For example, subsets of these events are related to landslides [*Ekström*, 2007] and to the movement of glaciers [*Ekström et al*., 2003]. The five earthquakes we investigate in this chapter are another subset of the Surface Wave catalog. An example record section for one of the newly detected Nyiragongo events is shown in Figure 1.4. It clearly shows the moveout of long-period body and surface wave phases with distance away

from the well-located source. We investigate potential physical mechanisms for these earthquakes, in an attempt to illuminate changes in the dynamics of Nyiragongo volcano.

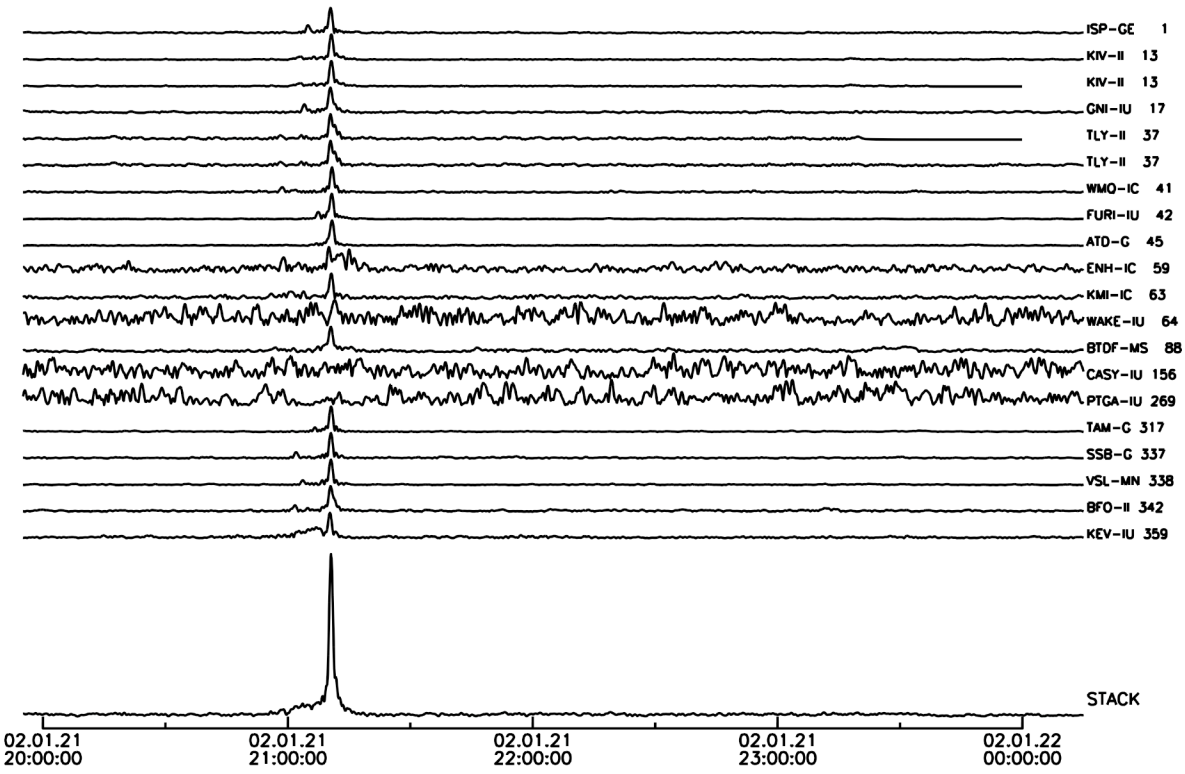

Figure 1.3. Long-period seismograms (35-150 s period) for the first newly detected event (21 January 2002). Each waveform shows seismograms after propagation effects from the target location, Nyiragongo, have been deconvolved and the envelope calculated. The station and azimuth is indicated to the right of each waveform. The lowest trace is a stack of the waveforms above. The clear peak in the stack indicates that a Rayleigh wave-producing seismic event occurred near Nyiragongo at approximately 21:10 UTC.

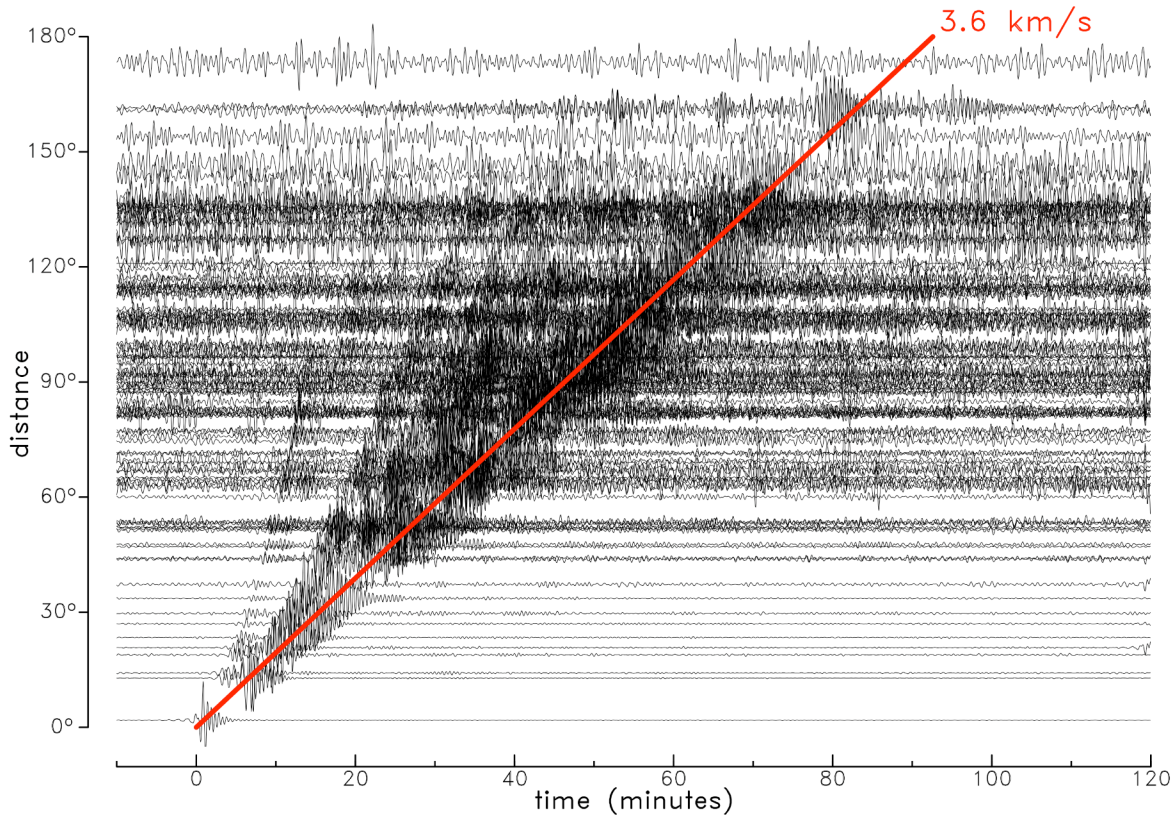

Figure 1.4. Record section of the first newly detected event (21 January 2002). This diagram shows seismograms from the GSN organized by distance from Nyiragongo. The seismograms have been bandpass filtered from 25 to 75 s period. Long-period body and surface wave phases are clearly visible. The red line shows the average velocity of surface waves.

1.3.2. Frequency Content and Spectral Analysis

Because the five Nyiragongo earthquakes do not appear in global seismicity catalogs, the frequency content of each earthquake was investigated using spectral analysis. To explore differences between the newly detected earthquakes and earthquakes that were detected using high-frequency body waves, we collected data from the nearest GSN station, the borehole seismometer in Mbarara, Uganda (MBAR). We examined seismograms for four of the five newly detected earthquakes as well as several earthquakes with similar locations and magnitudes

described in the ISC catalog. Unfortunately, the second Nyiragongo earthquake was not recorded by MBAR.

Visual inspection of the seismograms reveals that the newly detected events are greatly depleted in the high-frequency energy typical of standard tectonic earthquakes (Figure 1.5). Seismograms for earthquakes described in the ISC catalog have the expected characteristics for regional tectonic events, and show clearly defined P and S-wave phases. Newly detected events, on the other hand, seem to have little or no P-wave energy and are composed mainly of low-frequency surface waves.

We also observe differences in the seismograms that correspond to eruptive activity. The seismograms for the newly detected earthquakes associated with the 2002 eruption of Nyiragongo (Events 1 and 3) are similar to each other, but quite different from events not associated with an eruption (Events 4 and 5). Events 1 and 3 have more short-period energy compared to the smooth, longer-period seismograms of Events 4 and 5. We applied a number of bandpass filters to the seismic data and found distinct differences between these two sets of newly detected earthquakes. Additionally, cross-correlation analysis indicates that waveforms from Events 4 and 5 are similar in a variety of frequency bands. This parity was not seen with earthquakes associated with the 2002 eruption, and could be an indication that Events 4 and 5 have similar source locations and processes, perhaps different from the earlier events.

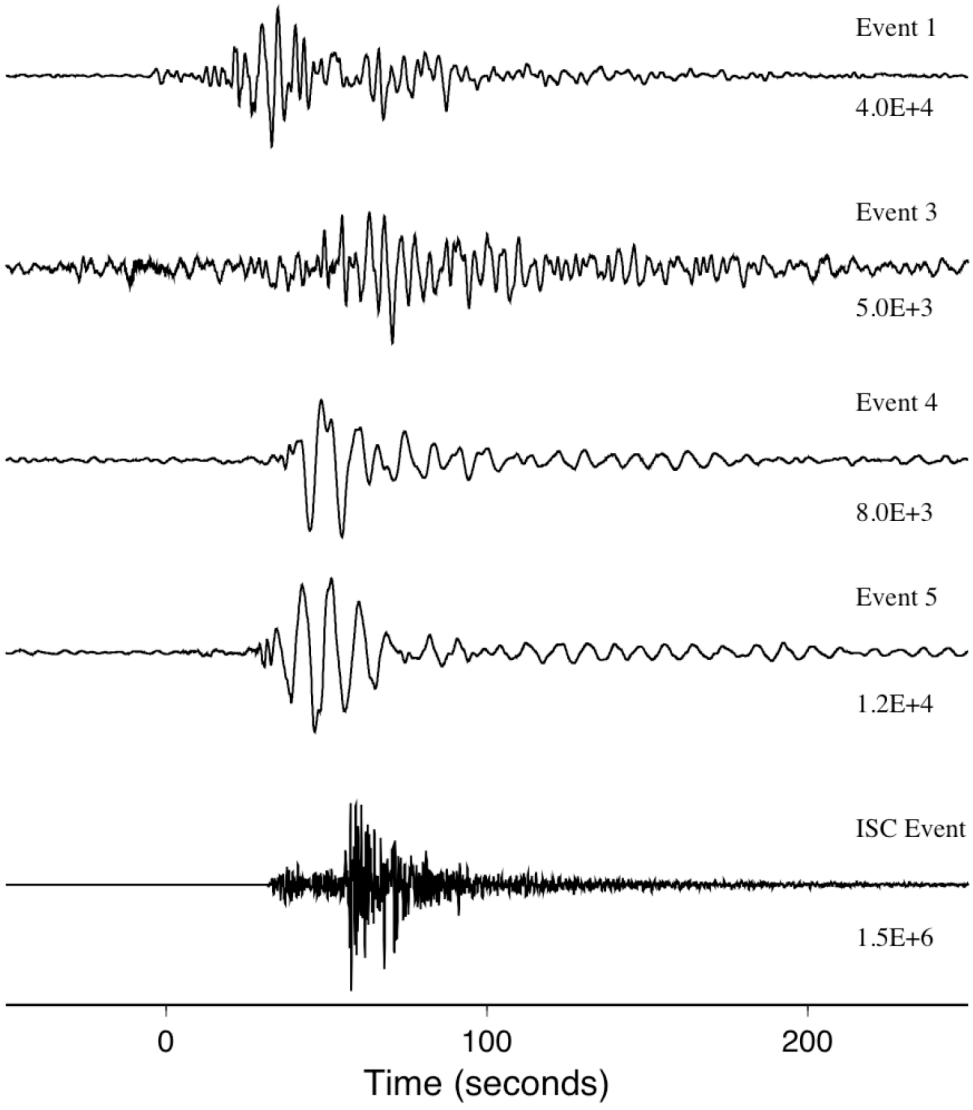

Figure 1.5. Unfiltered seismograms (counts/second) from the nearest GSN station, MBAR. The ISC event is an M_W 5.1 earthquake that took place on 20 January 2002 a few kilometers from Nyiragongo. The zero time for each newly detected event corresponds to the origin time as determined by the method of *Ekström* [2006], which uses a 0.25-degree grid of target locations. The events do not align because the initial locations differed slightly.

To evaluate these differences further, we used spectral analysis. We corrected each seismogram for instrument response, and calculated the single-sided displacement spectrum from a 400-s time window beginning at the origin time and including the entire earthquake signal. To investigate differences in spectral shape between different groups of earthquakes located near Nyiragongo, the frequency spectra were shifted to have equal amplitude at long periods (100 s). Average spectra were calculated for earthquakes described in the ISC catalog, as well as for the two subsets of newly detected earthquakes, to highlight the differences between these groups (Figure 1.6). These differences can also be seen by comparing spectrograms for a newly detected event with an earthquake in the ISC catalog (Figure 1.7).

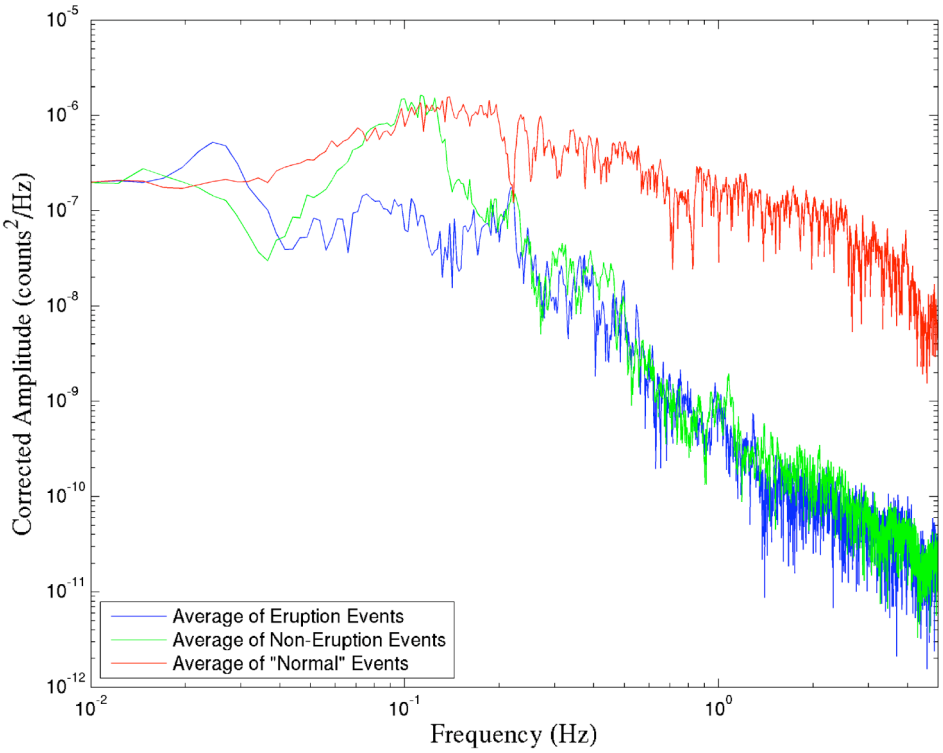

Figure 1.6. Average single-sided displacement spectra for newly detected events and earthquakes described in the ISC catalog. Frequency spectra were first calculated for each individual event. The spectra were then shifted to have equal amplitude at long period to account for differences in magnitude. Finally, average spectra were computed for the three groups. The newly detected events are greatly depleted in high frequencies, above approximately 0.1 Hz. Newly detected events have very similar frequency spectra at periods longer than five seconds, but those not associated with the 2002 eruption have a broad peak at roughly 0.1 Hz.

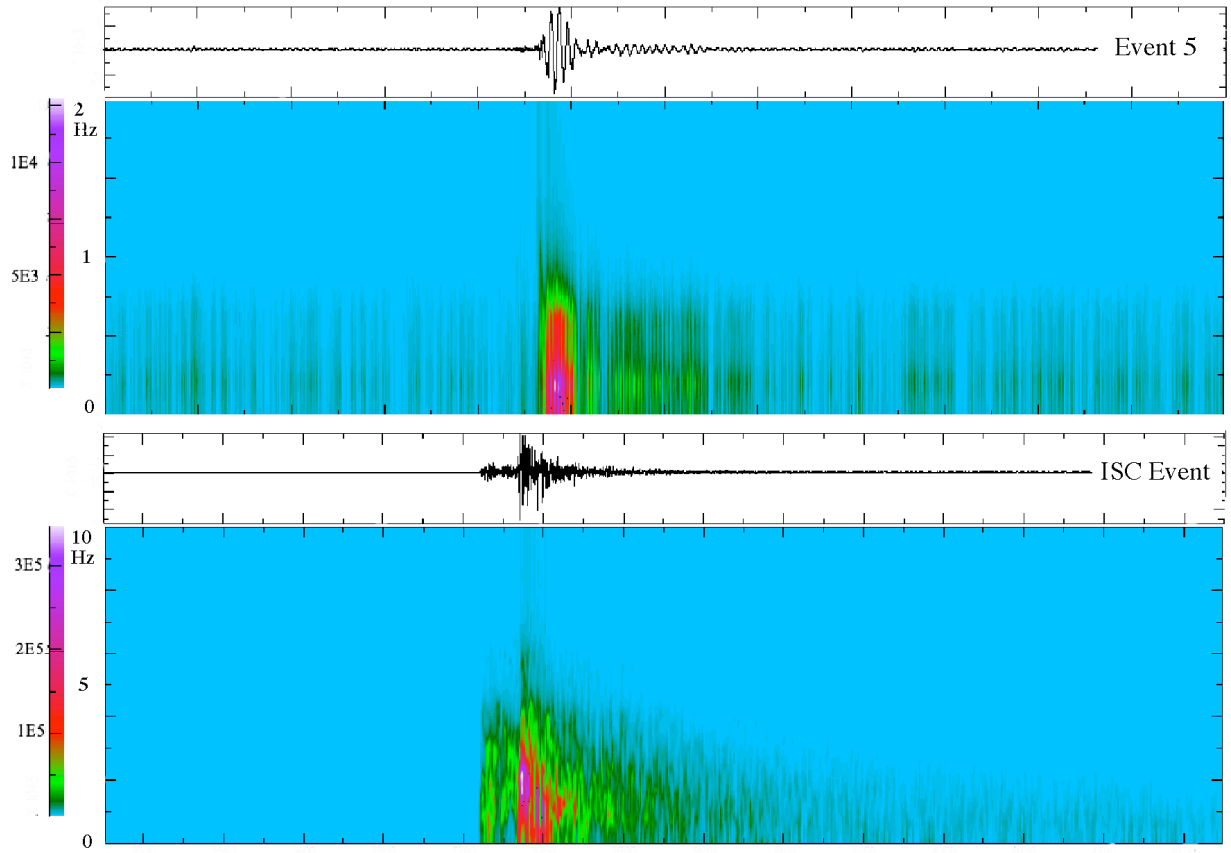

Figure 1.7. Spectrograms for Event 5 and the M_W 5.1 event featured in Figure 1.5. Each spectrogram was calculated from a 700-s timeseries with a 2-s sliding data window. The colors show the amplitude of the power spectra at each frequency for each time slice. The top plot shows frequencies from 0 to 2 Hz while the bottom plot shows frequencies from 0 to 10 Hz. The newly detected earthquake is dominated by energy at frequencies less than 1 Hz. The earthquake from the ISC catalog, however, has energy at frequencies up to 5Hz. The clear arrival of two phases (P and S-waves) can be seen for the ISC event, whereas this feature is not observed in the spectrogram of the newly detected earthquake.

As seen in Figure 1.6, the corrected amplitude spectrum for events in the ISC catalog has a slope that gradually decreases for frequencies over approximately 0.1 Hz. Spectra for the newly detected events, however, have amplitudes that decay rapidly in this same frequency band. At 1 Hz, the difference in amplitude between the two groups is nearly three orders of magnitude. Furthermore, the average corner frequency for earthquakes in the ISC catalog is higher than the

average corner frequencies for the newly detected earthquakes at Nyiragongo. The source duration of an earthquake is inversely related to its corner frequency [*Beresnev*, 2002 and references therein], so this is an indication that the newly detected earthquakes have longer source durations. Since all of the earthquakes have approximately the same long-period amplitude, the longer source duration implies that the newly detected events are slow earthquakes. The lack of seismically radiated high-frequency energy likely prevented these earthquakes from being detected using traditional methods.

Whereas the two sets of newly detected earthquakes have nearly identical spectra for their highest frequencies, at periods of 5 s and longer there are differences between events associated with the 2002 eruption of Nyiragongo and events that are not associated with eruptive activity. Newly detected events not associated with the 2002 eruption have a broad spectral peak at approximately 10 s period, which is also the dominant period in the unfiltered seismograms for these events. These spectral differences and the temporal association of the two subsets of newly detected events with changes in Nyiragongo's eruptive behavior suggest that more than one physical mechanism may be needed to explain these unusual events. Therefore, it is important to interpret our observations in the context of Nyiragongo's eruptive activity.

1.4. Source Models

1.4.1. Centroid-Moment-Tensor Models

To constrain the physical mechanisms of the newly detected earthquakes, we compared synthetic seismograms from a variety of source models to our data. Centroid-moment-tensor (CMT) solutions were calculated for each earthquake using standard methods [*Dziewonski et al*., 1981;

Arvidsson and Ekström, 1998]. We mainly used data recorded on the GSN, although data from the Ethiopia and Kenya broadband seismic experiments [*Nyblade and Langston*, 2002] were also used to calculate CMT solutions for the first three earthquakes. The CMT solutions were primarily constrained by long-period surface-wave data, but body-wave data were also included in the inversion whenever possible. Care was taken to ensure that the CMT solutions were based on waveforms from many azimuths and distances.

Because the newly detected events occurred in a volcanic setting where diking events presumably could cause earthquakes with net volume changes, we also calculated full moment-tensor solutions. However, the existence of an isotropic component was difficult to constrain due to the shallow depths of the earthquakes. For long-period surface-wave data, it is impossible to independently resolve the isotropic and pure vertical-CLVD components of shallow earthquakes [*Kawakatsu*, 1996]. As the introduction of an isotropic component did not significantly improve the fit to the data or alter the CMT solutions, the trace of each moment tensor was constrained to be zero for our preferred solutions (Table 1.2).

The likely location for the newly detected earthquakes is Nyiragongo volcano, based on the temporal association of the first three events with the 2002 eruption. Although the best-fitting centroid locations for the earthquakes are several kilometers away from Nyiragongo, they are not inconsistent with the source being located at the volcano. The CMT solutions were determined from long-period seismic data, which results in location uncertainties of several kilometers, and a comparable fit is achieved if the events are constrained to occur at Nyiragongo. To verify that all five newly detected events occurred in approximately the same location, waveforms for pairs of

newly detected events were cross-correlated at stations within 30° distance of Nyiragongo. At a given station, for event pairs with high correlation coefficients, the time lags between events were within 2 s of each other, which indicates that the earthquakes occurred within ~6 km of one another. As Nyamuragira is located ~14 kilometers away from Nyiragongo, it is unlikely that a subset of the newly detected events occurred there.

Earthquake Source Parameters and CMT Solutions

Event	Time Shift (s)	Latitude	Longitude	Depth (km)	M_W	Epsilon
1	-3.77±0.17	-1.43±0.01	29.07±0.01	15.00f	5.3	-0.38
2	-1.79±0.32	-1.44±0.02	29.05±0.02	19.83±0.60	5.3	-0.38
3	8.35±0.41	-1.58±0.03	29.22±0.05	12.00f	4.6	-0.23
4	-11.61±0.44	-1.34±0.03	29.40±0.03	18.20±0.97	4.6	-0.33
5	-10.74±0.51	-1.34±0.03	29.31±0.04	20.77±0.70	4.7	-0.37

Moment Tensor Elements (Trace = $M_{rr}+M_{\theta\theta}+M_{\phi\phi} = 0$)

Event	Exp.	M_{rr}	$M_{\theta\theta}$	$M_{\phi\phi}$	$M_{r\theta}$	$M_{r\phi}$	$M_{\theta\phi}$
1	17	-1.35±0.02	0.80±0.01	0.55±0.02	0.14±0.05	-0.06±0.06	0.11±0.01
2	17	-1.60±0.01	0.95±0.04	0.65±0.04	0.02±0.07	-0.02±0.08	0.11±0.03
3	15	-8.73±0.07	8.54±0.06	0.02±0.09	-2.03±1.40	-5.88±1.64	0.66±0.42
4	16	-1.10±0.08	0.66±0.06	0.44±0.05	0.05±0.09	-0.62±0.99	0.25±0.04
5	16	-1.75±0.01	0.84±0.07	0.91±0.07	0.03±0.08	-0.28±0.11	0.23±0.05

Table 1.2. Earthquake source parameters for the deviatoric CMT solutions at the best-fitting locations. The time shift corresponds to the time difference between the origin time defined by the detection grid search (Table 1.1) and the centroid time as determined in the inversion. Fixed depths are indicated by the letter 'f'. Although formal uncertainties are given for depths, these are most likely underestimated due to the lack of body wave phases. As with any standard CMT solution for a shallow event, we can only say that the events most likely occurred at a depth of 15 kilometers or less. Elements of the moment tensor are given in Nm. All parameters were allowed to vary for these solutions with the constraint that the trace of the moment tensor was zero.

The focal mechanisms for the newly detected earthquakes are robust and stable, even when parameters such as centroid depth and location are slightly perturbed. The CMT solutions provide excellent fits to the seismic data (average residual misfit of 0.42). Comparisons of observed and synthetic seismograms for Event 1 can be found in Figure 1.8.

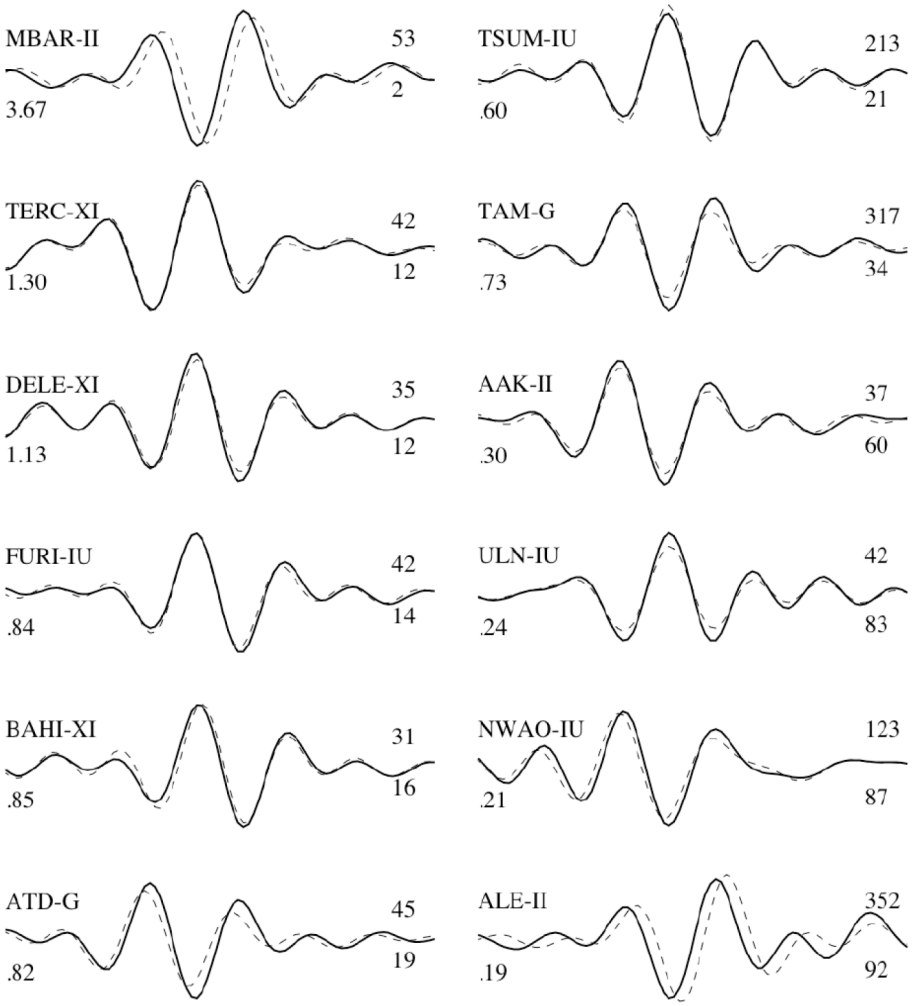

Figure 1.8. A comparison of observed and synthetic vertical-component seismograms for Event 1 (dashed and solid black, respectively). Waveforms have been filtered between 30 and 150 s. Synthetic seismograms were calculated using the parameters for the best-fitting CMT solution (see Table 1.2). The time window is the same for each waveform (332 s). Seismograms are aligned on the extrema in this time range. Station names and network codes appear on the top left of each waveform. The number on the lower left side is the maximum amplitude in microns. The numbers on the right side are the azimuth and the distance in degrees from the original surface wave location.

The five newly detected earthquakes at Nyiragongo are highly non-double-couple. Each earthquake has a large compensated-linear-vector-dipole (CLVD) component of the moment tensor, as reflected by the focal mechanisms in Figure 1.9, as well as by the values of the parameter epsilon in Table 1.2. Epsilon is a measure of the departure of a source from a pure double-couple. A pure double-couple event would have an epsilon value of zero, whereas pure CLVD events would have epsilon values of ± 0.50. Four out of five of the newly detected earthquakes have epsilon values lower than –0.30, which is rare for shallow earthquakes [*Ekström*, 1994]. Although earthquakes with significant non-double-couple components have been observed in volcanic regions, this particular type of focal mechanism is highly unusual [*Miller et al.*, 1998]. Furthermore, the newly detected events are not representative of seismicity in the area. Focal mechanisms of large local tectonic events show an overall pattern of east-west extension, as expected for the nearly north-south trending rift zone [*Tanaka*, 1983]. For example, an M_W 5.0 earthquake that took place on 21 January 2002, just a few hours prior to the first newly detected event, has a nearly perfect double-couple normal-faulting solution [*Ekström et al.*, 2005]. The fact that double-couple and non-double-couple earthquakes are observed at the same time suggests that the anomalous focal mechanisms of the newly detected events are unlikely to be due to instrument errors or propagation through a heterogeneous structure. Instead, these focal mechanisms likely represent an anomalous earthquake source.

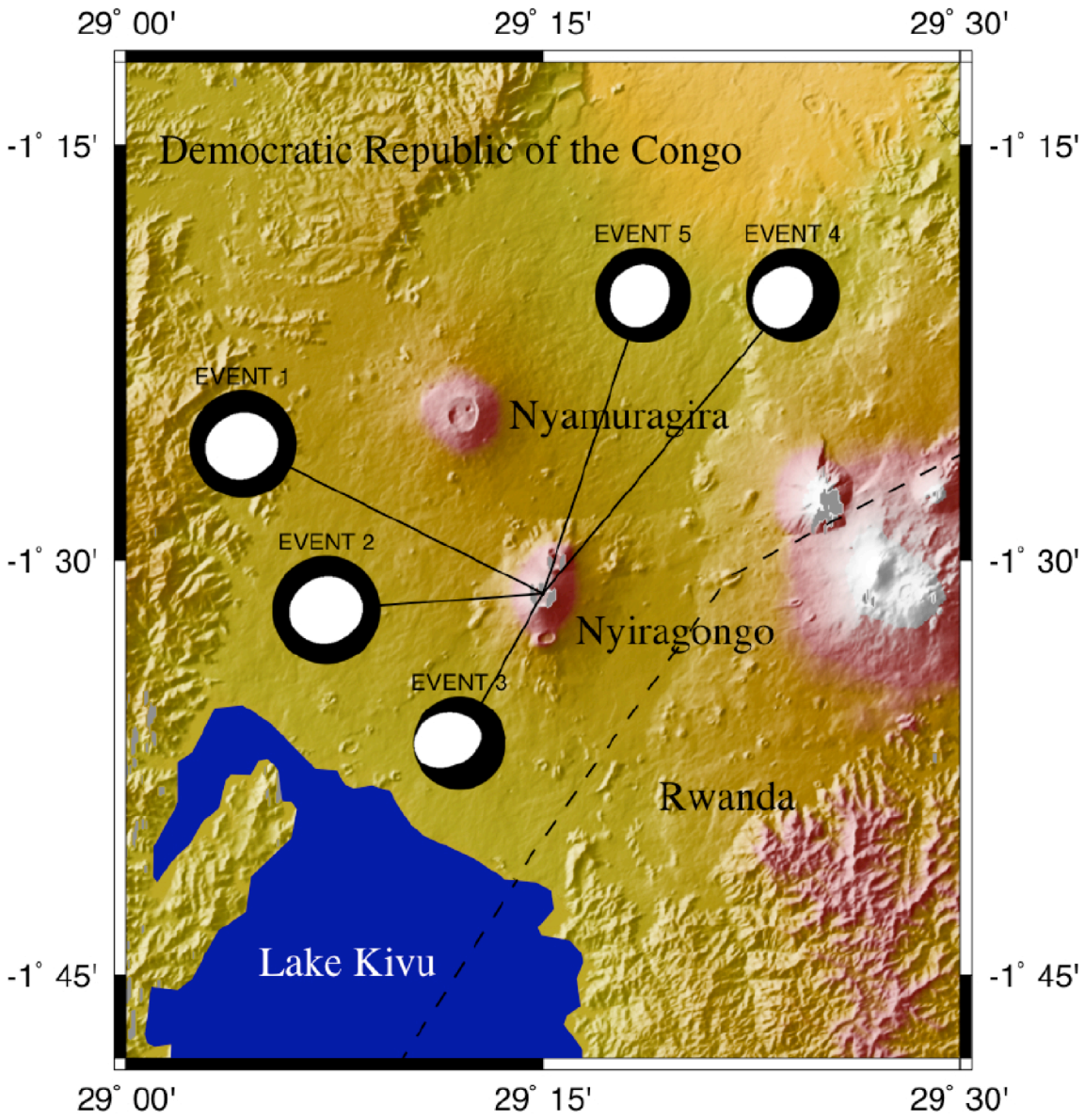

Figure 1.9. Focal mechanisms of five newly detected earthquakes overlain on SRTM topography. Nyiragongo is indicated to be the location for all the events because a solution with comparable fit is obtained when the location is constrained to be the volcano. The earthquakes are highly non-double couple.

1.4.2. Time-Varying Force Solutions

In addition to CMT solutions, the newly detected earthquakes were modeled with a time-varying force model. Similar models have been have been applied to sources such as landslides and cavern collapses, which cannot be explained by the double-couple force system typically used to represent a shear dislocation. Time-varying force models have also been used to explain seismic events originating inside and beneath volcanoes where gravitational energy is released instead of elastic strain energy [*Takeo et al*., 1990; *Takei and Kumazawa*, 1994]. Recently, time-varying forces were used to model long-period seismic waves associated with the caldera collapse of Miyakejima volcano in 2000 [*Kikuchi et al*., 2001], an event that also produced numerous slow earthquakes that were detected using long-period surface waves [*Ekström and Nettles*, 2002]. Collapse events produce long-period seismic energy because the source duration is limited by gravitational acceleration instead of the speed of elastic rupture propagation [*Fukao*, 1995]. As the first three newly detected events occurred just prior to the collapse of Nyiragongo's summit crater, such a source model seemed possible for these slow, non-double couple events.

The source of each newly detected event was parameterized by a force system composed of overlapping triangular basis functions subject to a zero-net-force constraint. To reduce the number of free parameters, each event was constrained to take place at Nyiragongo (-1.52º, 29.25º) at a depth of fifteen kilometers. This depth indicates that the source was shallow, and has little effect on the results of the inversion. For each earthquake, an iterative method was used to solve for the time-varying amplitudes and directions of the forces. We included both long-period and intermediate-period seismic data to ensure that the solution provided a good fit to the data in

a variety of frequency bands. A CMT solution at the same fixed location was determined for the same dataset to enable direct comparison of the two types of source models.

Because the results of the inversions depend on the number of modeled forces and their source durations, and since many combinations of these parameters can produce synthetic seismograms with approximately equal fit to the data, multiple inversions were performed to produce a family of solutions. A representative source model consists of six triangular basis functions with a half-duration of 15 s. At the same location and depth, time-varying force models have an average residual misfit of 0.72, whereas CMT solutions have an average residual misfit of 0.68.

The time-varying force model for each earthquake consists primarily of an upward vertical force followed by a longer-duration downward vertical force. Although significant horizontal components exist, they are much smaller than the vertical forces and tend to oscillate around zero for the later part of the solution. The pattern of an upward force followed by a downward force is thought to arise from collapse events [*Takei and Kumazawa*, 1994]. For example, the collapse of the roof of a magma chamber generates an upward force as the rest of the volcano rebounds from the loss of mass. When the roof impacts the magma below, a downward force is transferred to the solid earth. A time-varying force solution is investigated for Nyiragongo since the first three newly detected events took place just prior to the catastrophic collapse of the summit crater. We investigate the possibility that these events were caused by incremental collapse of the solidified lava lake crust or a shallow magma chamber.

1.5. Physical Mechanisms

1.5.1. Gravitational Collapse

Based on our observations, we formulated two potential mechanisms for the physical mechanism of the newly detected events, one based on gravitational collapse, and one involving slip on a non-planar fault. In the gravitational-collapse model, the earthquakes are caused by incremental collapse of a portion of the volcano. Because the first three earthquakes occurred only a few hours before the crater collapse associated with the 2002 eruption, we investigate the possibility that those events could have been caused by repeated collapse of fractions of the solidified lava lake surface, which was weakened by the removal of its support below. We also explore cases where the newly detected events are caused by the collapse of the roof of a shallow magma chamber. Both of these interpretations are consistent with our observations that the earthquakes can be modeled by time-varying force solutions consisting of an upward force followed by a downward force.

Although each earthquake can be modeled using time-varying forces, the moment tensor models provide a better fit to the data, despite the fact that they have fewer free parameters. Furthermore, a model based solely on time-varying forces seems physically implausible when the magnitude of the modeled forces is considered. Assuming that vertical forces are dominant, we obtain the product of mass (m) and the displacement of the center of mass ($\boldsymbol{D}(t)$) of the rock involved in the seismic event if we twice integrate the vertical force calculated in our force model ($\boldsymbol{F}(t)_{on\ Earth}$),

$$\mathbf{F}(t)_{\text{on Earth}} = -\mathbf{F}(t)_{\text{collapse}} - \frac{d(m\mathbf{v}(t))_{\text{collapse}}}{dt} = -\frac{d\mathbf{p}(t)}{dt} \tag{1.1}$$

$$\iint \mathbf{F}(t)dt = \int -\mathbf{p}(t)dt = -m\mathbf{D}(t)\,. \tag{1.2}$$

The product of mass and displacement corresponding to the time-varying force model for the first newly detected event is 9.2 x10^{14} kg-m.

If we consider the possibility that this event was caused by gravitational collapse of the solidified lava lake surface, the maximum displacement is constrained by the 620 m increase in the depth of the summit crater following the collapse. Using this value for the maximum displacement, we can determine the thickness of the solidified lava lake required to generate such forces. If the entire solidified lava lake surface, of radius 300 m, fell this distance in a single collapse event, an unrealistic thickness of nearly 2 km is required to generate the forces required by our model.

Likewise, we can evaluate the possibility that the events were caused by collapse of the roof of a shallow magma chamber. Such a mechanism seems favorable for the first three newly detected events considering their proximity to the 2002 eruption. During the eruption, magma originated from several locations including shallow and deeper reservoirs [*Tedesco et al*., 2007]. The evacuation of magma from shallow magma chambers decreases the pressure in these reservoirs, making them susceptible to collapse. Currently, there are few constraints on the depths of magma bodies beneath Nyiragongo volcano. Past studies of seismicity interpreted an aseismic region beneath Nyiragongo as a plastic zone occupied by a magma complex [*Tanak*a, 1983]. This aseismic zone ranged from the ground surface to a depth of 14 km. There have been no recent studies to further constrain the depths of magma reservoirs beneath the volcano. Because we used long-period seismic data in our analysis, we can only state that the newly detected events are shallow and most likely occurred at a depth of 15 km or less.

If we assume, arbitrarily, that the roof of the shallow magma chamber can be approximated by a 2-km thick cylinder of rock with a radius of 1 km, the roof of the shallow magma chamber would have to collapse a distance of roughly 50 m to generate the forces required by Event 1. This estimate was made assuming perfect seismic efficiency, whereby all of the potential energy of the collapse is available for creating seismic disturbances. In reality, this is very unlikely. A study of the caldera collapse at Fernandina volcano in the Galápagos Islands showed a large discrepancy between the potential energy of the caldera collapse in 1968 [*Francis*, 1974] and the seismic energy released by a swarm of earthquakes believed to be caused by the collapse of the roof of a shallow magma chamber [*Simkin and Howard*, 1970]. The seismic efficiency during the caldera collapse of Fernandina is estimated to be between 0.25% and 3.6 % [*Francis*, 1974]. Considering these observations, we conclude that gravitational collapse alone cannot explain the occurrence of the newly detected events, although it may have played a role in their generation.

1.5.2. Slip on Non-Planar Faults

Faults and dikes that are circular or elliptical in plan view are commonly observed at eroded volcanoes [*Cole et al*., 2005; *Gudmundsson and Nilsen*, 2006]. At active volcanoes, they are sometimes indicated by a distribution of earthquakes creating a conical shape at depth [*Mori and McKee*, 1987; *Saunders*, 2001]. These ring faults are shear fractures that form at steep angles, either towards or away from the center of the volcano. The inward-dipping ring faults are normal faults associated with tensile stresses, while the outward-dipping faults are reverse faults associated with compressive stresses [*Julian et al*., 1998]. Both types may be present in the same volcano, each formed during different inflation and deflation periods.

The formation of new ring faults, as well as slip on pre-existing ring-fault structures is rare, and requires very specific conditions. Experimental and modeling work indicates that slip on pre-existing ring faults can be triggered by the presence of a shallow, sill-like magma chamber subject to tension and/or doming from a deep magma reservoir [*Gudmundsson and Nilsen*, 2006; *A. Gudmundsson et al.*, 1997]. While there are no constraints on the shape or depths of the magmatic plumbing system beneath Nyiragongo, the presence of shallow and deeper magma reservoirs was verified from studies of short-lived isotopes in lavas from the 2002 eruption [*Tedesco et al*., 2007]. Currently, there is no evidence of crustal doming from the deep magma reservoir, however, the Virunga Volcanic Complex is subject to significant regional extension associated with active continental rifting, and thus the area is favorable for the existence of ring faults. Although slip on pre-existing ring faults is believed to be strongly dependent on the history of individual volcanoes, slip can be triggered by the evacuation of magma from a shallow magma chamber [*Druitt and Sparks*, 1984; *Folch and Marti*, 2003]. In this case, the roof of an underpressured magma chamber, which is no longer supported from below, can subside into the evacuating magma chamber along ring faults [*Druitt and Sparks*, 1984; *Cole et al*., 2005]. Indeed, the presence of Nyiragongo's large summit crater is likely related to multiple roof collapses of the shallow magma chamber [*Platz et al*., 2004].

As we explored a ring-faulting mechanism, we drew on models based on similar observations from other volcanoes. Slip on conical ring faults has been used to explain a number of highly non-double-couple earthquakes in volcanic locations such as Tori Shima, Japan and Bárdarbunga volcano in Iceland [*Ekström*, 1994]. *Nettles and Ekström* [1998] worked towards determining the physical mechanism that generated 10 shallow earthquakes that took place at Bárdarbunga prior

to a lateral eruption in 1996. There is no indication that the Bárdarbunga earthquakes were slow events, however the moment tensor of each earthquake is dominated by the pure vertical-CLVD component. The events we are investigating have vertical pressure axes, and the Bárdarbunga events have vertical tension axes, but the focal mechanisms are very similar. The Bárdarbunga earthquakes are interpreted as slip on an outward-dipping cone-shaped ring fault located beneath Bárdarbunga's edifice. *Nettles and Ekström* [1998] reason that as the volcano inflated over a period of twenty years, increased pressure in a shallow magma chamber led to incremental slip on a deeper pre-existing ring fault. At Nyiragongo, however, the timing of the first three events in relation to the 2002 eruption supports the association of the newly detected events with a deflating magma chamber. The focal mechanisms suggest that the newly detected events may have been caused by slip on an inward-dipping cone-shaped ring fault [*Ekström*, 1994], most likely located above an underpressured shallow magma chamber.

The caldera collapse of Miyakejima volcano in Japan was accompanied by numerous moderate-sized, slow earthquakes with focal mechanisms similar to the newly detected events in this study [*Ekström and Nettles*, 2002]. Like Nyiragongo and Bárdarbunga, Miyakejima is a stratovolcano that erupts in fissure eruptions. In mid-2000, a massive dike intrusion began beneath Miyakejima and migrated northwestward at a rate of 5 km per day, producing intense seismicity [*Fujita et al*., 2001]. A collapsed caldera began to grow in the summit of the volcano a few weeks later, following a brief eruption, and subsidence and widening continued for over a month [*Kikuchi et al*., 2001; *Kumagai et al*., 2001]. During the incremental caldera collapse, sequences of step-like inflation followed by slower deflation were recorded by local tiltmeters, generally once or twice per day [*Yamamoto et al*., 2001]. These tilt steps are associated with very-long-period (50 s)

seismic pulses that were recorded globally [*Ekström and Nettles*, 2002]. The VLP seismic signals have been modeled as explosive sources, having dominant volumetric components of the moment tensor [*Kikuchi et al.,* 2001; *Kumagai et al*., 2001]. Interestingly, the VLP events are not well-modeled by a series of time-varying forces, despite the fact that the initial collapse of the summit crater was well characterized by a single-force directed upwards and then downwards [*Kikuchi et al*., 2001].

Several source mechanisms have been suggested for the VLP events associated with the caldera collapse of Miyakejima. *Kumagai et al*. [2001] explains the VLP events as a vertical piston of solid materials in the conduit being intermittently pulled into the evacuating magma chamber. As magma flows out of the chamber during dike injection, the pressure in the magma chamber decreases, causing the piston to slide down into the magma chamber. The VLP signal is generated as magma chamber expands during the intrusion of the piston and then gradually deflates as magma continues to flow out of the chamber. *Filson et al.* [1973] suggests that the caldera collapse earthquakes at Fernandina were also caused by intermittent slip of a cylindrical block into an evacuating magma chamber. These mechanisms can be interpreted as repeated slip on a vertical ring fault with radius smaller than the magma chamber below. *Geshi et al.* [2002] proposed a comparable mechanism for subsidence at Miyakejima, in which a stoping column of brecciated rock subsides into a deflating magma reservoir. On the other hand, *Kikuchi et al.*, [2001] explains the VLP signals using a buried geyser model, in which steam pushes a lower conduit piston into the magma reservoir.

Considering these models, we explored cases in which the newly detected events were generated by incremental slip on ring-fault structures. We initially considered the possibility that the first three events were caused by incremental slip of the solidified lava lake surface. This process releases elastic energy, and the scalar moment, M_0, can be calculated by multiplying the rigidity (μ) by the area (A) and the average slip ($\bar{d}$) in each event:

$$M_o = \mu A \bar{d} \tag{1.3}$$

The scalar moment determined in the CMT solution for Event 1 was 1.1×10^{17} Nm. Using this simple relationship, we determined that a solidified lava lake thickness of 100 m requires an average slip of 18 m. However, this is a minimum estimate because the ring fault geometry results in the partial cancellation of seismically radiated long-period moment. For example, the scalar moment for Event 1 is also consistent with over 130 m of displacement caused by 360º failure on a ring-fault with a dip angle of 85º [*Ekström*, 1994]. It is highly unlikely that the lava lake surface could have survived three consecutive large falls, and thus we rule out this explanation. Slip on a ring fault beneath the edifice, however, is plausible. If we assume a fault geometry approximated by a cylinder 1 km in radius with a height of 2 km, the required average displacements are between 0.26 and 2 m.

Based on our observations, and comparisons to other active volcanoes, we suggest that the five newly detected earthquakes at Nyiragongo were caused by slip on pre-existing ring faults located above deflating shallow magma chambers (Figure 1.10). The first three newly detected events occurred within days of the 2002 fissure eruption of Nyiragongo, which was caused by a local rifting event. Considering that there was heightened seismicity and ongoing ground deformation following the eruption, we can infer that the rifting event endured longer, and that there was

continued dike injection in the rift graben for several days following the eruption. These diking events resulted from evacuation of magma from a shallow magma chamber beneath the volcanic edifice. Continued diking reduced the pressure in the shallow magma chamber, leading it to collapse along pre-existing ring faults. Motion along the ring fault most likely further destabilized the solidified lava lake surface, leading to the collapse of the summit crater. The crater collapse compacted the plumbing system of the volcano, which could have cut off the flow of magma to the dikes. This could provide an explanation for the sudden cessation in seismicity following the crater collapse.

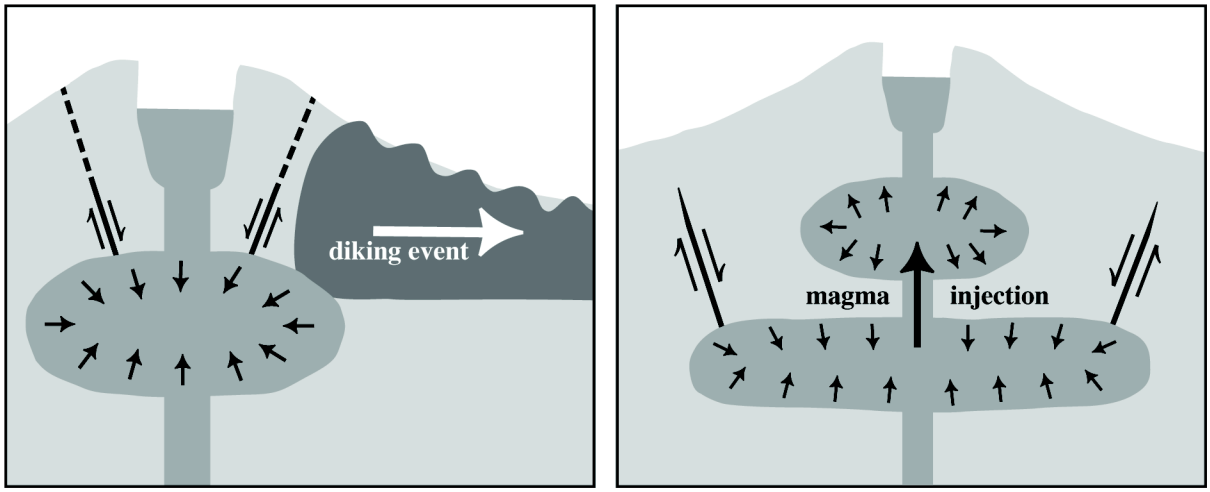

Fig. 1.10. Schematic diagram of ring-faulting mechanisms. Slip on a pre-existing inward-dipping ring-fault can be triggered by the depressurization of a shallow magma chamber. This could occur following a diking event (left panel), or after the injection of magma from a deeper reservoir to a more shallow reservoir (right panel). Both panels show north-south cross-sections, parallel to the strike of the rift. The left panel shows the mechanism preferred for the first three newly detected events. A vertical dike, oriented parallel to the rift valley, propagates from the volcano towards Lake Kivu. The evacuation of magma causes the shallow magma chamber to become underpressured, and leads to incremental slip along an inward-dipping ring fault. This ring fault may extend to the surface (indicated by dashed lines). The right panel shows the mechanism given for the final two newly detected events. The injection of magma into a shallow magma reservoir causes a deeper magma reservoir to become underpressured, which triggers slip on a deeper inward-dipping ring fault. The figure is vertically exaggerated, and is not to scale. Figure by L. Starin.

The final two newly detected events can also be explained by slip on a ring fault. It is unlikely that these events were preceded by dike injection events, as there are no reports of elevated seismicity or deformation during these time periods. A more likely explanation is that the final two events were triggered by the injection of magma from a deeper source. Following the 2002 eruption of Nyiragongo, vigorous degassing accompanied the refilling of lava lake in the summit crater. This indicates the addition of undegassed magma from below [*Durieux*, 2002/2003a; *Tazieff*, 1994; *Harris et al*., 1999; *Harris*, 2008]. The added weight and pressure of this magma in the upper conduit and shallow magma chamber could have lead to collapse along a pre-existing ring fault deeper in the volcano. This deeper location may explain why the last two events have slightly different frequency characteristics from the first three newly detected events.

1.6. Conclusions

Detailed analysis of long-period seismic data has demonstrated that five previously undetected earthquakes of moderate size occurred in the vicinity of Nyiragongo volcano between 2002 and 2005. These earthquakes have long source durations and unusual source characteristics. Modeling has shown that these events cannot be explained by gravitational collapse alone. Instead, seismic data from these events are modeled well by highly non-double-couple centroid-moment tensors. We interpret these events as being generated by slip on inward-dipping conical ring faults located under the volcano. This slip is triggered by the deflation of a shallow magma chamber beneath the ring fault, following diking events or magma injection into a shallower reservoir. The presence of ring-fault structures could be verified by the precise location of long-period seismicity at the volcano. However, this would require the installation of a dense seismic

array to monitor the volcano. A discussion of how this mechanism results in slow earthquakes is beyond the scope of this chapter, and remains to be investigated.

Nyiragongo is one of Africa's most active volcanoes, and based on its recent eruptive history, it is also one of the volcanoes posing the greatest risk to its local population. Nyiragongo has had two catastrophic eruptions in the last 50 years. During the 1977 eruption, highly fluid lava flows traveled down the volcano's flanks at speeds up to 60 km per hour, resulting in over 100 deaths, the highest number of people killed by a single lava flow [*Durieux*, 2002/2003b]. Lava flows from the 2002 eruption traveled further south to the city of Goma, resulting in even more damage and loss of life. As the populations of the villages and cities on the banks of Lake Kivu swell, the risk posed by Nyiragongo continues to grow. If the two previous eruptions are any indication of what may happen in the future, it is easy to see why there is a great need for understanding the dynamics of Nyiragongo volcano, and of the rift in general. This study of previously undetected seismicity has allowed us to infer the existence of ring faults underneath the volcano, and to suggest that slip on these structures may be initiated by volcanic activity. It is only one example of how we can use seismology to learn more about the dynamics of an active volcano. Considering the volatility of the region, indirect methods of observation like seismology are especially useful, and these must be utilized to their full potential.

Chapter 2

Global observation of vertical-CLVD earthquakes at active volcanoes

This work has been submitted for publication:
Shuler, A., Nettles, M., and G. Ekström, Global observation of vertical-CLVD earthquakes at active volcanoes, submitted to *J. Geophys. Res.,* 2012.

Abstract

Some of the largest and most anomalous volcanic earthquakes are those with dominant vertical compensated-linear-vector-dipole (vertical-CLVD) components. Here we use both the standard and surface-wave catalogs of the Global Centroid Moment Tensor Project to search for vertical-CLVD earthquakes near active volcanoes in order to evaluate the link between these earthquakes and dynamic processes occurring inside volcanic edifices or magmatic plumbing systems. We determine focal mechanisms for 313 target earthquakes and identify 86 shallow $4.3 \leq M_W \leq 5.8$ vertical-CLVD earthquakes located near volcanoes that have erupted in the last ~100 years. The majority of vertical-CLVD earthquakes occur in subduction zones, in association with basaltic-to-andesitic stratovolcanoes or submarine volcanoes, although vertical-CLVD earthquakes are also located in continental rifts and in regions of hot-spot volcanism. Vertical-CLVD earthquakes are associated with a wide variety of confirmed or suspected eruptive activity at nearby volcanoes, including volcanic earthquake swarms as well as effusive and explosive eruptions and caldera collapse. Approximately 70% of all vertical-CLVD earthquakes studied occur during episodes of documented volcanic unrest at a nearby volcano. Given that volcanic unrest is underreported, most shallow vertical-CLVD earthquakes near active volcanoes are likely related to magma migration or eruption processes. Vertical-CLVD earthquakes with dominant vertical pressure axes generally occur after volcanic eruptions, whereas vertical-CLVD earthquakes with dominant vertical tension axes generally occur before the start of volcanic

unrest. The occurrence of these events may be useful for identifying volcanoes that have recently erupted and those that are likely to erupt in the future.

2.1. Introduction

Most shallow earthquakes have seismic radiation patterns that are consistent with the double-couple model for shear failure on planar faults [*Sykes*, 1967; *Isacks et al*., 1968; *Dziewonski and Woodhouse*, 1983; *Frohlich*, 1995]. However, in volcanic and geothermal areas, other processes such as the migration of magmatic and/or hydrothermal fluids or rupture on non-planar faults can produce earthquakes with significant non-double-couple components. Although the majority of these anomalous earthquakes are small (M < 3) and only recorded by seismometers deployed close to the source regions [*Takeo*, 1990; *Foulger and Julian*, 1993; *Ross et al*., 1996; *Miller et al*., 1998b; *Ohminato et al*., 1998, 2006; *Foulger et al*., 2004; *Kumagai et al.,* 2005; *Nakano and Kumagai*, 2005; *Ohminato*, 2008], non-double-couple earthquakes with magnitudes up to M~6 have been observed near a small number of volcanoes around the world [*Julian*, 1983; *Julian and Sipkin*, 1985; *Kanamori et al.,* 1993; *Ekström*, 1994; *Dziewonski et al*., 1997; *Nettles and Ekström*, 1998; *Dreger et al*., 2000; *Kumagai et al*., 2001; *Templeton and Dreger*, 2006; *Minson and Dreger*, 2008; *Shuler and Ekström*, 2009].

In this study, we investigate 'vertical-CLVD' earthquakes, which are a specific type of non-double-couple earthquake that has been shown to occur near volcanic centers [*Ekström,* 1994]. Notable examples of vertical-CLVD earthquakes include the 1984 Tori Shima earthquake [*Kanamori et al.,* 1993], and the two series of earthquakes that occurred near Bárdarbunga volcano between 1976 and 1996 [*Nettles and Ekström,* 1998] and near Nyiragongo volcano

between 2002 and 2005 [*Shuler and Ekström,* 2009]. In addition to having anomalous source properties, these earthquakes are associated with documented episodes of volcanic unrest, and their occurrence and unusual focal mechanisms are interpreted to result from active volcanic processes. However, it is not clear how widespread the association between vertical-CLVD earthquakes and active volcanism may be.

The focal mechanisms for earthquakes like those observed at Tori Shima, Bárdarbunga, and Nyiragongo have unusually large non-double-couple components. The size of the non-double-couple component is typically quantified by examination of the eigenvalues of the moment tensor. In the principal axis coordinate system, earthquakes are described by three eigenvectors with eigenvalues ordered $\lambda_1 \geq \lambda_2 \geq \lambda_3$, where λ_1 is the tension axis and λ_3 is the pressure axis. For double-couple earthquakes, the value of the intermediate eigenvalue, λ_2, is zero and $\lambda_3 = -\lambda_1$, whereas for non-double-couple earthquakes, λ_2 assumes a non-zero value due to isotropic or compensated-linear-vector-dipole (CLVD) components of the moment tensor [*Knopoff and Randall*, 1970; *Frohlich*, 1990a; *Julian et al*., 1998]. The isotropic component, $(M_{rr} + M_{\theta\theta} + M_{\phi\phi})/3$, represents a net volume change, which is expected to be small for tectonic earthquakes. In routine moment tensor inversions, the isotropic component is typically constrained to be zero [*Dziewonski et al*., 1981; *Dufumier and Rivera*, 1997]. The CLVD component accounts for the portion of the moment tensor that can be explained by three orthogonal dipoles, two that have the same polarity and magnitude, and a third that is twice as large with opposite polarity.

The deviatoric component of the moment tensor can be decomposed into double-couple and CLVD components by assuming that the principal stress axes for these components are parallel. The non-double-couple component is described by the parameter ε, which is defined as

$$\varepsilon = -\lambda_2/\max(|\lambda_1|, |\lambda_3|), \quad (2.1)$$

where $\varepsilon = 0$ for a double-couple earthquake and $\varepsilon = \pm 0.5$ for earthquakes that are pure CLVDs. In this framework, each earthquake can be described by a deviatoric moment tensor that is $200*|\varepsilon|$% non-double-couple and $(100-200*|\varepsilon|)$% double-couple. In the Global Centroid Moment Tensor (GCMT) catalog, ~18% of earthquakes with centroid depths less than 50 km have moment tensors with 40% or more non-double-couple component.

In this chapter, we focus on vertical-CLVD earthquakes, which have large non-double-couple components and approximately vertical pressure or tension axes like those previously reported at active volcanoes [*Kanamori et al.*, 1993; *Ekström,* 1994; *Nettles and Ekström,* 1998; *Shuler and Ekström*, 2009]. We identify two types of vertical-CLVD earthquakes depending on whether the dominant dipole is dilatational or compressional. 'Vertical-T' earthquakes have dominant tension axes that plunge more steeply than 60° with $\varepsilon > 0.20$, and 'vertical-P' earthquakes have dominant pressure axes that plunge more steeply than 60° with $\varepsilon < -0.20$ (Figure 2.1). Our definitions are similar, but not identical, to the P_V and T_V designations given by *Frohlich* [1995]. Earthquakes meeting our criteria represent less than 3% of all shallow ($h < 50$ km) earthquakes documented in the GCMT catalog.

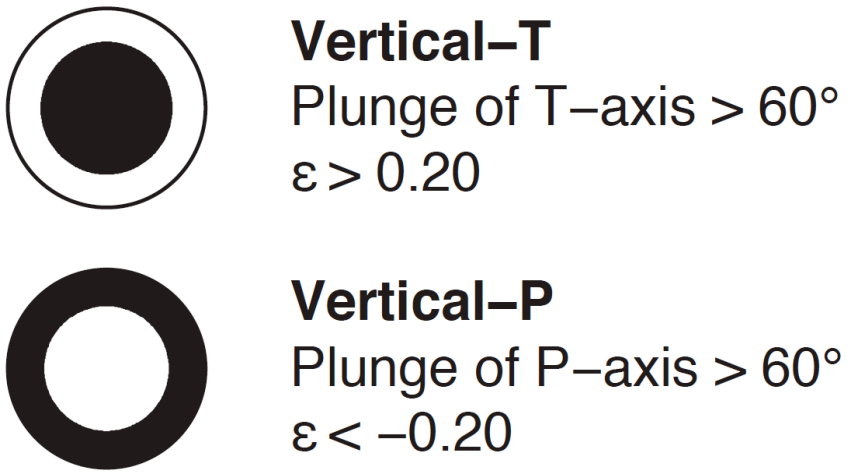

Figure 2.1. Criteria for the two types of vertical-CLVD earthquakes. Vertical-T events have dominant tension axes that plunge more steeply than 60° and ε values greater than 0.20, and vertical-P events have dominant pressure axes that plunge more steeply than 60° and ε values less than -0.20. The focal mechanisms shown are for pure vertical-CLVD earthquakes, which have vertical dominant tension or pressure axes (plunges of 90°) and $|\varepsilon| = \pm 0.50$.

Ekström [1994] performed a search for vertical-T earthquakes in the Harvard CMT catalog (now known as the GCMT catalog), and identified 18 shallow $M_W > 5.0$ earthquakes with $\varepsilon > 0.33$ and tension axes that plunge more steeply than 60°. Ten of the vertical-T earthquakes are located in close proximity to volcanic centers, which demonstrates an association between these earthquakes and volcanism. Vertical-T earthquakes reported by *Ekström* [1994] include the Tori Shima earthquake and six Bárdarbunga earthquakes in addition to events in North Honshu, the Volcano Islands and the South Sandwich Islands.

The Tori Shima earthquake is an M_W 5.6 vertical-T earthquake that occurred on 13 June 1984 between Smith Rock and Bayonnaise Rocks volcanoes in the Izu-Bonin volcanic arc southeast of Honshu. In the GCMT catalog, the Tori Shima earthquake has an ε value of 0.33 and a tension

axis that plunges 87°. Rayleigh waves from this earthquake were radiated with nearly equal amplitude and phase in all directions, whereas Love waves were either absent or of very low amplitude [*Kanamori et al*., 1993]. The Tori Shima earthquake also generated a disproportionately large tsunami given its moderate magnitude. Whereas typically tsunamis have tsunami magnitudes, M_t, that are comparable to the M_W estimates for the source earthquake, the Tori Shima earthquake produced an M_t 7.3 tsunami [*Abe*, 1988; *Satake and Kanamori*, 1991].

Several physical mechanisms have been proposed to explain the Tori Shima earthquake. In the model of *Kanamori et al.* [1993], the vertical-T earthquake is generated by rapid expansion of supercritical water following horizontal injection of magma into water-filled sediments. However, *Ekström* [1994] suggests that the Tori Shima earthquake may be better explained by dip-slip motion on a volcano ring fault. Ring-fault structures are observed in eroded volcanoes [*Cole et al*., 2005 and references therein] and their presence can be inferred beneath some active volcanoes by dense cone-shaped patterns of microearthquakes [*Mori and McKee*, 1987; *Mori et al*., 1996]. In analog and numerical models, slip on ring-fault structures is directly related to the inflation or deflation of shallow magma chambers (see *Marti et al*., [2008], *Acocella* [2008] and *Gudmundsson* [2008] for review). Dip-slip motion on cone-shaped ring faults can generate earthquakes with vertical-CLVD focal mechanisms [*Frohlich et al*., 1989; *Frohlich*, 1990a/b, 1995; *Ekström*, 1994; *Julian et al*., 1998], and slip on curved faults results in the partial cancellation of long-period seismic moment, which could account for the discrepancy between seismic and tsunami magnitudes [*Ekström*, 1994].

The non-double-couple earthquakes at Bárdarbunga and Nyiragongo volcanoes have also been explained as resulting from slip on ring-fault structures. In total, 10 vertical-T earthquakes with magnitudes $5.1 \leq M_W \leq 5.6$ occurred near Bárdarbunga volcano in Iceland between 1976 and 1996 [*Nettles and Ekström*, 1998]. The last earthquake occurred only days before a large, subglacial fissure eruption between Bárdarbunga and Grimsvötn volcanoes [*M.T. Gudmundsson et al*., 1997], which suggests that, at least in this case, vertical-T earthquakes are associated with the inflation of a shallow magma chamber. According to the faulting model presented by *Nettles and Ekström* [1998], the vertical-T earthquakes are generated by slip on an outward-dipping ring fault located below an inflating shallow magma chamber.

Five vertical-P earthquakes with magnitudes $4.6 \leq M_W \leq 5.3$ took place near Nyiragongo volcano in the Democratic Republic of the Congo between 2002 and 2005. The first three vertical-P earthquakes occurred several days after a catastrophic fissure eruption of Nyiragongo in January 2002, and are attributed to slip on inward-dipping ring faults located above a deflating shallow magma chamber [*Shuler and Ekström,* 2009]. The final two earthquakes occurred in 2003 and 2005 as the lava lake in Nyiragongo's summit crater refilled, and are explained as slip on a deeper inward-dipping ring fault triggered by the upward flux of magma into shallow levels of the magmatic plumbing system.

Although there is still controversy over the physical mechanisms that generate vertical-CLVD earthquakes [e.g., *Konstantinou et al.,* 2003; *Tkalčić et al*., 2009], the Tori Shima, Bárdarbunga and Nyiragongo events illustrate that vertical-CLVD earthquakes are closely linked to dynamic processes occurring inside volcanic systems. The Tori Shima and Bárdarbunga events suggest

that, in some cases, vertical-CLVD earthquakes may be triggered by the ascent of magma through the shallow crust, and the occurrence of these earthquakes may signal that a nearby volcano is likely to erupt in the future. The Nyiragongo events suggest that some vertical-CLVD earthquakes may be a response to magma migration, which would make these earthquakes useful for identifying the locations of recent eruptions.

In this study, we explore the relationship between vertical-CLVD earthquakes and volcanic unrest. Using two global seismicity catalogs and seismic data from many regional and global seismic networks, we perform a systematic global search for additional examples of moderate-sized vertical-CLVD earthquakes located near active volcanoes. We quantify where and how often vertical-CLVD earthquakes occur near these volcanoes, and investigate whether vertical-CLVD earthquakes are preferentially associated with particular tectonic settings or categories of volcanoes, or with specific types of eruptive activity. We characterize these earthquakes and document their relationships to volcanic unrest in detail in an effort to learn how vertical-CLVD earthquakes are linked to active deformation and eruption processes. Chapter 3 investigates the physical mechanisms that may be responsible for generating vertical-CLVD earthquakes at volcanoes.

2.2. Data and Methods

We search for vertical-CLVD earthquakes near volcanoes using two catalogs from the Global CMT Project (www.globalcmt.org). The first catalog is the standard GCMT catalog [*Dziewonski et al.,* 1981; *Ekström et al.,* 2012], which contains centroid times, locations and moment tensors for over 30,000 earthquakes since 1976. We investigate target earthquakes that have centroid

locations near volcanoes and vertical-CLVD moment tensors in the GCMT catalog. To identify those earthquakes that have robust vertical-CLVD focal mechanisms, we recalculate CMT solutions for the target earthquakes using additional data and updated methodology. The second catalog is the Surface Wave catalog, which contains epicenters, times and magnitude estimates for earthquakes that are detected using intermediate-period surface waves following the method of *Ekström* [2006]. Although the Surface Wave catalog has reported approximately 2000 earthquakes each year since 1991, we only investigate those earthquakes occurring near volcanoes that were not reported in other seismicity catalogs, or that have surface-wave magnitudes significantly larger than reported elsewhere. We calculate CMT solutions for these earthquakes in the same manner as for events from the GCMT catalog. We also model teleseismic body waves to constrain the depths of shallow earthquakes we find to have vertical-CLVD focal mechanisms.

2.2.1. Selection of Target Earthquakes

In order to assess the link between vertical-CLVD earthquakes and volcanic unrest, we investigate target earthquakes from the GCMT and Surface Wave catalogs that are located within 100 km of a recently active volcano. We restrict our search to the 429 D1 and D2 volcanoes in the Smithsonian Institution's Global Volcanism Program (GVP) database [*Siebert and Simkin*, 2002-], which have last known eruptions later than 2000 and 1900, respectively. This list is biased towards subaerial eruptions, and represents only a fraction of volcanoes that are active or potentially active worldwide. However, since our primary goal is to explore the relationships between vertical-CLVD earthquakes and active volcanic processess, we limit our scope to those volcanoes with recently documented eruptions. The distance threshold of 100 km accounts for

the uncertainty in locations from the GCMT [*Smith and Ekström*, 1997; *Hjórleifsdöttir and Ekström*, 2010] and Surface Wave catalogs, as well as the size and spacing of volcanic centers [*de Bremond d'Ars et al*., 1995; *Schmincke*, 2004]. A map of the recently active volcanoes and the target earthquakes is shown in Figure 2.2.

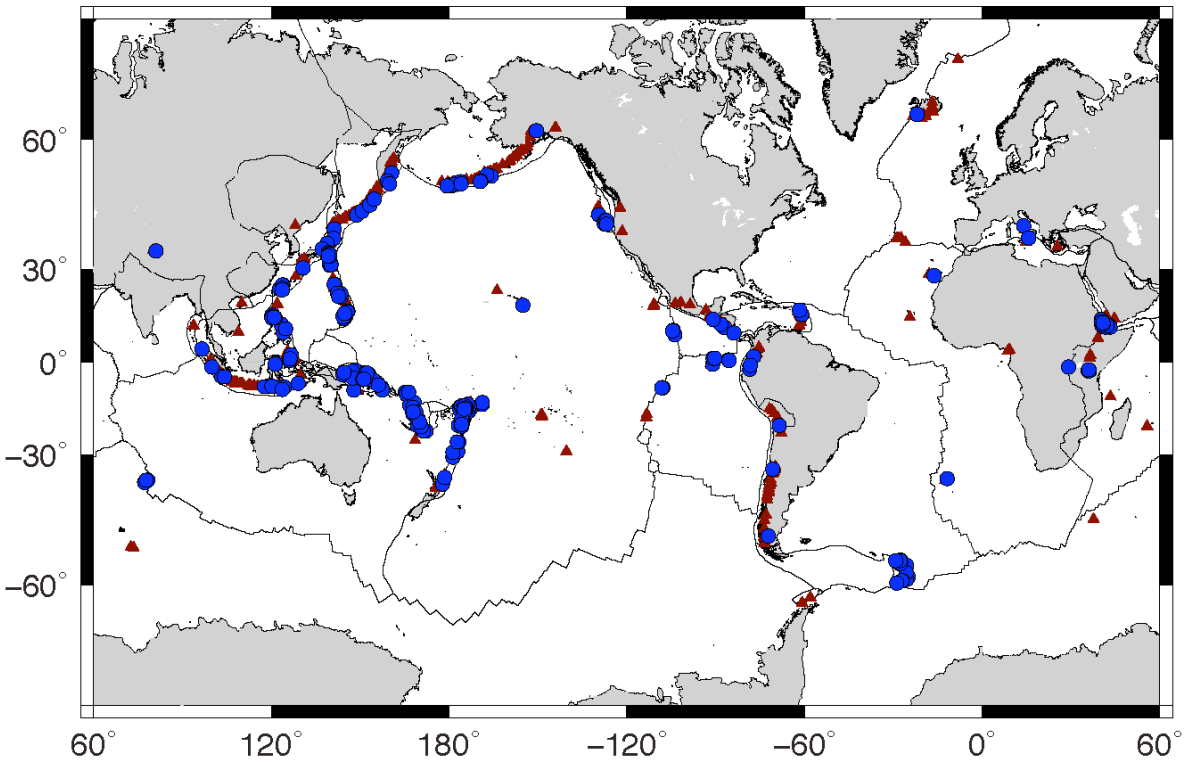

Figure 2.2. Map showing the locations of the 429 recently active volcanoes (maroon triangles) and 395 target earthquakes (blue circles) studied here. Recently active volcanoes have last known eruptions later than 1900. The target earthquakes include 135 earthquakes from the Global CMT catalog and 261 earthquakes from the Surface Wave catalog (71 and 190 earthquakes from Category 1 and Category 2, respectively). Category 1 earthquakes are reported in the ISC catalog, but have surface-wave magnitudes, M_{SW} [*Ekström,* 2006], that are at least one magnitude unit larger than the m_b estimates provided by the ISC. Category 2 earthquakes are newly detected earthquakes that were were detected and located using intermediate-period surface waves [*Ekström,* 2006], but which are missing from the ISC and NEIC bulletins. An earthquake on 26 May 2009 is a Category 1 earthquake that is also described in the GCMT catalog. Plate boundaries are from *Bird* [2003].

The Global CMT Catalog (1976-2009)

The GCMT catalog contains moment-tensor and location information for most earthquakes larger than M_W 5.0-5.5 since 1976 [*Dziewonski et al.,* 1981; *Ekström et al*., 2012]. The vast majority of GCMT solutions are calculated using initial hypocentral parameters provided by the National Earthquake Information Center (NEIC) of the United States Geological Survey (USGS), and long-period data primarily recorded on the IRIS-USGS Global Seismographic Network (GSN) or its historical equivalent. Prior to 2004, CMT solutions for earthquakes with $M_W < 5.5$ were constrained using long-period ($T > 45$ s) body-wave seismograms, whereas long-period surface-wave ($T > 135$ s, 'mantle wave') seismograms were included for larger earthquakes [*Dziewonski et al*., 1981; *Dziewonski and Woodhouse*, 1983]. Since 2004, intermediate-period ($35 < T < 150$ s) surface-wave data have also been incorporated in source-parameter inversions for shallow and intermediate-depth $M_W < 7.5$ earthquakes [*Arvidsson and Ekström*, 1998; *Ekström et al*., 2012]. Because intermediate-period surface waves are the largest seismic phases in long-period seismograms for shallow earthquakes, their use in CMT inversions has allowed smaller-magnitude earthquakes to be analyzed by the Global CMT Project. The inclusion of surface waves also improves the quality of GCMT solutions in general since the number of waveforms available for analysis is greatly increased.

Because most GCMT solutions were calculated without intermediate-period surface-wave data, we recalculate CMT solutions for vertical-CLVD earthquakes located near recently active volcanoes. Intermediate-period surface waves have different frequency contents and leave the source at different angles than body waves, and including these data allows us to obtain more robust source parameters. Target events from the GCMT catalog are identified using the

following criteria: $\varepsilon > 0.20$ and plunge of tension axis > 50°, or $\varepsilon < -0.20$ and plunge of pressure axis > 50°. We restrict our search to those earthquakes with centroid depths less than 50 km that are also located within a 100-km radius of a recently active volcano. Focal mechanisms for the earthquakes near Bárdarbunga were recalculated by *Nettles and Ekström* [1998] using methodology similar to that employed here, and we do not include those earthquakes as target events in our study. A total of 134 target earthquakes meet our criteria. We also identify as a target earthquake an M_W 5.8 vertical-T earthquake that occurred on 17 February 2009 in the Kermadec Islands. Although this earthquake did not occur within 100 km of a recently active volcano, it may be associated with volcanic activity at Curtis Island, a remote volcano for which the time of last eruption is unknown [*Smithsonian Institution*, 2009].

The Surface Wave Catalog (1991-2009)

Additional target earthquakes are identified from the Global CMT Project's catalog of surface-wave event locations. The Surface Wave catalog includes most shallow M > 4.8 earthquakes reported by global seismicity catalogs, such as the bulletins of the International Seismological Centre (ISC) and the USGS NEIC, for which event detection is based on the arrival times of high-frequency body-wave phases. The Surface Wave catalog also contains information about other earthquakes that are missing from the ISC and NEIC catalogs due to their small body-wave magnitudes or unusual source properties [*Ekström*, 2006]. Focal mechanisms have so far been calculated for only a small number of earthquakes from the Surface Wave catalog that are not reported in the ISC or NEIC catalogs.

We limit our scope to two categories of earthquakes from the Surface Wave catalog. Category 1 events are earthquakes that are reported in the ISC catalog, but which have surface-wave magnitudes, M_{SW} [*Ekström*, 2006], that are at least one magnitude unit larger than the m_b estimates provided by the ISC. Seventy-four Category 1 earthquakes have surface-wave detections with Quality C or better [*Ekström*, 2006] and initial locations within 100 km of a recently active volcano. Excluding three earthquakes that have non-vertical-CLVD solutions in the GCMT catalog, we identify 71 target earthquakes between 1991 and 2009. We note that one target event from Category 1, an earthquake in the Fiji Islands region on 26 May 2009, has a vertical-CLVD solution in the GCMT catalog. This earthquake is especially unusual because it is listed as an m_b 4.5 earthquake with a hypocentral depth of 100 km in the weekly listing of the NEIC's Preliminary Determination of Epicenters (PDEW), while in the GCMT catalog, it is listed as an M_W 5.5 earthquake with a centroid depth fixed to 12 km. With the exception of the May 2009 event, no focal mechanisms are available for the target earthquakes in Category 1.

The second category of earthquakes that we investigate from the Surface Wave catalog are 'new' earthquakes that are missing from the ISC and NEIC bulletins, but which were detected and located using intermediate-period surface waves using the method of *Ekström* [2006]. We restrict our search to newly detected earthquakes from 1991 to 2009 that have surface-wave detections with Quality C or better [*Ekström*, 2006] and initial locations within 100 km of a recently active volcano. The Nyiragongo earthquakes from *Shuler and Ekström* [2009] are examples of Category 2 events. Excluding those five events, which have focal mechanisms that were recalculated using methodology similar to that employed here, we identify 190 target earthquakes. No focal mechanisms are available for target earthquakes from Category 2.

2.2.2. Centroid-Moment-Tensor Solutions

For each of our target earthquakes, we collect three-component long-period and very-long-period seismic data from global and regional networks archived by the IRIS Data Management Center (DMC). The data sources vary depending on the year, but include stations from the following networks: the Modified High Gain Long Period Observatory (AS), the Black Forest Observatory (BF), the China Digital Seismic Network (CD), the Canadian National Seismic Network (CN), the Czech Seismic Network (CZ), the Digital World-Wide Standardized Seismograph Network (DW), GEOSCOPE (G), GEOFON (GE), the High-Gain Long-Period Network (HG), MEDNET (MN), the Singapore Seismological Network (MS), the Regional Seismic Test Network (RS), the Seismic Research Observatory (SR), TERRAscope (TS), and the IRIS-USGS Global Seismographic Network (GSN), which is a cooperative partnership between the following networks: the IRIS/IDA network (II), the IRIS/USGS Network (IU), the IRIS China Digital Seismic Network (IC), the Global Telemetered Southern Hemisphere Network (GT), and the CariUSGS Caribbean Network (CU). For target earthquakes from the GCMT catalog, the new data sets are typically more complete than those used for the original analysis.

We calculate centroid moment tensors, locations and times for each target earthquake generally following the standard GCMT approach [*Dziewonski et al*., 1981; *Dziewonski and Woodhouse*, 1983; *Arvidsson and Ekström*, 1998; *Ekström et al.*, 2005], and specifically the methods employed since 2004 [*Ekström et al.,* 2012]. We manually select and edit seismograms from three frequency bands and time windows. CMT solutions for events with $M_W < 5.5$ are calculated using body-wave data filtered from 40 to 150 and surface-wave data filtered from 50 to 150 s, while solutions for larger earthquakes also include mantle-wave data filtered from 125

to 350 s. For the smallest earthquakes, we filter the surface-wave data from 40 to 100 s or 35 to 75 s on a case-by-case basis to increase the signal-to-noise ratio. The CMT inversions are based on data from 14 to 163 stations, depending on the year and magnitude of individual target earthquakes.

As in the GCMT catalog, we constrain the sum of the diagonal elements of the moment tensor to equal zero ($M_{rr} + M_{\theta\theta} + M_{\phi\phi} = 0$), which is equivalent to imposing the condition that the moment tensor has no volumetric component. We recognize that exclusion of the isotropic component can result in deviatoric moment tensors with dominant vertical-CLVD components for earthquakes that have net volume changes [*Strelitz*, 1989; *Frohlich*, 1990b; *Kawakatsu*, 1996]. We discuss this issue in detail in Chapter 3.

We assess the quality of each CMT solution, and only report solutions that meet the Global CMT Project's quality standards. In particular, we reject unstable solutions, solutions based on a small number of waveforms and solutions with high residual misfit. We classify earthquakes as 'vertical-CLVD' if their moment tensors have 40% or more non-double-couple component and dominant tension or pressure axes that plunge more steeply than 60° (Figure 2.1). Because we are concerned with vertical-CLVD earthquakes associated with volcanic processes, we restrict our discussion to those events with centroid depths shallower than 25 km.

2.2.3. Teleseismic Body-Wave Modeling

The vertical-CLVD earthquakes that we identify near active volcanoes are shallow and their depths cannot be determined accurately using the long-period seismic data required for standard

GCMT analysis. To constrain the focal depths of these earthquakes, we attempt to model the broadband teleseismic body waves for vertical-CLVD earthquakes with magnitudes $M_W \geq 5.0$. We follow the method of *Ekström* [1989], and invert teleseismic P and SH waveforms for focal mechanism, focal depth and moment-rate function. For this analysis, we collect broadband seismic records from the IRIS DMC and deconvolve the instrument response to obtain displacement records filtered from 1 to 100 s period. Following the method of *Harvey and Choy* [1982], broadband records for the oldest earthquakes are constructed from digital long- and short-period seismograms, as in *Ekström* [1989]. Synthetic seismograms are calculated using ray theory and the Preliminary Reference Earth Model [PREM; *Dziewonski and Anderson*, 1981]. Reflections and conversions near the source are modeled using a layer-matrix method for a regional velocity model. For a small number of subaerial volcanoes, we construct the regional velocity models using the local crustal structure from CRUST2.0 [*Bassin et al.,* 2000]. However, for those earthquakes near island arc or submarine volcanoes, we use the CRUST2.0 model for a Japanese island arc (J1) and adjust the thickness of the water layer to match the summit elevation of the nearest volcano. We include the CMT estimate of the point-source moment tensor as a soft constraint in the inversions to ensure that focal mechanisms calculated from the broadband data are compatible with the long-period seismic data used in the CMT analysis.

2.3. Results

Of the 395 target earthquakes investigated, we obtain robust CMT solutions for 313 earthquakes. Focal mechanisms are plotted in Figure 2.3 and source-parameter information is available in the Appendix A as well as on our website (www.globalcmt.org). We report updated CMT solutions for 124 earthquakes from the GCMT catalog (Tables A1 and A2) and new CMT solutions for

190 earthquakes from the Surface Wave catalog, including 59 Category 1 earthquakes (Tables A3 and A4) and 131 Category 2 earthquakes (Tables A5 and A6). We note that the 26 May 2009 earthquake is reported in both the GCMT and Surface Wave catalogs.

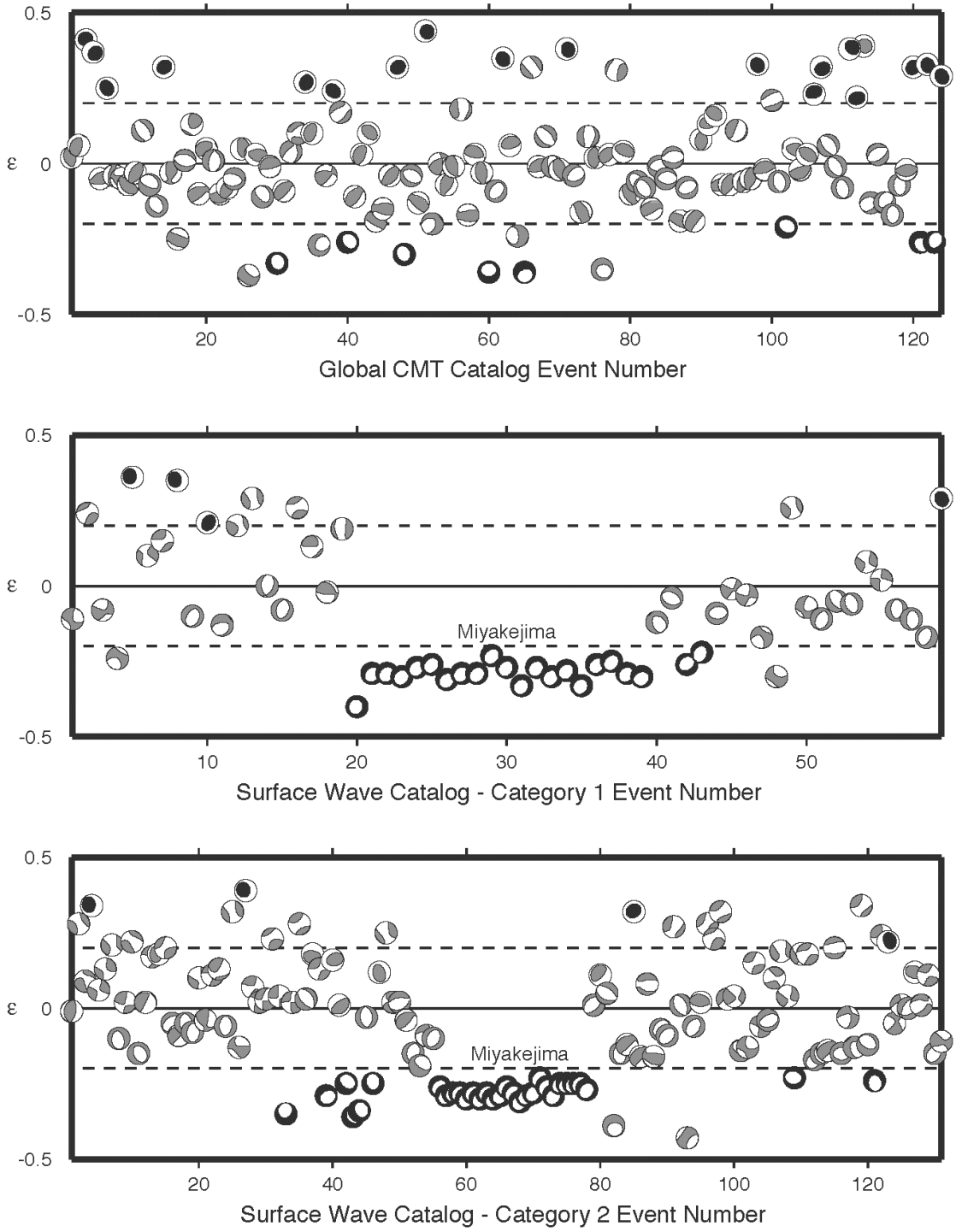

(Figure caption on next page)

Figure 2.3. Focal mechanisms for all of the target earthquakes for which we were able to obtain robust CMT solutions, plotted against their ε values. Shallow vertical-CLVD earthquakes are plotted in black, and the dashed lines indicate $\varepsilon = \pm 0.20$. The top panel shows focal mechanisms for 124 earthquakes from the Global CMT catalog after reanalysis. The middle panel shows focal mechanisms for 59 Category 1 earthquakes from the Surface Wave catalog, and the bottom panel shows focal mechanisms for 131 Category 2 earthquakes from the Surface Wave catalog. The event numbers correspond to the event numbers reported Tables A1-A6. The 43 vertical-P earthquakes associated with the caldera collapse of Miyakejima in 2000 are indicated in the middle and bottom panels.

From this group of 313 earthquakes, we identify 86 shallow vertical-CLVD earthquakes located near recently active volcanoes. We are able to model teleseismic body waves from 18 of these events. Along with the 15 vertical-CLVD earthquakes already documented at Bárdarbunga [*Nettles and Ekström*, 1998] and Nyiragongo volcanoes [*Shuler and Ekström*, 2009], this study increases the number of well-documented moderate-sized shallow vertical-CLVD earthquakes known to occur near volcanic centers to 101.

2.3.1. All Target Earthquakes

The recalculated CMT solutions for target events from the GCMT catalog are based on both body and surface-wave data that were manually selected and edited. Because the new solutions described in Tables A1 and A2 were calculated using additional data and updated methodology, we prefer them over those reported in the standard GCMT catalog. Compared to the original GCMT solutions, the recalculated moment tensors changed by ~0.1 magnitude units, and the centroid locations moved ~30 km on average. As expected, differences between the original and recalculated CMT solutions are smaller for earthquakes that occurred after 2004, when the Global CMT Project began to use surface-wave data routinely.

For most target earthquakes from the GCMT catalog, we find that the addition of surface-wave data reduces the size of the non-double-couple component, resulting in new moment tensors that are approximately double couple. Recalculated moment tensors for most vertical-T and vertical-P earthquakes are typical of reverse- and normal-faulting earthquakes. In many cases, the new focal mechanisms are consistent with those reported in the GCMT catalog for other nearby earthquakes. Only 26 of the earthquakes considered, 18 vertical-T and 8 vertical-P earthquakes, have vertical-CLVD moment tensors and centroid depths less than 25 km after the addition of surface-wave data. Included in this dataset are the four vertical-T earthquakes identified by *Ekström* [1994] that did not occur near Bárdarbunga. In Figure 2.4, we illustrate how the addition of surface-wave data affects the CMT solutions for one earthquake that became more double-couple and one that remained vertical-CLVD.

Target earthquakes from the Surface Wave catalog have a wide variety of focal mechanisms, reflecting the diversity of tectonic settings located with a 100-km radius of recently active volcanoes. In Tables A3-A6, we provide CMT solutions for these earthquakes. For both Category 1 and Category 2 events, we find that moment tensors for most of the target earthquakes are close to double-couple. The most commonly observed earthquake types are strike-slip and normal-faulting earthquakes along the ridge-transform systems near Tonga, Vanuatu, Samoa, Fiji, and the Mariana Islands. Shallow strike-slip earthquakes in the southern oceans are particularly difficult to detect using traditional methods due to their nearly nodal teleseismic P-wave radiation patterns, their remoteness from seismic stations and the presence of strong microseismic noise [*Rouland et al.,* 1992; *Shearer,* 1994], and some go unreported in standard global seismicity catalogs.

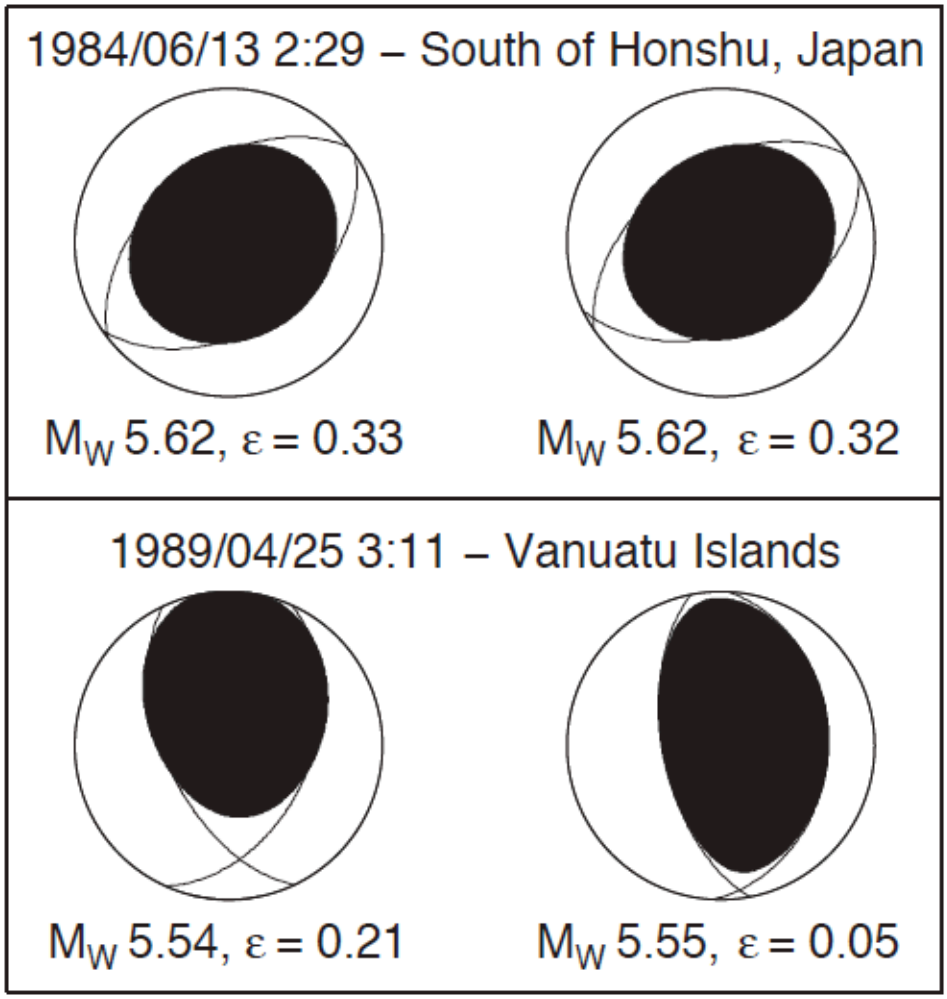

Figure 2.4. A comparison between the original CMT solutions (left), calculated using body waves, and new CMT solutions (right), calculated in this study using body and surface waves, for two earthquakes. The moment magnitude and ε value associated with each CMT solution are indicated below the focal mechanisms. Thin solid lines show the double-couple part of the focal mechanisms. The top panel is for the Tori Shima earthquake. The original solution was calculated using body-wave data from 15 stations, and the new solution was calculated using body-wave data from 20 stations, mantle-wave data from 6 stations, and surface-wave data from 22 stations. The bottom panel is for an earthquake in the Vanuatu Islands. The original solution was calculated using body-wave data from 22 stations, and the new solution was calculated using body-wave data from 15 stations, mantle-wave data from 12 stations, and surface-wave data from 27 stations. The Tori Shima earthquake remained vertical-CLVD after the addition of surface-wave data whereas the Vanuatu earthquake became approximately double-couple.

Of the 190 target earthquakes investigated from the Surface Wave catalog, 61 have vertical-CLVD moment tensors. Eight earthquakes have vertical-T moment tensors and 53 have vertical-P moment tensors. We find that CMT solutions for vertical-CLVD earthquakes are based on a greater number of waveforms compared to other target earthquakes with similar M_W magnitudes from the Surface Wave catalog. This suggests that some aspect of the source properties of vertical-CLVD earthquakes, other than small magnitude, prevents them from being detected and located using high-frequency body waves.

We were not able to calculate CMT solutions for several Category 2 target earthquakes that are spatially and temporally associated with explosive eruptions that produced large-scale pyroclastic density currents. These events include the sector collapse and lateral blast event at Soufrière Hills volcano in the West Indies on 26 December 1997 [*Calder et al*., 2002; *Druitt et al*., 2002; *Ritchie et al*., 2002; *Sparks et al*., 2002; *Voight et al*., 2002; *Woods et al*., 2002; *Young et al*., 2002], and several pre-climactic eruptions at Pinatubo volcano in the Philippines on 14 and 15 June 1991 [*Harlow et al*., 1996; *Hoblitt et al*., 1996; *Lynch and Stephens*, 1996; *Power et al*., 1996; *Wolfe and Hoblitt*, 1996]. If the seismic signals that we observe are produced by gravity-driven flows, it may be more appropriate to model these events using time-varying forces.

2.3.2. Vertical-CLVD Earthquakes

In total, we have identified 101 shallow vertical-CLVD earthquakes with centroid locations near recently active volcanoes. In Figures 2.5 and 2.6, we show the locations and focal mechanisms of vertical-CLVD earthquakes from the GCMT and Surface Wave catalogs. Figure 2.7 shows a map of the vertical-P earthquakes associated with Miyakejima volcano. In these three maps, red

focal mechanisms denote earthquakes that are associated with volcanic unrest at a volcano within ~60 km (Section 2.4). For each of the 86 vertical-CLVD earthquakes analyzed in this study, in Table 2.1, we provide a summary of source parameters including centroid times and locations, m_b values from the NEIC, as well as M_W values, ε values and plunges of the dominant principal axes derived from the CMT solutions.

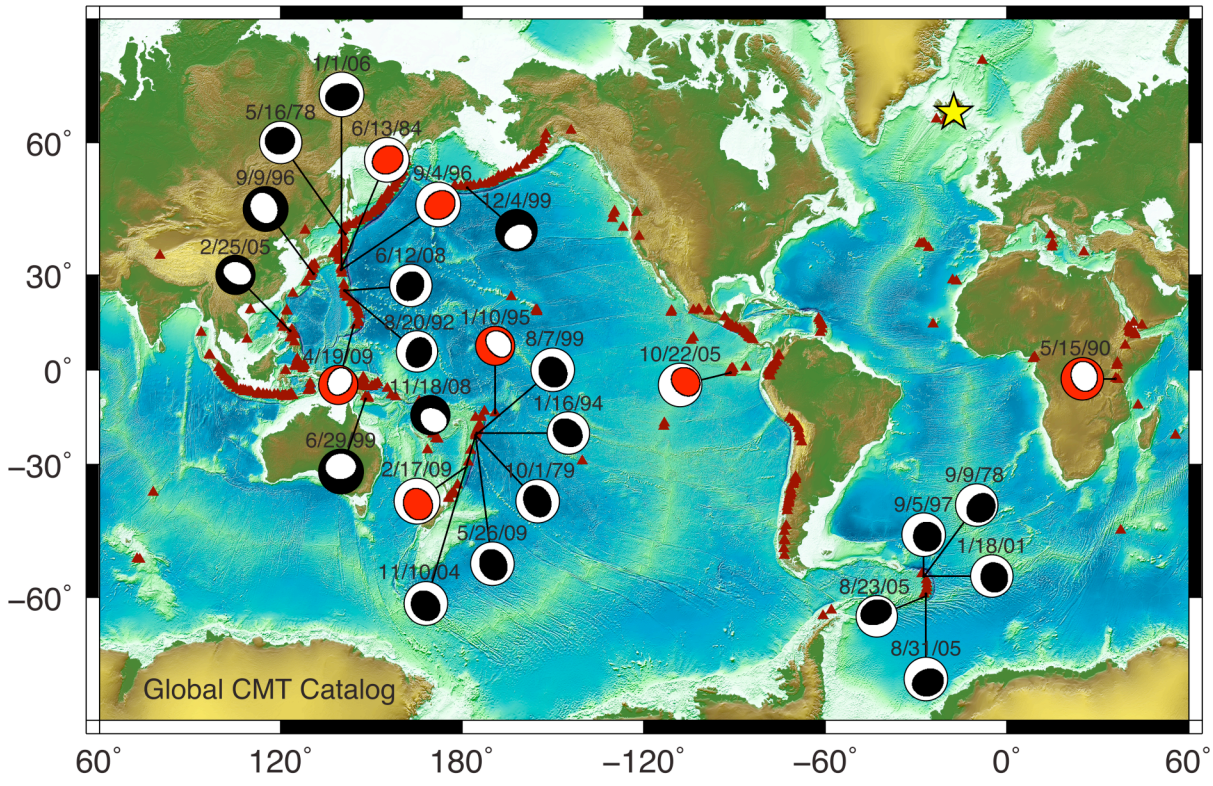

Figure 2.5. Map showing focal mechanisms for the 26 shallow vertical-CLVD earthquakes identified from the Global CMT catalog. Red focal mechanisms indicate that the earthquakes are associated with a documented episode of volcanic unrest at a nearby volcano (see text for details). The dates of the earthquakes are listed above the focal mechanisms. Maroon triangles indicate the locations of the 429 recently active volcanoes. A yellow star indicates the location of Bárdarbunga volcano, where 10 vertical-T earthquakes occurred between 1976 and 1996 [*Nettles and Ekström*, 1998]. Bathymetry and topography are from the ETOPO1 dataset.

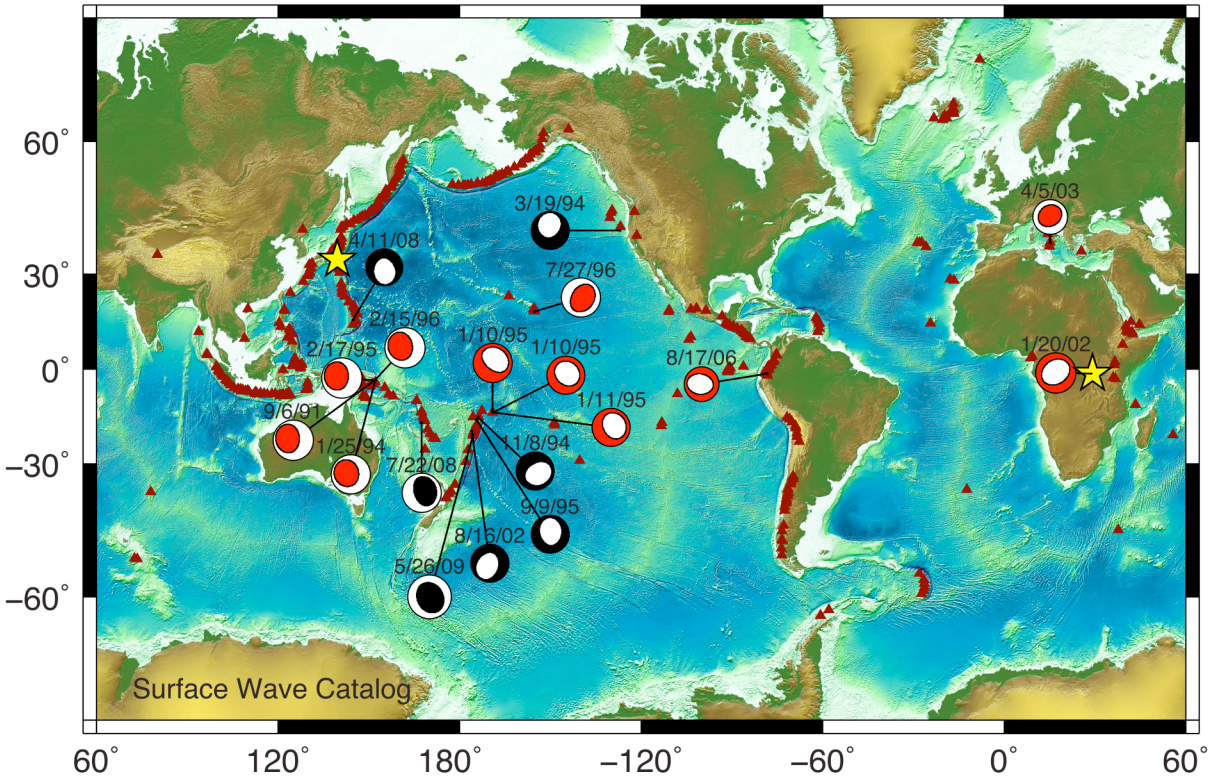

Figure 2.6. Map showing focal mechanisms for 18 shallow vertical-CLVD earthquakes after CMT analysis of events in the Surface Wave catalog. The vertical-T earthquake on 26 May 2009 is repeated from Figure 2.5. Red focal mechanisms indicate that the earthquakes are associated with a documented episode of volcanic unrest at a nearby volcano (see text for details). The dates of the earthquakes are listed above the focal mechanisms. Maroon triangles indicate the locations of the 429 recently active volcanoes. Yellow stars indicate the locations of Miyakejima volcano, where another 43 vertical-P earthquakes occurred in 2000 (Figure 2.7), and Nyiragongo, where 5 vertical-P earthquakes occurred between 2002 and 2005 [*Shuler and Ekström*, 2009]. Bathymetry and topography are from the ETOPO1 dataset.

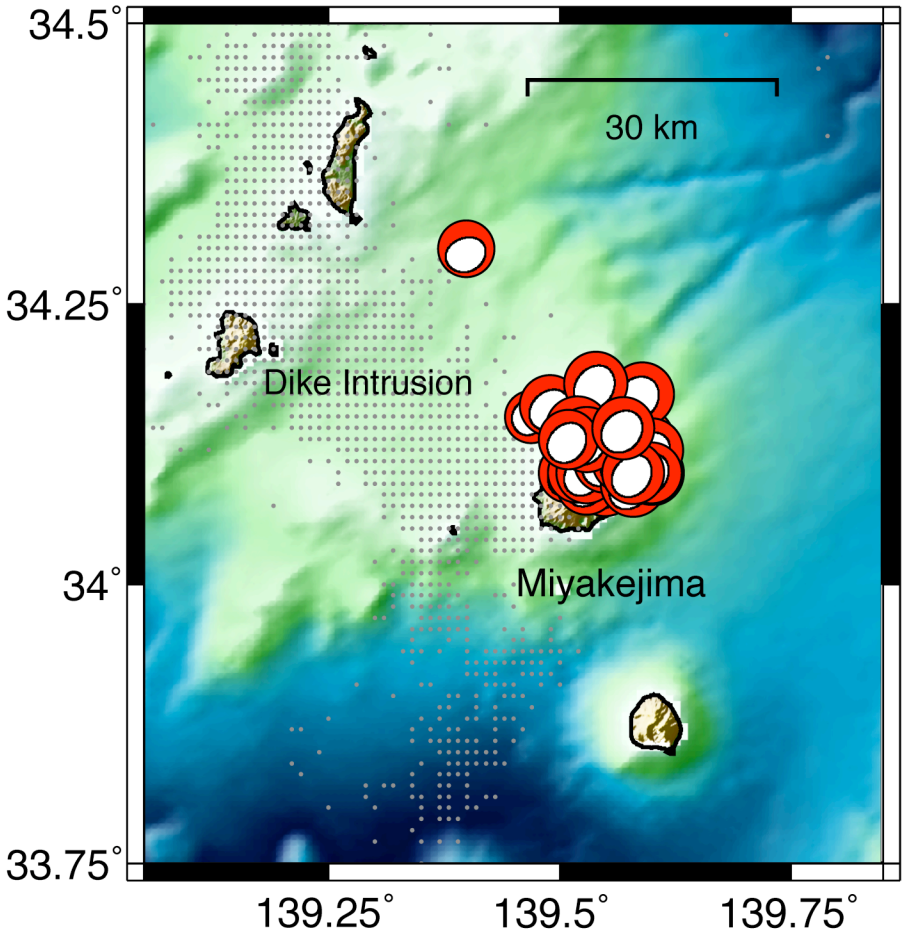

Figure 2.7. Map showing focal mechanisms for the 43 vertical-P earthquakes associated with the caldera collapse of Miyakejima volcano between 7 July and 18 August 2000. Focal mechanisms are plotted at their centroid locations. The earthquake with the centroid location that is farthest away from Miyakejima occurred on 18 August 2000 at 9:09 UTC. Grey dots show the locations of earthquakes associated with the dike intrusion that began at Miyakejima on 26 June 2000. Epicenters for earthquakes from June to December 2000 are provided by the Japan Meteorological Agency. The grid-like pattern is due to the reported precision of the epicenters. Topography is from the Shuttle Radar Topography Mission (SRTM). Bathymetry is from the Japan Oceanographic Data Center J-EGG500 dataset.

Table 2.1. Source Parameters for 86 Shallow Vertical-CLVD Earthquakes Located Near Recently Active Volcanoes[a]

	Source	Date			Time			Centroid	Centroid	Geographical				Plunge of	CMT
No.	Catalog	Y	M	D	h	m	sec	Latitude	Longitude	Location	m_b	M_W	ε	P/T Axis	Quality
1	GCMT	1978	5	16	7	35	49.1	40.99	141.44	Hokkaido, Japan	5.7	5.3	0.41	82	A
2	GCMT	1978	9	9	6	1	7.6	-56.34	-27.31	South Sandwich Islands Region	5.4	5.4	0.37	68	B
3	GCMT	1979	10	1	12	23	51.2	-21.29	-175.66	Tonga Islands	5.1	5.5	0.25	88	B
4	GCMT	1984	6	13	2	29	29.8	31.57	139.97	South of Honshu, Japan	5.6	5.6	0.32	85	A
5	GCMT	1990	5	15	15	21	31.1	-2.96	35.80	Tanzania	5.5	5.4	-0.33	77	B
6	SW-2	1991	9	6	5	40	54.6	-3.85	152.03	New Ireland, Papua New Guinea		5.0	0.34	63	A
7	GCMT	1992	8	20	18	31	39.9	25.43	141.13	Volcano Islands, Japan		5.2	0.27	80	A
8	GCMT	1994	1	16	10	18	41.5	-20.62	-175.20	Tonga Islands	4.8	5.3	0.24	87	A
9	SW-2	1994	1	25	23	15	1.9	-3.82	152.05	New Ireland, Papua New Guinea		5.0	0.39	70	B
10	SW-2	1994	3	19	21	49	42.9	41.67	-127.06	Off Coast of Oregon		4.7	-0.35	62	B
11	SW-2	1994	11	8	13	7	56.8	-15.91	-173.97	Tonga Islands		4.8	-0.29	69	B
12	GCMT	1995	1	10	13	43	37.3	-14.22	-169.06	Samoa Islands		4.9	-0.26	70	C
13	SW-2	1995	1	10	17	44	0.1	-14.24	-169.03	Samoa Islands		4.9	-0.25	68	B
14	SW-2	1995	1	10	23	49	26.3	-14.25	-168.97	Samoa Islands		4.8	-0.36	79	B
15	SW-2	1995	1	11	18	16	5.9	-14.18	-169.00	Samoa Islands		4.8	-0.34	71	B
16	SW-1	1995	2	17	17	45	42.7	-3.85	152.10	New Ireland, Papua New Guinea	3.5	5.0	0.36	64	B
17	SW-2	1995	9	9	15	53	17.4	-16.59	-174.38	Tonga Islands		4.8	-0.25	75	C
18	SW-1	1996	2	15	1	11	43.0	-3.85	152.03	New Ireland, Papua New Guinea	3.7	5.0	0.35	67	B
19	SW-1	1996	7	27	13	6	38.6	18.77	-155.18	Hawaii		4.9	0.21	79	C
20	GCMT	1996	9	4	18	16	7.7	31.51	139.99	South of Honshu, Japan	5.4	5.7	0.32	82	A
21	GCMT	1996	9	9	4	34	21.9	30.44	130.95	Kyushu, Japan	5.5	5.7	-0.30	83	A
22	GCMT	1997	9	5	3	23	17.0	-56.41	-27.47	South Sandwich Islands Region	5.2	5.4	0.44	73	A
23	GCMT	1999	6	29	5	50	9.2	-9.59	147.97	East Papua New Guinea	5.8	5.6	-0.36	69	B
24	GCMT	1999	8	7	6	17	30.5	-21.24	-175.61	Fiji Islands Region	5.0	5.5	0.35	81	A
25	GCMT	1999	12	4	8	46	57.7	51.56	-178.29	Andreanof Islands, Aleutian Islands	5.2	5.1	-0.36	60	B
26	SW-1	2000	7	7	11	22	4.3	34.15	139.47	Near South Coast of Honshu, Japan	3.4	4.4	-0.40	79	C
27	SW-1	2000	7	9	13	40	15.3	34.11	139.56	Near South Coast of Honshu, Japan	2.5	5.2	-0.29	79	B
28	SW-2	2000	7	10	17	11	52.0	34.09	139.55	Near South Coast of Honshu, Japan		5.4	-0.26	80	A
29	SW-1	2000	7	11	15	37	31.5	34.10	139.59	Near South Coast of Honshu, Japan	4.0	5.3	-0.29	80	A
30	SW-1	2000	7	12	4	7	0.0	34.13	139.57	Near South Coast of Honshu, Japan	3.4	5.2	-0.30	79	A
31	SW-1	2000	7	12	18	45	55.6	34.12	139.58	Near South Coast of Honshu, Japan	2.7	5.3	-0.27	79	A
32	SW-1	2000	7	13	17	12	29.8	34.10	139.60	Near South Coast of Honshu, Japan	2.6	5.5	-0.26	79	A
33	SW-1	2000	7	15	14	34	46.4	34.14	139.57	Near South Coast of Honshu, Japan	2.4	5.3	-0.31	79	A
34	SW-2	2000	7	16	1	37	55.0	34.12	139.59	Near South Coast of Honshu, Japan		5.2	-0.29	79	A
35	SW-2	2000	7	16	17	11	51.3	34.12	139.55	Near South Coast of Honshu, Japan		5.2	-0.28	80	C
36	SW-2	2000	7	17	8	26	41.3	34.10	139.58	Near South Coast of Honshu, Japan		5.2	-0.28	79	A
37	SW-2	2000	7	17	21	35	45.4	34.10	139.60	Near South Coast of Honshu, Japan		5.2	-0.30	78	A
38	SW-2	2000	7	18	20	32	29.5	34.13	139.59	Near South Coast of Honshu, Japan		5.4	-0.28	81	A
39	SW-2	2000	7	19	16	15	40.0	34.10	139.51	Near South Coast of Honshu, Japan		5.1	-0.30	80	B
40	SW-1	2000	7	20	8	24	17.4	34.11	139.58	Near South Coast of Honshu, Japan	1.5	5.3	-0.29	78	A
41	SW-1	2000	7	21	0	27	51.4	34.16	139.49	Near South Coast of Honshu, Japan	2.5	5.2	-0.29	77	B
42	SW-2	2000	7	21	15	7	21.3	34.09	139.53	Near South Coast of Honshu, Japan		5.1	-0.28	83	A
43	SW-2	2000	7	22	5	1	23.9	34.14	139.53	Near South Coast of Honshu, Japan		5.2	-0.30	77	A
44	SW-2	2000	7	22	17	20	43.9	34.10	139.52	Near South Coast of Honshu, Japan		5.0	-0.29	83	A
45	SW-1	2000	7	23	16	36	44.5	34.13	139.55	Near South Coast of Honshu, Japan	3.8	5.2	-0.23	80	A
46	SW-2	2000	7	24	5	25	20.0	34.10	139.53	Near South Coast of Honshu, Japan		5.2	-0.26	79	A
47	SW-1	2000	7	24	19	55	37.3	34.11	139.55	Near South Coast of Honshu, Japan	2.3	5.3	-0.27	76	A
48	SW-2	2000	7	25	9	55	32.1	34.09	139.58	Near South Coast of Honshu, Japan		5.1	-0.28	80	A

Table 2.1. (Continued)

No.	Source Catalog	Date Y	M	D	Time h	m	sec	Centroid Latitude	Centroid Longitude	Geographical Location	m_b	M_w	ε	Plunge of P/T Axis	CMT Quality
49	SW-1	2000	7	25	20	10	28.0	34.14	139.55	Near South Coast of Honshu, Japan	1.7	5.2	-0.33	76	A
50	SW-2	2000	7	26	3	57	54.9	34.12	139.56	Near South Coast of Honshu, Japan		5.1	-0.31	79	A
51	SW-2	2000	7	26	13	29	43.8	34.11	139.55	Near South Coast of Honshu, Japan		5.3	-0.29	76	A
52	SW-1	2000	7	27	7	22	50.4	34.13	139.59	Near South Coast of Honshu, Japan	2.9	5.4	-0.27	77	A
53	SW-1	2000	7	28	7	7	39.3	34.10	139.58	Near South Coast of Honshu, Japan	2.8	5.4	-0.30	75	A
54	SW-1	2000	7	29	7	51	38.8	34.12	139.57	Near South Coast of Honshu, Japan	2.7	5.5	-0.28	77	A
55	SW-1	2000	7	30	13	36	33.5	34.17	139.59	Near South Coast of Honshu, Japan	3.2	5.5	-0.33	75	B
56	SW-2	2000	7	31	22	45	0.9	34.18	139.54	Near South Coast of Honshu, Japan		5.4	-0.28	78	B
57	SW-2	2000	8	2	6	15	35.8	34.09	139.58	Near South Coast of Honshu, Japan		5.6	-0.23	80	A
58	SW-1	2000	8	3	19	16	42.1	34.14	139.52	Near South Coast of Honshu, Japan	3.7	5.5	-0.26	78	B
59	SW-2	2000	8	4	16	11	13.6	34.11	139.57	Near South Coast of Honshu, Japan		5.4	-0.26	79	A
60	SW-1	2000	8	6	0	23	22.7	34.13	139.53	Near South Coast of Honshu, Japan	3.4	5.5	-0.25	78	B
61	SW-2	2000	8	8	0	3	29.3	34.13	139.51	Near South Coast of Honshu, Japan		5.1	-0.29	78	A
62	SW-2	2000	8	8	17	11	58.6	34.10	139.60	Near South Coast of Honshu, Japan		5.4	-0.25	80	A
63	SW-2	2000	8	10	22	2	47.4	34.11	139.59	Near South Coast of Honshu, Japan		5.5	-0.25	79	A
64	SW-2	2000	8	13	6	40	21.4	34.12	139.60	Near South Coast of Honshu, Japan		5.5	-0.25	78	A
65	SW-2	2000	8	16	0	7	29.2	34.10	139.60	Near South Coast of Honshu, Japan		5.2	-0.25	80	B
66	SW-2	2000	8	16	15	57	6.7	34.10	139.58	Near South Coast of Honshu, Japan		5.3	-0.27	80	A
67	SW-1	2000	8	17	19	7	44.2	34.14	139.57	Near South Coast of Honshu, Japan	1.9	5.4	-0.29	78	A
68	SW-1	2000	8	18	9	9	16.3	34.30	139.40	Near South Coast of Honshu, Japan	2.4	4.8	-0.30	70	B
69	GCMT	2001	1	18	20	17	17.4	-56.31	-27.43	South Sandwich Islands Region	5.2	5.3	0.38	77	B
70	SW-1	2002	1	20	23	45	31.6	-1.42	29.13	Lake Tanganyika Region	4.1	5.1	-0.26	84	C
71	SW-1	2002	8	16	21	30	47.5	-20.28	-175.99	Tonga Islands	3.7	4.7	-0.22	72	C
72	SW-2	2003	4	5	7	13	45.5	38.65	15.19	Sicily, Italy		4.3	0.32	83	C
73	GCMT	2004	11	10	10	35	38.0	-21.26	-175.62	Fiji Islands Region	5.0	5.5	0.33	80	A
74	GCMT	2005	2	25	16	17	1.6	12.77	123.23	Luzon, Philippines	4.9	4.9	-0.21	76	B
75	GCMT	2005	8	23	1	38	20.1	-59.80	-26.68	South Sandwich Islands Region	5.1	5.1	0.23	71	B
76	GCMT	2005	8	31	1	24	54.9	-59.48	-26.86	South Sandwich Islands Region	5.3	5.5	0.32	71	B
77	GCMT	2005	10	22	20	34	47.9	-1.06	-91.31	Galapagos Islands, Ecuador	4.9	5.5	0.38	62	A
78	GCMT	2006	1	1	7	12	8.8	31.60	140.17	Southeast of Honshu, Japan	5.3	5.6	0.22	81	A
79	SW-2	2006	8	17	5	37	21.2	-1.47	-78.44	Ecuador		4.4	-0.23	82	C
80	SW-2	2008	4	11	0	46	13.3	16.09	144.69	Mariana Islands		4.7	-0.24	69	C
81	GCMT	2008	6	12	13	10	14.7	25.53	141.18	Volcano Islands, Japan	5.1	5.3	0.32	86	A
82	SW-2	2008	7	22	8	45	22.4	-17.36	167.52	Vanuatu Islands		4.9	0.22	71	C
83	GCMT	2008	11	18	12	46	3.8	-18.76	169.55	Vanuatu Islands	4.9	5.0	-0.26	65	C
84	GCMT	2009	2	17	3	30	58.8	-30.54	-178.58	Kermadec Islands, New Zealand	5.4	5.8	0.33	78	A
85	GCMT	2009	4	19	8	54	52.8	14.66	144.23	Mariana Islands	4.7	4.9	-0.26	72	C
86	GCMT/SW-1	2009	5	26	0	49	42.9	-21.24	-175.62	Fiji Islands Region	4.5	5.5	0.29	85	A

[a]Source Catalogs are Global CMT catalog (GCMT) or Surface Wave Catalog (SW). SW-1 denotes events reported in the ISC or NEIC catalogs where M_{SW}-m_b > 1.0. SW-2 denotes earthquakes that were newly detected using surface waves *Ekström* [2006]. The date, time, centroid longitude and latitude, and values of M_w, ε, and the plunge of the dominant P or T axes are derived from our CMT solutions. The m_b values are from the ISC or NEIC catalogs. See text for explanation of CMT quality. Broadband depth and source duration are derived from broadband modeling of teleseismic body waves. Note that all centroid depths from the CMT solutions were fixed to 12 km.

In Tables A7 and A8 in the Auxiliary Material, we provide detailed information about the CMT solutions for vertical-CLVD earthquakes, including estimates of the standard errors for the source parameters. The standard errors associated with the latitude and longitude components are ~3 km on average, although due to uneven station distributions, the presence of noise and unmodeled structural heterogeneity [*Nakanishi and Kanamori*, 1982; *Dziewonski and Woodhouse*, 1983; *Dziewonski et al.,* 1983; *Dziewonski et al.,* 1984; *Smith and Ekström*, 1997; *Hjörleifsdóttir and Ekström*, 2010], the actual uncertainties are likely larger. For example, the centroid locations for vertical-CLVD earthquakes linked to specific episodes of volcanic unrest are sometimes tens of kilometers from their source volcanoes.

We assess the quality of each CMT solution based on the station coverage, the variance reduction, and the percentage of available waveforms used in the inversion (Table 2.1). A-quality CMT solutions have variance reductions of 50% or more and are calculated using data from 75% or more of the available stations. CMT solutions that have variance reductions of 40-50%, azimuthal gaps greater than 90°, and those that are calculated using data from 50-75% of the available stations are assigned B quality. We assign the two earthquakes that have fixed centroid locations to be C quality, in addition to those solutions that are calculated using less than 50% of the available stations, or those that have variance reductions less than 40%. We find that 47 earthquakes have A-quality solutions, 26 have B-quality solutions, and 13 have C-quality solutions. However, all of the solutions meet the quality standards of the Global CMT Project. Our confidence in the significance of the vertical-CLVD component is a function of both the CMT solution quality and the magnitude of the non-double-couple component.

We do not report the centroid depths of vertical-CLVD earthquakes in Table 2.1 because they were all fixed to 12 km during the inversion process, as is standard for shallow earthquakes. To obtain better constraints on focal depth, we attempted to model the broadband teleseismic body waves for vertical-CLVD earthquakes with magnitudes $M_W \geq 5.0$. However, we were only able to model 18 earthquakes, all from the GCMT catalog. Body waves for earthquakes in the Surface Wave catalog are of lower amplitude than the background noise across the frequency band we examine.

Earthquakes in this magnitude range typically show clear, impulsive direct arrivals and surface reflections. In contrast, we find that the body waves for vertical-CLVD earthquakes are dominated by low-frequency energy. Figure 2.8 shows an example body-wave solution for the M_W 5.7 vertical-T earthquake that occurred South of Honshu on 4 September 1996. We find that focal-depth estimates depend on the weight of the soft constraint of the long-period moment tensors from the CMT inversions, and there is a tradeoff between focal depth and source duration. Despite the uncertainties associated with modeling body waves for earthquakes depleted in high-frequency energy, the character of the waveforms for all 18 earthquakes is consistent with focal depths in the top 10 km of the crust.

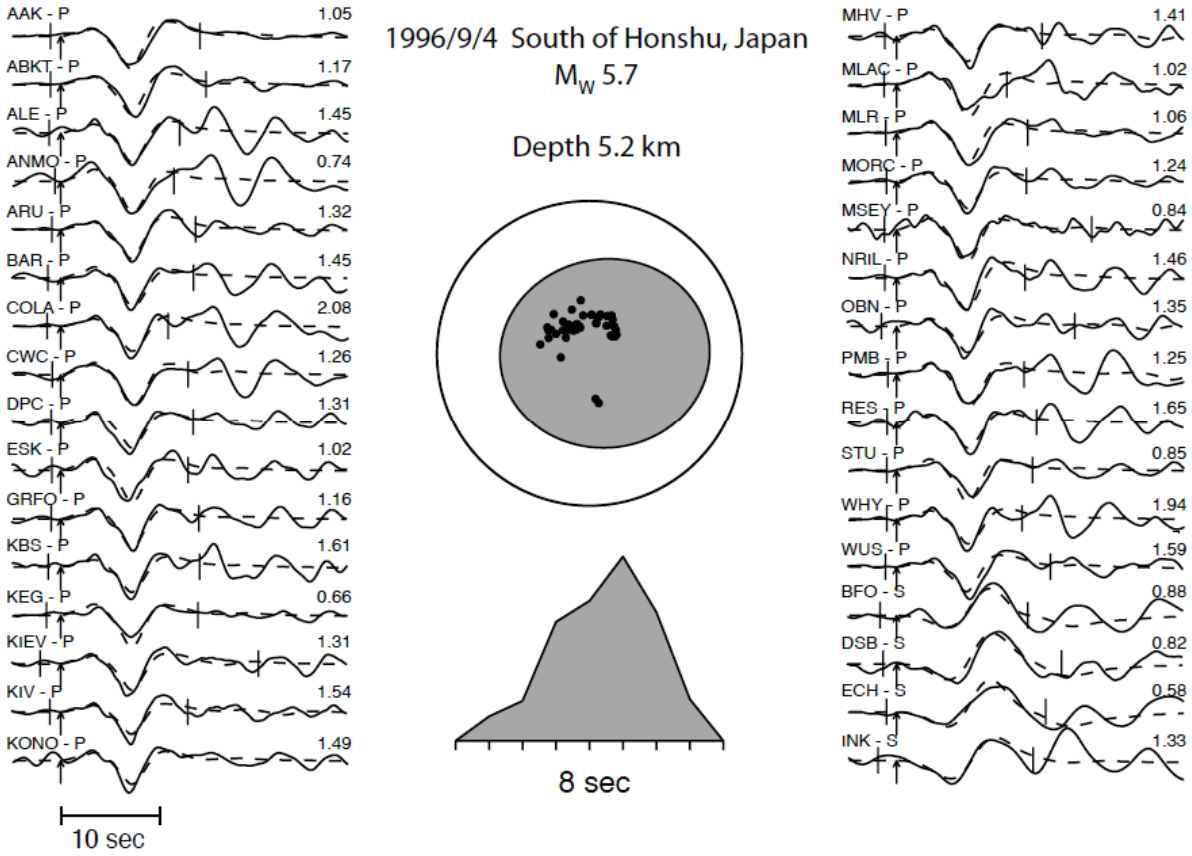

Figure 2.8. Focal-depth analysis for the M_W 5.7 earthquake that occurred on 4 September 1996 near Smith Rock volcano in the Izu-Bonin volcanic arc. Solid lines are broadband teleseismic P and SH waveforms, and dashed lines are synthetic seismograms. Brackets across the waveforms show the portions of the seismograms that were used in the inversion, and arrows indicate the picked first arrivals. The station name, data type and maximum amplitude (in microns) are printed above each waveform. The focal mechanism and moment-rate function determined in the body-wave inversion are plotted in the center of the figure. Black dots on the focal mechanism show where the plotted waveforms exited the focal sphere. The estimated focal depth of the earthquake is ~5.2 km below sea level.

2.4. Links to Volcanic Activity

Our target earthquakes were selected because they occurred near active volcanoes, but there were no restrictions on volcano type or location. In our dataset of shallow vertical-CLVD earthquakes, we observe events near active volcanoes in a wide variety of geographical locations and tectonic settings. In Table 2.2, we list the three closest volcanoes to each vertical-CLVD earthquake. We report the distances from the centroid location of each earthquake to the three closest volcanoes using the latitude and longitude coordinates provided by the GVP [*Siebert and Simkin*, 2002-]. The length scales of volcanic systems, which range from a few hundred meters to tens of kilometers, should be considered when interpreting these distances. We also report the volcano type, or morphology, of the closest volcanoes and indicate whether the earthquakes occurred during documented episodes of volcanic unrest. Most vertical-CLVD earthquakes are located within ~30 km of arc volcanoes in subduction zones in the Pacific, Indian and Southern Oceans and the Mediterranean Sea. However, vertical-CLVD earthquakes also occur in the East African Rift, along a mid-ocean ridge segment in the northeastern Pacific Ocean, and near hotspot volcanoes in Hawaii, the Galápagos Islands and Samoa Islands. This result suggests that many types of volcanoes are capable of generating vertical-CLVD earthquakes, and strengthens the link between volcanoes and these anomalous earthquakes.

Table 2.2. Volcanoes Located Near Shallow Vertical-CLVD Earthquakes[a]

	Three Nearest Volcanoes Within 100 km of Shallow Vertical-CLVD Earthquakes										
No.	Volcano 1	D1 (km)	Type	Unrest?	Volcano 2	D2 (km)	Type	Unrest?	Volcano 3	D3 (km)	Type	Unrest?
1	*Osore-yama*	42	Stratovolcano	No	*Hakkoda Group*	60	Stratovolcanoes	No	*Towada*	73	Caldera	No
2	*Zavodovski*	17	Stratovolcano	No	*Hodson*	41	Stratovolcano	No	*Leskov Island*	62	Stratovolcano	No
3	Unnamed (0403-01)	10	Submarine Volcano	No	*Unnamed (0403-011)*	18	Submarine Volcano	No	Unnamed (0403-03)	51	Submarine Volcano	No
*4	Smith Rock	16	Submarine Volcano	Yes	Bayonnaise Rocks	35	Submarine Volcano	No	*Myojin Knoll*	60	Submarine Volcano	No
*5	Ol Doinyo Lengai	25	Stratovolcano	Yes								
*6	*Tavui*	35	Caldera	No	Rabaul	50	Pyroclastic Shield	Yes				
7	Kita-Iwo-jima	15	Stratovolcano	No	Kaitoku Seamount	77	Submarine Volcano	No	Ioto [Iwo-jima]	77	Caldera	No
8	Hunga Tonga-Hunga Ha'apai	20	Submarine Volcano	No	Falcon Island	40	Submarine Volcano	No	Unnamed (0403-03)	43	Submarine Volcano	No
*9	*Tavui*	37	Caldera	No	Rabaul	53	Pyroclastic Shield	Yes				
10	*Escanaba Segment*	85	Submarine Volcano	No								
11	*Tafahi*	28	Stratovolcano	No	Curacoa	46	Submarine Volcano	No	Tafu-Maka	66	Submarine Volcano	No
*12	Vailulu'u	0[b]	Submarine Volcano	Yes	*Ta'u*	42	Shield Volcano	No	*Ofu-Olosega*	61	Shield Volcanoes	No
*13	Vailulu'u	4	Submarine Volcano	Yes	*Ta'u*	45	Shield Volcano	No	*Ofu-Olosega*	64	Shield Volcanoes	No
*14	Vailulu'u	10	Submarine Volcano	Yes	*Ta'u*	55	Shield Volcano	No	*Ofu-Olosega*	70	Shield Volcanoes	No
*15	Vailulu'u	8	Submarine Volcano	Yes	*Ta'u*	49	Shield Volcano	No	*Ofu-Olosega*	67	Shield Volcanoes	No
*16	*Tavui*	32	Caldera	No	Rabaul	48	Pyroclastic Shield	Yes				
17												
*18	*Tavui*	35	Caldera	No	Rabaul	50	Pyroclastic Shield	Yes				
*19	Loihi	19	Submarine Volcano	Yes	Kilauea	73	Shield Volcano	Yes	Mauna Loa	91	Shield Volcano	No
*20	Smith Rock	10	Submarine Volcano	Yes	Bayonnaise Rocks	42	Submarine Volcano	No	*Myojin Knoll*	67	Submarine Volcano	No
21	Kuchinoerabu-jima	70	Stratovolcanoes	Yes	Kikai	73	Caldera	No	*Ibusuki Volcanic Field*	94	Calderas	No
22	*Zavodovski*	14	Stratovolcano	No	*Hodson*	38	Stratovolcano	No	*Leskov Island*	50	Stratovolcano	No
23	*Musa River*	36	Hydrothermal Field	No	*Madilogo*	62	Pyroclastic Cone	No	*Managlase Plateau*	69	Volcanic Field	No
24	Unnamed (0403-01)	16	Submarine Volcano	No	*Unnamed (0403-011)*	18	Submarine Volcano	No	Unnamed (0403-03)	44	Submarine Volcano	No
25	Tanaga	38	Stratovolcanoes	No	*Takawangha*	40	Stratovolcano	No	Gareloi	43	Stratovolcano	No
*26	Miyakejima	10	Stratovolcano	Yes	*Kozu-shima*	30	Lava Domes	No	*Nii-jima*	32	Lava Domes	No
*27	Miyakejima	4	Stratovolcano	Yes	*Mikura-jima*	27	Stratovolcano	No	*Kozu-shima*	39	Lava Domes	No
*28	Miyakejima	2	Stratovolcano	Yes	*Mikura-jima*	25	Stratovolcano	No	*Kozu-shima*	39	Lava Domes	No
*29	Miyakejima	6	Stratovolcano	Yes	*Mikura-jima*	26	Stratovolcano	No	*Kozu-shima*	42	Lava Domes	No
*30	Miyakejima	7	Stratovolcano	Yes	*Mikura-jima*	29	Stratovolcano	No	*Kozu-shima*	39	Lava Domes	No
*31	Miyakejima	6	Stratovolcano	Yes	*Mikura-jima*	28	Stratovolcano	No	*Kozu-shima*	40	Lava Domes	No
*32	Miyakejima	7	Stratovolcano	Yes	*Mikura-jima*	26	Stratovolcano	No	*Kozu-shima*	43	Lava Domes	No
*33	Miyakejima	8	Stratovolcano	Yes	*Mikura-jima*	30	Stratovolcano	No	*Kozu-shima*	39	Lava Domes	No
*34	Miyakejima	7	Stratovolcano	Yes	*Mikura-jima*	28	Stratovolcano	No	*Kozu-shima*	41	Lava Domes	No
*35	Miyakejima	5	Stratovolcano	Yes	*Mikura-jima*	28	Stratovolcano	No	*Kozu-shima*	38	Lava Domes	No
*36	Miyakejima	5	Stratovolcano	Yes	*Mikura-jima*	26	Stratovolcano	No	*Kozu-shima*	41	Lava Domes	No
*37	Miyakejima	7	Stratovolcano	Yes	*Mikura-jima*	26	Stratovolcano	No	*Kozu-shima*	43	Lava Domes	No
*38	Miyakejima	8	Stratovolcano	Yes	*Mikura-jima*	29	Stratovolcano	No	*Kozu-shima*	41	Lava Domes	No
*39	Miyakejima	3	Stratovolcano	Yes	*Mikura-jima*	27	Stratovolcano	No	*Kozu-shima*	35	Lava Domes	No
*40	Miyakejima	6	Stratovolcano	Yes	*Mikura-jima*	27	Stratovolcano	No	*Kozu-shima*	41	Lava Domes	No
*41	Miyakejima	10	Stratovolcano	Yes	*Kozu-shima*	31	Lava Domes	No	*Nii-jima*	33	Lava Domes	No
*42	Miyakejima	1	Stratovolcano	Yes	*Mikura-jima*	26	Stratovolcano	No	*Kozu-shima*	37	Lava Domes	No
*43	Miyakejima	7	Stratovolcano	Yes	*Mikura-jima*	31	Stratovolcano	No	*Kozu-shima*	35	Lava Domes	No
*44	Miyakejima	2	Stratovolcano	Yes	*Mikura-jima*	27	Stratovolcano	No	*Kozu-shima*	36	Lava Domes	No
*45	Miyakejima	6	Stratovolcano	Yes	*Mikura-jima*	29	Stratovolcano	No	*Kozu-shima*	37	Lava Domes	No
*46	Miyakejima	2	Stratovolcano	Yes	*Mikura-jima*	27	Stratovolcano	No	*Kozu-shima*	37	Lava Domes	No
*47	Miyakejima	4	Stratovolcano	Yes	*Mikura-jima*	27	Stratovolcano	No	*Kozu-shima*	38	Lava Domes	No
*48	Miyakejima	5	Stratovolcano	Yes	*Mikura-jima*	25	Stratovolcano	No	*Kozu-shima*	41	Lava Domes	No

Table 2.2. (Continued).

	Three Nearest Volcanoes Within 100 km of Shallow Vertical-CLVD Earthquakes											
No.	Volcano 1	D1 (km)	Type	Unrest?	Volcano 2	D2 (km)	Type	Unrest?	Volcano 3	D3 (km)	Type	Unrest?
*49	Miyakejima	7	Stratovolcano	Yes	*Mikura-jima*	31	Stratovolcano	No	*Kozu-shima*	37	Lava Domes	No
*50	Miyakejima	5	Stratovolcano	Yes	*Mikura-jima*	28	Stratovolcano	No	*Kozu-shima*	38	Lava Domes	No
*51	Miyakejima	4	Stratovolcano	Yes	*Mikura-jima*	27	Stratovolcano	No	*Kozu-shima*	38	Lava Domes	No
*52	Miyakejima	8	Stratovolcano	Yes	*Mikura-jima*	29	Stratovolcano	No	*Kozu-shima*	41	Lava Domes	No
*53	Miyakejima	5	Stratovolcano	Yes	*Mikura-jima*	26	Stratovolcano	No	*Kozu-shima*	41	Lava Domes	No
*54	Miyakejima	6	Stratovolcano	Yes	*Mikura-jima*	28	Stratovolcano	No	*Kozu-shima*	39	Lava Domes	No
*55	Miyakejima	11	Stratovolcano	Yes	*Mikura-jima*	33	Stratovolcano	No	*Nii-jima*	38	Lava Domes	No
*56	Miyakejima	11	Stratovolcano	Yes	*Nii-jima*	34	Lava Domes	No	*Kozu-shima*	35	Lava Domes	No
*57	Miyakejima	5	Stratovolcano	Yes	*Mikura-jima*	25	Stratovolcano	No	*Kozu-shima*	41	Lava Domes	No
*58	Miyakejima	7	Stratovolcano	Yes	*Mikura-jima*	31	Stratovolcano	No	*Kozu-shima*	34	Lava Domes	No
*59	Miyakejima	5	Stratovolcano	Yes	*Mikura-jima*	27	Stratovolcano	No	*Kozu-shima*	40	Lava Domes	No
*60	Miyakejima	6	Stratovolcano	Yes	*Mikura-jima*	30	Stratovolcano	No	*Kozu-shima*	35	Lava Domes	No
*61	Miyakejima	6	Stratovolcano	Yes	*Mikura-jima*	30	Stratovolcano	No	*Kozu-shima*	34	Lava Domes	No
*62	Miyakejima	7	Stratovolcano	Yes	*Mikura-jima*	26	Stratovolcano	No	*Kozu-shima*	43	Lava Domes	No
*63	Miyakejima	6	Stratovolcano	Yes	*Mikura-jima*	27	Stratovolcano	No	*Kozu-shima*	41	Lava Domes	No
*64	Miyakejima	8	Stratovolcano	Yes	*Mikura-jima*	28	Stratovolcano	No	*Kozu-shima*	42	Lava Domes	No
*65	Miyakejima	7	Stratovolcano	Yes	*Mikura-jima*	26	Stratovolcano	No	*Kozu-shima*	43	Lava Domes	No
*66	Miyakejima	5	Stratovolcano	Yes	*Mikura-jima*	26	Stratovolcano	No	*Kozu-shima*	41	Lava Domes	No
*67	Miyakejima	8	Stratovolcano	Yes	*Mikura-jima*	30	Stratovolcano	No	*Kozu-shima*	39	Lava Domes	No
*68	*Nii-jima*	16	Lava Domes	No	*Kozu-shima*	24	Lava Domes	No	Miyakejima	27	Stratovolcano	Yes
69	*Zavodovski*	9	Stratovolcano	No	*Hodson*	47	Stratovolcano	No	Protector Shoal	59	Submarine Volcano	No
*70	Nyamuragira	8	Shield Volcano	No	Nyiragongo	17	Stratovolcano	Yes	*Karisimbi*	37	Stratovolcano	No
71	Falcon Island	60	Submarine Volcano	No	Hunga Tonga-Hunga Ha'apai	71	Submarine Volcano	No	Unnamed (0403-03)	79	Submarine Volcano	No
*72	*Panarea*	11	Stratovolcano	Yes	Stromboli	16	Stratovolcano	Yes	*Lipari*	28	Stratovolcanoes	No
73	Unnamed (0403-01)	14	Submarine Volcano	No	*Unnamed (0403-011)*	18	Submarine Volcano	No	Unnamed (0403-03)	47	Submarine Volcano	No
74	*Masaraga*	73	Stratovolcano	No	Mayon	74	Stratovolcano	No	*Iriga*	81	Stratovolcano	No
75	Thule Islands	55	Stratovolcanoes	No	Bristol Island	86	Stratovolcano	No				
76	Thule Islands	29	Stratovolcanoes	No	Bristol Island	53	Stratovolcano	No				
*77	Cerro Azul	19	Shield Volcano	No	Sierra Negra	30	Shield Volcano	Yes	Alcedo	73	Shield Volcano	No
78	Smith Rock	21	Submarine Volcano	No	Bayonnaise Roks	39	Submarine Volcano	No	*Myojin Knoll*	63	Submarine Volcano	No
*79	Tungurahua	0[b]	Stratovolcano	Yes	*Licto*	39	Scoria Cones	No	*Chimborazo*	42	Stratovolcano	No
80												
81	Kita-Iwo-jima	16	Stratovolcano	No	Kaitoku Seamount	66	Submarine Volcano	No	Ioto [Iwo-jima]	87	Caldera	No
82	*North Vate*	89	Stratovolcanoes	No								
83	*Traitor's Head*	34	Stratovolcano	No	Yasur	86	Stratovolcano	Yes				
*84	*Curtis Island*	2	Submarine Volcano	Yes	*Macauley Island*	39	Caldera	No	Giggenbach	57	Submarine Volcano	No
*85	NW Rota-1	60	Submarine Volcano	Yes								
86	Unnamed (0403-01)	16	Submarine Volcano	No	*Unnamed (0403-011)*	17	Submarine Volcano	No	Unnamed (0403-03)	44	Submarine Volcano	No

[a]Three nearest volcanoes within 100 km of the 86 shallow vertical-CLVD earthquakes reported in Table 1. We report the name of the volcanoes in addition to the distances between the volcanoes and the earthquake centroid locations (D1-D3). Volcano names written in italic have last known eruptions before 1900. We also report the volcano type (morphology) and indicate whether the vertical-CLVD earthquakes occurred during documented episodes of volcanic unrest at each nearby volcano. An asterisk next to the event number in Column 1 indicates that the earthquake occurred during an episode of unrest at a volcano within ~60 km. See text for details.

[b]Centroid Location fixed to the volcano.

We wish to assess not only the spatial but also the temporal relationships between the vertical-CLVD earthquakes and volcanism. To assess the likelihood that the earthquakes result, directly or indirectly, from active magma transport in the crust, we evaluate whether each vertical-CLVD earthquake in our dataset is associated with known eruptive or other volcanic activity. Below, we summarize the location of each vertical-CLVD earthquake and its temporal relationship to volcanic unrest at nearby volcanoes. First, in chronological order by the first earthquake at each volcano, we discuss the 61 vertical-CLVD earthquakes that are spatially and temporally associated with volcanic unrest, using eruption reports from the literature. We then summarize the locations of the remaining 24 vertical-CLVD earthquakes by geographic location. Unless otherwise indicated, the CMT solutions discussed are A-quality and the information about specific volcanoes is from the GVP [*Siebert and Simkin*, 2002-].

2.4.1. Smith Rock

Three M_W 5.6-5.7 vertical-T earthquakes in the Izu-Bonin volcanic arc have centroid locations that are ~10-20 km from Smith Rock, a basaltic pinnacle that forms the southern flank of a 20-km-wide seamount with an 8-9 km-wide submarine caldera. The first earthquake in the sequence is the 13 June 1984 Tori Shima earthquake discussed in Section 2.1. The Tori Shima earthquake produced an M_t=7.3 tsunami [*Abe*, 1988; *Satake and Kanamori*, 1991], and was followed within hours by earthquakes with T-wave trains, which are characteristic for submarine volcanic activity [*Talandier and Okal*, 1987]. The second and third earthquakes occurred on 4 September 1996 and 1 January 2006. Similar to the Tori Shima earthquake, the 1996 earthquake produced an M_t = 7.5 tsunami and is associated with a swarm of low-frequency earthquakes that produced T-waves [*Sugioka et al*., 2000], again suggesting volcanic activity. Both the 1984 and 1996

earthquakes are likely associated with magma ascent processes at Smith Rock. The 2006 earthquake, which has the smallest non-double-couple component, is not linked to any known volcanic unrest.

2.4.2. Ol Doinyo Lengai

An M_W 5.4 vertical-P earthquake with a B-quality CMT solution took place in Tanzania on 15 May 1990. The centroid location is ~25 km from Ol Doinyo Lengai, one of the most active volcanoes in the East African Rift. Ol Doinyo Lengai is a stratovolcano, and the only known active volcano to erupt natrocarbonatite, a silica-poor, low-temperature, and low-viscosity lava [*Oppenheimer*, 1998]. Before erupting explosively in 2007, Ol Doinyo Lengai erupted effusively for nearly 25 years, producing lava flows and spatter cones that were confined to the summit crater. Effusive activity was observed both before and after the 15 May earthquake, during overflights on 2 May and 9 July 1990 [*Smithsonian Institution*, 1990a/b], suggesting that the vertical-P earthquake is related to this effusive eruption.

2.4.3. Rabaul

Four M_W 5.0 vertical-T earthquakes took place north of New Britain in Papua New Guinea between 1991 and 1996. These earthquakes occurred on 6 September 1991, 25 January 1994, 17 February 1995 and 15 February 1996. The vertical-CLVD earthquakes have A or B-quality CMT solutions, and focal mechanisms that are remarkably similar between events. The centroid locations are tightly clustered near the tip of the Gazelle Peninsula, ~35 km north of Tavui, a 10-by-12-km submarine caldera, and ~50 km north of Rabaul, an active pyroclastic shield volcano with a nested 9-by-14-km caldera complex surrounded by several small volcanic cones. The last

eruption of Tavui occurred approximately 7000 years ago [*Nairn et al*., 1995; *Wood et al*., 1995], although recent seismic tomography studies indicate the presence of a low-velocity zone beneath the submarine caldera [*Bai and Greenhalgh*, 2005; *Itikarai*, 2008 as referenced in *Johnson et al*., 2010]. Rabaul, on the other hand, has erupted frequently in the last several hundred years. Seismic tomography indicates that Rabaul is underlain by two magma chambers, one extending from 2-4 km depth, and a deeper chamber extending from 12-18 km depth [*Finlayson et al*., 2003; *Bai and Greenhalgh*, 2005; *Itikarai*, 2008; *Johnson et al*., 2010].

The most recent episode of volcanic unrest at Rabaul began in 1971, and was characterized by uplift of the caldera interior and increased seismicity concentrated along an annular structure [*McKee et al*., 1984]. Beginning in September 1983, Rabaul experienced a seismic crisis during which tens of thousands of small magnitude, high-frequency earthquakes occurred along an outward-dipping ring-fault structure extending to 4-5 km [*McKee et al*., 1984; *Mori and McKee*, 1987; *Mori et al.*, 1989; *Jones and Stewart*, 1997; *Itikarai*, 2008; *Johnson et al.*, 2010]. The seismic crisis was accompanied by ~80 cm of uplift in the central part of the caldera, although it is debated whether the deformation was due to the pressurization of shallow magmatic or hydrothermal sources in the caldera block [*McKee et al*., 1984; *Mori and McKee*, 1987; *Geyer and Gottsman*, 2010], overpressure of a deep magma reservoir [*De Natale and Pingue*, 1993], or the partial intrusion of a dike along the ring-fault structure [*Saunders*, 2001; 2005]. After May 1985, seismicity decreased at Rabaul, and the volcano did not erupt until 1994.

On 19 September 1994, Rabaul began an explosive phase that continues today. Initially, the explosive eruption occurred simultaneously at two volcanic cones, Tavurvur on the northeast

side, and Vulcan on the west side of the caldera. Activity at Vulcan ceased by 2 October 1994, although explosive eruptions at Tavurvur continue to occur intermittently. The first two vertical-CLVD earthquakes occur before the start of explosive activity in September 1994, and are not associated with increases in the rate of seismicity or other unusual activity at the volcano. The remaining two vertical-CLVD earthquakes occur after the start of the 1994 eruption, and are associated with elevated seismicity and explosions at Tavurvur [*Smithsonian Institution*, 1995a; 1996]. Leveling measurements indicate that the 1995 earthquake is associated with deflation, whereas the 1996 earthquake is associated with slight inflation of the central caldera block [*Smithsonian Institution*, 1995; 1996*b*]. All four vertical-CLVD earthquakes at Rabaul are temporally associated with volcanic unrest. However, the events do not seem to be linked to a specific type of shallow eruptive activity in the caldera itself. This suggests that the earthquakes are linked to deformation occurring at deeper levels of the volcano.

2.4.4. Vailulu'u

Four M_W 4.8-4.9 vertical-P earthquakes with B or C-quality CMT solutions took place in the Samoa Islands on 10 and 11 January 1995 (Figure 2.9). These earthquakes have centroid locations within 10 km of Vailulu'u, a recently discovered massive submarine volcano with a 2-km-wide caldera. Vailulu'u is believed to mark the current location of the Samoan hotspot [*Hart et al*., 2000]. The vertical-P earthquakes are spatially and temporally associated with an anomalous swarm of $m_b < 5.0$ earthquakes that occurred northwest of the volcano from 9-29 January 1995. Acoustic T-waves were also recorded by a local hydrophone array from 8 January through early February 1995 [*Smithsonian Institution*, 1995b]. Besides the January 1995 swarm, a search of the NEIC catalog (1973-present) finds no other examples of teleseismically-detected

earthquakes located within 100 km of Vailulu'u. Both the unusual locations of the January 1995 earthquakes, and the fact that all of the earthquakes have similar magnitudes, suggest that the swarm is associated with magmatic activity [*Konter et al*., 2004]. Indeed, radiometric ages of dredge samples from a 1999 cruise confirm that a volcanic eruption occurred in the summit crater of Vailulu'u within the prior 5-10 years [*Hart et al*., 2000]. The four events for which we have obtained CMT solutions show a clear association with this volcanic activity.

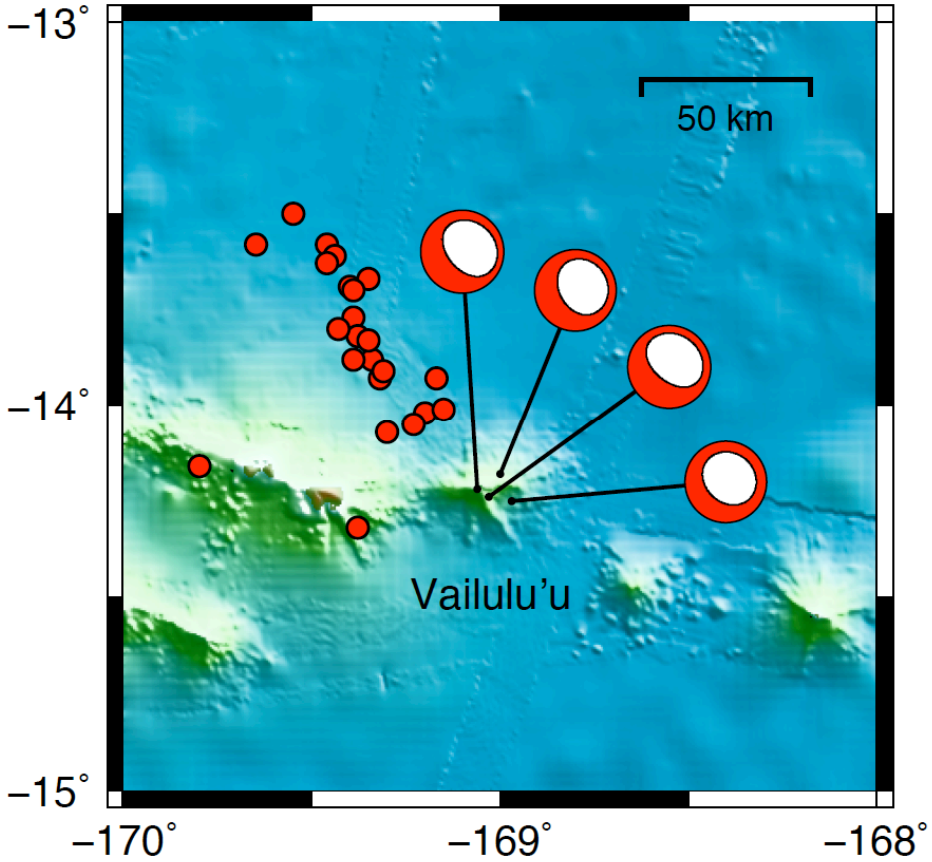

Figure 2.9. Map showing focal mechanisms for the four vertical-P earthquakes associated with an anomalous earthquake swarm that occurred at Vailulu'u volcano in January 1995. Red dots show the locations of M > 4 earthquakes from the NEIC catalog that occurred between 9 and 129 January 1995. Bathymetry is from the Global Multi-Resolution Topography (GMRT) synthesis [*Ryan et al.,* 2009] used in GeoMapApp (http://www.geomapapp.org).

2.4.5. Loihi

An M_W 4.9 vertical-T earthquake with a C-quality CMT solution occurred in Hawaii on 27 July 1996. The centroid location for this earthquake is ~20 km from Loihi, the youngest volcano in the Hawaiian chain. Loihi is a submarine volcano with a well-defined summit platform that contains several pit craters and an active hydrothermal system. Eleven days prior to the vertical-T earthquake, on 16 July 1996, the largest earthquake swarm ever recorded in the Hawaiian Islands began at Loihi. The following description of the swarm is a summary of results from *Duennebier et al.* [1997] and *Caplan-Auerbach and Duennebier* [2001].

The 1996 swarm can be divided into two distinct phases. The initial phase lasted from 16 to 18 July, and was characterized by 170 $M_L > 1$ high-frequency volcano-tectonic earthquakes. After a brief hiatus on 19 July, when there were no locatable earthquakes at Loihi, the second phase commenced and the cumulative seismic moment increased dramatically. Thousands of earthquakes with magnitudes up to M_L 4.9 were located near Loihi through 9 August. The second phase of the swarm, which consisted of predominantly long-period earthquakes, had two main pulses of activity, the first occurring between 20 and 25 July, and the second occurring between 26 July and 5 August. The vertical-T earthquake occurred during the second pulse of seismic activity in Phase 2.

Beginning on 6 August, submersible dives and bathymetry surveys confirmed that Pele's Peak, formerly the locus of Loihi's hydrothermal activity, had collapsed to form a new pit crater, Pele's Pit, with a diameter of 600 m and a depth of 300 m [*Duennebier et al.*, 1997]. Although high-temperature hydrothermal plumes were observed, and popping noises were detected by

sonobuoys, evidence of an ongoing eruption was not observed, and fresh lava recovered from the summit has been shown to predate the earthquake swarm by several months [*Duennebier et al*., 1997; *Garcia et al*., 1998, 2006]. The cause of the 1996 collapse of Pele's Pit is unknown, although it may have been triggered by a rapid draining of a shallow magma chamber, either into a volcanic rift zone or a deeper magma reservoir [*Davis and Clague*, 1998; *Caplan-Auerbach and Duennebier*, 2001]. The vertical-T earthquake was likely triggered by rapid magma migration or the collapse of the pit crater.

2.4.6. Miyakejima

Forty-three $4.4 \leq M_W \leq 5.6$ vertical-P earthquakes occurred in the Izu-Bonin volcanic arc between 7 July and 18 August 2000 (Figure 2.7). Most of the earthquakes have A-quality CMT solutions, although a few CMT solutions have B- or C-quality CMT solutions due to their small magnitudes or interference from other earthquakes. With the exception of the final earthquake, centroid locations for all of the vertical-P earthquakes are tightly clustered within ~10 km of Miyakejima, an 8-km-wide volcanic island formed by a basaltic stratovolcano with several small summit calderas. In the summer of 2000, the most intense swarm of earthquakes ever observed in Japan began at Miyakejima and migrated northwestwards to Kozushima, signaling the lateral propagation of a massive dike intrusion. Following a small submarine eruption, the summit crater of Miyakejima began to collapse on 8 July 2000. The collapse continued incrementally over a period of ~40 days, producing unusual tilt signals and vertical-P earthquakes. We summarize this eruptive activity below.

On 26 June 2000, a swarm of small volcanic earthquakes was observed beneath Miyakejima's southwestern flank. Over a period of a few hours, seismicity intensified and migrated westwards from the island, resulting in a small submarine eruption of basaltic andesite from four craters off the west coast of Miyakejima on 27 July [*Fujita et al*., 2001; *Sakai et al*., 2001; *Amma-Miyasaka et al*., 2005; *Kaneko et al*., 2005; *Uhira et al*., 2005]. Following the eruption, the swarm continued to migrate ~30 km northwestward, and reached the area between Kozushima and Niijima islands by 1 July [*Sakai et al*., 2001; *Fujita et al*., 2001]. Intense seismicity was observed in the area between Miyakejima and Kozushima through September 2000, and over 600 $M \geq 4$ earthquakes, and five $M \geq 6$ earthquakes were observed in total [*Ito and Yoshioka*, 2002; *Toda et al*., 2002; *Minson et al*., 2007]. Analysis of data from island GPS stations indicates that 1-2 km^3 of magma was intruded during this episode [*Nishimura et al*., 2001; *Toda et al*., 2002; *Ozawa et al*., 2004]. Crustal extension northwest of Miyakejima was coincident with contraction of the island, which indicates that a large portion of the magma was sourced from crustal magma chambers beneath the volcano, although additional magma may have been sourced from sub-crustal magma reservoirs located between Miyakejima and Kozushima [*Nishimura et al*., 2001; *Ozawa et al*., 2004; *Yamaoka et al*., 2005; *Murase et al*., 2006].

Beginning on 4 July, seismicity beneath the summit area of Miyakejima was reactivated as the roof of the magma reservoir began to collapse [*Nakada et al*., 2005; *Sakai et al*., 2001]. As confirmed by gravity and electromagnetic data, shallowing seismicity resulted from the upward migration of a stoping column and the formation of a shallow cavity beneath the summit area [*Kikuchi et al*., 2001; *Geshi et al*., 2002; *Sasai et al*., 2002; *Furuya et al*., 2003]. On 8 July, coincident with a small phreatic eruption, an 800-m-wide area of the summit collapsed ~200 m,

producing a caldera with an initial volume of 5.6×10^7 m^3 [*Nakada et al.,* 2005]. Miyakejima's caldera continued to collapse incrementally through mid-August, resulting in a 1.6-km-wide caldera with an average depth of 450 m [*Nakada et al*., 2005]. Small phreatic or phreatomagmatic eruptions took place along the southern rim of the volcano on 14-15 July, 10 August and 13 August [*Nakada et al*., 2005; *Geshi and Oikawa*, 2008]. On 13 August, the composition of the erupted magma changed from basaltic andesite sourced from a shallow magma chamber at 3-5 km depth to basalt sourced from a deeper magma reservoir between 8-10 km depth [*Amma-Miyasaka et al*., 2005; *Kaneko et al*., 2005; *Saito et al*., 2005]. On 18 August, a vulcanian to subplinian eruption produced a 16-km-high eruption column [*Nakada et al.*, 2005]. After this eruption, extremely large amounts of volcanic gases began to be emitted from the summit crater of Miyakejima, and the island was evacuated [*Kazahaya et al*., 2004].

The caldera collapse of Miyakejima is believed to have been accommodated by slip on inward- and outward-dipping ring-fault structures [*Geshi et al*., 2002; *Geshi*, 2009]. Individual collapse episodes produced simultaneous tilt changes [*Ukawa et al*., 2000; *Yamamoto et al*., 2001] and variations in the electric and magnetic fields [*Sasai et al*., 2001; 2002], as well as, in most cases, very-long-period (VLP) seismic signals [*Kikuchi et al*., 2001; *Kumagai et al*., 2001]. In total, 46 major tilt steps were identified between the first explosive eruption on 8 July and the largest explosive eruption on 18 August [*Yamamoto et al*., 2001]. These tilt steps, which are characterized by an abrupt uplift of the summit area [*Ukawa et al*., 2000], have been variably explained by the opening of sill-like tensile cracks [*Fujita et al*., 2002; 2004] and the elastic response of the edifice to downward motion of the caldera block [*Michon et al*., 2009; 2011]. Thirty-nine of these tilt steps were also accompanied by regionally recorded VLP seismic pulses

with durations of ~30-65 s [*Kikuchi et al*., 2001; *Kumagai et al.,* 2001; *Ohminato and Kumagai*, 2001]. In several cases, the VLP pulses were preceded by swarms of shallow M1-2 earthquakes that increased in frequency before each event [*Kobayashi et al*., 2003]. Full-moment-tensor solutions for the VLP signals calculated by *Kikuchi et al*. [2001] and *Kumagai et al*. [2001] are dominated by positive volumetric components, and those events with larger volumetric changes tend to have longer recurrence intervals. So far, the VLP signals have been explained by piston collapse [*Kumagai et al*., 2001; *Stix and Kobayashi*, 2008] and a hydrothermal expansion model [*Kikuchi et al*., 2001]. However, a source process consisting of dip-slip motion on a caldera ring fault may be a viable alternative [*Ekström and Nettles*, 2002].

Of the 43 vertical-P earthquakes we identify in this study, 39 correspond to the VLP signals described in *Kikuchi et al.* [2001]. The four additional events we study occurred on 7 July, 9 July, 30 July and 18 August. The 7 July event is an M_W 4.4 earthquake that took place before the start of the caldera collapse, and the remaining three events are associated with tilt steps [*Fujita et al*., 2004]. The 18 August earthquake occurred during the climax of the Miyakejima's largest explosive eruption [*Nakada et al*., 2005]. The centroid location for the 18 August earthquake is ~25 km away from Miyakejima, whereas all of the other events are within ~10 km of the volcano. CMT solutions with the centroid location fixed to the volcano provide a poorer fit to the data, which may suggest that the final earthquake has a slightly different location or source process. All of the vertical-P earthquakes are closely linked to volcanic activity at Miyakejima, and specifically to the collapse of the caldera roof block into the deflating shallow magma reservoir.

2.4.7. Nyiragongo

As discussed in Section 2.1, *Shuler and Ekström* [2009] identified five $4.6 \leq M_W \leq 5.3$ vertical-P earthquakes near Nyiragongo, a stratovolcano in the Democratic Republic of the Congo, between 2002 and 2005. The first three vertical-P earthquakes occurred on 21 and 22 January 2002, days after a regional rifting episode reopened fractures on Nyiragongo's southern flanks and ruptured the volcanic edifice resulting in a catastrophic fissure eruption on 17 January [*Allard et al*., 2002; *Komorowski et al*., 2002/2003; *Tedesco et al*., 2007]. These three vertical-P earthquakes occurred between the end of the 12-hr effusive eruption and the collapse of Nyiragongo's summit crater, which had previously contained a solidified lava lake. These earthquakes are attributed to dip-slip motion along an inward-dipping ring fault located above a deflating shallow magma reservoir [*Shuler and Ekström,* 2009].

The five earthquakes identified by *Shuler and Ekström* [2009] are Category 2 events from the Surface Wave catalog. Analysis of Category 1 earthquakes in this study allowed us to identify one additional vertical-P earthquake associated with the 2002 eruption, an M_W 5.1 earthquake that took place on 20 January 2002. This earthquake has a C-quality CMT solution and a centroid location ~15 km from Nyiragongo. This earthquake occurred before the three previously identified vertical-P earthquakes, between the end of the effusive eruption and the collapse of the summit crater, and can likely be explained by the same physical mechanism.

2.4.8. Stromboli

An M_W 4.3 vertical-T earthquake with a C-quality CMT solution took place on 5 April 2003. The centroid location for this earthquake is ~15 km from Stromboli, the northernmost

stratovolcano in the Aeolian Islands near Sicily, Italy. This earthquake occurred during a paroxysmal explosion, the largest vulcanian eruption at Stromboli since 1930. The so-called 'paroxysm' was recorded by the local multiparametric monitoring network and directly observed from a helicopter. We summarize the main results from the literature below.

The 2003 paroxysm occurred during an effusive eruption at Stromboli that began in December 2002. Although the paroxysm was not preceded by any obvious precursors, in hindsight, increased release of magmatic gases was observed in the month before the event, which may have indicated that gas-rich magma had ascended in the shallow plumbing system [*Aiuppa and Federico*, 2004; *Carapezza et al*., 2004; *Rizzo et al*., 2008]. Ash emission and temperature increase at the bottom of the obstructed summit craters were also observed immediately before the paroxysm [*Calvari et al*., 2006]. Three minutes before the explosion, on 5 April 2003 at 7:10:25 UTC, the temperature of one summit crater increased dramatically and a thick gas plume was erupted [*Calvari et al*., 2006]. At 7:13:05, reddish ash was emitted and a dark cloud with a cauliflower-shape grew above the crater [*Calvari et al*., 2006; *Rosi et al*., 2006; *Harris et al*., 2008]. After the initial explosion expanded to a second summit crater, an extremely powerful blast produced a shock wave that was observed on a local seismic station at 7:13:37 [*Calvari et al*., 2006; *Harris et al*., 2008]. The 2003 paroxysm, which lasted 9 min, launched meter-sized ballistic blocks from the summit crater and produced an eruptive column that collapsed into pyroclastic flows [*Calvari et al*., 2006]. Like other paroxysms at Stromboli, the 2003 paroxysm erupted aphyric golden pumice, likely caused by the rapid ascent of undegassed basaltic magma [*Bertagnini et al*., 2003; *Métrich et al*., 2005; *Francalanci et al*., 2008; *Allard*, 2009].

The 2003 paroxysm was recorded by broadband seismometers deployed on and around Stromboli. At 7:12:42, a high-frequency signal likely associated with vesiculation began, and at 7:13:35, a powerful 12-s VLP event was observed in association with the main blast [*D'Auria et al*., 2006; *Ripepe and Harris*, 2008]. A source inversion of the main blast signal retrieved a combination of a vertical-CLVD earthquake and a downward force with an equivalent magnitude of M_W 3.7 [*Cesca et al*., 2007]. Additionally, an ultra-long-period (ULP) signal starting 4 min before and terminating 1 min after the main blast was also observed [*Cesca et al*., 2007]. The ULP signal has been variably interpreted as tilt caused by the rapid ascent and ejection of magma [*D'Auria et al*., 2006] and as an M_W 3.0 slow thrust-faulting event [*Cesca et al*., 2007]. This signal is unlikely to be source of the vertical-T earthquake that we identify in this study because the amplitude of the ULP signal on the vertical component is more than an order of magnitude lower than the amplitude of the horizontal components. The vertical-T earthquake at Stromboli has a centroid time of 7:13:45.5, which suggests that the earthquake is associated with the VLP event and the main blast of the paroxysmal explosion.

2.4.9. Sierra Negra

An M_W 5.5 vertical-T earthquake took place in the western Galápagos Islands on 22 October 2005. The centroid location for this event is immediately south of Isabela Island, ~30 km from Sierra Negra, the largest shield volcano in the Galápagos Islands. Sierra Negra has a subaerial extent of 60-by-40 km, and contains a shallow 7-by-10-km summit caldera. The interior of Sierra Negra's caldera contains a 14-km-long C-shaped sinuous ridge composed of normally-faulted blocks with steep outward-dipping fault scarps [*Reynolds et al*., 1995]. It has been suggested that this fault system was formed by a series of repeated trapdoor-faulting events driven by magma

accumulation [*Reynolds et al*., 1995; *Amelung et al*., 2000; *Jónsson et al*., 2005; *Chadwick et al*., 2006; *Jónsson*, 2009] in Sierra Negra's ~2-km deep sill-like magma chamber [*Amelung et al*., 2000; *Yun et al*., 2005]. During a trapdoor-faulting event, the crust above the magma chamber hinges upwards like a trapdoor on one side of the caldera [*Amelung et al.,* 2000].

Trapdoor-faulting events in 1997-1998 and on 16 April 2005 are characterized by maximum uplift just north of the sinuous ridge in the southern part of the caldera [*Amelung et al*., 2000; *Jónsson et al*., 2005; *Chadwick et al*., 2006; *Jónsson*, 2009]. An m_b 4.6 earthquake is associated with the April 2005 trapdoor-faulting event, during which a GPS station located near the sinuous ridge was uplifted 84 cm within 10 s [*Chadwick et al*., 2006]. Although the 1997-1998 trapdoor-faulting event was originally attributed to slip along steep outward-dipping normal faults [*Amelung et al*., 2000], a revised faulting model consisting of 67-74° inward-dipping thrust faults is compatible with the deformation data from both the 1997-1998 and April 2005 trapdoor-faulting events [*Chadwick et al*., 2006; *Jónsson*, 2009].

On 22 October 2005 at 23:30 UTC, Sierra Negra began erupting after a repose period of 26 years. The start of the eruption was accompanied by a 13-km-high plume of ash and steam, after which the eruption transitioned to a 2-km-long curtain of fire fountains inside the northern rim of the caldera [*Geist et al*., 2008]. Over the next 8 days, ~150×10^6 m^3 of basalt were erupted and the center of the caldera subsided over 5 m [*Yun*, 2007; *Geist et al*., 2008]. No precursors to the eruption were observed, except for the M_W 5.5 vertical-T earthquake that occurred at 20:34 on 22 October, approximately 3 hours before the start of the eruption. Unfortunately, the GPS network failed 16 hours prior to the start of the eruption so deformation associated with this event is

poorly constrained [*Geist et al*., 2008]. *Yun* [2007] modeled interferograms that span the earthquake and the eruption, and found that the deformation can be explained by a model that includes a trapdoor-faulting event centered on the western part of the sinuous ridge. The 1.5 m of maximum dip-slip at the surface estimated by *Yun* [2007] is consistent with field measurements of dip-slip displacements on vertical fault scarps in the southern and western parts of the sinuous ridge [*Geist et al*., 2008]. The vertical-T earthquake is closely associated with this period of eruptive activity, and may be associated with a trapdoor-faulting event.

2.4.10. Tungurahua

An M_W 4.4 vertical-P earthquake with a C-quality CMT solution took place in Ecuador on 17 August 2006. The centroid location for this earthquake is ~25 km from Tungurahua, one of the most active volcanoes in the Andes [*Hall et al*., 1999]. Tungurahua is a large andesitic stratovolcano that has been erupting intermittently since 1999. In 2006, explosive eruptions on 14 July and 16-17 August produced widespread pyroclastic flows, resulting in loss of life and evacuation of settlements along the flanks of the volcano. The vertical-P earthquake occurred during the paroxysmal phase of the VEI 3 (Volcanic Explosivity Index, *Newhall and Self*, 1982) 16-17 August eruption, Tungurahua's most violent eruption since activity began in 1999.

The August 2006 eruption was preceded by the growth of a bulge on the northern flank of the volcano between 11 and 16 August [*Smithsonian Institution*, 2006], and by 16 hours of uninterrupted, escalating seismic tremor and tephra fallout [*Arellano et al*., 2008]. The eruption began on 16 August at 19:30 UTC, and by 22:00, lava fountains reached a height of 100-200 m above the vent [*Barba et al*., 2006]. Around 03:00 on 17 August, numerous pyroclastic density

currents were observed [*Barba et al*., 2006] and the ash plume rose to a height of 13.25 km [*Fee et al*., 2010]. Between 04:00 and 05:00, the lava fountains reached ~1.5 km, and at ~05:30 the start of the paroxysmal phase of the eruption began [*Barba et al*., 2006; *Fee et al*., 2010]. The vertical-P earthquake took place shortly thereafter, at 05:37 UTC.

The paroxysmal phase of the 16-17 August eruption lasted 50 minutes, and was characterized by a dramatic increase in acoustic power, as well as a shift in the infrasonic jetting spectrum towards lower frequencies [*Matoza et al*., 2009; *Fee et al*., 2010]. The height of the ash cloud grew to over 24 km, and ash was injected into the stratosphere while lava fountaining continued at heights of over 1 km [*Fee et al*., 2010; *Steffke et al*., 2010]. Numerous pyroclastic density currents and heavy ashfall were observed [*Barba et al*., 2006]. At 06:20, the eruptive activity dropped off sharply and by ~07:30, the tremor was at background levels [*Fee et al*., 2010]. In total, the eruption lasted 11 hours, and produced $2x10^7$ m^3 of magma and 35,000 tons of SO_2 [*Arellano et al*., 2008; *Carn et al*., 2008; *Fee et al*., 2010]. Hours after the end of the eruption, the effusion of slow-moving blocky lava flows was observed [*Arellano et al*., 2008; *Hanson et al*., 2011; *Samaniego et al*., 2011]. It has been suggested that the end of the August 2006 eruption may have resulted from the slow ascent of a more-viscous magma [*Hanson et al*., 2011].

A series of VLP events was observed during the August 2006 eruption [*Kumagai et al*., 2007a/b; *Kumagai et al*., 2010]. These events started at 05:30 UTC on 17 August, and are characterized by impulsive signatures with dominant periods of 20-50 s [*Kumagai et al*., 2007b]. The vertical-P earthquake that we identify in this study is likely the same event as 'VLP2' from *Kumagai et al*.

[2010]. In a waveform inversion using seismic data from two local broadband stations, *Kumagai et al*. [2010] modeled this event as an isotropic source at 3 km depth, and hypothesized that the volumetric change was caused by bubble growth due to newly supplied magma. However, it seems possible that the vertical-P earthquake could have been generated by a collapse inside the magmatic plumbing system, as at Nyiragongo and Miyakejima.

2.4.11. Curtis Island

On 17 February 2009, the largest well-documented vertical-CLVD earthquake, an M_W 5.8 vertical-T event took place in the Kermadec Islands north of New Zealand. The centroid location is ~2 km from Curtis Island. Together with Cheeseman Island, Curtis Island is the subaerial portion of a submarine dacitic volcano located along the Kermadec Ridge [*Doyle et al*., 1979; *Smith et al*., 1988]. Curtis Island has a subaerial extent of 500-by-800 m and contains a crater with active fumaroles. Although uplift of 7 m was documented at Curtis Island between 1929 and 1964 [*Doyle et al*., 1979], the date of Curtis Island's last eruption is unknown. One month prior to the vertical-T earthquake, from 17 to 19 January 2009, earthquakes with T-wave phases were recorded on the Polynesian seismic network [*Smithsonian Institution*, 2009], suggesting a possible eruption near the volcano. As Curtis Island is a remote volcano, this activity was not confirmed. Because no thermal alerts were issued by the MODVOLC system [*Wright et al*., 2002, 2004] through April 2009 [Smithsonian Institution, 2009], the vertical-T earthquake is likely associated with magma migration within the volcanic edifice or magmatic plumbing system of Curtis Island rather than a volcanic eruption.

2.4.12. NW Rota-1

On 19 April 2009, an M_W 4.9 vertical-P earthquake with a C-quality CMT solution took place in the Mariana Islands. The centroid location for this earthquake is ~60 km from NW Rota-1, a recently detected submarine volcano with an active hydrothermal system [*Embley et al*., 2006]. NW Rota-1 is a steep-sided basaltic to basaltic-andesitic cone with a diameter of 16 km and a summit depth of ~500 m [*Embley et al*., 2006; *Chadwick et al*., 2008]. In 2004, the first explosive submarine eruptions ever to be observed were witnessed at NW Rota-1 [*Embley et al*., 2006]. Repeated dives indicate eruptive activity is characterized by nearly continuous Strombolian eruptions [*Chadwick et al*., 2008].

In mid-April 2009, an unusual sequence of earthquakes near NW Rota-1 was detected by both the NEIC and by a hydrophone moored in the summit of the volcano [*Chadwick et al*., 2012]. The peak seismicity was observed on 17 April, the first day of the 4-day swarm, when the hydrophone recorded a continuous broadband acoustic signal that lasted for ~24 hours [*Chadwick et al*., 2012]. The April 2009 swarm closely resembles another earthquake sequence that occurred near NW Rota-1 in 1997 [*Heeszel et al*., 2008; *Chadwick et al*., 2012]. Both swarms have been attributed to magmatic sources [*Heeszel et al*., 2008; *Chadwick et al*., 2012]. The seismic swarm and the vertical-P earthquake may be associated with a magmatic intrusion or the inflation of a shallow magma chamber. A large volcanic eruption and subsequent landslide took place at NW Rota-1 in August 2009 [*Chadwick et al*., 2012].

2.4.13. Other Vertical-CLVD Earthquakes

The remaining 24 vertical-CLVD earthquakes identified in this study are not associated with documented episodes of volcanic unrest at nearby volcanoes. Several of these earthquakes occur in spatial clusters near individual volcanoes. We summarize the locations of the vertical-CLVD earthquakes, starting in Cascadia and moving counterclockwise around the Pacific Ocean. Unless otherwise indicated, the earthquakes have A-quality CMT solutions.

An M_W 4.7 vertical-P earthquake with a B-quality CMT solution took place on 19 March 1994 along the Gorda Ridge, north of the Mendocino Fracture Zone off the coast of Oregon. This earthquake occurred near the boundary between the Central and Phoenix ridge segments, and is not associated with any unusual earthquake swarms or reported eruptions along either segment.

On 4 December 1999, an M_W 5.1 vertical-P earthquake with a B-quality CMT solution occurred in the Andreanof Islands in the central Aleutians. The centroid location for this earthquake is ~40 km from Tanaga, Takawangha and Gareloi volcanoes. All three of these volcanoes are stratovolcanoes. Tanaga last erupted in 1914, and Gareloi last erupted in 1989. Takawangha has no known historical eruptions, although radiocarbon data indicates that explosive eruptions have occurred there in the past several hundred years.

Four vertical-CLVD earthquakes that are not associated with volcanic unrest took place in Japan. The first earthquake is an M_W 5.3 vertical-T earthquake that occurred on 16 May 1978 in Northern Honshu near Hokkaido. This earthquake is not located near any recently active

volcanoes, but the centroid location is ~40 km from Osore-yama, a historically active stratovolcano with a 5-km-wide caldera.

An M_W 5.7 vertical-P earthquake occurred on 9 September 1996 in the Ryukyu Islands near Kyushu. The centroid location for this earthquake is ~70 km from Kuchinoerabu-jima and Kikai volcanoes. Kikai is a 19-km-wide caldera that erupted in 1997 and 1998. Kuchinoerabu-jima is a group of young stratovolcanoes that produces frequent explosive eruptions. The vertical-P earthquake occurred during a seismic swarm at Kuchinoerabu-jima [*Iguchi et al.,* 2001]. However, an earthquake aftershock survey by *Sekitani et al.* [1997] confirms that the earthquake we study occurred on Tanegashima Island, ~60 km east of the volcanic arc. Therefore, it seems unlikely that this earthquake is associated with the Kuchinoerabu-jima magmatic activity.

Two M_W 5.2-5.3 vertical-T earthquakes have centroid locations ~15 km from Kita-Iwo-Jima, a deeply eroded stratovolcano in Japan's Volcano Islands. The first earthquake occurred on 20 August 1992 and the second earthquake occurred on 12 June 2008. Numerous eruptions have been reported from Funka-Asane, a submarine vent located 2 km northwest of Kita-Iwo-Jima, but no eruptions were reported during the times of the vertical-T earthquakes.

An M_W 4.7 vertical-P earthquake with a C-quality CMT solution took place on 11 April 2008 in the Mariana Islands. The centroid location for this earthquake is ~110 km west of the volcanic arc and is likely associated with the Mariana Trough, an actively spreading back-arc basin separating the Mariana Ridge, a remnant volcanic arc, from the active volcanoes of the Mariana

Arc. No specific volcanic activity has been reported at this location near the time of the earthquake.

On 25 February 2005, an M_W 4.9 vertical-P earthquake with a B-quality CMT solution occurred in Luzon in the Philippines. The centroid location for this earthquake is ~75 km from Masaraga and Mayon volcanoes. Masaraga is a Holocene stratovolcano, and Mayon is a stratovolcano that has frequent explosive eruptions. Mayon had small-scale explosive eruptions from June to September 2004, but was not erupting during the time of the vertical-P earthquake.

An M_W 5.6 vertical-P earthquake with a B-quality CMT solution took place on 29 June 1999 in East Papua New Guinea. The centroid location for this earthquake is ~35 km from an active hydrothermal field called Musa River, ~60 km from Madilogo, a Holocene pyroclastic cone, and ~70 km from Managlase Plateau, a Holocene volcanic field. The earthquake is also located ~75 km from Lamington, a stratovolcano that last erupted in 1956. The vertical-P earthquake is not linked to unrest at any of these volcanoes.

Two vertical-CLVD earthquakes with C-quality CMT solutions occurred in the Vanuatu Islands region in 2008. The first earthquake is an M_W 4.9 vertical-T earthquake that took place on 22 July 2008. The centroid location for this earthquake is ~90 km from North Vate, a Holocene stratovolcano. The second earthquake is an M_W 5.0 vertical-T earthquake that occurred on 18 November 2008. The centroid location for this earthquake is ~35 km from Traitor's Head, a historically active stratovolcano, and ~85 km from Yasur, a stratovolcano that was producing continuous strombolian and vulcanian eruptions during this time. We do not link the 18

November 2008 earthquake to the volcanic activity at Yasur due to the large distance between the centroid location and the volcano.

Eight vertical-CLVD earthquakes, three vertical-P and five vertical-T events, are located in the Tonga and Fiji Islands region. The vertical-P earthquakes occurred between 1994 and 2002. The first event is an M_W 4.8 earthquake with a B-quality CMT solution that occurred near the Mangatolo Triple Junction on 8 November 1994. The centroid location for this earthquake is ~30 km from Tafahi, a Holocene stratovolcano, and ~45 km from Curacoa, a submarine volcano that last erupted in 1979. The second event is an M_W 4.8 earthquake with a C-quality CMT solution that occurred on 9 September 1995 along the Fonualei Rift and Spreading Center (FRSC). The third event is an M_W 4.7 earthquake with a C-quality CMT solution that occurred on 16 August 2002. The centroid location for this earthquake is ~60 km from Falcon Island, a submarine volcano that last erupted in 1936, and ~70 km from Hunga Tonga-Hunga Ha'apai, a submarine volcano that erupted in 1988 and 2009. None of the vertical-P earthquakes are linked to documented episodes of volcanic unrest.

The five vertical-T earthquakes that took place in the Tonga and Fiji Islands regions occurred over a 20 year period between 1979 and 2009. The northernmost earthquake is an M_W 5.3 earthquake that took place on 16 January 1994. The centroid location for this earthquake is ~20 km from Hunga Tonga-Hunga Ha'apai, a submarine volcano with a 4-5-km-wide caldera that experienced a Surtseyan eruption in March 2009 [*Vaughan and Webley*, 2010]. The remaining four events are M_W 5.5 earthquakes that occurred on 1 October 1979, 7 August 1999, 10 November 2004, and 26 May 2009. The 1979 earthquake has a B-quality CMT solution and the

three other earthquakes have A-quality CMT solutions. All four of these vertical-T earthquakes have centroid locations clustered ~10-15 km from an Unnamed submarine volcano (0403-01 in IAVCEI's Catalog of Active Volcanoes of the World). The last confirmed eruption from Unnamed volcano (0403-01) was in 1932. The centroid locations for these earthquakes are also ~20 km from Unnamed volcano (0403-011), a Holocene submarine volcano, and ~45-50 km from Unnamed volcano (0403-03), a submarine volcano that last erupted in 1999. None of these vertical-T events are associated with documented eruptive activity.

Finally, five vertical-T earthquakes are located in the remote South Sandwich Islands. Three M_W 5.3-5.4 earthquakes took place in the northern South Sandwich Islands on 9 September 1978, 5 September 1997 and 18 January 2001. These earthquakes have A- or B-quality CMT solutions and centroid locations that are clustered within ~15 km of Zavodovski, the northernmost subaerial volcano in the South Sandwich Islands. Zavodovski is a stratovolcano with active fumaroles that last erupted in 1819. Centroid locations for these earthquakes are also ~40 km from Hodson, a Holocene stratovolcano. The remaining two vertical-T earthquakes took place in the southern South Sandwich Islands on 23 and 31 August 2005. Centroid locations for these M_W 5.1 and M_W 5.5 earthquakes are located ~30 and ~55 km from Thule Islands volcanoes. The Thule Islands consist of a group of stratovolcanoes and calderas that have produced several explosive eruptions in the last hundred years. The 2005 earthquakes also have centroid locations ~50 and ~85 km from Bristol Island, a historically active stratovolcano that last erupted in 1956. None of the vertical-T earthquakes in the South Sandwich Islands are associated with documented volcanic unrest, although visual observations of the South Sandwich Islands are limited to a few days each year [*LeMasurier et al.,* 1990].

2.5. Discussion

After investigating 395 target earthquakes located within ~100 km of volcanoes with documented eruptions in the last ~100 years, we have identified 86 shallow vertical-CLVD earthquakes with magnitudes $4.3 \leq M_W \leq 5.8$. We find that the vast majority of the vertical-CLVD earthquakes are located, within error, at volcanoes. Of the vertical-CLVD earthquakes investigated in this study, we find that ~80% are located within 30 km and ~90% are located within 50 km of a known volcanic center. For those earthquakes that are linked to documented episodes of volcanic unrest at active volcanoes, ~90% are located within 30 km of the source volcano, and the farthest earthquake is located ~60 km away. Even for vertical-CLVD earthquakes that are not linked to episodes of volcanic unrest, ~50% are located within 30 km of a known volcano. The vertical-CLVD earthquakes are associated with more than 20 active volcanoes around the world.

The vertical-CLVD earthquakes identified in this study all have shallow depths. During the CMT inversion process, all of the centroid depths were fixed by the inversion process to 12 km to prevent them from moving shallower, and body-wave modeling suggests that the vertical-CLVD earthquakes occur in the top 10 km of the crust. Given that most vertical-CLVD earthquakes are tightly clustered around active volcanoes, the shallow depth estimates suggest that they are likely associated with deformation inside or immediately beneath volcanic edifices.

Overall, ~70% of the vertical-CLVD earthquakes identified in this study are spatially and temporally associated with documented volcanic unrest. Breaking this down by earthquake type, ~40% of vertical-T earthquakes and ~85% of vertical-P earthquakes are linked to volcanic

unrest. If the earthquakes associated with the Miyakejima caldera collapse are excluded, ~45% of the remaining vertical-P earthquakes occur during documented episodes of volcanic unrest at a nearby volcano. Volcanic unrest is underreported, especially in remote regions and in cases where unrest is not soon followed by an eruption [*Moran et al.,* 2011], so the percentage of vertical-CLVD earthquakes associated with volcanic activity is likely to be even higher than is documented here. Most shallow vertical-CLVD earthquakes located near volcanoes are thus likely related to some type of volcanic unrest.

Shallow vertical-CLVD earthquakes near recently active volcanoes represent a small fraction of earthquakes described in the GCMT and Surface Wave catalogs. Including events analyzed by *Nettles and Ekström* [1998], only ~0.1% of earthquakes described in the GCMT catalog from 1976 to 2009 are shallow vertical-CLVD earthquakes located near recently active volcanoes. Likewise, including events analyzed by *Shuler and Ekström* [2009], only ~2% of Category 1 and 2 earthquakes in the Surface Wave catalog from 1991 to 2009 are shallow vertical-CLVD earthquakes located near recently active volcanoes. Considering that at least 20 volcanoes around the world are erupting at any given time, it is clear that not all volcanic activity generates vertical-CLVD earthquakes. Certain stress and/or structural conditions may be required to generate this type of earthquake. Below we examine potential correlations between vertical-CLVD earthquakes and tectonic setting as well as volcano type.

Shallow vertical-CLVD earthquakes are located near volcanoes in many tectonic and geographic settings. The majority of vertical-CLVD earthquakes are located near arc volcanoes in subduction zones, mostly in the circum-Pacific region. Although many vertical-CLVD

earthquakes are located in subduction zones along the western rim of the Pacific Ocean, and few vertical-CLVD earthquakes are located in South or Central America, or in the Cascade, Aleutian or Kurile-Kamchatka arcs, there does not seem to be an obvious link between the age, geometry, or velocity of subducting slabs reported by *Syracuse and Abers* [2006] and the occurrence of vertical-CLVD earthquakes. Vertical-CLVD earthquakes are also associated with hot-spot volcanoes in Iceland, Hawaii, the Samoa Islands, and the Galápagos Islands, as well as with volcanoes in the East African Rift.

Only a very small number of vertical-CLVD earthquakes, all of the vertical-P type, are located along mid-ocean ridge segments. Included in this category are the 19 March 1994, 9 September 1995 and 11 April 2008 earthquakes. The centroid locations of these earthquakes are over 80 km away from the nearest recently active volcano. The locations of these earthquakes, which are along back-arc or mid-ocean ridge segments, suggest that these events may be associated with extension processes rather than directly with volcanic processes. The small number of vertical-CLVD earthquakes located along mid-ocean ridges is partly the result of the fact that we identified target earthquakes using the database of the GVP, which contains few submarine volcanoes located along divergent plate boundaries. However, there is some evidence that vertical-CLVD earthquakes may be less likely to occur in the ridge environment. A search through the entire GCMT catalog for shallow vertical-CLVD earthquakes with $|\varepsilon| > 0.33$ and dominant P or T axes that plunge more steeply than 60° finds only 15 earthquakes located along the mid-ocean ridge system. All of the earthquakes are vertical-P events. Given our experience with how the addition of surface-wave data affects CMT solutions (Section 2.3.1, Figure 2.4), it is possible that many of these events are poorly resolved normal-faulting earthquakes.

Vertical-CLVD earthquakes are most commonly associated with submarine volcanoes and stratovolcanoes (Table 2.2). Additionally, most of the submarine volcanoes and stratovolcanoes closest to vertical-CLVD earthquakes have pre-existing calderas [*Siebert and Simkin,* 2002-]. In fact, the largest sequence of vertical-CLVD earthquakes is associated with the development of a new caldera at Miyakejima. Vertical-CLVD earthquakes are also associated with unrest at Rabaul, a pyroclastic shield volcano, and Sierra Negra, a shield volcano. Both of these shield volcanoes have calderas with well-documented ring-fault structures. Since ring faults are produced during the caldera collapse process, the fact that we observe most vertical-CLVD earthquakes at volcanoes with calderas may indicate that vertical-CLVD earthquakes are generated by slip on ring-fault structures.

Most volcanoes associated with vertical-CLVD earthquakes erupt basaltic and/or andesitic lavas [*Siebert and Simkin,* 2002-]. Nyiragongo and Ol Doinyo Lengai, the two volcanoes associated with vertical-CLVD earthquakes in the East African rift, erupt lavas with some of the lowest known silica contents on Earth [*Sahama,* 1973; *Bailey,* 1993; *Demant et al.,* 1994]. The correlation between vertical-CLVD earthquakes and basaltic-to-andesitic volcanoes may suggest that vertical-CLVD earthquakes preferentially occur at volcanoes that erupt low-viscosity magmas. However, this observation may also be a consequence of the relatively short time period covered by our study since basaltic volcanoes tend to erupt small volumes of lava frequently, whereas silicic volcanoes have longer repose periods and larger, less frequent eruptions [*White et al.,* 2006].

Vertical-CLVD earthquakes are observed during many different types of volcanic unrest. Half of all the vertical-CLVD earthquakes identified in this study are associated with the caldera collapse of Miyakejima. Vertical-CLVD earthquakes are also associated with a subglacial fissure eruption at Bárdarbunga, a fissure eruption at Nyiragongo, elevated seismicity and explosive eruptions at Rabaul, an effusive eruption at Sierra Negra, and explosive eruptions at Stromboli and Tungurahua. At submarine volcanoes, vertical-CLVD earthquakes are associated with anomalous earthquake swarms at Vailulu'u, Loihi, NW-Rota-1 and Curtis Island, as well as disproportionately large tsunamis at Smith Rock.

In Figure 2.10, we examine the temporal relationships between vertical-CLVD earthquakes and volcanic unrest at 10 volcanoes. We plot vertical-CLVD earthquakes that occurred within five years of the start of volcanic eruptions or episodes of unrest at each volcano. For some volcanoes, defining the start of an episode of unrest is arbitrary, but we use the following dates and times: 1) Bárdarbunga – 30 September 1996, 23:30 UTC [*Smithsonian Institution,* 1996a], 2) Loihi – 17 July 1996, 7:54 UTC, 3) Miyakejima – 26 June 2000, 9:00 UTC [*Nishimura et al*., 2001], 4) NW Rota-1 – 17 April 2009, 4:43 UTC, 5) Nyiragongo – 17 January 2002, 6:25 UTC [*Tedesco et al.*, 2007], 6) Rabaul 18 September 1994, 20:00 UTC [*Smithsonian Institution*, 1994], 7) Sierra Negra – 22 October 2005, 23:30 UTC [*Geist et al*., 2008], 8) Stromboli – 5 April 2003, 7:13 UTC [*Calvari et al*., 2006], 9) Tungurahua – 16 August 2006, 19:30 UTC [*Fee et al*., 2010], and 10) Vailulu'u – 9 January 1995, 14:13 UTC. For Loihi, NW Rota-1 and Vailulu'u, we use the NEIC catalog and define the start of volcanic unrest as the time of the first teleseismically-detected earthquake in each swarm.

Vertical-P earthquakes occur hours to years after the start of eruptions or episodes of unrest, whereas vertical-T earthquakes occur both before and after eruptive activity. At Sierra Negra, a vertical-T earthquake preceded the 2005 eruption by 3 hours, while at Bárdarbunga, a series of vertical-T earthquakes took place over 20 years, with the last occurring 1-2 days before the 1996 subglacial eruption. These results suggest that vertical-CLVD earthquakes may be used to infer the eruptive states of volcanoes. In particular, vertical-P earthquakes may be used to identify volcanoes where eruptions or large-scale magmatic intrusions have recently occurred. This may be especially useful for remote or submarine volcanoes. In addition, vertical-T earthquakes may be used to identify volcanoes that are likely to erupt in the near future. Clusters of vertical-T earthquakes are located at Kita-Iwo-Jima, Unnamed (0403-01) and Zavodovski volcanoes, and these earthquakes may be indicative of magma ascent and increased potential for eruptions at these volcanoes.

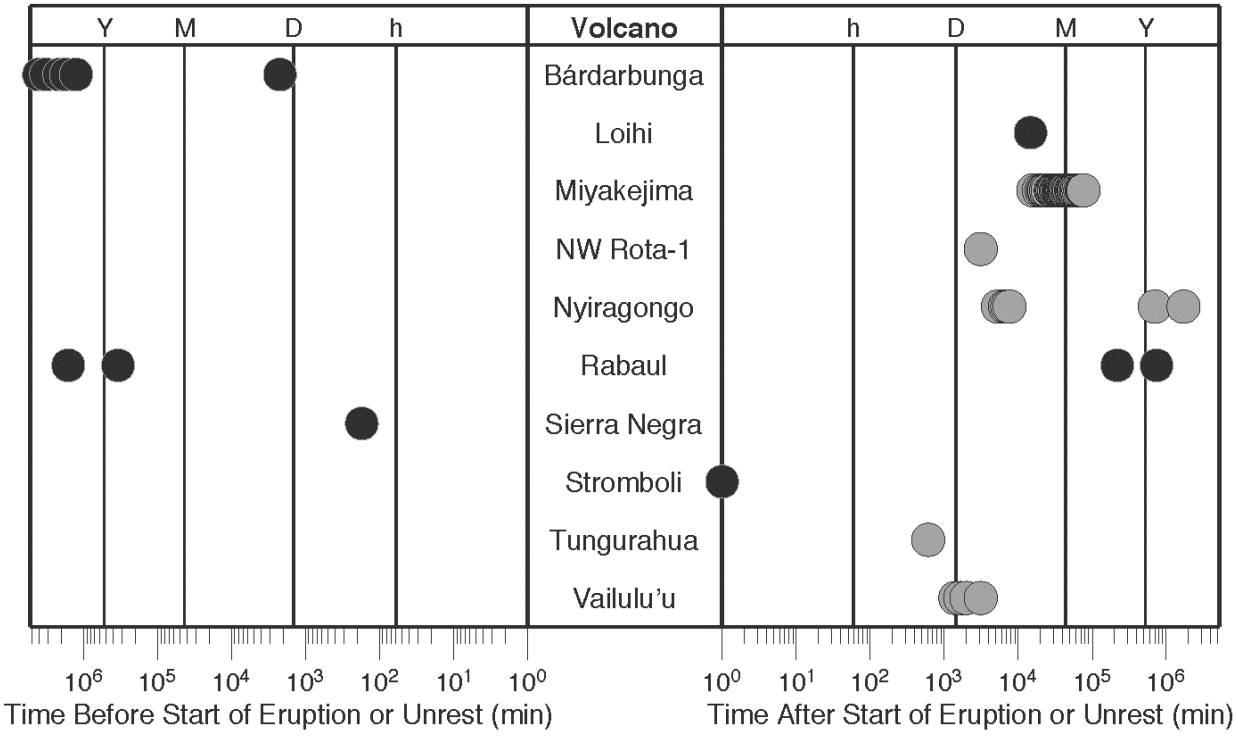

Figure 2.10. Plot showing the temporal relationships between vertical-CLVD earthquakes and volcanic unrest at 10 volcanoes. We plot five years of time (in min) before and after the start of eruptions or episodes of unrest. Vertical lines indicate one hour (*h*), one day (*D*), one month (*M*) and one year (*Y*). Vertical-P earthquakes are plotted as grey circles and vertical-T earthquakes are plotted as black circles. Earthquakes from Bárdarbunga are from *Nettles and Ekström* [1998], and earthquakes from Nyiragongo are from *Shuler and Ekström* [2009]. See the text for details on the dates and times of eruptions and episodes of volcanic unrest. Note that the vertical-T earthquake at Stromboli is plotted at 1 minute after the start of the eruption, although it actually occurred only a few seconds later.

2.6. Conclusions

Through an in-depth analysis of two global seismicity catalogs and the calculation of over 300 CMT solutions, we have identified 86 shallow vertical-CLVD earthquakes occurring near recently active volcanoes. These earthquakes have depths in the upper 10 km of the crust, and 80% are located within 30 km of a volcano. Additionally, ~70% of the vertical-CLVD earthquakes studied are spatially and temporally associated with volcanic unrest at a nearby volcano. Half of the vertical-CLVD earthquakes are associated with the caldera collapse of Miyakejima in 2000, and another 20% are linked to documented volcanic unrest or eruptions at other volcanoes. In addition to caldera collapse, vertical-CLVD earthquakes are associated with effusive and explosive eruptions and volcanic earthquake swarms. There is thus a clear link between the occurrence of vertical-CLVD earthquakes and volcanic activity. Our observations suggest that these unusual earthquakes likely occur within the edifices or magmatic plumbing systems of active volcanoes.

Vertical-CLVD earthquakes do not occur at all volcanoes, or even during all episodes of unrest at volcanoes where they are observed, so specific stress or structural conditions must be required to trigger these earthquakes. We have identified several correlations between the occurrence of vertical-CLVD earthquakes and specific tectonic settings and volcano types. Vertical-CLVD earthquakes are predominantly located in subduction zones, though they also occur in continental rifts and in areas of hotspot volcanism. Most vertical-CLVD earthquakes are associated with volcanoes with caldera structures. Additionally, most vertical-CLVD earthquakes are associated with volcanoes that erupt silica-poor magmas. These correlations may indicate that low-

viscosity magmas and/or ring-fault structures are required to generate vertical-CLVD earthquakes.

We examined the temporal relationships between vertical-CLVD earthquakes and volcanic unrest at 10 volcanoes, and found that vertical-P earthquakes occur after the start of volcanic unrest, whereas vertical-T earthquakes generally occur before volcanic eruptions. The occurrence of vertical-P earthquakes may be useful for identifying remote or submarine volcanoes that have recently erupted, and the occurrence of vertical-T earthquakes may signal that a source volcano is likely to erupt in the future. Vertical-CLVD earthquakes provide information about the stress and strain conditions internal to active volcanoes, and by studying these rare and unusual earthquakes, we may learn more about the deformation processes occurring inside active volcanoes during eruptions and magma ascent and migration. Because vertical-CLVD earthquakes are associated with many different types of volcanic unrest, it is likely that these events can be produced by multiple physical processes. Constraining the physical mechanisms that may be responsible for generating vertical-CLVD earthquakes will enable us to interpret these events in terms of related volcanic hazards.

Chapter 3

Physical mechanisms for vertical-CLVD earthquakes at active volcanoes

This work has been submitted for publication:
Shuler, A., Ekström, G., and M. Nettles, Physical mechanisms for vertical-CLVD earthquakes at active volcanoes, submitted to *J. Geophys. Res.*, 2012.

Abstract

Occasionally volcanoes generate earthquakes that are large enough to be detected globally. Many of these moderate-to-large volcanic earthquakes have anomalous focal mechanisms and frequency contents. In a previous study, we searched for shallow, non-double-couple earthquakes with approximately vertical tension or pressure axes that took place near active volcanoes between 1976 and 2009. We identified 101 vertical compensated-linear-vector-dipole (vertical-CLVD) earthquakes with magnitudes $4.3 \leq M_W \leq 5.8$, and found that the majority of these events occurred during episodes of volcanic unrest. Here, we explore the physical mechanisms that generate vertical-CLVD earthquakes. We model teleseismic body waves and examine the frequency contents of vertical-CLVD earthquakes, and find that they have longer source durations than tectonic earthquakes of similar magnitudes. Although vertical-CLVD earthquakes are identified based on the properties of deviatoric moment tensors, we explore the possibility that these earthquakes may have significant non-zero isotropic components. We examine the covariance matrix for one of the best-recorded events and confirm that the isotropic and pure vertical-CLVD components cannot be independently resolved using long-period seismic data. We explore several potential physical mechanisms that may generate earthquakes with deviatoric vertical-CLVD moment tensors, including slip on ring faults, volume exchange between two reservoirs, the opening and closing of tensile cracks, and volumetric changes. We evaluate these mechanisms using seismological, geological, and geodetic constraints from detailed studies of

individual earthquakes. Although none of the investigated physical mechanisms can explain all of our observations, a ring-faulting mechanism is preferred for most vertical-CLVD earthquakes.

3.1. Introduction

As magmas ascend from depth to intrude the crust or erupt on the surface, many different types of volcanic earthquakes are produced by processes such as brittle fracture, fluid flow, mass transport and volumetric changes [e.g., *Chouet*, 2003; *McNutt*, 2005; *Kumagai*, 2009; *Zobin*, 2011]. By observing, analyzing and interpreting these earthquakes, we can learn about the internal dynamics of volcanic systems, and better forecast volcanic eruptions and assess volcanic hazards. Because most volcanic earthquakes have small magnitudes (M_W < 2-3), much of volcano seismology is concerned with analyzing seismic signals recorded on local monitoring networks. However, in extraordinary cases such as during volcanic eruptions or caldera collapse, moderate and strong earthquakes with magnitudes up to M_W 6 or 7 have been observed [*McNutt*, 2000; *Zobin,* 2011]. In these cases, regional and global seismic data can be used to gain insight into the stress and strain conditions inside the edifices and magmatic plumbing systems of active volcanoes. Many moderate and large earthquakes associated with volcanic processes have been shown to have anomalous source properties, such as unusual radiation patterns or frequency contents [*Filson et al*., 1973; *Francis*, 1974; *Dreger et al*., 2000; *Kumagai et al*., 2001; *Minson et al*., 2007].

In this chapter and in Chapter 2, we investigate a specific type of earthquake linked to volcanoes, those with vertical compensated-linear-vector-dipole (vertical-CLVD) moment tensors. By definition, vertical-CLVD earthquakes have deviatoric moment tensors with large non-double-

couple components that are dominated by vertical compression or extension. Although rarely observed, vertical-CLVD earthquakes are some of the largest and most anomalous earthquakes to occur near volcanoes. Prior to our study in Chapter 2, $M_W \geq 5$ vertical-CLVD earthquakes had been identified near six volcanic centers around the world [*Kanamori et al.*, 1993; *Ekström*, 1994; *Nettles and Ekström,* 1998; *Shuler and Ekström*, 2009]. At Smith Rock, a submarine volcano in the Izu-Bonin arc, a vertical-CLVD earthquake produced a disproportionately large tsunami [*Kanamori et al.,* 1993], and at Bárdarbunga volcano in Iceland [*Nettles and Ekström,* 1998] and Nyiragongo volcano in the East African Rift [*Shuler and Ekström,* 2009], vertical-CLVD earthquakes are associated with damaging fissure eruptions.

In order to assess the relationship between vertical-CLVD earthquakes and volcanic unrest, we searched in Chapter 2 for additional examples of shallow, moderate-sized vertical-CLVD earthquakes located near volcanoes with documented eruptions in the last ~100 years. We investigated nearly 400 target earthquakes from the Global Centroid Moment Tensor catalog (GCMT, 1976-2009) and the Surface Wave catalog (1991-2009) of *Ekström* [2006], and applied well-defined criteria to the deviatoric moment tensors to classify earthquakes as vertical-CLVD. We considered events with dominant pressure or tension axes that plunge more steeply than 60°, and moment tensors that are distinctly non-double-couple with $|\varepsilon| > 0.20$, where

$$\varepsilon = -\lambda_2/\max(|\lambda_1|, |\lambda_3|), \tag{3.1}$$

and λ_1, λ_2 and λ_3 are the diagonal elements of the moment tensor in the principal axes coordinate system, ordered such that $\lambda_1 \geq \lambda_2 \geq \lambda_3$. Vertical-P earthquakes have dominant pressure axes ($|\lambda_3| > |\lambda_1|, |\lambda_2|$) and vertical-T earthquakes have dominant tension axes ($|\lambda_1| > |\lambda_3|, |\lambda_2|$).

In total, we identified 101 vertical-CLVD earthquakes located near active volcanoes. This number includes 86 vertical-CLVD earthquakes reported in Chapter 2 and 15 vertical-CLVD earthquakes previously reported in *Nettles and Ekström* [1998] and *Shuler and Ekström* [2009]. The largest vertical-CLVD earthquake we identified has a magnitude of M_W 5.8, and the smallest a magnitude of M_W 4.3. These earthquakes have shallow focal depths, and over 80% have centroid locations within ~30 km of a known volcano. Approximately two-thirds of these events are vertical-P earthquakes, and one-third are vertical-T earthquakes. A map of the earthquakes, color-coded by type, is shown in Figure 3.1.

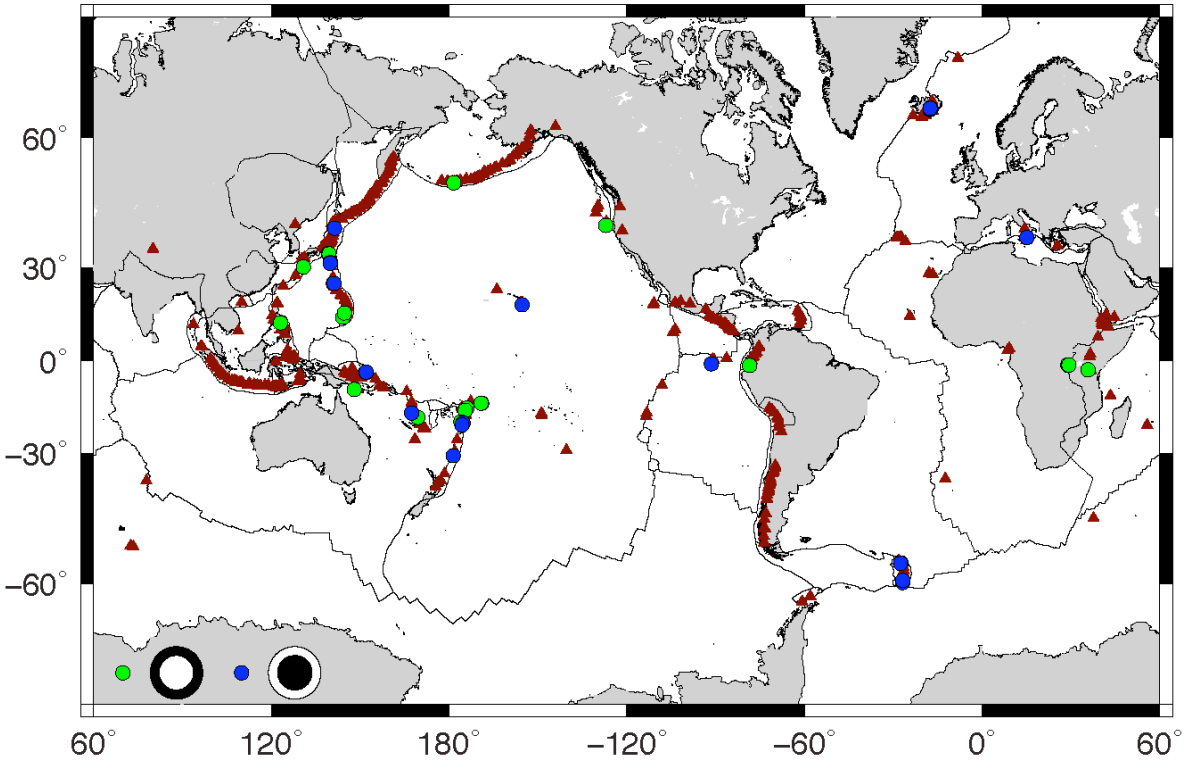

Figure 3.1. Map showing the locations of 101 vertical-CLVD earthquakes identified in Chapter 2, including those from *Nettles and Ekström* [1998] and *Shuler and Ekström* [2009]. Vertical-P earthquakes are plotted as green circles and vertical-T earthquakes are plotted as blue circles. Maroon triangles indicate the locations of 429 volcanoes with eruptions later than 1900 that are documented by the Global Volcanism Project [*Siebert and Simkin*, 2002-]. Plate boundaries are from *Bird* [2003].

As described in Chapter 2, vertical-CLVD earthquakes are associated with several different types of volcanoes located in a variety of tectonic and geographical settings. Most vertical-CLVD earthquakes are located near arc volcanoes in subduction zones, although a small number are located in continental rifts, along mid-ocean ridges, and in regions of hot-spot volcanism. Vertical-CLVD earthquakes occur most frequently at stratovolcanoes and submarine volcanoes with pre-existing caldera structures. Additionally, vertical-CLVD earthquakes are predominantly associated with volcanoes that erupt basaltic and/or andesitic lavas, which may suggest that low-viscosity magmas promote the occurrence of these events.

The vast majority of vertical-CLVD earthquakes occur during documented volcanic eruptions or episodes of unrest at nearby volcanoes, which suggests that these earthquakes are generated by magmatic and/or volcano-tectonic processes. As detailed in Chapter 2, vertical-CLVD earthquakes are spatially and temporally linked to 1) abnormally large tsunamis followed by volcanic *T*-wave events near Smith Rock volcano [*Kanamori et al*., 1993], 2) anomalous volcanic earthquake swarms near Curtis Island, Loihi, NW Rota-1 and Vailulu'u volcanoes, 3) effusive eruptions at Nyiragongo [*Shuler and Ekström*, 2009], Ol Doinyo Lengai and Sierra Negra volcanoes, 4) explosive eruptions at Rabaul, Stromboli and Tungurahua volcanoes, 5) a subglacial eruption near Bárdarbunga volcano [*Nettles and Ekström*, 1998], and 6) caldera collapse at Miyakejima volcano. Most vertical-P earthquakes occur after the start of volcanic eruptions or episodes of unrest at nearby volcanoes, which suggests that these earthquakes occur in response to volcanic eruptions or large-scale magmatic intrusions. Vertical-T earthquakes generally occur before eruptive activity and may be indicative of magma-ascent processes. As vertical-CLVD earthquakes take place at different types of volcanoes, in association with many

different types of volcanic unrest, it is possible that these earthquakes are produced by more than one physical mechanism.

To date, two main classes of physical mechanisms have been presented to explain vertical-CLVD earthquakes. The first class is composed of faulting mechanisms, in which vertical-CLVD earthquakes are produced by dip-slip motion on volcano ring faults [*Ekström,* 1994; *Nettles and Ekström,* 1998; *Shuler and Ekström*, 2009]. While motion along the ring fault is triggered by the inflation or deflation of shallow magma chambers, the earthquakes are generated by shear failure on curved or cone-shaped fault structures. No net volume change is expected for earthquakes produced by ring-faulting mechanisms, so these events should be modeled well using deviatoric moment tensors, as in Chapter 2.

The second class is composed of mechanisms related to fluid flow and volumetric changes. Examples of mechanisms in the second class include rapid magma injection [*Kanamori et al*., 1993; *Konstantinou et al.,* 2003] or withdrawal, rapid expansion or contraction, and volume or mass exchange between two magma chambers [*Tkalčić et al*., 2009]. Volume changes associated with fluid flow mechanisms can be either compensated or uncompensated. In the first case, deviatoric moment tensors are appropriate, but, in the second case, the earthquakes are expected to have moment tensors with non-zero isotropic components. In Chapter 2 and in our previous studies [*Nettles and Ekström,* 1998; *Shuler and Ekström*, 2009], we followed standard GCMT methodology and constrained the isotropic component to equal zero. For shallow earthquakes, there is a known tradeoff between the isotropic and pure vertical-CLVD components of the moment tensor [*Kawakatsu*, 1996], so it is possible that some earthquakes we have described

with vertical-CLVD focal mechanisms were generated by physical mechanisms with net volume changes.

Several earthquakes that we identified as having vertical-CLVD moment tensors in Chapter 2 have also been studied by other authors using different types of data, including local and regional seismic data and radar interferograms. Several models representing both of the main classes of physical mechanisms have been presented to explain these earthquakes. A vertical-P earthquake at Tungurahua volcano has been explained as the result of volumetric changes associated with bubble growth in magma [*Kumagai et al.*, 2010], and a vertical-T earthquake at Sierra Negra volcano has been explained using a trapdoor-faulting mechanism [*Yun*, 2007]. Multiple scenarios of caldera collapse involving the downward displacement of a rock piston into an underlying magma chamber have also been presented to explain dozens of vertical-P earthquakes at Miyakejima [*Kikuchi et al.,* 2001; *Kumagai et al.,* 2001]. For the Tungurahua and Miyakejima earthquakes, full moment-tensor solutions calculated using local seismic data are dominated by isotropic components [*Kikuchi et al.,* 2001; *Kumagai et al.,* 2001, 2010]. Clearly, a discussion of the physical mechanisms of vertical-CLVD earthquakes requires consideration of the isotropic component of the moment tensor.

The complexity of the vertical-CLVD events and the tradeoff between the pure vertical-CLVD and isotropic components of the moment tensor means additional constraints are needed to evaluate possible source mechanisms. From previous studies, there are several indications that vertical-CLVD earthquakes have unusually long source processes. For example, in order to model the teleseismic body waves of vertical-CLVD earthquakes at Smith Rock [*Kanamori et*

al., 1993] and Bárdarbunga [*Nettles and Ekström,* 1998] volcanoes, source durations exceeding the average magnitude-duration relationship for tectonic earthquakes [*Ekström et al.,* 1992] are required. Additionally, the frequency spectra of vertical-CLVD earthquakes at Nyiragongo volcano indicate that these events are depleted in high-frequency energy, and have lower corner frequencies than tectonic earthquakes with similar magnitudes and locations [*Shuler and Ekström*, 2009]. Likewise, waveforms from local and regional seismic stations indicate that the vertical-CLVD earthquakes associated with the incremental caldera collapse of Miyakejima have smooth source-time functions lasting ~30-65 s [*Kikuchi et al.,* 2001; *Kumagai et al.,* 2001; *Ohminato et al.,* 2001]. Azimuthal variations in the broadband waveforms for the Bárdarbunga earthquakes suggest that some vertical-CLVD earthquakes may be caused by multiple subevents [*Nettles and Ekström*, 1998]. A systematic analysis of source duration and frequency content could provide useful constraints on the physical mechanisms of vertical-CLVD earthquakes.

In this chapter, we explore a range of physical processes that may produce earthquakes with deviatoric vertical-CLVD moment tensors. We perform additional detailed analysis on the dataset of 86 shallow vertical-CLVD earthquakes located near active volcanoes identified in Chapter 2, and combine these results with those from *Nettles and Ekström* [1998] and *Shuler and Ekström* [2009]. We begin by systematically examining the broadband body waves of vertical-CLVD earthquakes to gain additional constraints on their source durations and frequency contents. We investigate the tradeoff between the isotropic and pure vertical-CLVD components of the moment tensor for our dataset, and calculate full moment-tensor solutions for vertical-CLVD earthquakes. We then examine several potential physical mechanisms that have been suggested to explain the anomalous seismic radiation patterns of vertical-CLVD earthquakes,

including slip on ring faults, volume exchange between two reservoirs, opening and closing of tensile cracks, and volumetric sources. Finally, we evaluate these mechanisms in light of our source-duration observations and the temporal relationships between vertical-CLVD earthquakes and volcanic unrest.

3.2. Data and Analysis

In Chapter 2, we used long-period seismic data from regional and global networks to identify 86 shallow vertical-CLVD earthquakes located near active volcanoes. Source parameters were calculated using the standard GCMT methodology [*Dziewonski et al.,* 1981; *Ekström et al.,* 2012]. The depths of shallow earthquakes are poorly resolved using long-period seismic data, and the centroid depths of all the vertical-CLVD earthquakes were fixed to 12 km during the CMT inversions. Similarly, long-period data have weak sensitivity to event duration, and earthquake durations in the CMT inversions are based on an empirical moment-duration relationship [*Ekström et al.,* 2012]. For long-period teleseismic data, there also exists a tradeoff between the isotropic and pure vertical-CLVD components, neither of which generates azimuthally varying seismic radiation [*Mendiguren and Aki*, 1978; *Kanamori and Given*, 1981; *Kawakatsu*, 1996; *Dufumier and Rivera,* 1997]. The isotropic component is expected to be small for tectonic earthquakes, but, in volcanic and geothermal areas, earthquakes with statistically significant isotropic components have been observed [e.g., *Miller et al.*, 1998*a*; *Dreger et al.*, 2000; *Foulger et al*., 2004; *Minson and Dreger*, 2008]. In GCMT analysis, the isotropic component of the moment tensor is typically constrained to zero.

In Section 3.2.1, we model the teleseismic body waves of vertical-CLVD earthquakes in order to obtain estimates of their source durations, and in doing so, we also obtain better constraints on their depths. We gain additional insight into the source processes of vertical-CLVD earthquakes by examining variations between the frequency contents and magnitude distributions of earthquakes reported in the GCMT and Surface Wave catalogs. In Section 3.2.2, we evaluate the tradeoff between the isotropic and vertical-CLVD components of the moment tensor for our dataset and calculate full moment-tensor solutions for the vertical-CLVD earthquakes reported in Chapter 2.

3.2.1. Earthquake Source Duration and Magnitude Distribution

In order to obtain additional constraints on the source processes of vertical-CLVD earthquakes, we attempt to model the teleseismic body waves for the 63 earthquakes from Chapter 2 that have $M_W \geq 5.1$. We collect broadband seismic records from the Data Management Center of the Incorporated Research Institutions for Seismology (IRIS), and deconvolve the instrument response to obtain displacement records filtered from 1 to 100 s period. Broadband records for the oldest earthquakes are constructed from digital long- and short-period seismograms, as in *Ekström* [1989] and *Kanamori et al.* [1993]. We manually pick arrival times for P and SH phases, and invert broadband waveforms for focal mechanism, moment-rate function and focal depth using the method of *Ekström* [1989]. This analysis provides estimates of the source durations of vertical-CLVD earthquakes as well as better constraints on their depths.

Synthetic seismograms are calculated using ray theory and the Preliminary Reference Earth Model [PREM; *Dziewonski and Anderson,* 1981]. Reflections and conversions near the source

are modeled using a layer-matrix method for a regional velocity model that varies depending on the location of the earthquake. For earthquakes in Tanzania and East Papua New Guinea, we use local velocity models X5 and K2 from CRUST2.0 [*Bassin et al.,* 2000]. For the remaining earthquakes, which are near island-arc or submarine volcanoes, we use the CRUST2.0 model for a Japanese island arc (J1), adding a water layer on top, if necessary, to match the summit bathymetry of the nearest submarine volcano.

We include the point-source moment tensors from Chapter 2 as soft constraints to ensure that focal mechanisms calculated from broadband data are compatible with the preferred focal mechanisms calculated using long-period data during the CMT inversions. We experiment with different weights of the soft constraint, and select the solutions that provide the best fit to the broadband data as our preferred solutions. We assign each solution a quality based on the fit to the data and the number of waveforms used in the broadband body-wave modeling. Solutions with A quality have the best fit to the data, especially for the initial P waves and the first crustal reflections. Solutions with B and C qualities have poorer fits and therefore greater uncertainties associated with estimates of depth and source duration. In Table 3.1, we list our preferred estimates of depth and source duration and describe the quality of each broadband solution. An example of an A-quality solution is shown in Figure 3.2 for an M_W 5.5 vertical-T earthquake that occurred in the Fiji Islands region near an Unnamed submarine volcano (0403-01 in IAVCEI's Catalog of Active Volcanoes of the World) on 7 August 1999.

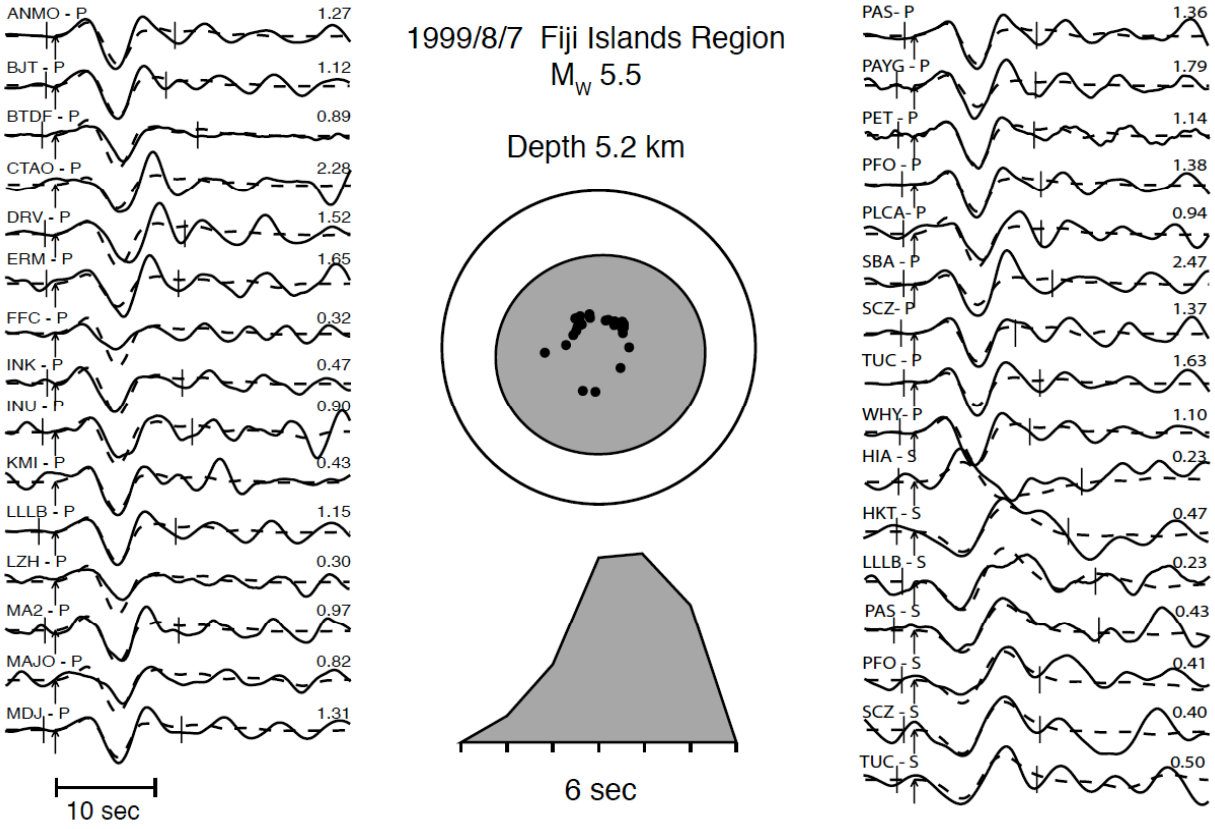

Figure 3.2. Focal-depth analysis for the M_W 5.5 vertical-T earthquake that occurred on 7 August 1999 near an Unnamed volcano (0403-01) in the Fiji Islands region. Solid lines are broadband teleseismic P and SH waveforms, and dashed lines are synthetic seismograms. Brackets across the waveform show the portions of the seismograms that were used in the inversion. Arrows indicate the picked first arrivals. The station name, data type and maximum amplitude (in microns) are printed above each waveform. The focal mechanism and moment-rate function determined by the body-wave inversion are plotted in the center of the figure. Black dots on the focal mechanism show the locations where the plotted waveforms exited the focal sphere. The focal depth of the earthquake is ~5.2 km below sea level. This is an example of an A-quality broadband body wave solution.

For most of the vertical-CLVD earthquakes we study ($M_W \geq 5.1$), we find that the broadband body waves are of lower amplitude than the background noise. However, we are able to model the body waves for 18 earthquakes, 3 of which are vertical-P earthquakes and 15 of which are vertical-T earthquakes. Eight solutions are A quality, 6 are B quality, and 4 are C quality. In general, we find the body waves to be emergent and dominated by low-frequency energy. We do not observe the impulsive direct arrivals and surface reflections typically observed for earthquakes in this magnitude range. Source durations range from ~4 to ~10 s, and depth estimates range from ~4 to ~8 km. For the same location, we find that focal-depth estimates for multiple vertical-CLVD earthquakes vary ~1-2 km. Our estimates of focal depth and source duration are consistent with those of *Nettles and Ekström* [1998], who reported focal depths of ~3-7 km and source durations of ~4-7 s for ten $5.1 \leq M_W \leq 5.6$ vertical-T earthquakes near Bárdarbunga volcano. We find that all of the vertical-CLVD earthquakes have moment-rate functions with smoothly varying, approximately triangular shapes, except for the M_W 5.6 vertical-P earthquake that occurred in East Papua New Guinea on 29 June 1999. This earthquake has the longest source duration, 10 s, and appears to be composed of several subevents. For the inversion weightings we choose, broadband estimates of M_W are up to 0.3 magnitude units higher than CMT estimates for individual earthquakes.

Due to the long source durations and partial overlap of direct and reflected phases, there is a tradeoff between focal depth and source duration. Our preferred solutions are listed in Table 3.1, but for most earthquakes, the broadband data can be fit nearly as well using shallower focal depths and slightly longer source time functions. We estimate that the uncertainties associated with focal-depth and source-duration estimates are at least 2 km and 1 second, respectively.

Table 3.1. Results of Broadband Body-Wave Modeling[a]

Earthquake Date and Time						Centroid	Centroid	Geographical	M_W	Depth	Source	Solution
Y	M	D	h	m	sec	Latitude	Longitude	Location		(km)	Duration (s)	Quality
1978	5	16	7	35	49.1	40.99	141.44	Hokkaido, Japan	5.3	5.8	4	B
1984	6	13	2	29	29.8	31.57	139.97	South of Honshu, Japan	5.6	3.8	7	B
1990	5	15	15	21	31.1	-2.96	35.80	Tanzania	5.4	5.5	4	A
1992	8	20	18	31	39.9	25.43	141.13	Volcano Islands, Japan	5.2	7.3	6	B
1994	1	16	10	18	41.5	-20.62	-175.20	Tonga Islands	5.3	4.1	4	A
1996	9	4	18	16	7.7	31.51	139.99	South of Honshu, Japan	5.7	5.2	8	A
1996	9	9	4	34	21.9	30.44	130.95	Kyushu, Japan	5.7	7.7	8	A
1997	9	5	3	23	17.0	-56.41	-27.47	South Sandwich Islands Region	5.4	5.2	7	C
1999	6	29	5	50	9.2	-9.59	147.97	East Papua New Guinea	5.6	5.5	10	A
1999	8	7	6	17	30.5	-21.24	-175.61	Fiji Islands Region	5.5	5.2	6	A
2001	1	18	20	17	17.4	-56.31	-27.43	South Sandwich Islands Region	5.3	4.9	6	C
2004	11	10	10	35	38.0	-21.26	-175.62	Fiji Islands Region	5.5	3.9	6	B
2005	8	23	1	38	20.1	-59.80	-26.68	South Sandwich Islands Region	5.1	5.2	4	B
2005	8	31	1	24	54.9	-59.48	-26.86	South Sandwich Islands Region	5.5	5.5	4	C
2006	1	1	7	12	8.8	31.60	140.17	Southeast of Honshu, Japan	5.6	5.2	7	A
2008	6	12	13	10	14.7	25.53	141.18	Volcano Islands, Japan	5.3	7.5	6	C
2009	2	17	3	30	58.8	-30.54	-178.58	Kermadec Islands, New Zealand	5.8	6.4	8	B
2009	5	26	0	49	42.9	-21.24	-175.62	Fiji Islands Region	5.5	5.8	6	A

[a] Centroid times, locations and magnitudes are from the CMT solutions presented in Chapter 2. Depth and source-duration estimates are from broadband body-wave modeling. See text for explanation of solution quality.

In Figure 3.3, we plot the source duration of each vertical-CLVD earthquake as a function of the scalar moment calculated from the CMT solutions in Chapter 2. We compare these results to the global average relationship between source duration and scalar moment, as derived from broadband body-wave modeling using the same method for moderate-to-large shallow earthquakes,

$$\tau = 4.52 \times 10^{-6} (M_0)^{1/3}, \quad (3.2)$$

where τ is the source duration in seconds and M_0 is the scalar moment in Nm [*Ekström et al.*, 2012]. All of the vertical-CLVD earthquakes we are able to model have longer-than-average source durations for their moment magnitudes. For example, M_W 5.8 earthquakes, on average, have source durations of ~4 s, whereas we observe a source duration of ~8 s for the M_W 5.8 vertical-T earthquake that occurred near Curtis Island in the Kermadec Islands on 17 February 2009. The vertical-CLVD earthquakes in Table 3.1 are thus all characterized by slower-than-average source processes.

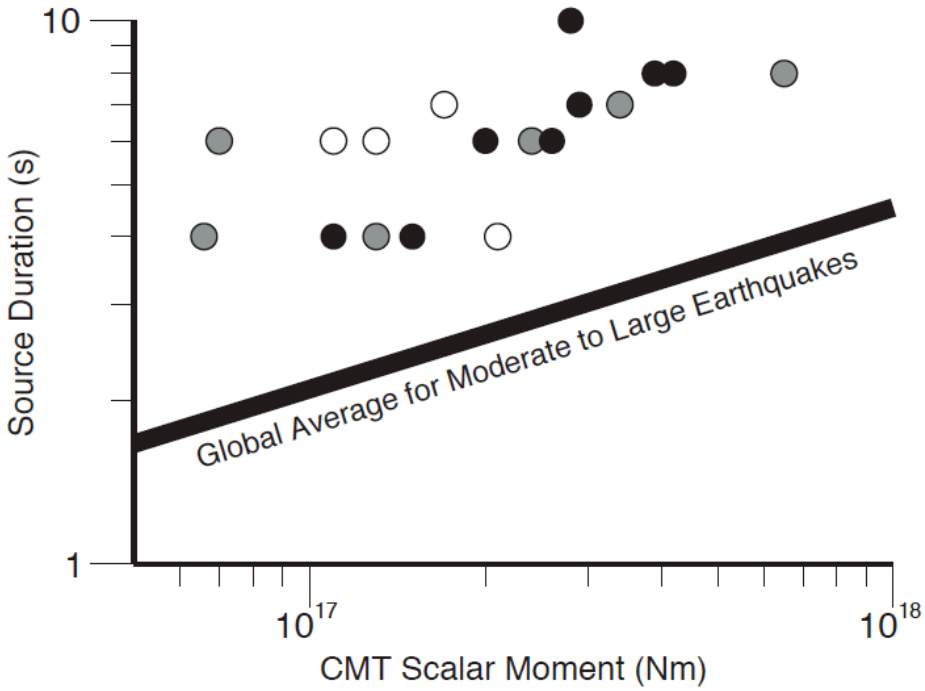

Figure 3.3. Log-log plot of the scalar moment (in Nm) and source duration (in seconds) of 18 vertical-CLVD earthquakes. The estimates of scalar moment are from the CMT solutions in Chapter 2, and the estimates of source duration are from broadband body-wave modeling. The color of the circles indicates the quality of the broadband body-wave solutions. Black circles are for A-quality solutions, grey circles are for B-quality solutions, and white circles are for C-quality solutions. The thick black line shows the global average relationship between scalar moment and source duration for shallow, moderate-to-large earthquakes [*Ekström et al*., 2012].

Although we are unable to model the broadband body waves for most of the vertical-CLVD earthquakes, we can assess their source durations by examining the general frequency contents of earthquakes reported in the GCMT and Surface Wave catalogs. Our lack of success in modeling more of the vertical-CLVD earthquakes is consistent with the pattern of longer-than-usual source durations. Twenty-six of the vertical-CLVD earthquakes from Chapter 2 are reported in the GCMT catalog. Before 2006, the GCMT Project used initial hypocentral parameters provided by the United States Geological Survey (USGS) National Earthquake Information Center (NEIC), where event detection is based on the arrival times of high-frequency body waves. Since 2006,

hypocentral parameters from the intermediate-period surface-wave event-detection algorithm of *Ekström* [2006] have been used for a small number of moderate-to-large earthquakes not detected by the USGS. However, fewer than 3% of earthquakes in the GCMT catalog since 2006 are based on surface-wave detections [*Ekström et al*., 2012], so nearly all earthquakes in the GCMT catalog have high-frequency body-wave phases. All of the earthquakes that we are able to model using broadband body-wave analysis are from the GCMT catalog, with initial detections from the NEIC.

The remaining 60 vertical-CLVD earthquakes from Chapter 2 are from two subsets of events reported in the Surface Wave catalog of *Ekström* [2006]. Category 1 earthquakes have surface-wave magnitudes, M_{SW} [*Ekström,* 2006], that are at least one magnitude unit larger than the m_b magnitudes reported in the International Seismological Centre (ISC) Bulletin. Body-wave magnitudes are calculated at a period of ~1 s, and surface-wave magnitudes, M_{SW}, are calculated between periods of 30 and 150 s. The discrepancy between these two magnitudes suggests that Category 1 earthquakes are slow earthquakes.

Category 2 earthquakes from the Surface Wave catalog are missing from the ISC and NEIC global seismicity catalogs, but were detected and located using intermediate-period surface waves and the method of *Ekström* [2006]. Compared to body waves, teleseismic surface waves are dominated by lower-frequency energy. Since the amplitudes of high-frequency body-wave phases were too small to be detected by the ISC and NEIC, despite the fact that they have magnitudes up to M_W 5.6, Category 2 vertical-CLVD earthquakes likely have slow source processes. Observations of Category 2 vertical-CLVD earthquakes at Miyakejima, Stromboli and

Nyiragongo support this interpretation. The 39 largest vertical-P earthquakes associated with the caldera collapse of Miyakejima, which are either Category 1 or 2 events, have, on average, source durations of ~50 s [*Kikuchi et al*., 2001*; Kumagai et al*., 2001; *Ohminato et al.*, 2001], which is ~20 times longer than expected considering their moment magnitudes of $5.0 \leq M_W \leq 5.6$. A Category 2 M_W 4.3 vertical-T earthquake at Stromboli is described as a very-long-period event that lasted ~12 s [*D'Auria et al*., 2006]. Likewise, Category 2 vertical-P earthquakes at Nyiragongo are depleted in high-frequency energy, and have lower corner frequencies than tectonic earthquakes with similar magnitudes and locations, also suggesting slower source processes [*Shuler and Ekström*, 2009].

Figure 3.4 shows the distributions of M_W for vertical-CLVD earthquakes by source catalog. Included are the 10 vertical-T earthquakes from Bárdarbunga [*Nettles and Ekström,* 1998], which are reported in the GCMT catalog, and the 5 vertical-P earthquakes from Nyiragongo [*Shuler and Ekström*, 2009], which are reported in the Surface Wave catalog. The GCMT catalog includes vertical-CLVD earthquakes in this group having magnitudes $4.8 \leq M_W \leq 5.8$, and we are able to model the teleseismic body waves for nearly all earthquakes with magnitudes $M_W \geq 5.1$. The Surface Wave catalog includes vertical-CLVD earthquakes with magnitudes $4.3 \leq M_W \leq 5.6$, and we are not able to model any of these earthquakes, even the largest events from Nyiragongo [*Shuler and Ekström*, 2009] and Miyakejima. The fact that we are unable to model the teleseismic body waves from any vertical-CLVD earthquakes in the Surface Wave catalog provides another indication that these events have long source durations, and suggests that they may have even slower source processes than vertical-CLVD earthquakes in the GCMT catalog. Since vertical-P earthquakes are predominantly from the Surface Wave catalog and vertical-T

earthquakes are predominantly from the GCMT catalog, we infer that vertical-P earthquakes may have slower source processes than vertical-T earthquakes.

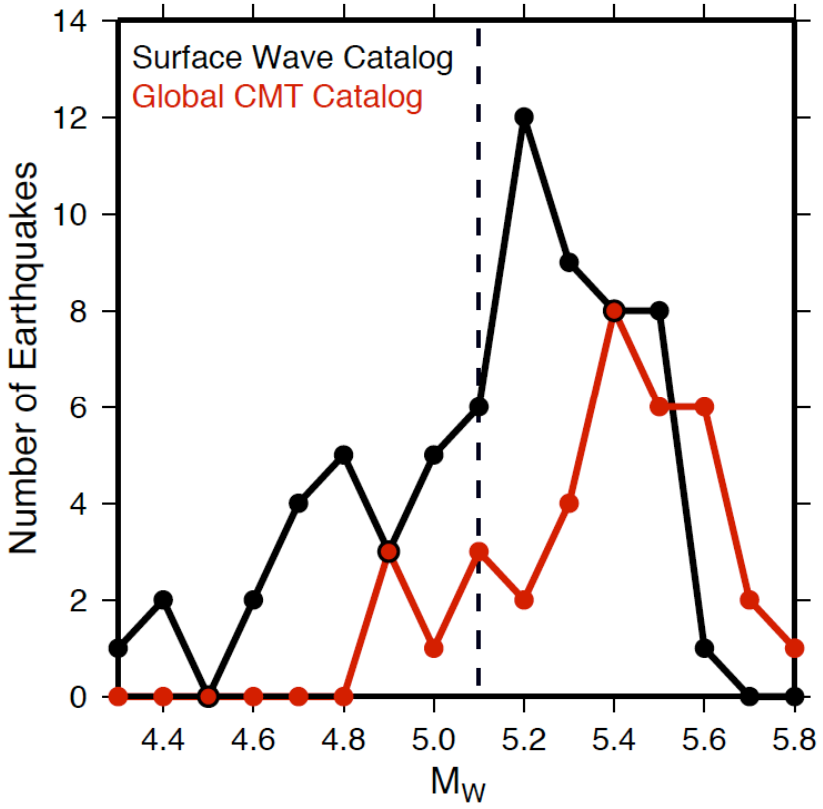

Figure 3.4. Distribution of vertical-CLVD earthquakes by source catalog and moment magnitude. Earthquakes are binned by 0.1 units of moment magnitude. Red dots and lines represent earthquakes from the Global CMT catalog, and black dots and lines represent earthquakes from the Surface Wave Catalog of *Ekström* [2006]. Included are vertical-CLVD earthquakes from *Nettles and Ekström* [1998], *Shuler and Ekström* [2009] and Chapter 2, and the M_W values are taken from these studies. We draw a dashed black line at M_W 5.1 because we are able to model the body waves for nearly all $M_W \geq 5.1$ vertical-CLVD earthquakes from the Global CMT catalog, while we are not able to model any $M_W \geq 5.1$ vertical-CLVD earthquakes from the Surface Wave catalog.

The distributions of M_W for vertical-CLVD earthquakes reported in the GCMT and Surface Wave catalogs closely resemble each other (Figure 3.4), except the distribution for the GCMT

catalog is shifted ~0.2 magnitude units higher than the distribution for the Surface Wave catalog. The low number of small-magnitude vertical-CLVD earthquakes reported in each catalog is likely due to the magnitude of completeness, which varies as a function of time and geographical location. However, the small number of large-magnitude vertical-CLVD earthquakes is surprising. In 34 years of observations from the GCMT catalog (1976-2009) and 19 years of observations from the Surface Wave catalog (1991-2009), we have observed ~75 earthquakes with magnitudes $M_W \geq 5.0$, but no earthquakes with $M_W \geq 6.0$. This observation suggests that vertical-CLVD earthquakes do not follow the Gutenberg-Richter magnitude-frequency distribution [*Gutenberg and Richter*, 1944] with the global average *b*-value of 1.0 [*Frohlich and Davis,* 1993]. Since our catalog of vertical-CLVD earthquakes ends below M_W 6.0, this may indicate that there is an upper limit on the source size for vertical-CLVD earthquakes at active volcanoes.

3.2.2. Tradeoff Between Isotropic and Pure Vertical-CLVD Components

For long-period teleseismic data, there is a tradeoff between the isotropic and pure vertical-CLVD components of the moment tensor [*Mendiguren and Aki*, 1978; *Kanamori and Given*, 1981; *Kawakatsu*, 1996; *Dufumier and Rivera,* 1997]. Below, we investigate this tradeoff for our dataset of vertical-CLVD earthquakes following the method of *Kawakatsu* [1996].

To begin, we consider the vector-matrix equation:

$$\mathbf{d} = \mathbf{G}\,\mathbf{m}, \tag{3.3}$$

where **d** is a vector composed of seismograms from several stations, **m** is a vector containing the moment tensor elements (M_{rr}, $M_{\theta\theta}$, $M_{\phi\phi}$, $M_{r\theta}$, $M_{r\phi}$, $M_{\theta\phi}$) and **G** is a matrix containing the Green functions for each moment-tensor element. The normal-equation matrix for this system is:

$$\mathbf{G}^{\mathbf{T}}\,\mathbf{d} = \mathbf{G}^{\mathbf{T}}\mathbf{G}\,\mathbf{m}, \tag{3.4}$$

which we can rewrite as

$$\mathbf{A}\,\mathbf{m} = \mathbf{b}, \tag{3.5}$$

where **A** is the inner product matrix and **b** is $\mathbf{G}^{\mathbf{T}}\mathbf{d}$. The covariance matrix for the moment-tensor elements, $\mathbf{C}_m$, is related to the inner product matrix by a scalar, $\mathbf{C}_m = \sigma^2_d\,\mathbf{A}^{-1}$, where σ^2_d is the variance of the data. The matrix $\mathbf{A}^{-1}$ can be calculated from synthetic waveforms using the centroid location of an earthquake and a distribution of available stations.

Since we are concerned with the tradeoff between the isotropic and pure vertical-CLVD components of the moment tensor, we rotate the diagonal elements of the moment tensor into a new basis, redefining them as the Isotropic (*I*), pure vertical-CLVD (*C*) and Difference (*D*) components, where

$$I = \frac{1}{3}\,(M_{rr} + M_{\theta\theta} + M_{\phi\phi}) \tag{3.6}$$

$$C = \frac{1}{3}\,(M_{\theta\theta} + M_{\phi\phi} - 2M_{rr}) \tag{3.7}$$

$$D = \frac{1}{2}\,(M_{\theta\theta} - M_{\phi\phi})\,. \tag{3.8}$$

As an example, we calculate $\mathbf{A}^{-1}$, for one of the best-recorded vertical-CLVD earthquakes, an M_W 5.6 vertical-P earthquake that took place at Miyakejima on 2 August 2000. We use the centroid location and the same station locations, time windows and frequency bands that were

used to calculate the CMT solution in Chapter 2. We include two datasets, body waves from 134 stations that were predominantly filtered from 40 to 150 s, and surface waves from 150 stations that were predominantly filtered from 50 to 150 s. Synthetic seismograms are calculated following the standard GCMT procedure [*Dziewonski et al*., 1981; *Arvidsson and Ekström*, 1998], and specifically the methods employed since 2004 [*Ekström et al*., 2012].

We calculate the eigenvalues and eigenvectors of $\mathbf{A}^{-1}$, and the relative standard deviation of each element, $\hat{\sigma}_i$, where

$$\hat{\sigma}_i = \sqrt{A_{ii}^{-1}} / \sigma_{\max} \tag{3.9}$$

and $\sigma_i = \sqrt{A_{ii}^{-1}}$. We also calculate the correlation matrix, **X**, where

$$X_{ij} = A_{ij}^{-1} / \sigma_i \sigma_j . \tag{3.10}$$

Our results are plotted in Figure 3.5. On the left, we plot a graphical representation of the eigenvectors. We plot these in descending order of relative eigenvalue, such that top eigenvector indicates the moment-tensor elements with maximum covariance, which are therefore the least well constrained. On the right, we plot the relative standard deviations of the moment tensor elements, $\hat{\sigma}$, and the correlation matrix, **X**.

We find that the eigenvector with the largest eigenvalue is (-0.87*I* + 0.49*C*). We also find that the isotropic and pure vertical-CLVD components of the moment tensor have the largest relative standard deviations. Additionally, the isotropic and pure vertical-CLVD components have a correlation coefficient of X_{IC} = -0.91, which demonstrates a strong linear dependence between the two components. Other combinations of the moment-tensor elements have small-to-negligible correlation coefficients. All of these pieces of information demonstrate that, even for

the best-recorded earthquakes in our dataset, the isotropic and pure vertical-CLVD components of the moment tensor cannot be independently resolved using long-period seismic data.

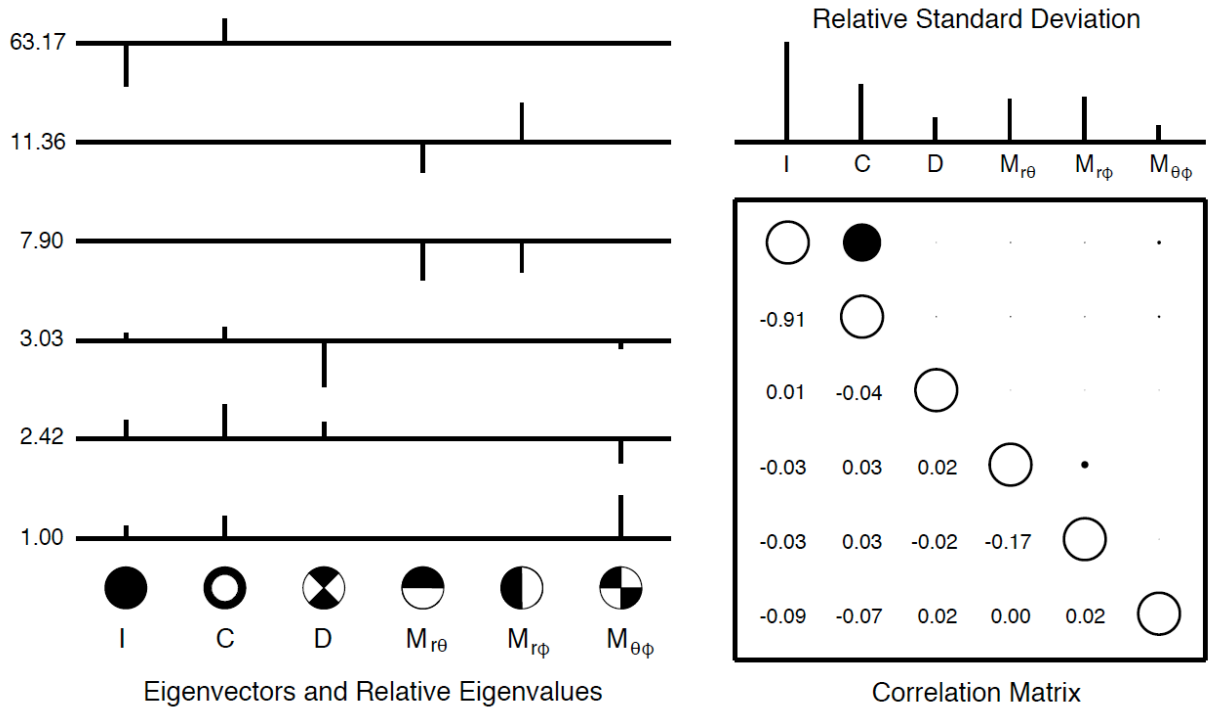

Figure 3.5. Results of an examination of the covariance matrix for the M_W 5.6 vertical-P earthquake that occurred at Miyakejima on 2 August 2000. On the left, we plot eigensolutions for $\mathbf{A}^{-1}$, which is related to the covariance matrix, $\mathbf{C}_m$, by $\mathbf{C}_m = \sigma^2_d \mathbf{A}^{-1}$, where σ^2_d is the variance of the data. Vertical lines in each row indicate the contributions of moment-tensor elements for each eigenvector, whose relative eigenvalue is given on the left. Positive contributions are plotted above the horizontal lines in each row, and negative contributions are plotted below. The eigenvectors are ordered by decreasing relative eigenvalue such that the top eigenvector shows the combination of moment-tensor elements that is the least well-constrained. Focal mechanisms for the six elements of the moment tensor are plotted below the eigenvectors. On the right, we plot the relative standard deviations of the moment-tensor elements and the correlation matrix. In the correlation matrix, the moment-tensor elements are ordered (I, C, D, $M_{r\theta}$, $M_{r\phi}$, $M_{\theta\phi}$). The size and color of the circles plotted in the upper right of the correlation matrix represent the magnitude and sign of the correlation coefficients, which are printed in the bottom left of the correlation matrix. White circles indicate positive correlation coefficients and black circles indicate negative correlation coefficients.

To explore the tradeoff between the isotropic and vertical-CLVD components further, we calculate full moment tensor solutions for the 86 vertical-CLVD earthquakes reported in Chapter 2. We use the same data selections as in the preferred CMT analysis, but allow the six independent elements of the moment tensor to vary freely. With the additional free parameter, full moment tensor solutions provide slightly better fits to the data, improving the variance reduction by 1% on average.

We decompose the full moment tensor, **M**, into isotropic and deviatoric (**M′**) components, where

$$M'_{ij} = M_{ij} - \frac{1}{3}(M_{rr} + M_{\theta\theta} + M_{\phi\phi})\delta_{ij}. \quad (3.11)$$

We define the isotropic moment, M_{ISO}, as

$$M_{ISO} = \frac{1}{3}(M_{rr} + M_{\theta\theta} + M_{\phi\phi}), \quad (3.12)$$

and the deviatoric moment, M_{DEV}, as

$$M_{DEV} = \frac{1}{2}(\lambda_1' - \lambda_3'), \quad (3.13)$$

where λ_1' and λ_3' are the maximum and minimum eigenvalues of **M′**. We also describe each earthquake in terms of two quantities, the ε value of the deviatoric fraction of the moment tensor, and k, which describes the relative contributions of the isotropic and deviatoric components. We define k as:

$$k = \frac{M_{ISO}}{|M_{ISO}| + M_{DEV}}. \quad (3.14)$$

Because we follow GCMT convention to define the deviatoric moment, our definition of k differs slightly from that given by *Hudson et al.* [1989].

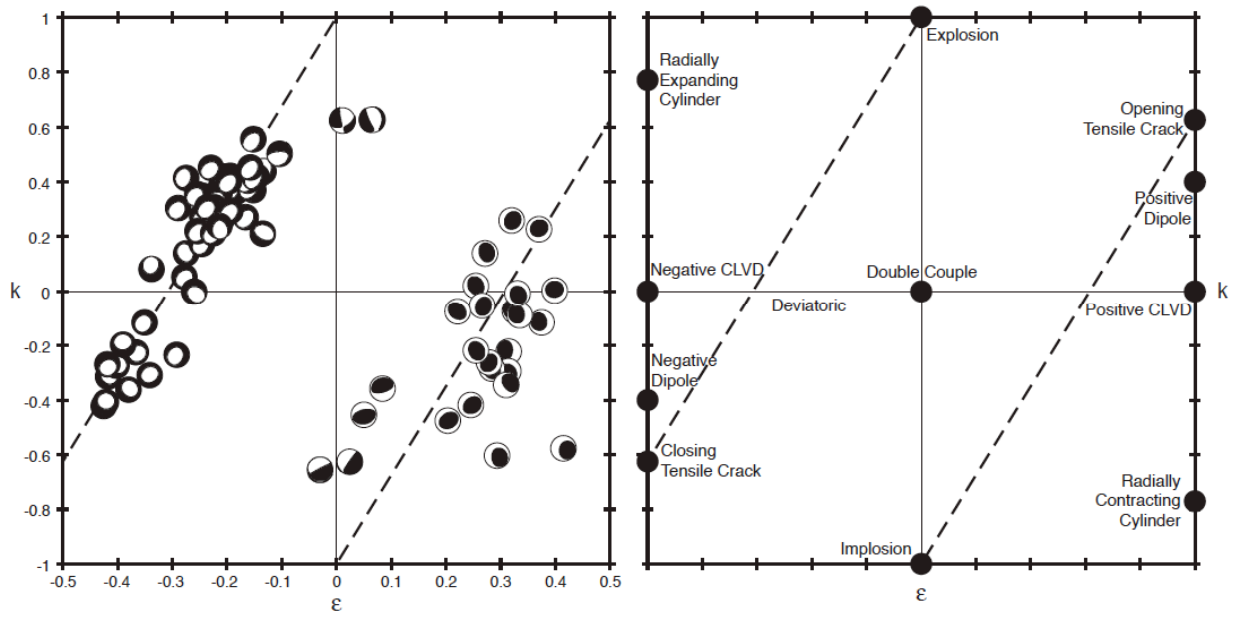

Figure 3.6. At left, we plot focal mechanisms for the deviatoric fraction of the full moment-tensor solutions for the 86 vertical-CLVD earthquakes analyzed here according to their k and ε values. On the right, we plot the locations of a variety of end-member seismic sources in k-ε space. Dashed lines in both panels illustrate the tradeoff between isotropic and vertical-CLVD components. See text for details.

In the left panel of Figure 3.6, we plot the deviatoric focal mechanisms ($\mathbf{M'}$) for each earthquake on axes corresponding to the k and ε values of the full moment-tensor solutions. On the right panel, we provide a key to illustrate the k and ε values of different types of earthquakes. Moment tensors for earthquakes with explosive and implosive components have positive and negative k values, respectively, and moment tensors for earthquakes with no net volume change plot along the line $k = 0$. Black circles indicate the k and ε values of double-couple earthquakes, pure implosions and explosions, positive and negative CLVDs, positive and negative dipoles, opening and closing tensile cracks, and radially expanding and contracting cylinders, assuming that the Lame constants, λ and μ, are equal [*Choue*t, 1996; *Kawakatsu and Yamamoto*, 2007; *Kumagai*, 2009].

We find that the full moment-tensor solutions for the vertical-CLVD earthquakes from Chapter 2 plot roughly along two lines that span wide ranges of k-ε space. Vertical-P earthquakes plot close to the line joining closing tensile cracks with pure explosions, and vertical-T earthquakes plot close to the line joining opening tensile cracks with pure implosions. Given that the dominant principal stress axes are close to vertical, the focal mechanisms are consistent with tensile cracks that are oriented approximately horizontally. Focal mechanisms for vertical positive and negative dipoles would also plot close to these lines.

The dashed lines in Figure 3.6 are drawn for illustrative purposes based on visual inspection of the trends of the full moment-tensor solutions for vertical-CLVD earthquakes in k-ε space. However, we also performed a numerical experiment for the M_W 5.6 vertical-P earthquake described in Figure 3.5 in order to examine the impact of the tradeoff between the isotropic and pure vertical-CLVD components of the moment tensor on our full moment-tensor solutions. We began with the deviatoric moment tensor presented in Chapter 2, and calculated a suite of additional moment tensors by adding combinations of the isotropic and pure vertical-CLVD components (Equations 3.6 and 3.7) in the proportions described by $(-0.87I + 0.49C)$, the eigenvector of the covariance matrix with the largest relative eigenvalue. We find an approximately linear relationship between the k and ε values for this suite of moment tensors, extending from $-0.55 < k < 0.55$ and $-0.5 < \varepsilon < 0$. The slope of this line is slightly lower than the dashed lines drawn in Figure 3.6, but approximates the observed trends of the full moment-tensor solutions for vertical-CLVD earthquakes well.

3.3. Discussion

In this section, we examine the two main classes of physical mechanisms that have been presented to explain vertical-CLVD earthquakes, ring-faulting mechanisms and mechanisms involving fluid flow and/or volumetric changes, using the constraints and understanding developed in Section 3.2. We describe the proposed physical mechanisms in detail, and use published results from field geology and analog and numerical models as further constraints on physical parameters such as the geometry of ring faults and the propagation velocity of fluid-filled tensile cracks.

Because we cannot constrain the relative contributions of the isotropic and pure vertical-CLVD components in our waveform inversions, we do not interpret individual full moment-tensor solutions. Instead, we choose to interpret the range of potential mechanisms allowed by the solution space for the full dataset of earthquakes. In particular, we consider ring-faulting mechanisms and volume exchange between two reservoirs, which do not require net volume changes. We also consider the opening and closing of subhorizontal tensile cracks and dominant isotropic sources, which do require net volume changes. Given that the isotropic and pure vertical-CLVD components of the moment tensor cannot be independently resolved for our dataset, all of these mechanisms are permissible if one only considers information from the CMT analysis. Additional data are required to assess which mechanisms are the most likely.

In Chapter 2 and in this study, we have identified several additional constraints that can be used to evaluate potential physical mechanisms for producing vertical-CLVD earthquakes. First, vertical-CLVD earthquakes have slower source processes than tectonic earthquakes of the same

magnitude. Additionally, vertical-P earthquakes appear to have longer source processes than vertical-T earthquakes. Vertical-T earthquakes have durations of ~10 s or less, whereas vertical-P earthquakes can have durations as long as ~60 s. Second, vertical-P earthquakes typically occur after volcanic eruptions or the start of volcanic unrest, whereas vertical-T earthquakes most often occur beforehand. Third, although seismic radiation from vertical-CLVD earthquakes is dominated by Rayleigh waves that are radiated in approximately equal amplitude in all directions, we do observe small-amplitude Love waves for many events. As demonstrated by the broadband body-wave modeling example in Figure 3.2, horizontally polarized shear (SH) waves are also observed for many vertical-CLVD earthquakes. Finally, vertical-CLVD earthquakes are most commonly associated with volcanoes that erupt basaltic and/or andesitic lavas, as well as volcanoes that have calderas. We search for physically plausible mechanisms that can explain these observations.

3.3.1. Ring-Faulting Mechanisms

Ring faults are curved or cone-shaped dip-slip faults that are circular to elliptical in plan view. These faults are formed by the inflation and deflation of shallow magma chambers, and can be either inward- or outward-dipping, as shown schematically in Figure 3.7. In nature, ring faults are inherently difficult to observe because they are often covered by pyroclastic flow deposits, lava flows, or crater lakes after forming during episodes of caldera collapse. However, both inward- and outward-dipping ring faults have been mapped at eroded volcanoes, where they occasionally are intruded with magma. Summaries of results from field studies on calderas are provided in *Lipman* [1997] and *Cole et al.* [2005], and a database of collapse calderas is provided by *Geyer and Marti* [2008]. At volcanoes such as Rabaul [*Mori and McKee*, 1987], Pinatubo

[*Mori et al.,* 1996], Mt. Spurr [*Jolly et al.,* 1994], Mt. St. Helens [*Scandone and Malone,* 1985], Mammoth Mountain in Long Valley Caldera [*Prejean et al.,* 2003], and Mauna Kea [*Wolfe et al.,* 2004], the presence of ring faults has been inferred from circular or elliptical patterns formed by the locations of microearthquakes. Although the geometries of ring faults are difficult to measure, most ring faults are believed to have steep, approximately subvertical, dip angles [*Gudmundsson and Nilsen*, 2006 and references therein].

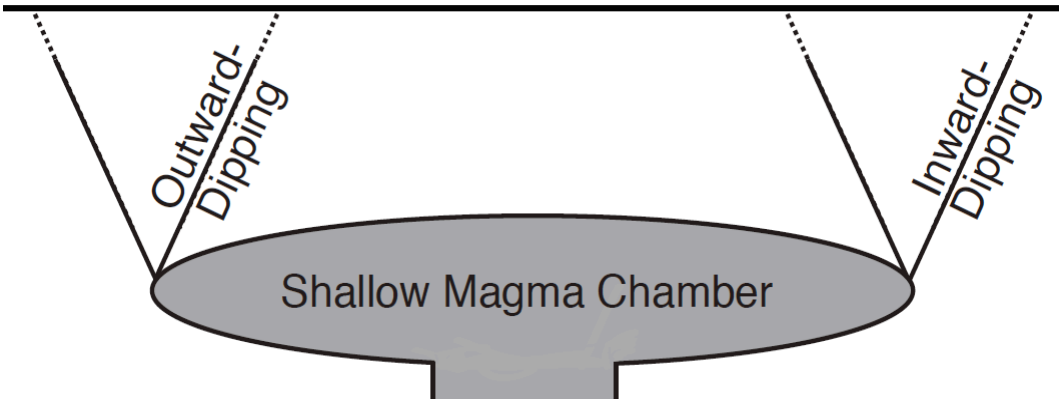

Figure 3.7. Schematic diagram for inward- and outward-dipping ring faults located above a shallow magma chamber/melt lens. The ring faults are cone shaped in three dimensions. Dashed lines indicate that the ring faults may terminate below the surface.

Ring faults and collapse calderas have been studied in detail through analytical and numerical models [e.g., *Anderson,* 1936; *Druitt and Sparks*, 1984; *Burov and Guillou-Frottier*, 2003; *Folch and Marti*, 2004; *Gray and Monaghan*, 2004; *Gudmundsson*, 1988, 1998, 2007; 2008; *A. Gudmundsson et al*., 1997; *Roche and Druitt*, 2001; *Pinel and Jaupart*, 2005; *Gudmundsson and Nilsen*, 2006; *Hardy*, 2008; *Kinvig et al*., 2009; *Kusumoto and Gudmundsson,* 2009; *Marti et al*., 2009; *Holohan et al*., 2011; *Pinel*, 2011], as well as analog models [e.g., *Marti et al*., 1994,

2008; *Acocella et al*., 2000; *Roche et al*., 2000, 2001; *Troll et al*., 2002; *Kennedy et al*., 2004; *Holohan et al*., 2005, 2008; *Aizawa et al*., 2006; *Geyer et al*., 2006; *Acocella*, 2006, 2007, 2008; *Walter*, 2008; *Burchardt and Walter*, 2010; *Howard*, 2010]. Although each type of modeling has its own assumptions, simplifications and limitations, together they provide insight into how ring-fault structures develop and evolve. Numerical models indicate that sill-like magma chambers are a requirement for the formation of inward-dipping ring faults, in addition to specific stress conditions such as magma chamber underpressure or overpressure, extension or regional doming [*Marti et al*., 2008 and references therein]. As described below, analog models of caldera collapse and dome resurgence suggest that slip on outward- and inward-dipping ring faults is triggered by the deflation and inflation of shallow magma chambers.

In general, analog models suggest that the caldera collapse process can be described by four stages of progressive subsidence [*Acocella,* 2006]. During the first stage, the surface gently subsides as the deflation of a shallow magma chamber results in the upward propagation of outward-dipping reverse ring faults. In the second stage, well-defined caldera fault scarps form when the reverse ring faults reach the surface. The outer rim of the caldera moves outwards as additional subsidence produces multiple sets of reverse ring faults that become progressively steeper. In the third stage, the outer periphery of the reverse ring faults tilts inward due the upward propagation of steep, inward-dipping, normal ring faults. Finally, in the last stage, two nested collapse structures are produced when the normal ring faults reach the surface and begin to accommodate the majority of later subsidence. Dome resurgence following caldera collapse reverses the kinematics of pre-existing ring faults such that magma chamber inflation following deflation is accommodated by slip on inward-dipping, reverse ring faults and outward-dipping

normal ring faults. In scaled analog models, the dips of ring faults produced during caldera collapse vary as a function of depth. In *Roche et al.* [2000], both the outward-dipping reverse ring faults and the inward-dipping normal ring faults are subvertical at depth and more shallowly dipping near the surface. Depending on the aspect ratio of the roof (thickness/width) for a given model, the dips of the reverse faults range from ~45° to ~85°, and the dips of the normal faults vary from ~50° to ~65° at the surface.

Dip-slip motion on ring-faults can produce vertical-CLVD earthquakes with source parameters that depend on the geometry and kinematics of the ring fault, as well as the scale and speed of rupture. Slip on curved normal faults can produce vertical-P earthquakes, whereas slip on curved reverse ring faults can produce vertical-T earthquakes [*Ekström*, 1994]. Below, we model the moment tensors of theoretical ring-faulting earthquakes in order to determine how ring fault geometry and rupture extent influence earthquake size, the magnitude of the non-double-couple component and the plunge of the dominant principal stress axis. We explore reasons that ring-faulting earthquakes might have longer source processes than tectonic earthquakes, and evaluate the ring-faulting model using the observations of vertical-CLVD earthquakes presented in Chapter 2 and Section 3.2.

Because long-period seismic radiation patterns only depend on the final distribution of slip along a fault, we approximate the moment tensors of reverse and normal ring-faulting earthquakes by summing the contributions of moment tensors for planar faults with constant dip and smoothly varying strike angles, similar to the approach taken by *Ekström* [1994]. We fix the rake to ±90° and, for constant dip angles ranging from 45° to 90°, we vary the strike angles from 0° to 360° to

simulate earthquakes rupturing different arc angles of a conical ring fault. We calculate hypothetical moment tensors following Box 4.4 of *Aki and Richards* [2002]. For each combination of ring-fault dip and arc angle, we calculate the value of ε, the plunge of the dominant pressure or tension axis, and the normalized scalar moment, which is the ratio between the scalar moment of the composite moment tensor and the sum of the scalar moments for individual subfaults. Variations of these three parameters with arc and dip angle are plotted in Figure 3.8. Except for vertically symmetric sources, which are produced when the entire arc of the ring fault is ruptured in a single earthquake, small-amplitude SH and Love waves will be generated, as observed for our dataset of vertical-CLVD earthquakes.

We find that the value of $|\varepsilon|$ is largely controlled by the arc angle of the ring fault. Earthquakes that rupture small portions of the ring fault are approximately double-couple and, in general, earthquakes that rupture greater arc angles have higher non-double-couple components. However, for ruptures extending past ~180° of arc, the non-double-couple component does not always increase with arc angle. The plunge of the dominant principal stress axis for a ring-faulting earthquake is largely controlled by the dip angle of the ring fault. For equal arc angles, earthquakes on more steeply dipping ring faults have dominant principal stress axes with shallower plunges. Earthquakes that rupture the entire circumference of a ring fault are pure vertical-CLVD events with $\varepsilon = \pm 0.5$ and vertical pressure or tension axes.

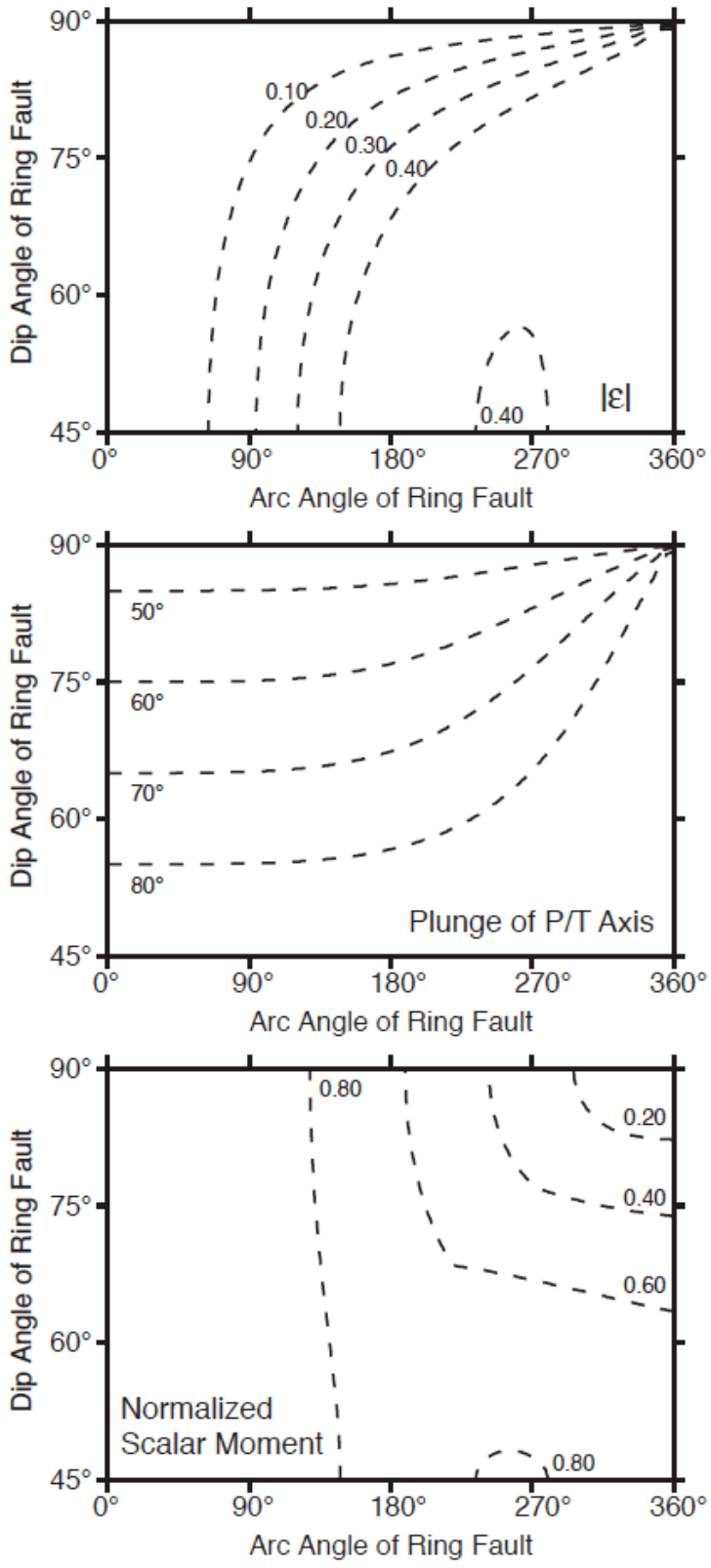

(Figure caption on next page)

Figure 3.8. Source parameters for the composite radiation patterns resulting from different slip distributions along cone-shaped ring faults. Ring-fault dip is plotted on the y-axis and the ruptured arc angle on the x-axis. All simulated earthquakes are pure dip-slip events. The top panel shows $|\varepsilon|$, which represents the strength of the non-double-couple component of the composite moment tensor. The middle panel shows the plunge of the dominant principal stress axis. The bottom panel shows the normalized scalar moment, which is the ratio between the scalar moment for the composite moment tensor and the sum of the scalar moments for individual subfaults.

As demonstrated in the bottom panel of Figure 3.8, dip-slip motion on ring-fault structures also results in the partial cancellation of seismically radiated long-period moment [*Ekström,* 1994]. For some combinations of dip and arc angle, the sum of the scalar moments (product of shear modulus, fault area, and displacement) resulting from slip on individual subfaults will be larger than the scalar moment of the composite moment tensor determined by CMT analysis. As a consequence, the actual displacement during a ring-faulting earthquake will also be larger than expected from empirical relationships between average displacement and M_W like those developed by *Wells and Coppersmith* [1994]. In the end-member case, slip on a cylindrical fault surface will not produce any long-period seismic radiation. *Ekström* [1994] suggests that the partial cancellation of long-period seismic moment resulting from slip on ring-fault structures could explain why vertical-T earthquakes near Smith Rock volcano are associated with disproportionately large tsunamis.

If we consider a ring fault circumscribing a conical crustal block, four distinctly different moment tensors can be produced for the same combination of dip and arc angles, depending on whether the ring fault dips inward or outward, and whether the central crustal block moves up or down relative to the rest of the volcano. In Figure 3.9, we show composite moment tensors for earthquakes generated by dip-slip motion along the same 120° of arc for ring faults dipping 65°.

Following the convention of *Aki and Richards* [2002], in which the fault dips down to the right of the strike direction, we use strike angles varying between 0° and 120° for inward-dipping ring faults, and strike angles varying between 180° and 300° for outward-dipping ring faults. We set the rake to ±90° to simulate pure normal and reverse ring-faulting earthquakes.

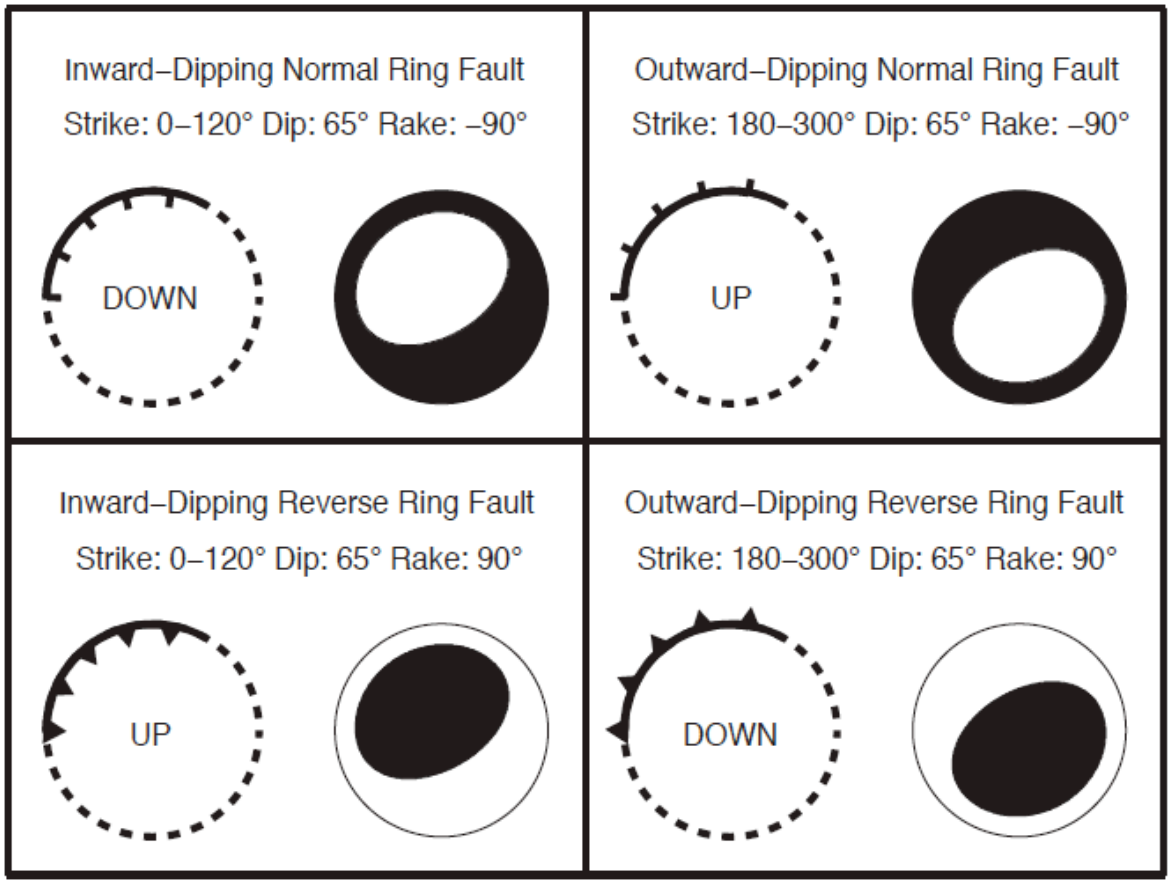

Figure 3.9. A comparison of the composite moment tensors that result from dip-slip motion along a fixed arc segment. In each quadrant, we plot a schematic indicating the direction of the ring fault (inward or outward) and the relative motion of the central crustal block (up or down) as well as the matching focal mechanism. Details of the fault parameters are listed at the top of each quadrant.

As illustrated in Figure 3.9, for cases in which the ring fault is inward-dipping and the crustal block moves downward, either due to the deflation of an underlying magma chamber or the inflation of an overlying magma chamber, vertical-P earthquakes are produced. Vertical-T earthquakes are produced if the kinematics are reversed and the crustal block moves upward due to the inflation of an underlying magma chamber. Similarly, the upward motion of an outward-dipping crustal block can produce vertical-P earthquakes, whereas the downward motion of the crustal block produces vertical-T earthquakes. For inward-dipping ring faults, the azimuth of the dominant principal stress axis bisects the ring fault slip distribution, whereas for outward-dipping ring faults, the midpoint of the ruptured arc segment is offset by 180° from the azimuth of the dominant principal stress axis.

With the expected behavior for ring-faulting earthquakes outlined above, we use our observations of vertical-CLVD earthquakes to evaluate the ring-faulting mechanism. If vertical-CLVD earthquakes are generated by slip on ring faults, deviatoric moment-tensor solutions should contain information about the ring-fault geometry and the extent of rupture. In Figure 3.10, assuming that the rupture patterns can be approximated by uniform slip along a conical ring fault as in Figure 3.8, we use the values of ε and the plunges of the dominant principal stress axes retrieved from the CMT solutions in Chapter 2 to plot estimated ring-fault dip and arc angles. For most earthquakes, the values of ε and the plunges of the pressure or tension axes result in unique estimates of arc and dip angles. However, because the ε patterns become complicated for ruptures extending past 180° of arc, the source parameters for a small number of earthquakes with $|\varepsilon| > 0.40$ are consistent with several possible combinations of dip and arc

angles. For these earthquakes, we prefer solutions with the smallest arc angles in order to be consistent with the results for the majority of the other earthquakes.

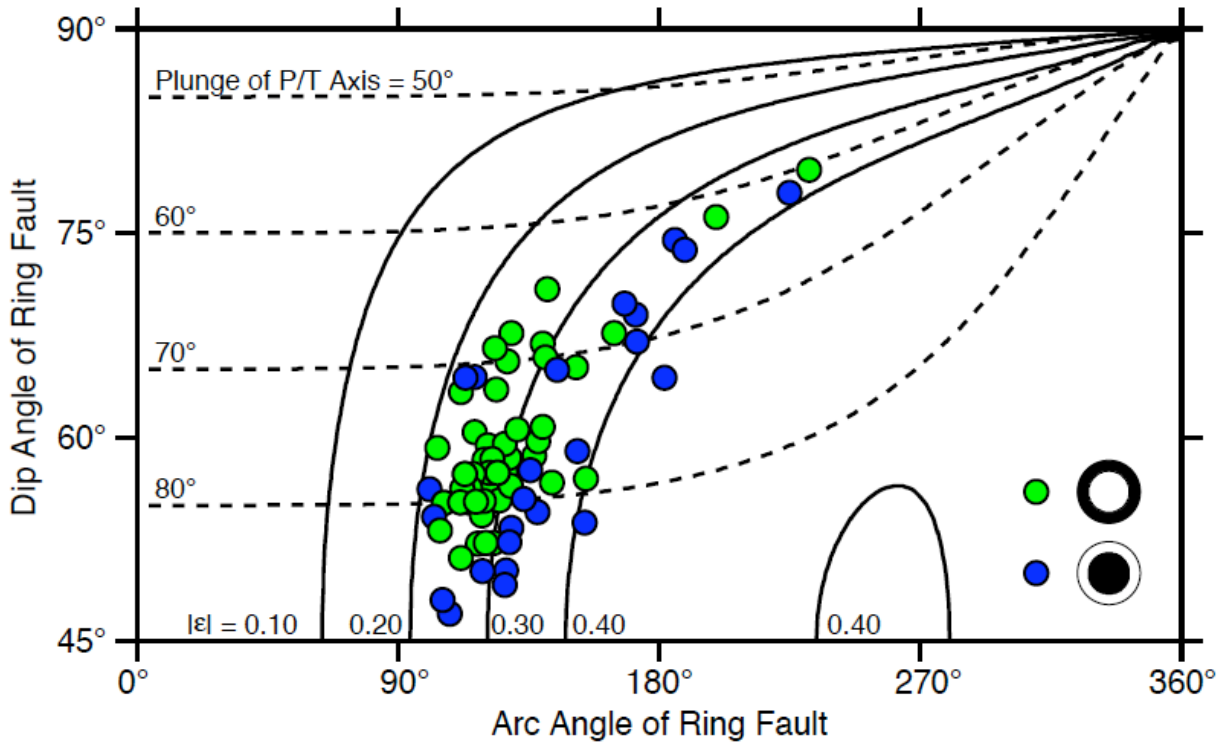

Figure 3.10. Application of the conical ring-faulting model from Figure 3.7 to the 86 vertical-CLVD earthquakes from Chapter 2. We invert the values of $|\varepsilon|$ and the plunges of the dominant principal stress axes to obtain estimates of the dip and arc angles of ring faults. Green circles represent vertical-P earthquakes and blue circles represent vertical-T earthquakes. Black lines show contours of $|\varepsilon|$ and dashed lines show contours of the plunge of the pressure or tension axes.

Overall, we find that the source parameters of the 86 vertical-CLVD earthquakes identified in Chapter 2 are consistent with slip along ~100°-250° of arc on ring faults that dip 45°-80°. The vast majority of vertical-CLVD earthquakes cluster between arc angles of 100°-160° and dip angles of 50°-70°, and we do not observe systematic differences between the ring-fault parameters estimated for vertical-P and vertical-T earthquakes. In cases where multiple vertical-

CLVD earthquakes are associated with the same volcano, we find that the estimated ring-fault parameters are similar. For example, the 39 largest vertical-P earthquakes at Miyakejima have CMT solutions that are consistent with slip along ~110°-125° of arc on ring faults dipping ~55°-60°. The dip angles that we retrieve in Figure 3.10 are relatively shallow compared to the subvertical dip angles observed for ring faults in nature and in analog models. In fact, slip on subvertical ring faults should produce non-double-couple earthquakes with dominant principal stress axes that plunge 45°-60°, and those earthquakes would not be considered vertical-CLVD earthquakes according to our criteria, which require the plunge of the dominant principal stress axis to be greater than 60°. We estimate that the uncertainties associated with the plunges of the dominant stress axes are on the order of 5-10°, and the uncertainties associated with the ε values are ~0.05-0.10, which translates to uncertainties of ~30° in arc angle and ~10° in dip angle.

Some of the steepest estimates of ring-fault dip are retrieved for vertical-T earthquakes at Sierra Negra and Rabaul, two volcanoes with known ring-fault structures. Although the estimates of ring-fault dip obtained from our CMT solutions are reasonably consistent with geophysical observations at these volcanoes, as outlined below, the relationships between vertical-CLVD earthquakes and deformation is not clear.

Sierra Negra is a shield volcano with a large summit caldera located in the Galápagos Islands. The interior of Sierra Negra's caldera contains a 14-km-long sinuous ridge formed by a series of repeating trapdoor-faulting events driven by magma accumulation in the volcano's sill-like magma chamber [Figure 3.11; *Reynolds et al.,* 1995; *Amelung et al.,* 2000; *Jónsson et al.,* 2005; *Chadwick et al.,* 2006; *Jónsson,* 2009]. On 22 October 2005 at 23:40 UTC, an M_W 5.5 vertical-T

earthquake took place at Sierra Negra, three hours prior to the start of an explosive and effusive eruption sourced from the northern rim of the caldera [*Geist et al.,* 2008]. *Yun* [2007] interpreted InSAR data spanning the 2005 eruption to suggest that the precursory earthquake was generated by uplift of the caldera floor along the sinuous ridge located along the southern and western rims of the caldera. Vertical fault scarps measured along the sinuous ridge [*Geist et al.,* 2008] support this model (Figure 3.10). Although *Yun* [2007] modeled the earthquake as dip-slip motion along a vertical fault, InSAR and GPS data from several other trapdoor-faulting episodes that were not followed by eruptions suggest that these events are generated by slip on curved, steeply inward-dipping (~71°) thrust faults located along the southern and western rims of the caldera [*Jónsson,* 2009].

From our CMT analysis, the M_W 5.5 earthquake at Sierra Negra has an ε value of 0.37 and a tension axis that plunges 62°, which is consistent with dip-slip motion along ~220° of arc on a ring fault dipping ~78° (Figures 3.9 and 3.10). As demonstrated in Figure 3.9, vertical-T focal mechanisms are consistent with either the subsidence of a caldera block bounded by an outward-dipping reverse ring fault, or uplift of a caldera block bounded by an inward-dipping reverse ring fault. The latter scenario is similar to that suggested by *Yun* [2007]. However, if the vertical-T earthquake took place on an inward-dipping reverse ring fault located along the southern and western rims of the caldera, the tension axis should plunge to the southwest. According to our CMT solution, which is A-quality and well constrained, the tension axis has an azimuth of 60°, which is consistent with uplift along an inward-dipping reverse ring fault located along the northern and eastern rims of the caldera, or subsidence along an outward-dipping reverse ring fault located on the southern and western rims of the caldera.

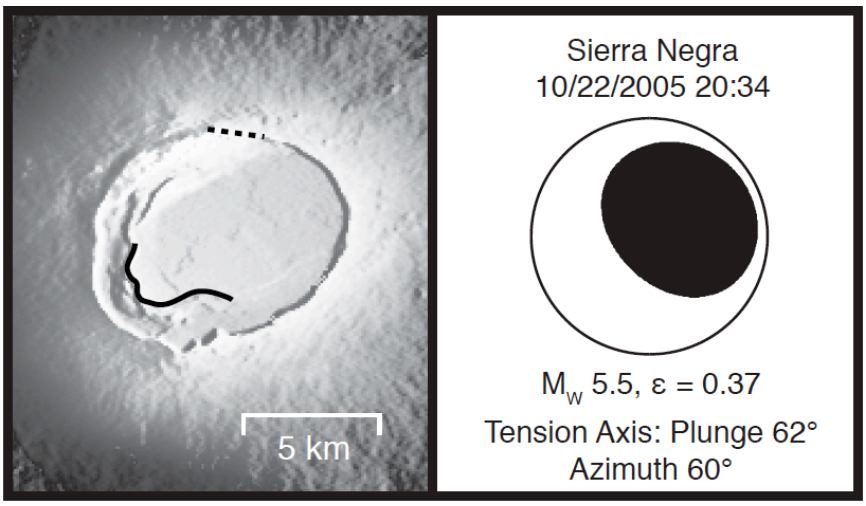

Figure 3.11. A map of the caldera of Sierra Negra volcano is plotted in the left panel. The dashed line indicates the location of the initial fissure for the 2005 eruption and the black line indicates the location of the vertical fault scarp reported in *Geist et al*. [2008]. Topography is from the Shuttle Radar Topography Mission. The focal mechanism for the M_W 5.5 vertical-T earthquake that occurred 3 hours prior to the start of the 2005 eruption is plotted on the right.

We note similar inconsistencies when we attempt to apply the ring-faulting model to four M_W 5.0 vertical-T earthquakes that took place at Rabaul between 1991 and 1996. Rabaul is a pyroclastic shield volcano in Papua New Guinea that entered an explosive phase in September 1994 following a 23-year seismic crisis. At Rabaul, the locations of microearthquakes delineate a steeply outward-dipping (~80°) elliptical ring fault extending to depths of 4-5 km [*McKee et al*., 1984; *Mori and McKee*, 1987; *Mori et al*., 1989; *Itikarai et al*., 2008 as referenced in *Johnson et al*., 2010]. The four vertical-T earthquakes from Rabaul have ε values of 0.34-0.39 and tension axes that plunge 63°-70°, which are consistent with dip-slip motion along ~170°-185° of arc along a ring fault dipping ~68°-75°. The first two vertical-T earthquakes took place during a period of caldera uplift prior to the 1994 eruption, which is a scenario that should produce vertical-P earthquakes provided the uplift is accommodated by slip on the observed outward-

dipping ring fault. As above, the vertical-T focal mechanisms for the Rabaul earthquakes are consistent with subsidence of a caldera block bounded by an outward-dipping reverse ring fault or uplift of a caldera block bounded by an inward-dipping reverse ring fault. If a shallow magmatic or hydrothermal system was inflating before the 1994 eruption [*McKee et al.,* 1984; *Mori and McKee,* 1987; *Geyer and Gottsman,* 2010], it could have triggered subsidence along the outward-dipping ring fault. The vertical-T earthquakes could also have been caused by slip on antithetic inward-dipping ring-fault structures [*Saunders,* 2001, 2005].

As demonstrated in Section 3.2.1, vertical-CLVD earthquakes have slow source processes, and there are several reasons ring-faulting earthquakes may have lower rupture velocities, and therefore slower source processes, than standard tectonic earthquakes. The velocity of rupture propagation during an earthquake is limited by the shear modulus of fault rocks. At volcanoes, the effective shear modulus of near-surface, fractured basalt is significantly lower than laboratory values [*Rubin and Pollard*, 1987], and as a result, the shear-wave velocity is lower and the rupture velocity is slower. Volcanic earthquakes with low rupture velocities were observed at Mt. St. Helens in association with the incremental extrusion of brittle rock spines during the 2004 eruption [*Harrington and Brodsky,* 2007]. Additionally, the rupture velocity along ring faults may be affected by unusual frictional and mechanical properties associated with hydrothermal circulation, magmatic intrusions, and the effects of repeated collapse events. Finally, ring faults may have complicated geometries composed of several approximately planar fault segments instead of one smooth cone-shaped fault surface. Rupture velocity is known to decrease near regions of slip transfer from one fault segment to the next [e.g., *Wald and Heaton,*

1994]. Any combination of these factors could explain why vertical-CLVD earthquakes have slower source processes than tectonic earthquakes.

In Chapter 2, we demonstrated that vertical-T earthquakes usually occur before volcanic eruptions or the start of episodes of volcanic unrest, whereas vertical-P earthquakes occur after the initiation of eruptive activity. Additionally, vertical-T earthquakes generally have shorter source processes than vertical-P earthquakes. If vertical-CLVD earthquakes are generated by dip-slip motion on ring faults, this may indicate that the inflation of shallow magma chambers generates earthquakes with faster rupture velocities than post-eruption deflation processes. Moderate-sized vertical-CLVD earthquakes are most commonly observed at basaltic and/or andesitic volcanoes with caldera structures, which may indicate that both ring faults and low-viscosity magmas are required to generate these events.

For equal dip and arc angles, the largest magnitude vertical-CLVD earthquakes are expected to occur on ring faults with the largest dimensions, or in cases where rapid changes in the volume of shallow magma chambers trigger large vertical displacements along ring-fault systems. The fact that we do not observe any vertical-CLVD earthquakes with magnitudes over M_W 5.8 could be due to the dimensions of ring faults at source volcanoes. Small calderas, and therefore small ring faults, are formed at volcanoes located in Mariana-type subduction zones or in oceanic crust, as well as at volcanoes that erupt tholeiite or alkaline magmas, which have low silica contents [*Sobradelo et al*., 2010]. In Chapter 2, we found that moderate-sized vertical-CLVD earthquakes most commonly occur at basaltic-to-andesitic stratovolcanoes and submarine volcanoes located

in subduction zones, which suggests that vertical-CLVD earthquakes may be generated by dip-slip motion on relatively small ring-fault structures.

The ring-faulting model can explain many characteristics of vertical-CLVD earthquakes, including their anomalous radiation patterns and frequency contents, as well as their magnitudes. However, it is difficult to relate the source parameters of vertical-CLVD earthquakes to specific faulting scenarios, even in cases where the earthquakes occur at volcanoes where deformation and the geometries of ring-fault systems are reasonably well constrained. If the deviatoric moment-tensor solutions for vertical-CLVD earthquakes can be directly related to slip distributions on ring faults, these structures must have shallower dips than expected from field studies and analog models. On the other hand, if vertical-CLVD earthquakes are caused by slip on steeply dipping ring faults, we must explain the discrepancies between expected and observed source parameters. Small differences may be attributed to uncertainties in our CMT solutions. Larger differences could be the result of complexity associated with the ring-fault geometry or the rupture process. For example, the conical ring fault geometry and the ±90° rake angles used in Figures 3.8-3.10 may not be appropriate. These discrepancies may also be artifacts introduced by the existence of unmodeled, non-zero isotropic components generated by the inflation or deflation of shallow magma chambers. Below, we evaluate this possibility.

3.3.2. Fluid-Transport and Volumetric-Change Mechanisms

In volcano seismology, small earthquakes are routinely attributed to sources with net volume changes. Common sources associated with magma or fluid transport include spherical isotropic sources, opening or closing tensile cracks, and radially expanding or contracting cylinders

[Figure 3.6; *Chouet,* 1996; *Kawakatsu and Yamamoto,* 2007*; Kumagai,* 2009]. Below, we present the moment tensors for volume-change mechanisms of these end-member reservoir types [*Kawakatsu and Yamamoto*, 2007]. In each case, ΔV is the stress-free volumetric strain that characterizes the amount of fluid that is injected or withdrawn from the reservoir [*Aki and Richards*, 2002]. Due to the confining pressure of the medium and the geometry of the reservoir, the actual volume change of the reservoir, or Mogi volume ΔV_m, may be smaller than ΔV [*Richards and Kim*, 2005; *Kawakatsu and Yamamoto*, 2007].

In standard spherical coordinates (r, θ, ϕ), the moment tensor for a spherical reservoir is given by:

$$M_{sphere} = \Delta V \begin{bmatrix} \lambda + \frac{2}{3}\mu & 0 & 0 \\ 0 & \lambda + \frac{2}{3}\mu & 0 \\ 0 & 0 & \lambda + \frac{2}{3}\mu \end{bmatrix}, \tag{3.15}$$

where

$$\frac{\Delta V_m}{\Delta V} = \frac{\lambda + (2/3)\mu}{\lambda + 2\mu}. \tag{3.16}$$

The moment tensor corresponding to a horizontal tensile crack that opens or closes vertically is:

$$M_{crack} = \Delta V \begin{bmatrix} \lambda + 2\mu & 0 & 0 \\ 0 & \lambda & 0 \\ 0 & 0 & \lambda \end{bmatrix}. \tag{3.17}$$

In this case,

$$\Delta V = \Delta V_m = S\Delta\bar{u}, \tag{3.18}$$

where S is the crack area and $\Delta\bar{u}$ is the crack opening or closing width.

The moment tensor corresponding to the radial expansion of a cylinder with a vertical symmetry axis is:

$$M_{cylinder} = \Delta V \begin{bmatrix} \lambda & 0 & 0 \\ 0 & \lambda+\mu & 0 \\ 0 & 0 & \lambda+\mu \end{bmatrix}, \tag{3.19}$$

where

$$\frac{\Delta V_m}{\Delta V} = \frac{\lambda+\mu}{\lambda+2\mu}. \tag{3.20}$$

By applying a rotation matrix to Equations 3.17 and 3.19, we can obtain moment tensors for tensile cracks or cylindrical sources of any orientation. As demonstrated by *Kawakatsu and Yamamoto* [2007], the isotropic component of spherical sources, opening and closing tensile cracks and radially expanding or contracting cylinders are all the same when expressed in terms of ΔV:

$$I = \frac{1}{3} trace(M) = \left(\lambda + \frac{2}{3}\mu\right)\Delta V = \kappa \Delta V \tag{3.21}$$

where κ is the bulk modulus, or incompressibility, of the surrounding medium.

Volume Exchange

When fluid is transported from one reservoir to another, perhaps due to asperity failure, composite seismic sources are generated by the expansion and contraction of two reservoirs. These volumetric sources have equal magnitude and opposite sign, so the composite moment tensor is a pure CLVD with no net isotropic component. Depending on the orientations and types

of the reservoirs, vertical-CLVD earthquakes can be produced by a mass or volume exchange process. For example, pure vertical-P moment tensors can be produced by the transport of fluid from a horizontal tensile crack into a vertical cylinder. Likewise, pure vertical-T moment tensors can be produced by fluid flow from a vertical cylinder into a horizontal tensile crack [*Chouet,* 1996]. Vertical-CLVD moment tensors can also be produced by volume exchange between reservoirs that are not perfectly spherical, cylindrical or planar. In these cases, the radiation pattern of Rayleigh waves is not azimuthally isotropic and SH and Love waves are produced. Theoretically, larger vertical-CLVD earthquakes should be produced when greater amounts of mass or volume are exchanged between two reservoirs. Likewise, the frequency contents of the earthquakes caused by mass or volume exchange processes should be influenced by the duration of the exchange process, such that longer exchanges produce slower, lower-frequency earthquakes.

A volume-exchange process has been investigated as a way to explain the M_W 5.6 vertical-T earthquake that occurred in Iceland prior to a subglacial eruption between Bárdarbunga and Grimsvötn in September 1996. *Tkalčić et al.* [2009] calculated a full moment-tensor solution for this event using regional seismic data and found it to have a statistically insignificant isotropic component, which they attempted to replicate using volume exchange between two magma chambers separated by varying vertical distances. After calculating moment tensors for synthetic data generated by various configurations of inflating and deflating magma chambers with full volume compensation, *Tkalčić et al.* [2009] concluded that a mass exchange mechanism is likely to result in a statistically significant observed isotropic component, even using long-period seismic data. The volume exchange mechanism is unlikely to explain the Bárdarbunga

earthquake, and we consider it an unlikely mechanism to explain most vertical-CLVD earthquakes because it requires very special conditions. Furthermore, as we discuss below, the volumes of fluids and the rates of fluid flow that would be required to generate vertical-CLVD earthquakes with the observed magnitudes and source durations are extremely large. Below, we consider mechanisms that do not require volume compensation.

Tensile Cracks

In volcanic and geothermal areas, at depths of up to several km, high fluid pressure can force open tensile cracks. As illustrated in Figure 3.6, the opening and closing of subhorizontal tensile cracks can produce earthquakes with deviatoric vertical-CLVD moment tensors. Horizontal tensile cracks have seismic radiation patterns with several unusual characteristics. In addition to having first motions that are all up or down, depending on whether the crack is opening or closing, horizontal tensile cracks radiate Rayleigh waves with equal amplitude in all directions and they do not excite SH or Love waves. Small amplitude SH and Love waves can be produced by tensile cracks that are not perfectly horizontal, but which are tilted slightly, so a tensile-crack mechanism could explain the anomalous seismic radiation patterns of vertical-CLVD earthquakes.

The observation that most vertical-T earthquakes occur before volcanic eruptions is consistent with the idea that the opening of subhorizontal tensile cracks may generate earthquakes with deviatoric vertical-T moment tensors. Likewise, the observation that most vertical-P earthquakes occur after the start of volcanic unrest is consistent with the idea that the closing of subhorizontal tensile cracks may generate earthquakes with deviatoric vertical-P moment tensors. However, if

vertical-CLVD earthquakes can be explained by such a mechanism, the process of opening subhorizontal tensile cracks must be faster than the process of closing them in order to explain our observation that vertical-P earthquakes have longer source durations than vertical-T earthquakes. Below, we evaluate this mechanism by considering the volumes of fluid injection or withdrawal and the propagation velocities of tensile cracks that are required to generate the vertical-CLVD earthquakes reported in Chapter 2.

The magnitude of an earthquake generated by the opening or closing of a tensile crack is dependent on the elastic properties of the surrounding matrix and the volume of emplaced fluid. Using the range of scalar moments from the CMT solutions in Chapter 2, 3.8×10^{15} Nm – 6.5×10^{17} Nm, we can estimate the fluid volumes that would be required to match our observations. We calculate the Mogi volumes and tensile-crack dimensions using Equations 3.17 and 3.18, assuming that 62.5% of the scalar moment is due to the isotropic component and 37.5% is due to the deviatoric remainder as in Equations 3.12-3.14. Assuming $\lambda = \mu = 3.0 \times 10^{10}$ N/m^2, vertical-CLVD earthquakes are consistent with subhorizontal tensile cracks with volume changes ranging from ~5×10^4 m^3 to ~8×10^6 m^3. These volumes are equivalent to the opening or closing of square tensile cracks with side lengths of ~200 m to ~ 3 km and widths of 1 m. These estimates will be larger for smaller values of λ.

Generally, it is assumed that fluid-driven tensile cracks cannot propagate faster than the fluid can flow following the crack tip. The propagation velocity of fluid-driven tensile cracks is therefore limited by the crack width and the fluid viscosity, among other factors. Typical dike propagation velocities range from 0.01 to 10 m/s [*Rubin,* 1995], which is far too slow to radiate seismic

waves. Tensile cracks driven by hydrothermal fluids, however, can propagate fast enough to generate seismic waves [*Miller et al*., 1998b *Ross et al*., 1999; *Foulger et al*., 2004]. Mechanisms involving the opening of tensile cracks due to the rapid injection of high-pressure, non-magmatic fluids have been used to explain several $M_W > 4.5$ earthquakes, including CLVD events at Long Valley Caldera [*Dreger et al*., 2000; *Templeton and Dreger,* 2006; *Minson and Dreger,* 2008], the M_W 5.6 vertical-T earthquake that occurred in Iceland in September 1996 before a subglacial eruption between Bárdarbunga and Grimsvötn [*Konstantinou et al*., 2003], and the M_W 5.6 vertical-T earthquake that generated a disproportionately large tsunami near Smith Rock in Japan in 1984 [*Kanamori et al.,* 1993].

Under certain conditions, it may be possible for tensile cracks to propagate ahead of the driving fluid at elastic wave speeds, generating earthquakes. It has been suggested that tensile cracks may propagate unstably as they approach the free surface or other tensile cracks, and when they initially propagate outwards from magma chambers [*Sammis and Julian,* 1987]. Three M_W 5-6 CLVD earthquakes at Long Valley caldera in 1980 have been attributed to dike propagation [*Julian,* 1983; *Aki,* 1984; *Julian and Sipkin*, 1985], although this interpretation is controversial. The data can also be explained using a composite faulting model consisting of normal and strike-slip subfaults [*Ekström and Dziewonski,* 1983]. Given that vertical-T earthquakes have source dimensions of at least several hundred meters and source time functions ranging from a few seconds to a few tens of seconds, our observations require propagation velocities of at least ~100 m/s. Some special condition would be required to allow faster-than-normal crack propagation in order to explain vertical-T earthquakes by the opening of magma-filled tensile cracks.

Although fluid-driven tensile cracks can open rapidly, they are generally expected to close slowly and not radiate seismic waves [*Julian et al.*, 1998]. At mines, however, the sudden collapse of cavities has produced earthquakes with full moment tensors that closely resemble closing horizontal tensile cracks [*Pechmann et al*., 1995; *Bowers and Walter,* 2002; *Ford et al*., 2008; *Pechmann et al.*, 2008], some with magnitudes up to M~5 [*Knoll*, 1990; *Pechmann et al*., 1995; *Gibowicz and Lasocki*, 2001]. At shallow depths, a moment tensor representing a closing horizontal tensile crack [*Day and McLaughlin*, 1991; *Bowers and Walter*, 2002] produces approximately the same waveforms as a single vertical force representing the downward motion of a crustal block [*Taylor*, 1994]. Below, we consider this mechanism for the special case of caldera collapse.

In Chapter 2, we describe 43 vertical-P earthquakes that took place at Miyakejima volcano. These earthquakes occurred between 7 July and 18 August 2000, and were associated with the ~40-day incremental collapse of the summit caldera, which began ~12 days after the start of a massive submarine dike intrusion between the volcano and Kozushima and Niijima islands. During most discrete collapse episodes, the downward motion of the caldera block produced very-long-period (VLP) earthquakes with deviatoric vertical-P moment tensors, and simultaneous outward tilt-steps [*Kikuchi et al*., 2001; *Kumagai et al*., 2001; *Ukawa et al*., 2000; *Yamamoto et al*., 2001]. There is a strong correlation between the caldera volume changes, the magnitudes of VLP earthquakes, and the amplitude of tilt-steps produced during individual caldera collapse episodes [*Michon et al.,* 2011]. Together the 43 vertical-P earthquakes have a combined scalar moment of ~5.1 x 10^{18} Nm. Assuming $\lambda = \mu = 3.0 \times 10^{10}$ N/m^2, these earthquakes are consistent with a closing subhorizontal tensile crack with a combined volume of

~6.4 x 10^7 m^3. The final volume of the Miyakejima's caldera is ~6 x 10^8 m^3 [*Geshi et al.,* 2002; *Nakada et al.,* 2005], so our estimate would represent only ~10% of the total volume change. However, this estimate is only based on collapse episodes that produced VLP signals, and does not include the initial and largest collapse episode that took place on 8 July. Given that λ may be significantly lower than 3.0 x 10^{10} N/m^2 in volcanic environments [*Rubin and Pollard*, 1987], it is possible that a source model resembling a closing subhorizontal tensile crack or downward single force could explain some characteristics of the Miyakejima earthquakes, and perhaps other shallow vertical-P earthquakes as well.

The opening and closing of tensile cracks is a physical mechanism that is most plausible for small earthquakes with depths in the upper few hundred meters of the crust. Due to overburden pressures, sizable voids cannot exist at depths greater than ~1 km, and high fluid pressures are required to open tensile cracks at greater depths [*Rubin,* 1995]. From teleseismic body-wave modeling, we know that some vertical-CLVD earthquakes have focal depths of ~4-8 km. Given the magnitudes, depths and source durations of the vertical-CLVD earthquakes, we consider the opening and closing of tensile cracks to be an unlikely physical mechanism for most events.

Volumetric Changes

Rapid volume changes can also produce seismic signals with deviatoric vertical-CLVD moment tensors. If the deforming reservoir has a sill-like or oblate ellipsoidal shape, the seismic radiation pattern will resemble a subhorizontal tensile crack [*Davi*s, 1986; *Fialko et al*., 2001; *Amoruso and Crescentini*, 2009]. We consider the rapid expansion or contraction of a sill-like magma chamber due to the injection of withdrawal of magma to be an unlikely mechanism for most

vertical-CLVD earthquakes due to the large magma volume fluxes that would be required to explain the observed magnitudes and source durations. For example, the M_W 5.8 vertical-T earthquake that took place in the Kermadec Islands on 17 February 2009 has a source duration of ~8 s (Table 3.1). A volume change of ~8 x 10^6 m^3 and, therefore, a magma volume flux of ~1 x 10^6 m^3/s, would be required to explain this earthquake using a physical mechanism consisting of an opening tensile crack. This estimate for the magma volume flux exceeds the estimated mass eruption rates for Pinatubo and Tambora [*Self,* 2012] and several flood-basalt eruptions [*Self et al*., 1998]. It is possible that some vertical-CLVD earthquakes are generated by volumetric changes of sill-like reservoirs filled with non-magmatic fluids. High-pressure hydrothermal fluids such as water or carbon dioxide have lower viscosities that would be consistent with faster volume fluxes. However, it is not clear why the injection or withdrawal of hydrothermal fluids should occur preferentially at volcanoes with low silica contents, or at volcanoes with caldera structures.

If the deforming reservoir is spherical, rapid volume changes can produce seismic signals that resemble spherical isotropic sources. As illustrated in Figure 3.6, vertical-P earthquakes may be consistent with sources that are predominantly explosive, whereas vertical-T earthquakes may be consistent with sources that are predominantly implosive. Just as we estimated the volume changes for tensile cracks, we can also estimate the isotropic volume changes that would be required to generate vertical-CLVD earthquakes with our observed scalar moments. As above, we use the minimum and maximum scalar moments, 3.8 x 10^{15} Nm – 6.5 x 10^{17} Nm, and calculate the Mogi volume changes using Equations 3.15 and 3.16 assuming $\lambda = \mu$ = 3.0 x 10^{10} N/m^2. The magnitudes of our vertical-CLVD earthquakes are consistent with spherical sources

with Mogi volumes ranging from ~4 x 10^4 m^3 to ~7 x 10^6 m^3, which is equivalent to spheres with radii between ~20 m and ~120 m. To explain the frequency content of our vertical-CLVD earthquakes, implosive processes would have to be faster than explosive processes. Since we believe it is unlikely that implosive processes would precede volcanic eruptions and explosive processes follow, we consider spherical isotropic source mechanisms unlikely to explain vertical-CLVD earthquakes.

3.4. Conclusions

Moderate-sized vertical-CLVD earthquakes are some of the most anomalous earthquakes to occur in volcanic systems. In Chapter 2, and *Nettles and Ekström* [1998] and *Shuler and Ekström* [2009], we identified 101 shallow vertical-CLVD earthquakes that occurred near active volcanoes. The majority of vertical-CLVD earthquakes are associated with basaltic and/or andesitic stratovolcanoes and submarine volcanoes located in subduction zones, although a small number of vertical-CLVD earthquakes are located in continental rifts, in areas of hotspot volcanism, and along mid-ocean ridges. Approximately 70% of vertical-CLVD earthquakes occur during episodes of volcanic unrest at nearby volcanoes, which suggests that these events are closely related to magma migration and eruption processes. Vertical-P earthquakes occur after the start of volcanic eruptions or episodes of unrest, whereas vertical-T earthquakes generally occur before volcanic eruptions.

In this study, we performed additional analysis of the teleseismic body waves of $5.1 \leq M_W \leq 5.8$ vertical-CLVD earthquakes and determined that these earthquakes have longer source durations than tectonic earthquakes of the same magnitude. We find that vertical-CLVD earthquakes from

the GCMT catalog have source durations up to ~10 s. We are unable to model any vertical-CLVD earthquakes detected only by analysis of surface waves [*Ekström*, 2006], but the inferred frequency contents of these earthquakes suggest that they have even longer source durations, up to approximately one minute. Most vertical-CLVD earthquakes identified originally from the GCMT catalog are vertical-T events and most vertical-CLVD earthquakes from the Surface Wave catalog are vertical-P events, leading us to infer that vertical-P earthquakes may have slower source processes than vertical-T events. Currently, it is unknown whether both types of vertical-CLVD earthquakes have a range of source durations extending from a few seconds to a few tens of seconds, or whether vertical-T and vertical-P earthquakes are produced by slightly different physical mechanisms that result in different frequency contents and source durations.

We also explored the possibility that the vertical-CLVD earthquakes may have significant non-zero isotropic components generated by net volume changes. We examined the covariance matrix of one of the best-recorded vertical-CLVD earthquakes to illustrate that, even for large earthquakes with excellent data coverage, there is a tradeoff between the isotropic and pure vertical-CLVD components of the moment tensor. As a result, many physical mechanisms can produce earthquakes with deviatoric vertical-CLVD moment tensors, including slip on ring faults, volume exchange between two reservoirs, the opening and closing of tensile cracks and volumetric changes.

We evaluated proposed physical mechanisms using additional constraints obtained from our detailed studies of vertical-CLVD earthquakes, and found that no single physical mechanism could explain all of our observations. In general, physical mechanisms involving only fluid

transport or volumetric changes seem unlikely to explain most vertical-CLVD earthquakes. Mechanisms involving isotropic volumetric changes cannot explain the temporal relationships between vertical-CLVD earthquakes and volcanic eruptions. Likewise, the source durations of vertical-CLVD earthquakes preclude mechanisms involving magma transport through tensile cracks. Even for basaltic or andesitic magmas, which have relatively low viscosities, the propagation velocities and volume fluxes required to explain our observations are physically implausible. It is possible that some vertical-CLVD earthquakes are caused by tensile cracks filled with less viscous hydrothermal fluids, such as water or carbon dioxide, although it is not clear why this mechanism should occur preferentially at basaltic stratovolcanoes and submarine volcanoes. In the special circumstance of caldera collapse, a mechanism resembling the closing of a subhorizontal tensile crack may explain the occurrence of vertical-CLVD earthquakes.

Ring-faulting mechanisms can explain many characteristics of vertical-CLVD earthquakes, including their anomalous seismic radiation patterns and source durations. The partial cancellation of long-period seismic moment that results from slip on curved fault structures can also explain why vertical-CLVD earthquakes near Smith Rock volcano are associated with disproportionately large tsunamis. Most vertical-CLVD earthquakes are associated with basaltic-to-andesitic volcanoes with calderas that are located in oceanic island arcs. Calderas with small dimensions, and therefore ring faults with small dimensions, are preferentially observed at volcanoes in these environments [*Sobradelo et al.*, 2010], and basaltic volcanoes erupt more frequently than silicic volcanoes [*White et al.,* 2006]. The geodynamic environments of the source volcanoes may thus explain why we have observed ~75 vertical-CLVD earthquakes with

$M_W \geq 5.0$ in the last ~35 years, yet we have not observed any vertical-CLVD earthquakes larger than M_W 5.8.

It remains difficult to interpret the deviatoric moment tensors of vertical-CLVD earthquakes in terms of specific ring-faulting scenarios. At Sierra Negra and Rabaul, two volcanoes with known ring faults, the patterns of ring-fault slip suggested by our deviatoric moment tensors do not match inferences from geodetic studies. Additionally, the plunges of the dominant stress axes and the ε values for vertical-CLVD earthquakes in Chapter 2 are consistent with ring faults with dip angles of ~50°-70°, though observations from field geology and models of caldera collapse suggest that ring faults are subvertical. These discrepancies cannot be explained by uncertainties in the CMT solutions alone.

The dip angles of volcano ring faults are not well constrained. Field studies of active calderas cannot constrain deep structures, and it is not clear that the surface expressions of ring faults are representative of deeper seismogenic zones. Similarly, the inferred geometries of ring faults outlined by microseismicity are dependent on local velocity models and seismic station distributions. Additionally, numerical and analog models of caldera collapse are simplified, and in most cases, the effects of heterogeneity, pre-existing faults, and magma intrusion and extrusion are not considered. Such factors may influence the stress field and affect the dip angles of the volcano ring faults. More work will be required to evaluate whether active volcanoes may have ring faults with shallower dip angles, consistent with our seismological observations.

Alternatively, vertical-CLVD earthquakes may be generated by a mechanism that is a hybrid of ring faulting and fluid flow. If dip-slip motion on ring faults is triggered by the inflation or deflation of a shallow magma chamber, rapid volume changes might contribute to the seismic wavefield and the recovered moment tensors. The tradeoff between the isotropic and pure vertical-CLVD components in CMT analysis means that, if we combine the moment tensors resulting from dip-slip motion on a steeply inward-dipping ring fault and either a closing tensile crack or an implosion, the composite moment tensor will fall close to the line in k-ε space that represents our solution space (Figure 3.6). If contributions from the isotropic component influence the deviatoric moment tensors we retrieve for vertical-CLVD earthquakes generated by ring faulting, it may not be possible to interpret the plunges and azimuths of the dominant stress axes and the ε values in terms of patterns of ring-fault slip without additional constraints.

Despite these ambiguities, it is clear that vertical-CLVD earthquakes are generated by large-scale deformation occurring inside the edifices and magmatic plumbing systems of active volcanoes. Vertical-T earthquakes are likely caused by inflation processes leading up to volcanic eruptions, whereas vertical-P earthquakes are likely caused by deflation processes that begin after the start of volcanic unrest. However, before vertical-CLVD earthquakes can be interpreted in terms of specific deformation processes at source volcanoes, it will be necessary to use other types of geophysical data, such as data from local seismic and GPS networks and interferograms, to constrain the precise physical mechanisms that generate vertical-CLVD earthquakes at individual volcanoes.

Concluding Remarks

In this dissertation, we investigated a rarely observed and poorly understood type of earthquake associated with volcanic centers. Using openly accessible global seismic data and two seismicity catalogs from the Global CMT Project, we were able to identify 91 shallow vertical-CLVD earthquakes located near volcanoes. By studying the source parameters and characteristics of these earthquakes, as well as their temporal relationships to volcanic unrest, we were able to gain insight into how these events are linked to deformation occurring inside the edifices or magmatic plumbing systems of active volcanoes. Below, we summarize our major findings by chapter and discuss a number of outstanding research questions.

In Chapter 1, we examined a series of five earthquakes that took place near Nyiragongo volcano in the Democratic Republic of the Congo between 2002 and 2005. Compared to tectonic earthquakes with similar magnitudes and locations, we find that these earthquakes are depleted in high-frequency energy, which prevented them from being detected using traditional methods. We find that each earthquake can be modeled using a time-varying force model consisting of an upward force followed by a downward force, which is typical for a collapse event. However, unrealistically large vertical forces are required to generate seismic events with the observed magnitudes. We find that better fits to the data can be achieved with vertical-P moment tensors. The first three earthquakes occurred days after a regional rifting episode ruptured the edifice of the volcano, resulting in a fissure eruption that inundated the city of Goma, ~20 km away. Hours after these three earthquakes, the summit crater collapsed ~600 m. We interpret these events as slip on inward-dipping ring faults triggered by the deflation of an underlying shallow magma chamber. The final two earthquakes took place one and three years later, respectively, when the

lava lake in Nyiragongo's summit crater was refilling. These events can be explained using a similar mechanism, in which magma ascent into shallow levels of the magmatic plumbing system triggers the collapse of a deeper magma reservoir. Depending on the size and geometry of the ring faults, displacements on the order of centimeters to meters are required to generate the observed vertical-P earthquakes.

In Chapter 2, we performed a systematic global search for shallow vertical-CLVD earthquakes located near volcanoes with documented eruptions in the last ~100 years. Of the nearly 400 target earthquakes investigated from the Global CMT catalog and the Surface Wave catalog of *Ekström* [2006], we identified 86 earthquakes with robust vertical-CLVD focal mechanisms. All of these earthquakes have shallow depths, and ~80% are located within 30 km of a volcano. The majority of vertical-CLVD earthquakes are associated with stratovolcanoes and submarine volcanoes in subduction zones, although a small number of events are associated with volcanoes located in continental rifts, along mid-ocean ridges, and above mantle plumes. Vertical-CLVD earthquakes occur preferentially at volcanoes with caldera structures, and at volcanoes that erupt magmas with low silica contents.

Half of all vertical-CLVD earthquakes are associated with caldera collapse at Miyakejima in 2000, and another 20% are associated with documented episodes of unrest at other volcanoes. Vertical-CLVD earthquakes are associated with effusive and explosive eruptions as well as anomalous tsunamis and submarine seismic swarms. Vertical-P earthquakes occur hours to years after the start of volcanic unrest, and vertical-T earthquakes occur before and after the start of eruptive activity. Our results suggest that vertical-P earthquakes may be useful for identifying

volcanoes where eruptions or large-scale magmatic intrusions have recently occurred, whereas vertical-T earthquakes may signal that a particular volcano is likely to erupt in the future. Given that volcanic unrest is underreported, we suspect that most vertical-CLVD earthquakes are related to some type of volcanic unrest. We observe series of vertical-T earthquakes at Zavodovski and an Unnamed volcano in the Tonga Islands. These volcanoes have no confirmed eruptions in the last ~80-200 years, but we suspect that the earthquakes may be indicative of magma ascent and increased potential for future eruptions, as at Bárdarbunga [*Nettles and Ekström*, 1998].

In Chapter 3, we explored the physical mechanisms that generate vertical-CLVD earthquakes at active volcanoes. In order to obtain further constraints on source processes, we performed several types of additional analysis. We attempted to model the body waves for the largest vertical-CLVD earthquakes and found we were only able to model 18 earthquakes, all of which are reported in the Global CMT catalog. These vertical-CLVD earthquakes have source durations of up to ~10 seconds, longer than tectonic earthquakes of the same magnitude. Vertical-CLVD earthquakes from the Surface Wave catalog likely have even longer source processes as they are depleted in high-frequency energy. As most vertical-T earthquakes are included in the Global CMT catalog and most vertical-P earthquakes are reported only in the Surface Wave catalog, we can infer that, on average, vertical-T earthquakes have faster source processes than vertical-P earthquakes. It is not clear why these two types of vertical-CLVD earthquakes have different frequency contents and source durations.

Additionally, we examined the magnitude distributions of vertical-CLVD earthquakes, and found that vertical-CLVD earthquakes do not follow the Gutenberg-Richter frequency-magnitude distribution with the global average *b*-value of 1.0. Whereas we have documented ~75 earthquakes with $M_W \geq 5.0$, there are no reported cases of volcanic vertical-CLVD earthquakes larger than M_W 5.8. This may indicate that there is a limiting factor on the source size for these earthquakes.

In Chapters 1 and 2, we defined vertical-CLVD earthquakes by the properties of their deviatoric moment tensors. However, as earthquakes with significant isotropic components have been observed in volcanic regions, we explored the possibility that vertical-CLVD earthquakes may have net volume changes. Through an examination of the covariance matrix for one of the best-recorded vertical-CLVD earthquakes, we confirmed that the isotropic and pure vertical-CLVD components cannot be independently resolved using long-period seismic data. Full moment-tensor solutions for vertical-CLVD earthquakes further demonstrated the tradeoff between isotropic and vertical-CLVD components, revealing that several different physical mechanisms can account for the anomalous seismic radiation patterns of vertical-CLVD earthquakes. We evaluated a range of potential physical mechanisms including dip-slip motion along ring faults, volume-exchange processes, opening and closing of tensile cracks and volumetric sources. Of these, only the ring-faulting mechanism can explain the observed source durations (~60 s or less) and the temporal relationships between vertical-CLVD earthquakes and volcanic unrest.

Ring faults are curved dip-slip faults that form as a result of inflation and deflation of shallow magma chambers. Motion along ring faults can produce vertical-CLVD earthquakes with source

parameters that depend on the geometry and kinematics of the ring fault, as well as the scale of rupture. Vertical-T earthquakes are caused by slip on curved reverse faults, and vertical-P earthquakes are caused by slip on curved normal faults. The magnitude of the non-double-couple component, the plunge of the dominant stress axis and the cancellation of long-period seismic moment are influenced by the dip angle of the ring fault and the arc angle of rupture. The rupture velocity along ring faults may be affected by unusual frictional and mechanical properties associated with nearby high-temperature magma bodies or hydrothermal fluids.

The ring-faulting model can explain many characteristics of vertical-CLVD earthquakes, including their anomalous seismic radiation patterns and frequency contents, and their temporal relationship to volcanic unrest. According to *Sobradelo et al.* [2010], the smallest calderas, and therefore the smallest ring faults, are formed at volcanoes that erupt magmas with low-silica contents, and at volcanoes located in oceanic crust or in Mariana-type subduction zones. Most of the source volcanoes for vertical-CLVD earthquakes meet these conditions, and this could explain why we do not observe $M_W \geq 6.0$ vertical-CLVD earthquakes.

The ring-faulting model cannot explain all of our observations, however. For example, it is difficult to interpret the source parameters of vertical-CLVD earthquakes directly in terms of specific faulting patterns. The deviatoric CMT solutions for vertical-CLVD earthquakes are consistent with slip on ring-fault structures dipping ~50-70º, whereas field geology studies, as well as analog and numerical models of caldera collapse suggest that most ring faults are subvertical. Also, as demonstrated for Sierra Negra and Rabaul, the source parameters of some vertical-CLVD earthquakes also appear inconsistent with geological and geophysical

observations of deformation. These differences cannot be explained by uncertainties in our CMT solutions.

If vertical-CLVD earthquakes are caused solely by slip on ring faults, our results suggest that these structures may be less steep than expected from field geology and modeling of caldera collapse. This possibility cannot be ruled out, as the dip angles of ring faults are poorly constrained. At active volcanoes, ring faults are often covered by lava and pyroclastic flows or crater lakes, and deep structures cannot be observed at the surface. Likewise, the dip angles of ring faults determined from microseismicity structures are dependent on the chosen velocity model and the azimuthal distribution of local seismic stations. Analog and numerical models are often oversimplified, and do not consider the effects of magma intrusion and extrusion, heterogeneity and pre-existing structures. Better constraints on the dip angles of ring faults would allow us to assess the ring-faulting model more thoroughly.

Alternatively, vertical-CLVD earthquakes may be generated by a mechanism that is a hybrid of ring faulting and fluid flow. If dip-slip motion on ring faults is triggered by rapid inflation and deflation of shallow magma chambers, net volume changes may influence the deviatoric moment-tensor solutions we retrieve. In the special case of caldera collapse, vertical-CLVD earthquakes may also be generated by a mechanism resembling the closing of subhorizontal tensile cracks.

Although our work suggests that vertical-T earthquakes are likely caused by inflation processes leading up to volcanic eruptions, and vertical-P earthquakes are likely caused by deflation

processes that occur after the start of volcanic unrest, it is currently not possible to interpret these earthquakes in terms of specific deformation processes. Multidisciplinary studies using complementary data, such as local seismic, GPS, and InSAR data, will be required to determine the physical mechanisms that produce vertical-CLVD earthquakes in specific locations. In the future, the occurrence of vertical-CLVD earthquakes may be combined with other data to assess hazards at source volcanoes.

References

Abe, K. (1988), Tsunami magnitude and the quantification of earthquake tsunamis around Japan, *Bull. Earthquake Res. Inst. Univ. Tokyo, 63*, 289-303.

Acocella, V. (2006), Caldera types: How end-members relate to evolutionary stages of collapse, *Geophys. Res., Lett., 33*, L18314, doi:10.1029/2006GL027434.

Acocella, V. (2007), Understanding caldera structure and development: An overview of analogue models compared to natural calderas, *Earth-Science Reviews, 85*, 125-160.

Acocella, V. (2008), Structural Development of Calderas: A Synthesis from Analogue Experiments, in *Caldera Volcanism: Analysis, Modelling and Response*, Developments in Volcanology, vol. 10, edited by J. Gottsman and J. Marti, pp. 285-311, Elsevier, Amsterdam.

Acocella, V., Cifelli, F., and R. Funiciello (2000), Analogue models of collapse calderas and resurgent domes, *J. Volcanol. Geotherm. Res*., 104, 81-96.

Aiuppa, A., and C. Federico (2004), Anomalous magmatic degassing prior to the 5th April 2003 paroxysm on Stromboli, *Geophys. Res. Lett., 31*, L14607, doi:10.1029/2004GL020458.

Aizawa, K., Acocella, V., and T. Yoshida (2006), How the development of magma chambers affects collapse calderas: insights from an overview, in *Mechanisms of Activity and Unrest at Large Calderas*, Geological Society of London Special Pub., vol. 269, edited by C. Troise, G. De Natale, and C. R. J. Kilburn, pp.65-81, Geological Society, London.

Aki, K. (1984), Evidence for magma intrusion during the Mammoth Lakes earthquakes of May 1980 and implications of the absence of volcanic (harmonic) tremor, *J. Geophys. Res., 89*, 7689-7696.

Aki, K., and P. G. Richards (2002), *Quantitative Seismology*, 2nd ed., University Science Books, Sausalito, CA.

Allard, P. (2009), A CO_2-rich gas trigger of explosive paroxysms at Stromboli basaltic volcano, Italy, *J. Volcanol. Geotherm. Res., 189*, 363-374.

Allard, P., Baxter, P., Halbwachs, M., and J.-C. Komorowski (2002), The January 2002 Eruption of Nyiragongo Volcano (Dem. Repub. Congo) and related hazards: observations and recommendations, Final Report of the French-British Scientific Team: submitted to the Ministry of Foreign Affairs, Paris, France, Foreign Office, London, United Kingdom, and respective embassies in Democratic Republic of Congo and Republic of Rwanda, pp. 1-24.

Amelung, F., Jónsson, S., Zebker, H., and P. Segall (2000), Widespread uplift and 'trapdoor' faulting on Galápagos volcanoes observed with radar interferometry, *Nature, 407*, 993-996.

Amma-Miyasaka, M., Nakagawa, M., and S. Nakada (2005), Magma plumbing system of the 2000 eruption of Miyakejima Volcano, Japan, *Bull. Volcanol., 67*, 254-267, doi:10.1007/s00445-004-0408-0.

Amoruso, A., and L. Crescentini (2009), Shape and volume change of pressurized ellipsoidal cavities from deformation and seismic data, *J. Geophys. Res., 114*, B02210, doi:10.1029/2008JB005946.

Anderson, E. M. (1936), The Dynamics of the Formation of Cone-sheets, Ring-dykes, and Caldron-subsidences, *Proc. R. Soc. Edinburgh, 56*(2), 128-157.

Arellano, S. R., Mall, M., Samaniego, P., Le Pennec, J.-L., Ruiz, A., Molina, I., and H. Yepes (2008), Degassing patterns of Tungurahua volcano (Ecuador) during the 1999-2006 eruptive period, inferring from remote spectroscopic measurements of SO2 emissions, *J. Volcanol. Geotherm. Res., 176*, 151-162, doi:10.1016/j.jvolgeores.208.07.007.

Arvidsson, R., and G. Ekström (1998), Global CMT Analysis of Moderate Earthquakes, $M_W \geq$ 4.5, Using Intermediate-Period Surface Waves, *Bull. Seism. Soc. Am., 88*(4), 1003-1013.

Bai, C.-Y., and S. Greenhalgh (2005), 3D multi-step travel time tomography: Imaging the local, deep velocity structure of Rabaul volcano, Papua New Guinea, *Phys. Earth Planet. Inter., 151*, 259-275.

Bailey, D. K. (1993), Carbonate magmas, J. Geolog. Soc. London, 150, 637-651, doi:10.1144/gsjgs.150.4.0637.

Barba, D., Arellano, S., Ramon, P., Mothes, P., Alvarado, A., Ruiz, G., and L. Troncoso (2006), Cronologia de los Eventos Eruptivos de Julio y Agosto del 2006 del Volcan Tungurahua, Resumenes extendidos de las 6th Jornadas en Ciencias de la Tierra, EPN-DG, Quito, Ecuador, pp. 177-180.

Bassin, C., Laske, G., and G. Masters (2000), The current limits of resolution for surface wave tomography in North America, *Eos Trans. AGU, 81*(48), Fall. Meet. Suppl., Abstract T31B-1820.

Beresnev, I. A. (2002), Source parameters observable from the corner frequency of earthquake spectra, *Bull. Seism. Soc. Am., 92*(5), 2047–2048.

Bertagnini, A., Métrich, N., Landi, P., and M. Rosi (2003), Stromboli volcano (Aeolian Archipelago, Italy): An open window on the deep-feeding system of a steady state basaltic volcano, *J. Geophys. Res., 108*(B7), 2336, doi:10.1029/2002JB002146.

Bird, P. (2003), An updated digital model of plate boundaries, *Geochem. Geophys. Geosys., 4*(3), doi:10.1029/2001GC000252.

Bowers, D., and W. R. Walter (2002), Discriminating Between Large Mine Collapses and Explosions Using Teleseismic P Waves, *Pure Appl. Geophys., 159*, 803-830.

Burchardt, S., and T. R. Walter (2010), Propagation, linkage, and interaction of caldera ring-faults: comparison between analogue experiments and caldera collapse at Miyakejima, Japan, in 2000, *Bull. Volcanol., 72*, 297-308, doi:10.1007/s00445-009-0321-7.

Burov, E. B., and L. Guillou-Frottier (1999), Thermomechanical behavior of large ash flow calderas, *J. Geophys. Res., 104*(B10), 23,081-23,109.

Calder, E. S., Luckett, R., Sparks, R. S. J., and B. Voight (2002), Mechanisms of lava dome instability and generation of rockfalls and pyroclastic flows at Soufrière Hills Volcano, Montserrat, in *The Eruption of Soufrière Hills Volcano, Montserrat, from 1995 to 1999*, edited by T. H. Druitt and B. P. Kokelaar, pp. 173-190, Geological Society, London.

Calvari, S., Spampinato, L., and L. Lodato (2006), The 5 April 2003 vulcanian paroxysmal explosion at Stromboli volcano (Italy) from field observations and thermal data, *J. Volcanol. Geotherm. Res., 149*, 160-175.

Caplan-Auerbach, J., and F. K. Duennebier (2001), Seismicity and Velocity Structure of Loihi Seamount from the 1996 Earthquake Swarm, *Bull. Seism. Soc. Am., 91*(2), 178-190.

Carapezza, M. L., Inguaggiato, S., Brusca, L., and M. Longo (2004), Geochemical precursors of the activity of an open-conduit volcano: The Stromboli 2002-2003 eruptive events, *Geophys. Res. Lett., 31*, L07620, doi:10.1029/2004GL019614.

Carn, S. A. (2002/2003), Eruptive and passive degassing of sulphur dioxide at Nyiragongo Volcano (D.R. Congo): The 17 January 2002 eruption and its aftermath, *Acta Vulcanologica, 14/15*(1–2), 75–86.

Carn, S. A., Kruegger, A. J., Krotkov, N. A., Arellano, S., and K. Yang (2008), Daily monitoring of Ecuadorian volcanic degassing from space, *J. Volcanol. Geotherm. Res., 176*(1), 151-162.

Cesca, S., Braun, T. Tessmer, E., and T. Dahm (2007), Modelling of the April 5, 2003, Stromboli (Italy) paroxysmal eruption from the inversion of broadband seismic data, *Earth Planet. Sci. Lett., 261*, 164-178.

Chadwick, W. W., Geist, D. J., Jónsson, S., Poland, M., Johnson, D. J., and C. M. Meertens (2006), A volcano bursting at the seams: Inflating, faulting, and eruption at Sierra Negra volcano, Galápagos, *Geology, 34*(12), 1025-1028, doi:10.1130/G22826A.1.

Chadwick, W. W., Cashman, K. V., Embley, R. W., Matsumoto, H., Dziak, R. P., de Ronde, C. E. J., Lau, T. K., Deardorff, N. D., and S. G. Merle (2008), Direct video and hydrophone observations of submarine explosive eruptions at NW Rota-1 volcano, Mariana arc, *J. Geophys. Res., 113*, B08S10, doi:10.1029/2007JB005215.

Chadwick, W. W., Dziak, R. P., Haxel, J. H., Embley, R. W., and H. Matsumoto (2012), Submarine landslide triggered by volcanic eruption recorded by in situ hydrophone, *Geology, 40*(1), doi:10.1130/G32495.1.

Chouet, B. A. (1996), New Methods and Future Trends in Seismological Volcano Monitoring, in *Monitoring and Mitigation of Volcano Hazards*, edited by R. Scarpa and R. I. Tilling, pp. 23-97, Springer-Verlag, Berlin.

Chouet, B., Dawson, P., Ohminato, T., Martini, M., Saccorotti, G., Giudicepietro, F., De Luca, G., Milana, G., and R. Scarpa (2003), Source mechanisms of explosions at Stromboli Volcano, Italy, determined from moment-tensor inversions of very-long-period data, *J. Geophys. Res*., *108*(B1), 2019, doi:10.1029/2002JB001919.

Cole, J. W., Milner, D. M., and K. D. Spinks (2005), Calderas and caldera structures: a review, *Earth-Science Reviews, 69*, 1-26.

D'Auria, L., Giudicepietro, F., Martini, M., and R. Peluso (2006), Seismological insights into the kinematics of the 5 April 2003 vulcanian explosion at Stromboli volcano (southern Italy), *Geophys. Res. Lett., 33*, L08308, doi:10.1029/2006GL026018.

Davis, P. M. (1986), Surface deformation due to inflation of an arbitrarily oriented triaxial ellipsoidal cavity in an elasatic half-space, with reference to Kilauea Volcano, Hawaii, *J. Geophys. Res., 91*, 7429-7438.

Davis, A. S., and D. A. Clague (1998), Changes in the hydrothermal system at Loihi Seamount after the formation of Pele's pit in 1996, *Geology, 26*(5), 399-402.

Day, S. M., and K. L. McLaughlin (1991), Seismic Source Representations for Spall, *Bull. Seism. Soc. Am., 81*(1), 191-201.

de Bromand d'Ars, J., Jaupart, C., and R. S. J. Sparks (1995), Distribution of volcanoes in active margins, *J. Geophys. Res., 100*(B10), 20,421-20,432, doi:10.1029/95JB02153.

De Natale, G., and F. Pingue (1993), Ground deformations in collapsed caldera structures, *J. Volanol. Geotherm. Res., 57*, 19-38.

Demant, A., Lestrade, P., Lubala, R. T., Kampunzu, A. B., and J. Durieux (1994), Volcanological and petrological evolution of Nyiragongo volcano, Virunga volcanic field, Zaire, *Bull. Volcanol., 56*, 47-61.

Doyle, A. C., Singleton, R. J., and J. C. Yaldwyn (1979), Volcanic activity and recent uplift on Curtis and Cheeseman Islands, Kermadec Group, Southwest Pacific, *J. Royal Soc. New Zealand, 9*(1), 123-140.

Dreger, D. S. (2000), Dilatational Processes Accompanying Earthquakes in the Long Valley Caldera, *Science, 228*(122), doi:10.1126/science.288.5463.122.

Druitt, T. H., and R. S. J. Sparks (1984), On the formation of calderas during ignimbrite eruptions, *Nature, 310*(23), 679-681.

Druitt, T. H., Calder, E. S., Cole, P. D., Hoblitt, R. P., Loughlin, S. C., Norton, G. E., Ritchie, L. J., Sparks, R. S. J., and B. Voight (2002), Small-volume, highly mobile pyroclastic flows formed by rapid sedimentation from pyroclastic surges at Soufrière Hills Volcano, Montserrat: an important volcanic hazard, in *The Eruption of Soufrière Hills Volcano, Montserrat, from 1995 to 1999*, edited by T. H. Druitt and B. P. Kokelaar, pp. 263-279, Geological Society, London.

Duennebier, F. K., Becker, N. C., Caplan-Auerbach, J., Clague, D. A., Cowen, J., Cremer, M., Garcia, M., Goff, F., Malahoff, A., McMurtry, G. M., Midson, B. P., Moyer, C. L., Norman, M., Okubo, P., Resing, J. A., Rhodes, J. M., Rubin, K., Sansone, F. J., Smith, J. R., Spencer, K., Wen, X., and C. G. Wheat (1997), Researchers Rapidly Respond to Submarine Activity at Loihi Volcano, *Hawaii, EOS, Trans. AGU, 78*(22), 229-233.

Dufumier, H., and L. Rivera (1997), On the resolution of the isotropic component in moment tensor inversion, *Geophys. J. Int., 131*, 595-606.

Durieux, J. (2002/2003a), Volcano Nyiragongo (D.R. Congo): evolution of the crater and Lava lakes from the discovery to the present., *Acta Vulcanologica, 14/15*(1–2), 137–144.

Durieux, J. (2002/2003b), Nyiragongo: the January 10th 1977 eruption, *Acta Vulcanologica 14/15*(1–2), 145–148.

Dziewonski, A. M., and D. L. Anderson (1981), Preliminary reference Earth model, *Phys. Earth Planet. Inter., 25*(4), 297-356.

Dziewonski, A. M., and J. H. Woodhouse (1983), An Experiment in Systematic Study of Global Seismicity: Centroid-Moment Tensor Solutions for 201 Moderate and Large Earthquakes of 1981, *J. Geophys. Res., 88*(B4), doi:10.1029/JB088iB04p03247.

Dziewonski, A. M., Chou, T.-A., and J. H. Woodhouse (1981), Determination of Earthquake Source Parameters From Waveform Data for Studies of Global and Regional Seismicity, *J. Geophys. Res., 86*(B4), 2825-2852.

Dziewonski, A. M., Friedman, A., Giardini, D., and J. H. Woodhouse (1983), Global seismicity of 1982: centroid-moment tensor solutions for 308 earthquakes, *Phys. Earth Planet. Inter., 33*, 76-90.

Dziewonski A. M., Franzen, J. E., and J. H. Woodhouse (1984), Centroid-moment tensor solutions for January-March 1984, *Phys. Earth Planet. Inter, 34*, 209-219.

Dziewonski, A. M., Ekström, G., and M. Nettles (1997), Harvard centroid-moment tensor solutions 1976-96: Significance of the non-double-couple component, in *Rockbursts and Seismicity in Mines*, edited by S. J. Gibowicz and S. Lasocki, pp. 3-16, A. A. Balkema, Brookfield, VT.

Ebinger, C., and T. Furman (2002/2003), Geodynamical setting of the Virunga Volcanic Province, East Africa, *Acta Vulcanologica, 14/15*(1–2), 9–16.

Ekström, G. (1989), A very broad band inversion method for the recovery of earthquake source parameters, *Tectonophysics, 166*, 73-100.

Ekström, G. (1994), Anomalous earthquakes on volcano ring-fault structures, *Earth Planet. Sci. Lett., 128*, 707-712.

Ekström, G. (2006), Global Detection and Location of Seismic Sources by Using Surface Waves, *Bull. Seism. Soc. Am., 96*(4A), 1201-1212, doi:10.1785/0120050175.

Ekström, G. (2007), Seismological detection and analysis of recent landslides in Alaska and the Yukon. *Eos. Trans. AGU, 88*, Fall Meeting Suppl., Abstract S52B-05.

Ekström, G., and A. M. Dziewonski (1983), Moment tensor solutions of Mammoth Lakes earthquakes (abstract), *Eos Trans. AGU, 64*, 262.

Ekström, G., and M. Nettles (2002), Detection and location of slow seismic sources using surface waves, *Eos Trans. AGU, 83*(47), Fall Meet. Suppl., Abstract S72E-06.

Ekström, G., Stein, R. S., Eaton, J. P., and D. Eberhart-Philipps (1992), Seismicity and Geometry of a 110-km-Long Blind Thrust Fault 1. The 1985 Kettleman Hills, California, Earthquake, *J. Geophys. Res., 97*(B4), 4843-4864.

Ekström, G., Nettles, M., and G.A. Abers (2003), Glacial earthquakes, *Science, 302*, 622–624.

Ekström, G., Dziewonski, A. M., Maternovskaya, N. N., and M. Nettles, M., (2005), Global seismicity of 2002: centroid-moment-tensor solutions for 1034 earthquakes *Phys. Earth Planet. Inter.,148*(2-4), 303–326.

Ekström, G., Dziewonski, A. M., Maternovskaya, N. N., and M. Nettles (2005), Global seismicity of 2003: centroid-moment-tensor solutions for 1087 earthquakes. *Phys. Earth Planet. Inter., 148*(2-4), 327-351, doi:10.1016/j.pepi.2004.09.006.

Ekström, G., Nettles, M., and A. M. Dziewonski (2012), The global CMT project 2004-2010: Centroid-moment tensors for 13,017 earthquakes, *Phys. Earth Planet. Inter., 200-201*, 1-9, doi:10.1016.j.pepi.2012.04.002.

Embley, R. W., Chadwick, W. W., Baker, E. T., Butterfield, D. A., Resing, J. A., de Ronde, C. E. J., Tunnicliffe, V., Lupton, J. E., Juniper, S. K., Rubin, K. H., Stern, R. J., Lebon, G. T., Nakamura, K., Merle, S. G., Hein, J. R., Wiens, D. A., and Y. Tamura (2006), Long-term eruptive activity at a submarine arc volcano, *Nature, 441*, 494-497, doi:10.1038/nature04762.

Fee, D., Garces, M., and A. Steffke (2010), Infrasound from Tungurahua Volcano 2006-2008: Strombolian to Plinian eruptive activity, *J. Volcanol. Geotherm. Res., 193*, 67-81, doi:10.1016/j.jvolgeores.2010.03.006.

Fialko, Y., Khazan, Y., and M. Simons (2001), Deformation due to a pressurized horizontal circular crack in an elastic half-space, with applications to volcano geodesy, *Geophys. J. Int., 146*, 181-190.

Filson, J., Simkin, T., and L.-K. Leu (1973), Seismicity of a Caldera Collapse: Galapagos Islands 1968, *J. Geophys. Res., 78*(35), 8591-8622.

Finlayson, D. M., Gudmundsson, O., Itikarai, I., Nishimura, Y., and H. Shimamura (2003), Rabaul volcano, Papua New Guinea: seismic tomographic imaging of an active caldera, J. Volcanol. Geotherm. Res., 124, 153-171.

Folch, A., and J. Marti (2004), Geometrical and mechanical constraints on the formation of ring-fault calderas, *Earth Planet. Sci. Lett., 221*, 215-225.

Ford, S. R., Dreger, D. S., and W. R. Walter (2008), Source Characterization of the 6 August 2007 Crandall Canyon Mine Seismic Event in Central Utah, *Seism. Res. Lett., 79*(5), 637-644, doi:10.1785/gssrl.79.5.637.

Foulger, G. R., and B. R. Julian (1993), Non-double-couple earthquakes at the Hengill-Grensdalur Volcanic Complex, Iceland: Are they artifacts of crustal heterogeneity? *Bull. Seism. Soc. Am., 83*(1), 38-52.

Foulger, G. R., Julian, B. R., Hill, D. P., Pitt, A. M., Malin, P. E., and E. Shalev (2004), Non-double-couple microearthquakes at Long Valley caldera, California, provide evidence for hydraulic fracturing, *J. Volcanol. Geotherm. Res., 132*, 45-71.

Francalanci, L., Bertagnini, A., Métrich, N., Renzulli, A., Vannucci, R., Landi, P., Del Moro, S., Menna, M., Petrone, C. M., and I. Nardini (2008), Mineralogical, Geochemical, and

Isotopic Characteristics of the Ejecta From the 5 April 2003 Paroxysm at Stromboli, Italy: Inferences on the Preeruptive Magma Dynamics, in *The Stromboli Volcano: An Integrated Study of the 2002-2003 Eruption*, edited by S. Calvari, S. Inguaggiato, G. Puglisi, M. Ripipe, and M. Rosi, pp. 331-345, AGU, Washington, D. C.

Francis, T. J. G. (1974), A New Interpretation of the 1968 Fernandina Caldera Collapse and its Implications for the Mid-Oceanic Ridges, *Geophys. J. R. Astr. Soc., 39*, 301-318.

Frohlich, C. (1989), Note Concerning Possible Mechanisms for Non-Double-Couple Earthquake Sources, *Geophys. Res. Lett., 16*(6), 523-526.

Frohlich, C. (1990a), Earthquakes with Non-Double-Couple Mechanisms, *Science, 264*, 804-809.

Frohlich, C. (1990b), Note Concerning Non-Double-Couple Source Components From Slip Along Surfaces of Revolution, *J. Geophys. Res., 95*(B5), 6861-6866.

Frohlich, C. (1995), Characteristics of well-determined non-double-couple earthquakes in the Harvard CMT catalog, *Phys. Earth Planet. Inter., 21*(4), 213-228, doi:10.1016/0031-9201(95)03031-Q.

Frohlich, C., and S. D. Davis (1993), Teleseismic *b* values; Or, Much Ado About 1.0*, J. Geophys. Res., 98*(B1), 631-644.

Fujita, E., Ukawa, M., Yamamoto, E., Okada, Y., and M. Kikuchi (2001), Volcanic Earthquakes and Tremors Associated with the 2000 Miyakejima Volcano Eruption (in Japanese with English abstract), *J. Geogr., 110*(2), 191-203.

Fujita, E., Ukawa, M., Yamamoto, E., and Y. Okada (2002), Cyclic jerky opening of magma sheet and caldera formation during the 2000 Miyakejima volcano eruption, *Geophys. Res. Lett., 29*(9), 1326, doi:10.1029/2001GL013848.

Fujita, E., Ukawa, M., and E. Yamamoto (2004), Subsurface cyclic magma sill expansions in the 2000 Miyakejima volcano eruption: Possibility of two-phase flow oscillation, *J. Geophys. Res., 109*, B04205, doi:10.1029/2003JB002556.

Fukao, Y. (1995), Single-force representation of earthquakes due to landslides or the collapse of caverns, *Geophys. J. Int., 122,* 243–248.

Furuya, M., Okubo, S., Sun, W., Tanaka, Y., Oikawa, J., and H. Watanabe (2003), Spatiotemporal gravity changes at Miyakejima Volcano, Japan: Caldera collapse, explosive eruptions and magma movement, *J. Geophys. Res., 108*(B4), 2219, doi:10.1029/2002JB001989.

Garcia, M. O., Rubin, K. H., Norman, M. D., Rhodes, J. M., Graham, D. W., Muenow, D. W., and K. Spencer (1998), Petrology and geochronology of basalt breccia from the 1996

earthquake swarm of Loihi seamount, Hawaii: magmatic history of its 1996 eruption, *Bull. Volcanol., 59*, 577-592.

Garcia, M. O., Caplan-Auerbach, J., De Carlo, E. H., Kurz, M. D., and N. Becker (2006), Geology, geochemistry and earthquake history of Loihi Seamount, Hawaii's youngest volcano, *Chemie der Erde, 66*, 81-108.

Geist, D. J., Harpp, K. S., Naumann, T. R., Poland, M., Chadwick, W. W., Hall, M., and E. Rader (2008), The 2005 eruption of Sierra Negra volcano, Galápagos, Ecuador, *Bull. Volcanol., 70*, 655-673, doi:10.1007/s00445-007-0160-3.

Geshi, N. (2009), Asymmetric growth of collapsed caldera by oblique subsidence during the 2000 eruption of Miyakejima, Japan, *Earth Planet. Sci. Lett., 280*, 149-158.

Geshi, N., and T. Oikawa (2008), Phreatomagmatic eruptions associated with the caldera collapse during the Miyakejima 2000 eruption, Japan, *J. Volcanol. Geotherm. Res., 176*, 457-468.

Geshi, N., Shimano, T., Chiba, T., and S. Nakada (2002), Caldera collapse during the 2000 eruption of Miyakejima Volcano, Japan, *Bull. Volcanol., 64*, 55-68, doi:10.1007/s00445-001-0184-z.

Geyer, A., and J. Gottsman (2010), The influence of mechanical stiffness on caldera deformation and implications for the 1971-1984 Rabaul uplift (Papua New Guinea), *Tectonophysics, 483*, 399-412.

Geyer, A., and J. Marti (2008), The new worldwide collapse caldera database (CCDB): A tool for studying and understanding caldera processes, *J. Volcanol. Geotherm. Res., 175*, 334-354, doi:10.1016/j.jvolgeores.2008.03.017.

Geyer, A., Folch, A., and J. Marti (2006), Relationship between caldera collapse and magma chamber withdrawal: An experimental approach, *J. Volcanol. Geotherm. Res., 157*, 375-386.

Gibowicz, S. J., and S. Lasocki (2001), Seismicity Induced by Mining: Ten Years Later, *Adv. Geophys., 44*, 39-181.

Gray, J. P., and J. J. Monaghan (2004), Numerical modeling of stress fields and fracture around magma chambers, *J. Volcanol. Geotherm. Res., 135*, 259-283.

Gudmundsson, A. (1988), Formation of collapse calderas, *Geology, 16*, 808-810.

Gudmundsson, A. (1998), Formation and development of normal-fault calderas and the initiation of large explosive eruption, *Bull. Volcanol., 60*, 160-170.

Gudmundsson, A. (2007), Conceptual and numerical models of ring-fault formation, *J. Volcanol. Geotherm. Res., 164*, 142-160.

Gudmundsson, A. (2008), Magma-Chamber Geometry, Fluid Transport, Local Stresses and Rock Behavior During Collapse Caldera Formation, in *Caldera Volcanism: Analysis, Modelling and Response*, Developments in Volcanology, vol. 10, edited by J. Gottsman and J. Marti, pp. 313-349, Elsevier, Amsterdam.

Gudmundsson, A., and K. Nilsen (2006), Ring-faults in composite volcanoes: structures, models and stress fields associated with their formation, in *Mechanisms of Activity and Unrest at Large Calderas*, Geological Society of London Special Pub., vol. 269, edited by C. Troise, G. De Natale, and C. R. J. Kilburn, pp.83-108, Geological Society, London.

Gudmundsson, A., Marti, J., and E. Turon (1997), Stress fields generating ring faults in volcanoes, *Geophys. Res. Lett., 24*(13), 1559-1562.

Gudmundsson, M. T., Sigmundsson, F., and H. Björnsson (1997), Ice-volcano interaction of the 1996 Gjálp subglacial eruption, Vatnajökull, Iceland, *Nature, 389*, 954-957, doi:10.1038/40122.

Gutenberg, B., and C. F. Richter (1944), Frequency of earthquakes in California, *Bull. Seism. Soc. Am., 34,* 185-188.

Hardy, S. (2008), Structural evolution of calderas: Insights from two-dimensional discrete element simulations, *Geology, 36*(12), 927-930, doi:10.1130/G25133A.1.

Harlow, D. H., Power, J. A., Laguerta, E. P., Ambubuyog, G., White, R. A., and R. P. Hoblitt (1996), Precursory Seismicity and Forecasting of the June 15, 1991, Eruption of Mount Pinatubo, in *Fire and Mud: Eruptions and Lahars of Mount Pinatubo, Philippines*, edited by C. G. Newhall and R. S. Punongbayan, pp.285-306, Univ. of Washington Press.

Hall, M. L., Robin, C., Beate, B., Mothes, P., and M. Monzier (1999), Tungurahua Volcano, Ecuador: structure, eruptive history and hazards, *J. Volcanol. Geotherm. Res., 91*, 1-21.

Hanson, J. B., Lavallée, Y., Goldstein, F., Kueppers, U., Hess, K.-U., and D. Dingwell (2011), A Rheological Map of Tungurahua Volcano (Ecuador): Explaining the Explosive-Effusive Transition, paper presented at Fragile Earth: Geological Processes from Global to Local Scales and Associated Hazards, München, Germany.

Harrington, R. M., and E. E. Brodsky (2007), Volcanic hybrid earthquakes that are brittle-failure events, *Geophys. Res. Lett., 34*, L06308, doi:10.1029/2006GL028714.

Harris, A. J. L. (2008), Modeling lava lake heat loss, rheology, and convection, *Geophys. Res. Lett., 35,* doi:10.1029/2008GL033190.

Harris, A. J. L., Flynn, L. P., Rothery, D. A., Oppenheimer, C., and S. B. Sherman (1999), Mass flux measurements at active lava lakes: implications for magma recycling, *J. Geophys. Res., 104*(B4), 7117–7136.

Harris, A. J. L., Ripepe, M., Calvari, S., Lodato, L., and L. Spampinato (2008), The 5 April 2003 Explosion of Stromboli: Timing of Eruption Dynamics Using Thermal Data, in *The Stromboli Volcano: An Integrated Study of the 2002-2003 Eruption*, edited by S. Calvari, S. Inguaggiato, G. Puglisi, M. Ripipe, and M. Rosi, pp. 306-316, AGU, Washington, D. C.

Hart, S. R., Staudigel, H., Koppers, A. A. P., Blusztajn, J., Baker, E. T., Workman, R., Jackson, M., Hauri, E., Kurz, M., Sims, K., Fornari, D., Saal, A., and S. Lyons (2000), Vailulu'u undersea volcano: The New Samoa, *Geochem. Geophys. Geosys., 8*(1), doi:10.1029/2000GC000108.

Harvey, D., and G. L. Choy (1982), Broad-band deconvolution of GDSN data, *Geophys. J. R. Astron. Soc., 69*(3), 659-668.

Heeszel, D. S., Wiens, D. A., Shore, P. J., Shiobara, H., and H. Sugioka (2008), Earthquake evidence for along-arc extension in the Mariana Islands, *Geochem. Geophys. Geosys., 9*(12), Q12X03, doi:10.1029/2008GC002186.

Hjörleifsdóttir, V., and G. Ekström (2010), Effects of three-dimensional Earth structure on CMT earthquake parameters, *Phys. Earth Planet. Inter., 179*, 178-190.

Hoblitt, R. P., Wolfe, E. W., Scott, W. E., Couchman, M. R., Pallister, J. S., and D. Javier (1996), The Preclimactic Eruptions of Mount Pinatubo, June 1991, in *Fire and Mud: Eruptions and Lahars of Mount Pinatubo, Philippines*, edited by C. G. Newhall and R. S. Punongbayan, pp.457-511, Univ. of Washington Press.

Holohan, E. P., Troll, V. R., Walter, T. R., Münn, S., McDonnell, S., and Z. K. Shipton (2005), Elliptical calderas in active tectonic settings: an experimental approach, *J. Volcanol. Geotherm. Res., 144*, 119-136.

Holohan, E. P., van Wyk de Vries, B., and V. R. Troll (2008), Analogue models of caldera collapse in strike-slip tectonic regimes, *Bull. Volcanol., 70*, 773-796, doi:10.1007/s00445-007-0166-x.

Holohan, E. P., Schöpfer, M. P. J., and J. J. Walsh (2011), Mechanical and geometric controls on the structural evolution of pit crater and caldera subsidence, *J. Geophys. Res., 116*, B07202, doi:10.1029/2010JB008032.

Howard, K. A. (2010), Caldera collapse: Perspectives from comparing Galápagos volcanoes, nuclear-test sinks, sandbox models, and volcanoes on Mars, *GSA Today, 20(*10), doi:10.1130/GSATG82A.1.

Hudson, J. A., Pearce, R. G., and R. M. Rogers (1989), Source Type Plot for Inversion of the Moment Tensor, *J. Geophys. Res., 94(*B1), 765-774.

Iguchi, M., Yamamoto, K., Takayama, T., Maekawa, T., Nishimura, T., Hashino, H., Yakihara, H., and S. Hirano (2001), Characteristics of Volcanic Earthquakes at Kuchierabujima Volcano. Geophysical and Geochemical Joint Observation of 2000 (in Japanese with English abstract), *Disaster Prev. Res. Inst., Kyoto Univ., 44B-1*, 317-326.

Isacks, B, Oliver, J., and L. R. Sykes (1968), Seismology and the New Global Tectonics, *J. Geophys. Res., 73*(18), 5855-5899, doi:10.1029/JB073i018p05855.

Itikarai, I. (2008), The 3-D structure and earthquake locations at Rabaul Caldera, Papua New Guinea. Unpublished Master of Philosophy thesis, Australian National University, Canberra, 137 pp.

Ito, T., and S. Yoshioka (2002), A dike intrusion model in and around Miyakejima, Niijima and Kozushima in 2000, *Tectonophysics, 359*, 171-187.

Johnson, R. W., Itikarai, I., Patia, H., and C. O. McKee (2010), Volcanic systems of the Northeastern Gazelle Peninsula, Papua New Guinea: synopsis, evaluation, and a model for Rabaul Volcano, Papua New Guinea, *Rabaul Volcano Workshop Report*, Papua New Guinea Department of Mineral Policy and Geohazards Management, and Australian Agency for International Development, Port Moresby, Papua New Guinea.

Jolly, A. D., Page, R. A., and J. A. Power (1994), Seismicity and stress in the vicinity of Mount Spurr volcano, south central Alaska, *J. Geophys. Res., 99*, 15,305-15,318.

Jones, R. H., and R. C. Stewart (1997), A method for determining significant structures in a cloud of earthquakes, *J. Geophys. Res., 102*(B4), 8245-8254.

Jónsson, S., Zebker, H., and F. Amelung (2005), On trapdoor faulting at Sierra Negra volcano, Galápagos, *J. Volcanol. Geotherm. Res., 144*, 59-71.

Jónsson, S. (2009), Stress interaction between magma accumulation and trapdoor faulting on Sierra Negra, Galápagos, *Tectonophysics, 471*, 36-44.

Julian, B. R. (1983), Evidence for dyke intrusion earthquake mechanisms near Long Valley caldera, California, *Nature, 303*, 323-325, doi:10.1038/303323a0.

Julian, B. R., and S. A. Sipkin (1985), Earthquake Processes in the Long Valley Caldera Area, California, J. *Geophys. Res., 90*(B13), 11,155-11,169, doi:10.1029/JB090iB13p11155.

Julian, B. R., Miller, A. D., and G. R. Foulger (1998), Non-Double-Couple Earthquakes 1. Theory, *Rev. Geophys., 36*(4), 525-549.

Kanamori, H., and J. W. Given (1981), Use of long-period surface waves for rapid determination of earthquake source parameters, *Phys. Earth Planet. Inter., 27*, 8-31.

Kanamori, H. Ekström, G., Dziewonski, A., Barker, J. S., and S. A. Sipkin (1993), Seismic Radiation by Magma Injection: An Anomalous Seismic Event Near Tori Shima, Japan, *J. Geophys. Res., 98*(B4), 6511-6522.

Kaneko, T., Yasuda, A., Shimano, T., Nakada, S., Fujii, T., Kanazawa, T., Nishizawa, A., and Y. Matsumoto (2005), Submarine flank eruption preceding caldera subsidence during the 2000 eruption of Miyakejima Volcano, Japan, Bull*. Volcanol., 67*, 243-253, doi:10.1007/s00445-004-0407-1.

Kasahara, M., Hamaguchi, H., Tanaka, K., Zana, N., and M. Kabwik (1992), Recent horizontal crustal movement in and around volcano Nyamuragira, Zaire, *Tectonophysics, 209*, 267–272.

Kavotha, S.K., Mavonga, T., Durieux, J., and K. Mukambilwa (2002/2003), Towards a more detailed seismic picture of the January 17th, 2002 Nyiragongo eruption, *Acta Vulcanologica, 14/15*(1–2), 87–100.

Kawakatsu, H. (1996), Observability of the isotropic component of a moment tensor, *Geophys. J. Int., 126*, 525-544.

Kawakatsu, H., and M. Yamamoto (2007), Volcano Seismology, in *Treatise on Geophysics*, vol. 4, edited by H. Kanamori, pp. 389-420, Elsevier, Amsterdam, doi:10.1016/B978-044452748-6.00073-0.

Kazahaya, K., Shinohara, H., Uto, K., Odai, M., Nakahori, Y., Mori, H., Iino, H., Miyashita, M., and J. Hirabayashi (2004), Gigantic SO_2 emission from Miyakejima volcano, Japan, caused by caldera collapse, *Geology, 32*(5), 425-428, doi:10.1130/G20399.1.

Kennedy, B., Stix, J., Vallance, J. W., Lavallée, Y., and M.-A. Longpré (2004), Controls on caldera structure: Results from analogue sandbox modeling, *Geolog. Soc. Am. Bull., 116*(5/6), 515-524, doi:10.1130/B25228.1.

Kikuchi, M., Yamanaka, Y., and K. Koketsu (2001), Source Process of the Long-period Seismic Pulses Associated with the 2000 Eruption of Miyake-jima Volcano, and its Implications (in Japanese with English abstract), *J. Geogr., 110*(2), 204-216.

Kinvig, H. S., Geyer, A., and J. Gottsman (2009), On the effect of crustal layering on ring-fault formation and the formation of collapse calderas, *J. Volcanol. Geotherm. Res., 186*, 293-304.

Knoll, P. (1990), The fluid-induced tectonic rockburst of March 13, 1989, in the "Werra" potash mining district of the GDR (first results). *Gerlands Beitrage zur Geophysik, 99*, 29-245.

Knopoff, L., and M. J. Randall (1970), The Compensated Linear-Vector Dipole: A Possible Mechanism for Deep Earthquakes, *J. Geophys. Res., 75*(26), 4957-4963.

Kobayashi, T., Ohminato, T., and Y. Ida (2003), Earthquake series preceding very long period seismic signals, observed during the 2000 Miyakejima volcanic activity, *Geophys. Res. Lett., 30*(8), 1423, doi:10.1029/2002GL016631.

Komorowski, J.-C., Tedesco, D., Kasereka, M., Allard, P., Papale, P., Vaselli, O., Durieux, J., Baxter, P., Halbwachs, M., Akumbe, M., Baluku, B., Briole, P., Ciraba, M., Dupin, J.-C., Etoy, O., Garcin, D., Hamaguchi, H., Houlié, N., Kavotha, K. S., Lemarchand, A., Lockwood, J., Lukaya, N., Mavonga, G., de Michele, M., Mpore, S., Mukambilwa, K., Munyololo, F., Newhall, C., Ruch, J., Yalire, M., and M. Wafula (2002/2003), The January 2002 Flank Eruption of Nyiragongo Volcano (Democratic Republic of Congo): Chronology, Evidence for a Tectonic Rift Trigger, and Impact of Lava Flows on the City of Goma, *Acta Vulcanol., 14/15*(1-2), 27-62.

Konstantinou, K. I., Kao, H., Lin, C. H., and W.-T. Liang (2003), Analysis of broad-band regional waveforms of the 1996 September 29 earthquake at Bárdarbunga volcano, central Iceland: investigation of the magma injection hypothesis, *Geophys. J. Int., 154*, 134-145.

Konter, J. G., Staudigel, H., Hart, S. R., and P. M. Shearer (2004), Seafloor seismic monitoring of an active submarine volcano: Local seismicity at Vailulu'u Seamount, Samoa, *Geochem. Geophys. Geosys., 5*(6), doi:10.1029/2004GC000702.

Kumagai, H. (2009), Source Quantification of Volcano Seismic Signals, in *Encyclopedia of Complexity and Systems Science*, edited by R. A. Meyers, pp. 9899-9932, Springer, New York.

Kumagai, H., Ohminato, T., Nakano, M., Ooi, M., Kubo, A., Inoue, H., and J. Oikawa (2001), Very-Long-Period Seismic Signals and Caldera Formation at Miyake Island, Japan, *Science, 293*(5530), 687-690.

Kumagai, H., Chouet, B. A., and P. B. Dawson (2005), Source process of a long-period event at Kilauea volcano, Hawaii, *Geophys. J. Int., 161*, 243-254.

Kumagai, H., Yepes, H., Vaca, M., Caceres, V., Naga, T., Yokoe, K., Imai, T., Miyakawa, K., Yamashina, T., Arrais, S., Vasconez, F., Pinajota, E., Cisneros, C., Ramos, C., Paredes, M., Gomezjurado, L., Garcia-Aristizabal, A., Molina, I., Ramon, P., Segovia, M., Palacios, P., Troncoso, L., Alvarado, A., Aguilar, J., Pozo, J., Enriquez, W., Mothes, P., Hall, M., Inoue, I., Nakano, M., and H. Inoue (2007a), Enhancing volcano-monitoring capabilities in Ecuador, *EOS, Trans. AGU, 88*(23), 245, doi:10.1029/2007EO230001.

Kumagai, H., Yepes, H., Nakano, M., and I. Molina (2007b), Very-long-period signals observed immediately before a Vulcanian eruption accompanying pyroclastic flows at Tungurahua, Ecuador, paper presented at Japan Geoscience Union Meeting, Chiba City, Japan.

Kumagai, H., Nakano, M., Maeda, T., Yepes, H., Palacios, P., Ruiz, M., Arrais, S., Vaca, M., Molina, I., and T. Yamashima (2010), Broadband seismic monitoring of active volcanoes using deterministic and stochastic approaches, *J. Geophys. Res., 115*, B08303, doi:10.1029/2009JB006889.

Kusumoto, S., and A. Gudmundsson (2009), Magma-chamber volume changes associated with ring-fault initiation using a finite-sphere model: Application to the Aira caldera, Japan, *Tectonophysics, 471*, 58-66, doi:10.1016/j.tecto.2008.09.001.

LeMasurier, W. E., Thomson, J., Baker, P., Kyle, P., Rowley, P., Smellie, J., and W. Verwoerd (Eds.) (1990), *Volcanoes of the Antarctic Plate and Southern Oceans, Antarctic Res. Ser., 48*, 487 pp., AGU, Washington, D. C., doi:10.1029/AR048.

Lipman, P. W. (1997), Subsidence of ash-flow calderas: relation to caldera size and magma-chamber geometry, *Bull. Volcanol*., 59, 198-218.

Lynch, J. S., and G. Stephens (1996), Mount Pinatubo: A Satellite Perspective of the June 1991 Eruptions, in *Fire and Mud: Eruptions and Lahars of Mount Pinatubo, Philippines*, edited by C. G. Newhall and R. S. Punongbayan, pp.637-645, Univ. of Washington Press.

Marti, J., Ablay, G. J., Redshaw, L. T., and R. S. J. Sparks (1994), Experimental studies of collapse calderas, *J. Geolog. Soc., London, 151*, 919-929.

Marti, J., Geyer, A., Folch, A., and J. Gottsman (2008), A Review on Collapse Caldera Modelling, in *Caldera Volcanism: Analysis, Modelling and Response*, Developments in Volcanology, vol. 10, edited by J. Gottsman and J. Marti, pp. 233-283, Elsevier, Amsterdam.

Marti, J., Geyer, A., and A. Folch (2009), A genetic classification of collapse calderas based on field studies, and analogue and theoretical modeling, in *Studies in Volcanology: The Legacy of George Walker*, Special Pub. of IAVCEI, vol. 2, edited by T. Thordarson, S. Self, G. Larsen, S. K. Rowland, and A. Hoskuldsson, pp. 249-266, Geological Society, London.

Matoza, R. S., Fee, D., Garcés, M. A., Seiner, J. M., Ramón, P. A., and M. A. H. Hedlin (2009), Infrasonic jet noise from volcanic eruptions, *Geophys. Res. Lett., 36*, L08303, doi:10.1029/2008GL036486.

McKee, C. O., Lowenstein, P. L., de Saint Ours, P., Talai, B., Itikaria, I., and J. J. Mori (1984), Seismic and Ground Deformation Crises at Rabaul Caldera: Prelude to an Eruption? *Bull. Volcanol., 47*(2), 397-411.

McNutt, S. R. (2000), Volcanic Seismicity, in *Encyclopedia of Volcanoes*, edited by H. Sigurdsson, B. Houghton, S. R. McNutt, H. Rymer, and J. Stix, pp. 1015-1033, Academic Press, San Diego.

McNutt, S. R. (2005), Volcanic Seismology, *Annu. Rev. Earth Planet. Sci., 32*, 461-491, doi:10.1146/annurev.earth.33.092203.122459.

Mendiguren, J. A., and K. Aki (1978), Source mechanism of the deep Colombian earthquake of 1970 July 31 from the free oscillation data, *Geophys. J. R. Astr. Soc., 55*, 539-556.

Métrich, N., Bertagnini, A., Landi, P., Rosi, M., and O. Belhadj (2005), Triggering mechanism at the origin of paroxysms at Stromboli (Aeolian Archipelago, Italy): The 5 April 2003 eruption, *Geophys. Res. Lett., 32*, L10305, doi:10.1029/2004GL022257.

Michon, L., Villeneuve, N., Catry, T., and O. Merle (2009), How summit calderas collapse on basaltic volcanoes: New insights from the April 2007 caldera collapse of Piton de la Fournaise volcano, *J. Volcanol. Geotherm. Res., 184*, 138-151.

Michon, L., Massin, F., Famin, V., Ferrazzini, V., and G. Roult (2011), Basaltic calderas: Collapse dynamics, edifice deformation, and variations of magma withdrawal., *J. Geophys. Res., 116*, B03209, doi:10.1029/2010JB007636.

Miller, A. D., Foulger, G. R., and B. R. Julian (1998a), Non-Double-Couple Earthquakes 2. Observations, *Rev. Geophys., 36*(4), 551-568.

Miller, A. D., Julian, B. R., and G. R. Foulger (1998b), Three-dimensional seismic structure and moment tensors of non-double-couple earthquakes at the Hengill-Grensdalur volcanic complex, Iceland, *Geophys. J. Int., 133*, 309-325.

Minson, S. E., and D. S. Dreger (2008), Stable inversions for complete moment tensors, *Geophys. J. Int., 174*, 585-592.

Minson, S. E., Dreger, D. S., Bürgmann, R., Kanamori, H., and K. M. Larson (2007), Seismically and geoetically determined nondouble-couple source mechanisms from the 2000 Miyakejima volcanic earthquake swarm, *J. Geophys. Res., 112*, B10308, doi:10.1029/2006JB004847.

Moran, S. C., Newhall, C., and D. C. Roman (2011), Failed magmatic eruptions: late-stage cessation of magma ascent, *Bull. Volcanol., 73*, 115-122, doi:10.1007/s00445-010-0444-x.

Mori, J., and C. McKee (1987), Outward-Dipping Ring-Fault Structure at Rabaul Caldera as Shown by Earthquake Locations, *Science, 235*, 193-195.

Mori, J., McKee, C., Itikarai, I., Lowenstein, P., de Saint Ours, P., and B. Talai (1989), Earthquakes of the Rabaul seismo-deformational crisis September 1983 to July 1985

seismicity on a ring fault. In *Volcanic Hazards: Assessment and Monitoring, IAVCEI Proceedings in Volcanology*, edited by J. H. Latter, pp. 429-462, SpringerVerlag, Berlin.

Mori, J., White, R. A., Harlow, D. H., Okubo, P., Power, J. A., Hoblitt, R. P., Laguerta, E. P., Lanzuza, A., Bautista, B. C. (1996), Volcanic earthquakes following the 1991 climactic eruption of Mount Pinatubo: Strong seismicity during a waning eruption, in *Fire and Mud: Eruptions and Lahars of Mount Pinatubo, Philippines*, edited by C. G. Newhall and R. S. Punongbayan, pp.339-350, Univ. of Washington Press.

Murase, M., Irwan, M., Kariya, S., Tabei, T., Okuda, T., Miyajima, R., Oikawa, J., Watanabe, H., Kato, T., Nakao, S., Ukawa, M., Fujita, E., Okayama, M., Kimata, F., and N. Fujii (2006), Time dependent model of magma intrusion in and around Miyake and Kozu Islands, Central Japan in June-August, 2000, *J. Volcanol. Geotherm. Res., 150*, 213-231.

Nairn, I. A., McKee, C. O., Talai, B., and C. P. Wood (1995), Geology and eruptive history of the Rabaul caldera area, Papua New Guinea, *J. Volcanol. Geotherm. Res., 69*(3-4), 255-284.

Nakada, S., Nagai, M., Kaneko, T., Nozawa, A., and K. Suzuki-Kamata (2005), Chronology and products of the 2000 eruption of Miyakejima Volcano, Japan, *Bull. Volcanol., 67*, 205-218, doi:10.1007/s00445-004-0404-4.

Nakanishi, I., and H. Kanamori (1982), Effects of lateral heterogeneity and source process time on the linear moment tensor inversion of long-period Rayleigh-waves, *Bull. Seism. Soc. Am., 72*(6), 2063-2080.

Nakano, M., and H. Kumagai (2005), Waveform inversion of volcano-seismic signals assuming possible source geometries, *Geophys. Res. Lett., 31*, L12302, doi:10.1029/2005GL022666.

Nettles, M., and G. Ekström (1998), Faulting mechanism of anomalous earthquakes near Bárdarbunga Volcano, Iceland, *J. Geophys. Res., 103*(B8), 17,973-17,983.

Newhall, C. G., and S. Self (1982), The Volcanic Explosivity Index (VEI): An Estimate of Explosive Magnitude for Historical Volcanism, *J. Geophys. Res., 87*(C2), 1231-1238.

Nishimura, T., Ozawa, S., Murakami, M., Sagiya, T., Tada, T., Kaidzu, M., and M. Ukawa (2001), Crustal Deformation caused by magma migration in the northern Izu Islands, Japan, *Geophys. Res. Lett., 28*(19), 3745-3748.

Nyblade, A. A. and C. A. Langston (2002), Broadband seismic experiment probe the East African rift, *Eos Trans. AGU, 83*(37), 405–409.

Ohminato, T. (2008), Source mechanisms of vulcanian eruptions at Mt. Asama, Japan, inferred from volcano seismic signals, *Geol. Soc. London, Special Pub. 2008, 307*, 189-206, doi:10.1144/SP307.11.

Ohminato, T., and H. Kumagai (2001), On the very-long-period seismic pulses observed during the 2000 Miyake-jima volcanic activity (in Japanese with English abstract), paper presented at Volcanic Structure in the Shallow Part and Volcanic Fluid, Disaster Prevention Research Institute, Kyoto University, available at http://www.dpri.kyoto-u.ac.jp/~kazan/12k03/ohminato.pdf.

Ohminato, T., Chouet, B. A., Dawson, P. and S. Kedar (1998), Waveform inversion of very long period impulsive signals associated with magmatic injection beneath Kilauea Volcano, Hawaii, *J. Geophys. Res., 103*(B10), 23,839-23,862.

Ohminato, T., Takeo, M., Kumagai, H., Yamashina, T., Oikawa, J., Koyama, E., Tsuji, H., and T. Urabe (2006), Vulcanian eruptions with dominant single force components observed during the Asama 2004 volcanic activity in Japan, *Earth Planets Space, 58*, 583-593.

Oppenheimer, C. (1998), Satellite observation of active carbonatite volcanism at Ol Doinyo Lengai, Tanzania, *Int. J. Remote Sensing, 19*(1), 55-64.

Ozawa, S., Miyazaki, S., Nishimura, T., Murakami, M., Kaidzu, M., Imakiire, T., and X. Ji (2004), Creep, dike intrusion, and magma chamber deflation model for the 2000 Miyake eruption and the Izu islands earthquakes, *J. Geophys. Res., 109*, B02410, doi:10.1029/2003JB002601.

Pechmann, J. C., Walter, W. R., Nava, S. J., and W. J. Arabasz (1995), The February 3, 1995, M_L 5.1 Seismic Event in the Trona Mining District of Southwestern Wyoming, *Seism. Res. Lett., 66*(3), 25-34.

Pechmann, J. C., Arabasz, W. J., Pankow, K. L., and R. Burlacu (2008), Seismological Report on the 6 August 2007 Crandall Canyon Mine Collapse in Utah, *Seism. Res. Lett., 79*(5), 620-636, doi:10.1785/gssrl.79.5.620.

Pinel, V. (2011), Influence of pre-existing volcanic edifice geometry on caldera formation, *Geophys. Res. Lett., 38*, L11305, doi:10.1029/2011GL047900.

Pinel, V., and C. Jaupart (2005), Caldera formation by magma withdrawal from a reservoir beneath a volcanic edifice, *Earth Planet. Sci. Lett., 230*, 273-287.

Platz, T., Foley, S. F., and L. Andre (2004), Low-pressure fractionation of the Nyiragongo volcanic rocks, Virunga Province, D.R. Congo, *J. Volcanol. Geotherm. Res., 136*(3–4), 269–295.

Poland, M., and Z. Lu (2004), Deformation associated with the January 17, 2002, eruption of Nyiragongo volcano, Democratic Republic of the Congo, from radar interferometry. *Eos. Trans. AGU, 89*, Spring Meeting Suppl., Abstract V53B-02P.

Power, J. A., Murray, T. L., Marso, J. N., and E. P. Laguerta (1996), Preliminary Observations of Seismicity at Mount Pinatubo by use of the Seismic Spectral Amplitude Measurement (SSAM) System, May 13-June 18, 1991, in *Fire and Mud: Eruptions and Lahars of Mount Pinatubo, Philippines*, edited by C. G. Newhall and R. S. Punongbayan, pp.269-284, Univ. of Washington Press.

Prejean, S., Stork, A., Ellsworth, W., Hill, D., and B. Julian (2003), High precision earthquake locations reveal seismogenic structure beneath Mammoth Mountain, California, *Geophys. Res. Lett., 30*(24), doi:10.1029/2003GL018334.

Reynolds, R. W., Geist, D., and M. D. Kurz (1995), Physical volcanology and structural development of Sierra Negra volcano, Isabela Island, Galápagos archipelago, *Geol. Soc. Am. Bull., 107*(12), 1398-1410, doi:10.1130/0016-7606(1995)107<1398:PVASDO>2.3.CO;2.

Richards, P. G., and W.-Y. Kim (2005), Equivalent Volume Sources for Explosions at Depth: Theory and Observations, *Bull. Seism. Soc. Am., 95*(2), 401-407, doi:10.1785/0120040034.

Ripepe, M., and A. J. L. Harris (2008), Dynamics of the 5 April 2003 explosive paroxysm observed at Stromboli by a near-vent thermal, seismic and infrasonic array, *Geophys. Res. Lett., 35*, L07306, doi:10.1029/2007GL032533.

Ritchie, L. J., Cole, P. D., and R. S. J. Sparks (2002), Sedimentology of deposits from the pyroclastic density current of 26 December 1997 at Soufrière Hills Volcano, Montserrat, in *The Eruption of Soufrière Hills Volcano, Montserrat, from 1995 to 1999*, edited by T. H. Druitt and B. P. Kokelaar, pp. 435-456, Geological Society, London.

Rizzo, A., Aiuppa, A., Capasso, G., Grassa, F., Inguaggiato, S., Longo, M., and M. L. Carapezza (2008), The 5 April 2003 Paroxysm at Stromboli: A Review of Geochemical Observations, in *The Stromboli Volcano: An Integrated Study of the 2002-2003 Eruption*, edited by S. Calvari, S. Inguaggiato, G. Puglisi, M. Ripipe, and M. Rosi, pp. 347-358, AGU, Washington, D. C.

Roche, O., and T. H. Druitt (2001), Onset of caldera collapse during ignimbrite eruptions, *Earth Planet. Sci. Lett., 191*, 191-202.

Roche, O., Druitt, T. H., and O. Merle (2000), Experimental study of caldera formation, *J. Geophys. Res., 105*(B1), 395-416.

Roche, O., van Wyk de Vries, B., and T. H. Druitt (2001), Sub-surface structures and collapse mechanisms of summit pit craters, *J. Volcanol. Geotherm. Res., 105*, 1-18.

Rosi, M., Bertagnini, A., Harris, A. J. L., Pioli, L., Pistolesi, M., and M. Ripepe (2006), A case history of paroxysmal explosion at Stromboli: Timing and dynamics of the April 5, 2003 event, *Earth Planet. Sci. Lett., 243*, 594-606.

Ross, A., Foulger, G. R., and B. R. Julian (1996), Non-double-couple earthquake mechanisms at the Geysers geothermal area, California, *Geophys. Res. Lett., 23*, 877-880.

Rouland, D., C. Condis, C. Parmentier, and A. Souriau (1992), Previously undetected earthquakes in the southern hemisphere located using long-period Geoscope data, *Bull. Seism. Soc. Am., 82(6),* 2448-2463.

Rubin, A. M. (1995), Propagation of Magma-Filled Cracks, *Annu. Rev. Earth Planet. Sci., 23*, 287-336.

Rubin, A. M., and D. D. Pollard (1987), Origins of blade-like dikes in volcanic rift zones. In *Volcanism in Hawaii*, U.S. Geological Survey Prof. Paper 1350, edited by R. W. Decker and T. Wright, pp.1449-1470.

Ryan, W. B. F., Carbotte, S. M., Coplan, J. O., O'Hara, S., Melkonian, A., Arko, R., Weissel, R. A., Ferrini, V., Goodwillie, A., Nitsche, F., Bonczkowski, J., and R. Zemsky (2009), Global Multi-Resolution Topography synthesis, *Geochem. Geophys. Geosys., 10*(3), doi:10.1029/2008GC002332.

Sahama, T. G. (1973), Evolution of the Nyiragongo Magma, *J. Petrolog., 14*(1), 33-48.

Saito, G., Uto, K., Kazahaya, K., Shinohara, H., Kawanabe, Y., and H. Satoh (2005), Petrological characteristics and volatile content of magma from the 2000 eruption of Miyakejima Volcano, Japan, *Bull. Volcanol., 67*, 268-280, doi:10.1007/s00445-004-0409-z.

Sakai, S., Yamada, T., Ide, S., Mochizuki, M., Shiobara, H., Urabe, T., Hirata, N., Shinohara, M., Kanazawa, T., Nishizawa, A., Fujie, G., and H. Mikada (2001), Magma Migration from the Point of View of Seismic Activity in the Volcanism of Miyake-jima Island in 2000 (in Japanese with English abstract), *J. Geogr., 110*(2), 145-155.

Samaniego, P., Le Pennec, J.-L., Robin, C., and S. Hidalgo (2011), Petrological analysis of the pre-eruptive magmatic process prior to the 2006 explosive eruptions at Tungurahua volcano (Ecuador), *J. Volcanol. Geotherm. Res., 199*, 69-84, doi:10.1016/j.jvolgeores.2010.10.010.

Sammis, C. G., and B. R. Julian (1987), Fracture Instabilities Accompanying Dike Intrusion, *J. Geophys. Res., 92*(B3), 2597-2605.

Sasai, Y., Uyeshima, M., Utada, H., Kagiyama, T., Zlotnicki, J., Hashimoto, T., and Y. Takahashi (2001), The 2000 Activity of Miyake-jima Volcano as Inferred from Electric and Magnetic Field Observations, *J. Geogr., 110*(2), 226-244.

Sasai, Y., Uyeshima, M., Zlotnicki, J., Utada, H., Kagiyama, T., Hashimoto, T., and Y. Takahashi (2002), Magnetic and electric field observations during the 2000 activity of Miyake-jima volcano, Central Japan, *Earth Planet. Sci. Lett., 203*, 769-666.

Satake, K., and H. Kanamori (1991), Abnormal Tsunami Caused by the June 13, 1984, Torishima, Japan, Earthquake, *J. Geophys. Res., 96*(B12), 19,933-19,939.

Saunders, S. J. (2001), The shallow plumbing system of Rabaul caldera: a partially intruded ring fault? *Bull. Volcanol., 63*, 406-420, doi:10.1007/s004450100159.

Saunders, S. J. (2005), The possible contribution of circumferential fault intrusion to caldera resurgence, *Bull. Volcanol., 67*, 57-71, doi:10.1007/s00445-004-0360-z.

Sawyer, G. M., Carn, S. A., Tsanev, V. I., Oppenheimer, C., and M. Burton (2008) Investigation into magma degassing at Nyiragongo volcano, Democratic Republic of the Congo, *Geochem. Geophys. Geosys., 9*(Q02017), doi:10.1029/2007GC001829.

Scandone, R., and S. D. Malone (1985), Magma supply, magma discharge, and readjustment of the feeding system of Mount St. Helens during 1980: *J. Volcanol. Geophys. Res., 23*, 239-262.

Schmincke, H. U. (2004), *Volcanism*, Springer, New York.

Sekitani, H., Goto, K., Miyamachi, H., Kakuta, T., and S. Hirano (1997), Aftershock Distribution of the September 9, 1996 Earthquake (M_{JMA}5.7) at Tanegashima, Japan (in Japanese with English abstract), *Rep. Fac. Sci., Kagoshima Univ., 30*, 89-99.

Self, S. (2012), The effects and consequences of very large explosive volcanic eruptions, *Phil. Trans. R. Soc. A, 364,* 2073-2097, doi:10.1098/rsta.2006.1814.

Self, S., Keszthelyi, L., and T. Thordarson (1998), The Importance of Pahoehoe, *Annu. Rev. Earth Planet. Sci., 26*, 81-110.

Shearer, P. M. (1994), Global seismic event detection using a matched filter on long-period seismograms, *J. Geophys. Res., 99,* 13,713-13,735.

Shuler, A., and G. Ekström (2009), Anomalous earthquakes associated with Nyiragongo Volcano: Observations and potential mechanisms, *J. Volcanol. Geotherm. Res., 181*(3-4), 219-230, doi:10.1016/j.jvolgeores.2009.01.011.

Shuler, A., and M. Nettles (2012), Earthquake source parameters for the 2010 western Gulf of Aden rifting episode, *Geophys. J. Int., 190*(2), 1111-1122, doi:10.1111/j.1365-246X.2012.05529.x.

Siebert, L., and Simkin T. (2002-), Volcanoes of the World: an Illustrated Catalog of Holocene Volcanoes and their Eruptions, Smithsonian Institution, Global Volcanism Program, Digital Information Series, GVP-3, http://www.volcano.si.edu/world.

Simkin, T., and K. A. Howard (1970), Caldera collapse in the Gálapagos Islands, 1968, *Science, 169*(3944), 429–437.

Smith, G. P., and G. Ekström (1997), Interpretation of earthquake epicenter and CMT centroid locations, in terms of rupture length and direction, *Phys. Earth Planet. Inter., 102*, 123-132.

Smith, I. E. M., Brothers, R. N., Muiruri, F. G., and P. R. L. Browne (1988), The Geochemistry of Rock and Water Samples from Curtis Island Volcano, Kermadec Group, Southwest Pacific, *J. Volcanol. Geotherm. Res., 34*, 233-240.

Smithsonian Institution (1990a), Ol Doinyo Lengai, *Bulletin of the Global Volcanism Network, 15*, 5.

Smithsonian Institution (1990a), Ol Doinyo Lengai, *Bulletin of the Global Volcanism Network, 15*, 8.

Smithsonian Institution (1994), Rabaul, *Bulletin of the Global Volcanism Network, 19*, 8.

Smithsonian Institution (1995a), Rabaul, *Bulletin of the Global Volcanism Network, 20*, 2.

Smithsonian Institution (1995b), Vailulu'u, *Bulletin of the Global Volcanism Network, 20*, 1.

Smithsonian Institution (1996a), Grimsvötn, *Bulletin of the Global Volcanism Network*, *21*, 9.

Smithsonian Institution (1996b), Rabaul, *Bulletin of the Global Volcanism Network*, *21*, 2.

Smithsonian Institution (2002), Nyiragongo, *Bulletin of the Global Volcanism Network*, *27*, 4.

Smithsonian Institution (2003), Nyiragongo, *Bulletin of the Global Volcanism Network, 28*, 5.

Smithsonian Institution (2006), Sierra Negra, *Bulletin of the Global Volcanism Network*, *3*1, 12.

Smithsonian Institution (2009), Curtis Island, *Bulletin of the Global Volcanism Network, 34,* 2.

Sobradelo, R., Geyer, A., and J. Marti (2010), Statistical data analysis of the CCDB (Collapse Caldera Database): Insights on the formation of caldera systems*, J. Volcanol. Geotherm. Res*., 198, 241-252.

Sparks, R. S. J., Barclay, J., Calder, E. S., Herd, R. A., Komorowski J.-C., Luckett, R., Norton, G. E., Ritchie, L. J., Voight, B., and A. W. Woods (2002), Generation of a debris avalanche and violent pyroclastic density current on 26 December (Boxing Day) 1997 at

Soufrière Hills Volcano, Montserrat, in *The Eruption of Soufrière Hills Volcano, Montserrat, from 1995 to 1999*, edited by T. H. Druitt and B. P. Kokelaar, pp. 409-434, Geological Society, London.

Steffke, A. M., Fee, D., Garces, M., and A. Harris (2010), Eruption chronologies, plume heights and eruption styles at Tungurahua Volcano: Integrating remote sensing techniques and infrasound, *J. Volcanol. Geotherm. Res., 193*, 143-160, doi:10.1016/j.jvolgeores.2010.03.004.

Stix, J., and T. Kobayashi (2008), Magma dynamics and collapse mechanisms during four historic caldera-forming events, *J. Geophys. Res., 113*, B09205, doi:10.1029/2007JB005073.

Strelitz, R. A. (1989), Choosing the 'best' double couple from a moment-tensor inversion, *Geophys. J. Int., 99*, 811-815.

Sugioka, H., Fukao, Y., Kanazawa, T., and K. Kanjo (2000), Volcanic events associated with an enigmatic submarine eruption, *Geophys. J. Int., 142*, 361-370.

Sykes, L. R. (1967), Mechanism of Earthquakes and Nature of Faulting on the Mid-Oceanic Ridges, *J. Geophys. Res., 72*(3), 2131-2153, doi:10.1029/JZ072i008p02131.

Syracuse, E. M., and G. A. Abers (2006), Global compilation of variations in slab depth beneath arc volcanoes and implications, *Geochem. Geophys. Geosys., 7*(5), Q05017, doi:10.1029/2005GC001045.

Takei, Y., and M. Kumazawa (1994), Why have the single force and torque been excluded from seismic source models? *Geophys. J. Int., 118*, 20–30.

Takeo, M. (1990), Analysis of Long-Period Seismic Waves Excited by the November 1987 Eruption of Izu-Oshima Volcano, *J. Geophys. Res., 95*(B12), 19,377-19,393.

Talandier, J., and E. A. Okal (1987), Seismic Detection of Underwater Volcanism: The Example of French Polynesia, *Pure Appl. Geophys., 125*(6), 919-950.

Tanaka, K. (1983), Seismicity and focal mechanism of the volcanic earthquakes in the Virunga volcanic region, in *Volcanoes Nyiragongo and Nyamuragira: Geophysical Aspects,* edited by H. Hamaguchi, pp. 19-28, Tohoku University, Sendai, Japan.

Taylor, S. R. (1994), False Alarms and Mine Seismicity: An Example from the Gentry Mountain Mining Region, Utah, *Bull. Seism. Soc. Am., 84*(2), 350-358.

Tazieff, H. (1994), Permanent lava lakes: observed facts and induced mechanisms, *J. Volanol. Geotherm. Res., 63*, 3–11.

Tedesco, D., Vaselli, O., Papale, P., Carn, S. A., Voltaggio, M., Sawyer, G. M., Durieux, J., Kasereka, M., and F. Tassi (2007), January 2002 volcano-tectonic eruption of Nyiragongo volcano, Democratic Republic of Congo, *J. Geophys. Res., 112*, B09202, doi:10.1029/2006JB004762.

Templeton, D. C., and D. S. Dreger (2006), Non-Double-Couple Earthquakes in the Long Valley Volcanic Region, *Bull. Seism. Soc. Am., 96*(1), 69-79, doi:10.1785/0120040206.

Tkalčić, H., Dreger, D. S., Foulger, G. R., and B. R. Julian (2009), The Puzzle of the 1996 Bárdarbunga, Iceland, Earthquake: No Volumetric Component in the Source Mechanism, *Bull. Seism. Soc. Am., 99*(5), 3077-3085.

Toda, S., Stein, R. S., and T. Sagiya (2002), Evidence from the AD 2000 Izu islands earthquake swarm that stressing rate governs seismicity, *Nature, 419*, 58-61.

Troll, V. R., Walter, T. R., and H.-U. Schmincke (2002), Cyclic caldera collapse: Piston or piecemeal subsidence? Field and experimental evidence, *Geology, 30*(2), 135-138.

Uhira, K., Baba, T., Mori, H., Katayama, H., and N. Hamada (2005), Earthquake swarms preceding the 2000 eruption of Miyakejima volcano, Japan, *Bull. Volcanol., 67*, 219-230, doi:10.1007/s00445-004-0405-3.

Ukawa, M., Fujita, E., Yamamoto, E., Okada, Y., and M. Kikuchi (2000), The 2000 Miyakejima eruption: Crustal deformation and earthquakes observed by the NIED Miyakejima observation network, *Earth Planets Space, 52(*8), xix-xxvi.

Vaughan, R. G., and P. W. Webley (2010), Satellite observations of a surtseyan eruption: Hunga Ha'apai, Tonga, *J. Volcanol. Geotherm. Res., 198*, 177-186, doi:10.1016/j.jvolgeores.2010.08.017.

Voight, B., Komorowski, J.-C., Norton, G. E., Belousov, A. B., Belousova, M., Boudon, G., Francis, P. W., Franz, W., Heinrich, P., Sparks, R. S. J., and S. R. Young (2002), The 26 December (Boxing Day) 1997 sector collapse and debris avalanche at Soufrière Hills Volcano, Montserrat, in *The Eruption of Soufrière Hills Volcano, Montserrat, from 1995 to 1999*, edited by T. H. Druitt and B. P. Kokelaar, pp. 363-407, Geological Society, London.

Wald, D. J., and T. H. Heaton (1994), Spatial and Temporal Distribution of Slip for the 1992 Landers, California Earthquake, *Bull. Seism. Soc. Am., 84*, 668-691.

Walter, T. R. (2008), Facilitating Dike Intrusions into Ring-Faults, in *Caldera Volcanism: Analysis, Modelling and Response*, Developments in Volcanology, vol. 10, edited by J. Gottsman and J. Marti, pp. 351-374, Elsevier, Amsterdam.

Wells, D. L., and K. J. Coppersmith (1994), New Empirical Relationships among Magnitude, Rupture Length, Rupture Width, Rupture Area, and Surface Displacement, *Bull. Seism. Soc. Am., 84*(4), 974-1002.

White, S. M., Crisp, J. A., and F. J. Spera (2006), Long-term volumetric eruption rates and magma budgets, *Geochem. Geophys. Geosys., 7*(3), doi:10.1029/2005GC001002.

Woessner, J. and S. Wiemer (2005), Assessing the quality of earthquake catalogues: estimating the magnitude of completeness and its uncertainty, *Bull. Seism. Soc. Am., 95*(2), 684–698.

Wolfe, E. W., and R. P. Hoblitt (1996), Overview of the Eruptions, in *Fire and Mud: Eruptions and Lahars of Mount Pinatubo, Philippines*, edited by C. G. Newhall and R. S. Punongbayan, pp.3-20, Univ. of Washington Press.

Wolfe, C. J., Okubo, P. G., Ekström, G., Nettles, M., and P. M. Shearer (2004), Characteristics of deep (≥13 km) Hawaiian earthquakes and Hawaiian earthquakes west of 155.55°W, *Geochem. Geophys. Geosys., 5*(4), doi:10.1029/2003GC000618.

Wood, C. P., Nairn, I. A., McKee, C. O., and B. Talai (1995), Petrology of the Rabaul Caldera area, Papua New Guinea, *J. Volcanol. Geotherm. Res., 69*(3-4), 285-302.

Woods, A. W., Sparks, R. S. J., Ritchie, L. J., Batey, J., Gladstone, C., and M. I. Bursik (2002), The explosive decompression of a pressurized volcanic dome: the 26 December 1997 collapse and explosion of Soufrière Hills Volcano, Montserrat, in *The Eruption of Soufrière Hills Volcano, Montserrat, from 1995 to 1999*, edited by T. H. Druitt and B. P. Kokelaar, pp. 457-465, Geological Society, London.

Wright, R., Flynn, L., Garbeil, H., Harris, A., and E. Pilger (2002), Automated volcanic eruption detection using MODIS, *Remote Sensing of Environment, 82*, 135-155.

Wright, R., Flynn, L. P., Garbeil, H., Harris, A. J. L., and E. Pilger (2004), MODVOLC: near-real-time thermal monitoring of global volcanism, *J. Volcanol. Geotherm. Res., 135*, 29-49.

Yamamoto, E., Ukawa, M., Fujita, E., Okada, Y., and M. Kikuchi (2001), Step-like Tilt Change Occurred during the Caldera-forming Stage of the 2000 Miyakejima Volcanic Activity (in Japanese with English abstract), *J. Geogr., 110*(2), 181-190.

Yamaoka, K., Kawamura, M., Kimata, F., Fujii, N., and T. Kudo (2005), Dike intrusion associated with the 2000 eruption of Miyakejima Volcano, Japan, *Bull. Volcanol., 67*, 231-242, doi:10.1007/s00445-004-0406-2.

Young, S. R., Voight, B., Barclay, J., Herd, R. A., Komorowski, J.-C., Miller, A. D., Sparks, R. S. J., and R. C. Stewart (2002), Hazard implications of small-scale edifice instability and sector collapse: a case history from Soufrière Hills Volcano, Montserrat, in *The Eruption*

of Soufrière Hills Volcano, Montserrat, from 1995 to 1999, edited by T. H. Druitt and B. P. Kokelaar, pp. 349-361, Geological Society, London.

Yun, S., Segall, P., and H. Zebkar (2006), Constraints on magma chamber geometry at Sierra Negra Volcano, Galápagos Islands, based on InSAR observations, *J. Volcanol. Geotherm. Res., 150*, 232-243.

Yun, S.-H. (2007), A Mechanical Model of the Large-Deformation 2005 Sierra Negra Volcanic Eruption Derived from InSAR Measurements, Ph.D. Thesis, Department of Geophysics, Stanford University, 125 pp.

Zobin, V. M. (2003), *Introduction to Volcanic Seismology*, 1st ed., Elsevier, Amsterdam, 302 pp.

Zobin, V. M. (2011), *Introduction to Volcanic Seismology*, 2nd ed., Elsevier, Amsterdam, 474 pp.

Appendix A

This appendix contains Supplementary Information for Chapter 2. These data tables have been submitted as Auxiliary Material for:

Shuler, A., Nettles, M., and G. Ekström, Global observations of vertical-CLVD earthquakes at active volcanoes, submitted to J. *Geophys. Res*., 2012.

Table A1. Centroid-moment-tensor solutions for 124 target earthquakes in the Global CMT catalog (1976-2009). The number in the first column is the event number for each earthquake. An asterisk next to the event number indicates that the earthquake is a shallow vertical-CLVD earthquake (see text). The event number is followed by the year, month, day and origin time of the earthquake. The origin time listed is that of the centroid solution, where δt_0 indicates the time shift (in seconds) with respect to the time reported by the NEIC in its Preliminary Determination of Epicenters (PDE) or the Global CMT Project's Surface Wave Catalog.

The hypocentral coordinates are for the centroid locations, and $\delta\lambda_0$ and $\delta\phi_0$ indicate the perturbations in latitude and longitude obtained with respect to the original epicenter.

The half duration (*Half Drtn*) of the earthquake is a fixed parameter in the inversion, estimated from the scalar moment using the empirical relationship

$$Half\ Drtn = 2.26 \times 10^{-6}\ M_0^{1/3}, \qquad \text{(A1)}$$

where the half duration is measured in seconds and M_0 is the scalar moment measured in Nm [*Ekström et al.,* 2012]. The moment-rate function is modeled as a triangle.

The scale factor (10^{ex}) is the number by which the scalar seismic moment and moment-tensor elements must be multiplied to obtain a result in Nm. The scale factor entries in the table represent the exponent (*ex*) values. The scalar moment (M_0) is defined as

$$M_0 = (\sigma_{max} - \sigma_{min})/2, \quad \text{(A2)}$$

where σ_{max} and σ_{min} are the maximum and minimum eigenvalues of the moment tensor.

The elements of the moment tensor are given in the standard spherical coordinate system [*Gilbert and Dziewonski*, 1975]. In Cartesian coordinates, $M_{rr} = M_{zz}$, $M_{\theta\theta} = M_{xx}$, $M_{\phi\phi} = M_{yy}$, $M_{r\theta} = M_{xz}$, $M_{r\phi} = -M_{yz}$, and $M_{\theta\phi} = -M_{xy}$ [*Aki and Richards*, 2002]. The CMT solutions are constrained to have no isotropic component, so that $M_{rr} + M_{\theta\theta} + M_{\phi\phi} = 0$. Each element of the moment tensor is followed by its estimated standard error.

Table A2. Moment tensors expressed in principal-axis system and best-double couple parameters for the 124 target earthquakes from the Global CMT catalog. As in Table A1, the number in the first column is the event number, and an asterisk next to the event number indicates that the earthquake is a shallow vertical-CLVD earthquake. The scale factor (10^{ex}) is the number by which the scalar seismic moment and eigenvalues must be multiplied to obtain a result in Nm. Each principal axis is described by an eigenvalue, plunge and azimuth. The scalar moment (M_0) is repeated from Table A1. The strike, dip, and rake of the nodal planes of the best-double-couple mechanism are listed, following the convention of *Aki and Richards* [2002].

Table A3. Centroid-moment-tensor solutions for 59 Category 1 target earthquakes in the Surface Wave catalog (1991-2009). Columns are as in Table A1, except the origin time listed is that of the centroid solution, where δt_0 indicates the time shift (in seconds) with respect to the time reported by the Global CMT Project's Surface Wave Catalog.

Table A4. Principal axes and best double-couple parameters for 59 Category 1 target earthquakes in the Surface Wave catalog (1991-2009). Columns are as in Table A2.

Table A5. Centroid-moment-tensor solutions for 131 Category 2 target earthquakes in the Surface Wave catalog (1991-2009). Columns are as in Table A1, except the origin time listed is that of the centroid solution, where δt_0, indicates the time shift (in seconds) with respect to the time reported by the Global CMT Project's Surface Wave Catalog.

Table A6. Principal axes and best double-couple parameters for 131 Category 2 target earthquakes in the Surface Wave catalog (1991-2009). Columns are as in Table A2.

Table A7. Centroid-moment-tensor solutions for 86 target earthquakes in the Global CMT catalog (1976-2009) and the Surface Wave catalog (1991-2009). This table is a compilation of all of the shallow vertical-CLVD earthquakes described in Tables A1, A3 and A5. Columns are as in Table A1. Because all of the earthquakes are shallow, their centroid depths were constrained by the inversion to be 12 km, so no standard error in depth is given.

Table A8. Principal axes and best double-couple parameters for 86 target earthquakes in the Global CMT catalog (1976-2009) and the Surface Wave catalog (1991-2009). This table is a compilation of all the shallow vertical-CLVD earthquakes described in Tables A2, A4 and A6. Columns are as in Table A2.

References:

Aki, K., and P. G. Richards (2002), *Quantitative Seismology*, 2nd ed., University Science Books, Sausalito, CA.

Ekström, G., Nettles, M., and A. M. Dziewonski (2012), The global CMT project 2004-210: Centroid-moment tensors for 13,017 earthquakes, *Phys. Earth Planet. Inter., 200-201*, 1-9, doi:10.1016.j.pepi.2012.04.002.

Gilbert, F., and A. M. Dziewonski (1975), An application of normal mode theory to the retrieval of structural parameters and source mechanisms from seismic spectra, *Philos. Trans. R. Soc. London Ser. A., 278*, 187-269.

Table A1. Recalculated centroid-moment-tensor solutions for 124 vertical-CLVD earthquakes in the Global CMT Catalog, 1976 - 2009.

No.	Centroid Parameters														Half Drtn	Scale Factor 10^{ex}	M_0	Elements of Moment Tensor					
	Date			Time				Latitude		Longitude		Depth						M_{rr}	$M_{\theta\theta}$	$M_{\phi\phi}$	$M_{r\theta}$	$M_{r\phi}$	$M_{\theta\phi}$
	Y	M	D	h	m	sec	δt_0	l	$\delta\lambda_0$	ϕ	$\delta\phi_0$	h	δh_0										
1	1977	9	11	14	8	15.4 ± 0.6	10.8	-15.19 ± 0.05	0.20	-172.97 ± 0.04	0.24	29.5 ± 1.8	-3.5	1.6	17	3.3	2.86 ± 0.30	-0.10 ± 0.22	-2.76 ± 0.22	0.37 ± 0.31	1.60 ± 0.30	0.73 ± 0.16
2	1977	9	13	0	21	59.3 ± 0.3	6.7	-15.19 ± 0.02	0.26	-172.94 ± 0.02	0.35	28.6 ± 0.8	-4.4	2.5	18	1.3	1.01 ± 0.03	-0.21 ± 0.03	-0.81 ± 0.02	-0.11 ± 0.04	0.81 ± 0.05	-0.51 ± 0.02
*3	1978	5	16	7	35	49.1 ± 0.3	2.1	40.99 ± 0.02	0.00	141.44 ± 0.03	0.18	12.0		1.2	17	1.3	1.53 ± 0.04	-0.90 ± 0.04	-0.63 ± 0.04	0.35 ± 0.11	0.11 ± 0.11	-0.02 ± 0.04
*4	1978	9	9	6	1	7.6 ± 0.3	0.7	-56.34 ± 0.02	-0.03	-27.31 ± 0.04	0.35	12.0		1.3	17	1.6	1.48 ± 0.05	-0.87 ± 0.04	-0.62 ± 0.05	-0.59 ± 0.11	-0.92 ± 0.11	-0.05 ± 0.04
5	1979	6	11	19	14	19.5 ± 0.4	1.9	-5.16 ± 0.02	-0.11	152.37 ± 0.04	0.28	54.8 ± 1.5	-18.2	1.7	17	3.9	3.59 ± 0.19	-3.50 ± 0.12	-0.09 ± 0.15	0.44 ± 0.12	-0.76 ± 0.14	-1.38 ± 0.11
*6	1979	10	1	12	23	51.2 ± 0.2	2.6	-21.29 ± 0.01	-0.21	-175.66 ± 0.01	0.05	12.0		1.4	17	2.2	2.53 ± 0.04	-0.91 ± 0.05	-1.62 ± 0.04	0.03 ± 0.11	0.12 ± 0.10	0.52 ± 0.03
7	1979	10	27	4	4	50.8 ± 0.8	4.4	-58.85 ± 0.06	-0.09	-24.50 ± 0.06	0.74	36.0 ± 1.9	3.0	0.9	16	6.2	5.62 ± 0.76	0.68 ± 0.49	-6.31 ± 0.42	-1.50 ± 0.49	0.67 ± 0.44	0.10 ± 0.38
8	1981	7	6	1	2	35.9 ± 0.4	10.4	-15.09 ± 0.03	0.20	-173.22 ± 0.02	0.24	61.0 ± 1.9	28.0	1.8	17	4.7	2.93 ± 0.16	-2.76 ± 0.13	-0.17 ± 0.12	-3.00 ± 0.13	-0.37 ± 0.09	2.13 ± 0.12
9	1981	11	9	16	45	10.3 ± 0.2	4.4	53.36 ± 0.02	0.14	-165.56 ± 0.02	0.19	35.7 ± 0.8	2.7	1.8	17	5.3	4.54 ± 0.15	-2.44 ± 0.14	-2.09 ± 0.13	-2.04 ± 0.20	0.99 ± 0.13	2.76 ± 0.08
10	1982	11	12	12	16	14.6 ± 0.3	6.4	1.49 ± 0.02	0.01	126.46 ± 0.03	0.00	46.3 ± 1.2	2.3	1.3	17	1.7	1.66 ± 0.08	-0.39 ± 0.05	-1.27 ± 0.06	-0.18 ± 0.04	-0.28 ± 0.06	-0.78 ± 0.04
11	1982	12	31	3	47	34.5 ± 0.3	12.1	-21.38 ± 0.02	-0.33	-68.66 ± 0.02	-0.20	128.8 ± 1.5	61.8	2.4	18	1.2	-1.07 ± 0.02	0.30 ± 0.03	0.78 ± 0.04	0.11 ± 0.02	0.02 ± 0.03	-0.65 ± 0.02
12	1983	12	3	1	24	1.8 ± 0.2	3.3	-15.34 ± 0.01	0.31	-172.87 ± 0.02	0.09	44.7 ± 1.4	-37.3	2.7	18	1.6	-0.98 ± 0.03	0.56 ± 0.03	0.42 ± 0.03	-1.21 ± 0.04	0.36 ± 0.04	-0.46 ± 0.03
13	1984	5	11	10	41	55.0 ± 0.3	5.1	41.73 ± 0.02	-0.10	13.88 ± 0.02	-0.07	12.0		1.4	17	2.5	-2.55 ± 0.06	0.88 ± 0.05	1.67 ± 0.07	-0.65 ± 0.12	-0.25 ± 0.12	-0.99 ± 0.04
*14	1984	6	13	2	29	29.8 ± 0.2	5.2	31.57 ± 0.01	0.09	139.97 ± 0.02	-0.11	12.0		1.6	17	3.4	4.01 ± 0.09	-2.38 ± 0.07	-1.63 ± 0.10	-0.06 ± 0.19	-0.50 ± 0.22	-0.64 ± 0.07
15	1984	7	25	17	23	26.6 ± 0.4	5.8	1.25 ± 0.02	0.05	126.69 ± 0.03	0.22	20.2 ± 1.5	-21.8	1.3	17	2	1.45 ± 0.09	0.52 ± 0.06	-1.97 ± 0.09	0.84 ± 0.13	-0.22 ± 0.12	-0.50 ± 0.05
16	1984	8	30	19	2	37.3 ± 0.3	2.8	-4.15 ± 0.02	0.22	144.39 ± 0.04	0.13	37.5 ± 1.3	-15.5	0.9	16	5.3	4.17 ± 0.42	-4.67 ± 0.26	0.50 ± 0.36	-1.87 ± 0.20	0.47 ± 0.42	2.52 ± 0.14
17	1985	5	23	18	51	1.0 ± 0.3	0.7	-10.16 ± 0.01	0.05	165.25 ± 0.02	-0.01	16.0 ± 0.8	-17.0	0.9	16	5.5	-5.49 ± 0.27	5.31 ± 0.19	0.18 ± 0.17	-0.30 ± 0.39	0.08 ± 0.52	-1.18 ± 0.14
18	1985	11	21	2	27	22.1 ± 0.5	3.3	2.69 ± 0.03	0.33	126.88 ± 0.03	0.15	31.8 ± 2.1	-36.2	1.1	17	1.1	0.56 ± 0.10	0.04 ± 0.06	-0.60 ± 0.07	0.47 ± 0.08	-0.53 ± 0.08	-0.66 ± 0.05
19	1986	12	19	13	50	14.6 ± 0.4	4.2	51.51 ± 0.04	-0.01	-176.66 ± 0.04	0.33	49.2 ± 3.2	16.2	0.8	16	5	3.56 ± 0.35	-3.80 ± 0.30	0.24 ± 0.28	1.28 ± 0.27	2.32 ± 0.19	-2.17 ± 0.19
20	1987	2	18	5	28	26.3 ± 0.6	3.1	51.13 ± 0.05	-0.20	-179.11 ± 0.06	0.17	42.0 ± 3.5	9.0	1.1	17	1.2	0.90 ± 0.12	-0.85 ± 0.08	-0.06 ± 0.08	0.29 ± 0.07	0.60 ± 0.07	-0.39 ± 0.05
21	1987	3	16	17	20	48.8 ± 0.4	0.7	53.26 ± 0.04	-0.12	-167.19 ± 0.02	0.01	12.0		1.1	17	1.3	-1.13 ± 0.05	-0.04 ± 0.05	1.17 ± 0.04	0.26 ± 0.13	0.50 ± 0.11	0.07 ± 0.04
22	1988	3	21	13	17	41.7 ± 0.3	2.9	-8.14 ± 0.02	0.03	118.99 ± 0.04	0.05	17.1 ± 1.3	-15.9	1.0	16	7.7	4.65 ± 0.44	-4.95 ± 0.27	0.30 ± 0.34	-5.65 ± 0.73	-1.46 ± 0.73	-1.79 ± 0.20
23	1989	1	29	17	34	52.9 ± 0.4	4.0	44.65 ± 0.03	0.10	148.81 ± 0.04	0.07	50.7 ± 1.5	-0.3	0.9	16	6.1	5.75 ± 0.38	-0.92 ± 0.27	-4.83 ± 0.23	-0.84 ± 0.21	-0.35 ± 0.17	-2.84 ± 0.15
24	1989	3	1	4	26	33.7 ± 0.4	3.0	-4.99 ± 0.02	-0.04	149.87 ± 0.04	0.21	17.8 ± 1.0	-15.2	1.0	17	0.9	-0.72 ± 0.05	0.77 ± 0.03	-0.05 ± 0.03	0.34 ± 0.06	-0.29 ± 0.08	-0.02 ± 0.02
25	1989	4	25	3	11	24.6 ± 0.3	4.8	-17.31 ± 0.03	0.11	167.66 ± 0.02	-0.09	26.3 ± 1.0	-6.7	1.5	17	2.5	2.25 ± 0.14	-0.09 ± 0.08	-2.16 ± 0.09	0.41 ± 0.15	-1.16 ± 0.14	0.14 ± 0.05
26	1989	5	9	2	30	41.5 ± 0.6	6.0	28.45 ± 0.06	0.42	-16.31 ± 0.05	-0.14	25.0 ± 2.7	16.0	0.8	16	4.1	1.20 ± 0.29	-1.71 ± 0.20	0.50 ± 0.19	-2.61 ± 0.49	2.23 ± 0.41	2.38 ± 0.26
27	1989	5	28	10	20	4.4 ± 0.3	4.0	-16.62 ± 0.02	-0.09	-172.94 ± 0.02	0.48	38.0 ± 0.7	-12.0	1.1	17	1.2	0.96 ± 0.06	-1.10 ± 0.03	0.14 ± 0.04	-0.18 ± 0.03	-0.44 ± 0.03	0.26 ± 0.02
28	1989	12	4	6	42	35.9 ± 0.2	5.2	-15.17 ± 0.01	0.18	-172.86 ± 0.01	0.44	44.6 ± 0.8	-29.4	1.8	17	6.1	-4.77 ± 0.16	0.75 ± 0.10	4.02 ± 0.10	-3.53 ± 0.09	1.26 ± 0.10	-2.06 ± 0.09
29	1990	1	10	13	10	16.1 ± 0.2	4.0	52.03 ± 0.02	-0.10	-169.28 ± 0.03	-0.02	15.2 ± 1.1	-17.8	1.3	17	2.4	1.24 ± 0.07	-1.09 ± 0.06	-0.15 ± 0.04	1.94 ± 0.21	0.31 ± 0.12	-0.55 ± 0.03
*30	1990	5	15	15	21	31.1 ± 0.6	2.3	-2.96 ± 0.04	0.00	35.80 ± 0.02	-0.05	12.0		1.3	17	1.5	-1.67 ± 0.05	0.56 ± 0.04	1.11 ± 0.06	-0.46 ± 0.16	0.43 ± 0.14	-0.09 ± 0.04
31	1992	6	19	9	3	32.6 ± 0.4	5.3	53.78 ± 0.03	-0.09	160.99 ± 0.04	0.41	50.0 ± 2.7	17.0	0.8	16	2.9	2.41 ± 0.18	-1.36 ± 0.19	-1.05 ± 0.14	0.68 ± 0.11	1.10 ± 0.09	-1.53 ± 0.11
32	1992	6	27	13	21	27.5 ± 0.4	6.5	35.45 ± 0.03	0.27	80.94 ± 0.03	-0.18	24.9 ± 1.2	-8.1	0.9	16	5.3	-3.02 ± 0.35	-1.11 ± 0.27	4.13 ± 0.26	2.94 ± 0.50	1.01 ± 0.42	2.12 ± 0.17
33	1992	8	3	2	53	53.9 ± 0.3	2.0	15.87 ± 0.02	-0.06	-60.73 ± 0.02	0.11	32.5 ± 0.9	-11.5	1.2	17	1.4	-0.73 ± 0.04	1.19 ± 0.03	-0.47 ± 0.03	-0.43 ± 0.05	0.46 ± 0.05	0.66 ± 0.03
*34	1992	8	20	18	31	39.9 ± 0.2	5.2	25.43 ± 0.02	-0.05	141.13 ± 0.02	-0.20	12.0		1.0	17	0.7	0.79 ± 0.02	-0.28 ± 0.01	-0.51 ± 0.02	-0.09 ± 0.04	-0.24 ± 0.05	-0.11 ± 0.01
35	1992	10	23	4	27	54.9 ± 0.4	-5.8	-29.66 ± 0.03	-0.09	-176.72 ± 0.02	1.45	17.7 ± 0.9	-15.3	0.9	16	7.3	6.29 ± 0.36	-1.21 ± 0.23	-5.08 ± 0.25	1.64 ± 0.56	3.89 ± 0.47	-1.45 ± 0.15
36	1992	11	1	10	3	18.8 ± 0.3	1.0	-55.73 ± 0.02	-0.11	-27.32 ± 0.04	0.12	12.0		1.1	17	0.9	-0.71 ± 0.03	0.56 ± 0.02	0.15 ± 0.03	-0.16 ± 0.08	0.57 ± 0.07	0.35 ± 0.03
37	1993	5	19	12	3	32.1 ± 0.2	4.5	-8.40 ± 0.01	-0.02	122.23 ± 0.02	0.16	18.1 ± 0.6	-15.9	1.5	17	2.8	1.52 ± 0.08	-2.14 ± 0.05	0.62 ± 0.07	-0.29 ± 0.12	1.34 ± 0.16	-1.60 ± 0.05
*38	1994	1	16	10	18	41.5 ± 0.1	2.9	-20.62 ± 0.01	0.00	-175.20 ± 0.01	0.31	12.0		1.1	17	1.1	1.23 ± 0.02	-0.67 ± 0.02	-0.56 ± 0.02	0.07 ± 0.04	0.03 ± 0.05	0.32 ± 0.01
39	1994	7	15	16	4	31.6 ± 0.2	1.9	-16.49 ± 0.02	0.01	167.28 ± 0.01	-0.31	18.4 ± 0.7	-14.6	0.8	16	4.2	-3.20 ± 0.21	2.08 ± 0.14	1.11 ± 0.14	1.25 ± 0.26	-0.53 ± 0.23	2.94 ± 0.09
*40	1995	1	10	13	43	35.8 ± 0.0	1.9	-14.22		-169.06		12.0		0.9	16	0.9	-2.67 ± 0.10	1.44 ± 0.10	1.23 ± 0.08	-0.97 ± 0.20	1.52 ± 0.17	-0.51 ± 0.07
41	1995	4	8	19	13	55.7 ± 0.4	3.8	51.96 ± 0.02	-0.23	159.61 ± 0.04	0.48	51.1 ± 1.7	18.1	1.1	17	1.2	1.11 ± 0.10	-0.50 ± 0.07	-0.61 ± 0.07	0.11 ± 0.04	0.32 ± 0.04	-0.72 ± 0.04
42	1995	7	4	22	22	50.9 ± 0.4	1.2	-29.26 ± 0.03	0.05	-176.99 ± 0.03	0.48	36.3 ± 1.5	-9.7	0.8	16	4.1	3.47 ± 0.29	-0.76 ± 0.23	-2.71 ± 0.17	0.49 ± 0.16	2.25 ± 0.15	-1.37 ± 0.14
43	1995	8	26	9	9	3.9 ± 0.3	3.4	-6.63 ± 0.02	-0.34	154.34 ± 0.02	0.06	20.7 ± 0.8	-22.3	1.0	17	0.8	0.79 ± 0.05	-0.42 ± 0.03	-0.38 ± 0.03	0.29 ± 0.04	-0.23 ± 0.04	0.31 ± 0.02
44	1996	3	5	19	48	35.2 ± 0.3	4.0	11.56 ± 0.02	-0.08	-87.21 ± 0.02	-0.27	38.6 ± 0.8	-46.4	0.9	16	6.4	5.35 ± 0.33	-4.48 ± 0.19	-0.87 ± 0.23	2.10 ± 0.12	-0.90 ± 0.16	3.59 ± 0.17
45	1996	4	8	20	8	32.5 ± 0.2	1.9	-6.28 ± 0.01	-0.21	148.67 ± 0.02	0.21	53.2 ± 1.2	-33.8	0.8	16	3.9	3.08 ± 0.16	-4.10 ± 0.09	1.03 ± 0.13	0.22 ± 0.07	-1.08 ± 0.08	0.55 ± 0.08
46	1996	5	27	5	45	28.5 ± 0.1	-2.1	10.00 ± 0.01	0.05	124.00 ± 0.01	-0.09	12.0		1.0	17	0.9	0.82 ± 0.02	-0.34 ± 0.01	-0.48 ± 0.02	-0.13 ± 0.04	-0.20 ± 0.04	-0.45 ± 0.01
*47	1996	9	4	18	16	7.7 ± 0.1	5.8	31.51 ± 0.01	-0.05	139.99 ± 0.01	0.06	12.0		1.7	17	3.9	4.49 ± 0.04	-2.61 ± 0.04	-1.88 ± 0.05	-0.31 ± 0.10	-0.96 ± 0.10	-0.73 ± 0.04
*48	1996	9	9	4	34	21.9 ± 0.1	1.4	30.44 ± 0.01	0.01	130.95 ± 0.01	0.22	12.0		1.7	17	4.2	-4.79 ± 0.04	1.81 ± 0.04	2.98 ± 0.04	-0.49 ± 0.10	-0.69 ± 0.10	-0.85 ± 0.03
49	1996	12	10	16	57	43.6 ± 0.1	3.9	51.82 ± 0.01	0.00	-177.40 ± 0.02	0.16	12.0		1.1	17	1.2	-1.16 ± 0.02	0.92 ± 0.02	0.24 ± 0.01	0.11 ± 0.04	0.20 ± 0.04	-0.47 ± 0.01
50	1997	6	6	12	1	9.9 ± 0.2	5.7	-7.57 ± 0.01	-0.20	156.12 ± 0.01	0.10	28.1 ± 0.5	1.1	0.9	16	5.7	5.03 ± 0.22	-3.67 ± 0.14	-1.36 ± 0.14	0.40 ± 0.18	-1.41 ± 0.18	3.32 ± 0.10

* shallow vertical-CLVD earthquake

Table A1. (continued)

No.	Centroid Parameters													Half Drtn	Scale Factor 10^{ex}	M_0	Elements of Moment Tensor					
	Date			Time				Latitude		Longitude		Depth										
	Y	M	D	h	m	sec	δt_0	l	$\delta\lambda_0$	ϕ	$\delta\phi_0$	h	δh_0				M_{rr}	$M_{\theta\theta}$	$M_{\phi\phi}$	$M_{r\theta}$	$M_{r\phi}$	$M_{\theta\phi}$
*51	1997	9	5	3	23	17.0 ± 0.1	2.6	-56.41 ± 0.01	-0.15	-27.47 ± 0.01	0.35	12.0		1.3	17	1.7	1.86 ± 0.02	-0.95 ± 0.02	-0.89 ± 0.02	-0.34 ± 0.05	-0.83 ± 0.05	0.20 ± 0.02
52	1997	9	17	12	34	31.9 ± 0.2	5.6	-11.19 ± 0.01	-0.09	165.60 ± 0.01	-0.20	30.9 ± 0.8	-9.6	0.8	16	4.3	-2.66 ± 0.20	2.34 ± 0.12	0.33 ± 0.13	0.44 ± 0.12	-2.93 ± 0.14	1.93 ± 0.07
53	1997	9	27	11	28	20.5 ± 0.2	6.2	-10.79 ± 0.01	-0.04	165.45 ± 0.01	-0.07	29.5 ± 0.6	7.0	1.0	17	0.9	0.44 ± 0.03	0.04 ± 0.02	-0.48 ± 0.02	-0.31 ± 0.02	0.36 ± 0.02	-0.64 ± 0.01
54	1997	11	20	6	8	18.2 ± 0.1	7.8	-59.24 ± 0.01	-0.18	-25.01 ± 0.02	0.50	39.5 ± 0.4	6.5	1.4	17	2.6	2.29 ± 0.05	-0.06 ± 0.04	-2.24 ± 0.03	0.66 ± 0.04	0.12 ± 0.04	-1.01 ± 0.03
55	1998	10	3	6	0	13.4 ± 0.2	5.8	-56.67 ± 0.02	-0.06	-25.13 ± 0.02	0.27	18.4 ± 0.5	-14.6	1.0	17	1	0.87 ± 0.03	-0.05 ± 0.02	-0.81 ± 0.02	0.11 ± 0.04	0.39 ± 0.04	0.33 ± 0.01
56	1998	11	4	2	54	16.0 ± 0.2	2.1	51.64 ± 0.03	-0.45	-176.00 ± 0.03	0.14	50.4 ± 3.2	15.0	0.6	16	1.9	-0.97 ± 0.13	-0.54 ± 0.12	1.51 ± 0.08	-0.34 ± 0.07	1.35 ± 0.07	0.30 ± 0.07
57	1998	12	14	22	16	0.9 ± 0.3	-1.1	-7.05 ± 0.02	0.15	128.88 ± 0.05	-0.21	12.0		0.6	16	2	1.56 ± 0.13	-2.09 ± 0.07	0.53 ± 0.13	-0.59 ± 0.26	-0.47 ± 0.44	0.04 ± 0.09
58	1999	2	25	16	39	10.9 ± 0.2	4.9	-22.73 ± 0.01	-0.20	170.71 ± 0.02	0.02	17.2 ± 0.8	-15.8	1.1	17	1.2	0.86 ± 0.04	-0.74 ± 0.03	-0.12 ± 0.02	0.75 ± 0.06	0.01 ± 0.05	0.36 ± 0.01
59	1999	3	26	14	27	45.9 ± 0.2	1.1	-58.09 ± 0.02	-0.16	-25.15 ± 0.03	0.49	52.7 ± 1.0	-23.4	1.0	17	0.9	0.87 ± 0.03	0.02 ± 0.03	-0.89 ± 0.02	0.04 ± 0.02	0.17 ± 0.02	0.13 ± 0.02
*60	1999	6	29	5	50	9.2 ± 0.1	0.3	-9.59 ± 0.01	-0.12	147.97 ± 0.01	0.12	12.0		1.6	17	2.8	-2.72 ± 0.03	1.50 ± 0.03	1.23 ± 0.03	-1.88 ± 0.08	-0.13 ± 0.07	0.01 ± 0.03
61	1999	7	3	15	26	6.6 ± 0.3	1.1	61.42 ± 0.02	-0.03	-150.28 ± 0.05	0.17	53.8 ± 1.5	-6.9	0.6	16	1.5	-1.57 ± 0.08	0.61 ± 0.09	0.96 ± 0.10	0.10 ± 0.04	0.22 ± 0.04	0.61 ± 0.05
*62	1999	8	7	6	17	30.5 ± 0.1	1.6	-21.24 ± 0.01	-0.15	-175.61 ± 0.01	0.45	12.0		1.4	17	2.6	2.97 ± 0.03	-1.19 ± 0.03	-1.78 ± 0.03	-0.71 ± 0.07	0.08 ± 0.07	0.40 ± 0.02
63	1999	8	13	0	30	30.7 ± 0.2	2.9	51.96 ± 0.02	-0.09	-169.59 ± 0.02	-0.14	19.0 ± 0.8	-14.0	0.8	16	3.8	2.67 ± 0.14	-2.13 ± 0.09	-0.54 ± 0.09	2.73 ± 0.18	0.11 ± 0.13	-1.05 ± 0.05
64	1999	11	29	11	7	8.3 ± 0.2	5.5	0.75 ± 0.01	0.19	126.27 ± 0.01	0.16	12.0		1.7	17	3.5	-1.27 ± 0.03	1.13 ± 0.03	0.14 ± 0.04	0.11 ± 0.08	-3.31 ± 0.09	-0.67 ± 0.03
*65	1999	12	4	8	46	57.7 ± 0.2	0.9	51.56 ± 0.02	0.09	-178.29 ± 0.02	0.13	12.0		0.8	16	6.4	-4.64 ± 0.13	1.50 ± 0.13	3.14 ± 0.09	5.20 ± 0.29	1.77 ± 0.29	0.07 ± 0.09
66	2000	7	6	6	27	45.7 ± 0.2	6.1	34.08 ± 0.01	-0.03	139.40 ± 0.01	0.09	12.0		0.9	16	5.4	-4.20 ± 0.14	1.17 ± 0.13	3.03 ± 0.12	-0.73 ± 0.31	0.21 ± 0.31	-4.16 ± 0.10
67	2000	7	29	15	54	17.3 ± 0.2	0.4	51.10 ± 0.02	-0.05	-179.27 ± 0.02	0.06	22.8 ± 0.6	-26.3	0.8	16	3.7	3.48 ± 0.15	-2.93 ± 0.10	-0.56 ± 0.09	1.10 ± 0.11	0.06 ± 0.11	-1.41 ± 0.05
68	2000	8	3	11	27	10.5 ± 0.2	6.4	34.23 ± 0.01	0.13	139.33 ± 0.01	0.18	12.0		0.9	16	5.7	-5.44 ± 0.12	2.78 ± 0.11	2.66 ± 0.11	0.31 ± 0.30	-0.54 ± 0.32	-3.25 ± 0.08
69	2000	8	24	2	25	7.3 ± 0.2	4.7	31.06 ± 0.02	-0.09	139.88 ± 0.01	0.07	12.0		0.8	16	4	-3.45 ± 0.08	-0.13 ± 0.07	3.58 ± 0.08	-0.99 ± 0.23	1.52 ± 0.20	-0.28 ± 0.06
70	2000	12	27	7	26	37.1 ± 0.1	5.5	-4.25 ± 0.01	-0.02	152.71 ± 0.01	-0.02	29.3 ± 0.3	-3.7	1.8	17	4.4	4.31 ± 0.11	-0.27 ± 0.07	-4.03 ± 0.07	0.56 ± 0.10	0.01 ± 0.09	1.34 ± 0.05
*71	2001	1	18	20	17	17.4 ± 0.1	3.0	-56.31 ± 0.01	-0.10	-27.43 ± 0.02	0.07	12.0		1.2	17	1.3	1.52 ± 0.02	-0.64 ± 0.02	-0.88 ± 0.02	-0.20 ± 0.06	-0.49 ± 0.06	0.16 ± 0.02
72	2001	4	5	13	54	27.9 ± 0.4	1.7	15.97 ± 0.02	0.06	-60.70 ± 0.03	0.18	28.6 ± 0.8	-23.1	0.8	16	4.2	-3.57 ± 0.26	2.97 ± 0.17	0.61 ± 0.18	-0.73 ± 0.18	1.50 ± 0.19	2.02 ± 0.12
73	2001	5	22	0	12	32.5 ± 0.5	2.9	-4.39 ± 0.02	-0.18	153.17 ± 0.03	0.39	33.4 ± 1.5	0.4	0.7	16	3.3	2.80 ± 0.41	-0.26 ± 0.23	-2.54 ± 0.22	0.14 ± 0.14	-1.04 ± 0.20	1.67 ± 0.11
74	2001	7	4	10	23	33.9 ± 0.2	2.0	32.18 ± 0.02	-0.01	139.69 ± 0.01	0.19	12.0		1.0	17	0.8	-0.72 ± 0.02	-0.10 ± 0.02	0.82 ± 0.02	-0.11 ± 0.07	0.28 ± 0.05	0.08 ± 0.01
75	2001	8	26	4	17	8.3 ± 0.6	4.7	1.32 ± 0.04	0.18	126.73 ± 0.04	0.37	26.9 ± 1.4	-6.1	0.7	16	2.8	2.56 ± 0.25	-0.06 ± 0.14	-2.51 ± 0.18	-0.01 ± 0.23	1.07 ± 0.21	0.00 ± 0.09
76	2001	9	5	19	43	24.5 ± 0.2	6.1	-4.73 ± 0.01	-0.12	152.90 ± 0.02	0.04	50.3 ± 1.1	17.3	0.8	16	4.5	-4.39 ± 0.17	2.83 ± 0.12	1.56 ± 0.12	2.05 ± 0.10	1.63 ± 0.10	-0.93 ± 0.11
77	2001	9	11	18	21	15.7 ± 0.3	6.5	45.35 ± 0.02	-0.10	150.83 ± 0.03	0.15	37.9 ± 1.4	4.9	0.8	16	6.7	5.74 ± 0.62	-3.91 ± 0.39	-1.83 ± 0.37	0.72 ± 0.26	2.96 ± 0.20	-3.11 ± 0.16
78	2001	12	28	0	41	43.4 ± 0.3	4.8	23.96 ± 0.02	-0.16	122.94 ± 0.02	0.17	35.5 ± 1.9	25.5	0.8	16	4.8	-1.95 ± 0.25	-1.04 ± 0.18	2.99 ± 0.17	-0.69 ± 0.13	-3.58 ± 0.23	2.29 ± 0.13
79	2002	3	30	8	57	34.1 ± 0.5	7.9	-5.01 ± 0.04	-0.21	103.10 ± 0.05	-0.03	57.3 ± 6.0	24.3	0.5	16	1.1	0.93 ± 0.16	-0.84 ± 0.10	-0.09 ± 0.14	0.51 ± 0.07	-0.36 ± 0.08	0.25 ± 0.06
80	2002	5	18	4	22	49.5 ± 0.3	6.6	-14.39 ± 0.02	-0.06	166.72 ± 0.02	-0.27	41.6 ± 1.0	8.6	0.7	16	3.1	2.83 ± 0.16	-0.32 ± 0.11	-2.50 ± 0.10	0.03 ± 0.08	0.82 ± 0.08	1.42 ± 0.08
81	2002	6	19	22	45	52.7 ± 0.2	1.1	-19.17 ± 0.01	0.07	169.88 ± 0.01	0.22	12.0		1.2	17	1.2	-1.23 ± 0.02	0.46 ± 0.02	0.77 ± 0.03	0.12 ± 0.06	-0.22 ± 0.06	-0.52 ± 0.02
82	2002	6	19	23	8	26.8 ± 0.3	2.2	-19.14 ± 0.02	0.07	169.86 ± 0.02	0.22	12.0		1.3	17	1.7	-1.67 ± 0.04	0.61 ± 0.04	1.06 ± 0.04	0.33 ± 0.11	-0.46 ± 0.11	-0.64 ± 0.03
83	2002	8	21	17	11	18.9 ± 0.2	4.5	51.41 ± 0.02	-0.07	-178.14 ± 0.02	0.21	46.2 ± 1.5	13.2	0.7	16	3.1	2.29 ± 0.12	-2.45 ± 0.09	0.16 ± 0.10	1.22 ± 0.07	1.08 ± 0.06	-1.21 ± 0.06
84	2002	10	24	2	27	56.2 ± 0.2	4.2	25.20 ± 0.01	-0.02	123.78 ± 0.02	-0.01	12.0		0.9	16	5.9	-5.43 ± 0.15	5.61 ± 0.13	-0.17 ± 0.15	-1.78 ± 0.36	1.12 ± 0.44	0.58 ± 0.11
85	2002	10	24	3	22	26.4 ± 0.3	2.9	25.21 ± 0.01	-0.02	123.73 ± 0.03	-0.11	12.0		0.8	16	4.9	-4.57 ± 0.15	4.68 ± 0.14	-0.12 ± 0.15	-1.14 ± 0.35	1.33 ± 0.43	0.10 ± 0.11
86	2002	10	24	4	19	10.6 ± 0.2	3.4	25.18 ± 0.01	0.05	123.76 ± 0.02	-0.07	12.0		0.9	16	7.1	-6.76 ± 0.16	7.00 ± 0.14	-0.25 ± 0.16	-1.25 ± 0.37	0.92 ± 0.48	0.74 ± 0.12
87	2002	11	20	18	19	41.8 ± 0.3	4.6	12.45 ± 0.02	-0.21	-88.48 ± 0.03	-0.29	47.9 ± 1.1	-3.7	0.8	16	3.7	3.24 ± 0.15	-2.95 ± 0.11	-0.29 ± 0.14	0.59 ± 0.07	-0.21 ± 0.10	1.98 ± 0.09
88	2003	4	1	8	31	5.2 ± 0.2	2.8	46.84 ± 0.02	-0.11	153.44 ± 0.02	0.19	42.7 ± 0.7	-8.8	0.8	16	4.3	-4.37 ± 0.17	3.40 ± 0.12	0.97 ± 0.12	-0.43 ± 0.09	0.35 ± 0.08	1.45 ± 0.06
89	2003	5	17	1	46	24.8 ± 0.5	4.0	51.55 ± 0.03	-0.07	160.18 ± 0.04	0.38	19.3 ± 1.4	-16.0	0.5	16	1.4	0.97 ± 0.11	-0.20 ± 0.06	-0.77 ± 0.07	0.49 ± 0.12	0.58 ± 0.10	-0.73 ± 0.04
90	2003	7	27	19	8	8.6 ± 0.2	5.0	38.59 ± 0.02	0.05	141.14 ± 0.01	0.12	12.0		0.7	16	3.1	3.08 ± 0.06	-0.13 ± 0.06	-2.95 ± 0.05	-0.66 ± 0.20	-0.19 ± 0.16	-0.14 ± 0.04
91	2003	9	29	23	7	12.0 ± 0.5	3.7	-5.74 ± 0.03	-0.33	152.20 ± 0.04	0.60	27.9 ± 1.5	-5.1	0.7	16	3.3	2.96 ± 0.31	-2.37 ± 0.19	-0.58 ± 0.19	1.75 ± 0.20	0.05 ± 0.27	-0.58 ± 0.11
92	2004	8	28	16	13	17.1 ± 0.3	2.8	-9.01 ± 0.02	-0.35	157.55 ± 0.02	0.31	12.0		1.4	17	1.6	1.48 ± 0.05	-0.79 ± 0.05	-0.69 ± 0.05	0.67 ± 0.16	0.12 ± 0.16	0.62 ± 0.04
93	2004	9	28	18	28	5.3 ± 0.6	2.1	51.62 ± 0.06	0.00	-175.77 ± 0.06	0.21	59.4 ± 7.5	13.6	0.7	16	3.1	2.88 ± 0.34	-3.05 ± 0.29	0.17 ± 0.31	0.20 ± 0.32	0.63 ± 0.16	-0.76 ± 0.28
94	2004	10	23	9	57	30.0 ± 0.9	3.6	37.31 ± 0.06	0.12	138.82 ± 0.06	0.08	12.0		1.0	16	7.6	6.54 ± 0.79	-1.43 ± 0.65	-5.12 ± 0.68	2.07 ± 1.32	2.71 ± 1.48	-3.38 ± 0.50
95	2004	10	25	1	22	5.0 ± 0.5	7.2	16.78 ± 0.03	-0.17	145.22 ± 0.04	-0.66	12.0		0.7	16	1.4	-0.53 ± 0.08	0.01 ± 0.05	0.52 ± 0.07	0.46 ± 0.12	1.18 ± 0.12	0.34 ± 0.04
96	2004	11	5	17	53	25.2 ± 0.6	3.8	37.41 ± 0.03	0.07	138.90 ± 0.04	0.02	12.0		0.7	16	2.6	2.47 ± 0.14	-0.23 ± 0.11	-2.24 ± 0.11	0.14 ± 0.37	-0.16 ± 0.31	-1.00 ± 0.10
97	2004	11	8	2	27	14.6 ± 0.5	4.2	37.39 ± 0.03	0.06	138.90 ± 0.03	0.06	12.0		0.6	16	1.9	1.76 ± 0.08	0.04 ± 0.07	-1.79 ± 0.07	0.44 ± 0.24	0.22 ± 0.21	-0.50 ± 0.06
*98	2004	11	10	10	35	38.0 ± 0.1	4.0	-21.26 ± 0.01	-0.07	-175.62 ± 0.01	0.48	12.0		1.4	17	2.4	2.74 ± 0.03	-1.20 ± 0.03	-1.54 ± 0.03	-0.71 ± 0.07	0.17 ± 0.07	0.44 ± 0.02
99	2004	11	23	3	15	32.4 ± 0.4	-0.2	50.88 ± 0.03	-0.29	179.32 ± 0.03	0.01	23.6 ± 2.1	-21.5	1.0	16	6.3	4.51 ± 0.88	-4.45 ± 0.51	-0.06 ± 0.43	4.14 ± 0.45	1.36 ± 0.31	-1.04 ± 0.14
100	2005	2	11	0	38	19.6 ± 0.6	8.0	-17.43 ± 0.03	0.06	168.01 ± 0.03	-0.39	12.0		0.6	16	1	-0.84 ± 0.07	0.88 ± 0.05	-0.04 ± 0.05	-0.15 ± 0.12	0.08 ± 0.16	0.50 ± 0.05

* shallow vertical-CLVD earthquake

Table A1. (continued)

No.	Centroid Parameters													Half Drtn	Scale Factor 10^{ex}	M_0	Elements of Moment Tensor					
	Date			Time				Latitude		Longitude		Depth					M_{rr}	$M_{\theta\theta}$	$M_{\phi\phi}$	$M_{r\theta}$	$M_{r\phi}$	$M_{\theta\phi}$
	Y	M	D	h	m	sec	δt_0	l	$\delta\lambda_0$	ϕ	$\delta\phi_0$	h	δh_0									
101	2005	2	25	8	33	3.1 ± 0.3	1.9	15.87 ± 0.03	-0.04	144.83 ± 0.02	-0.16	12.0		0.6	16	1.8	-1.82 ± 0.05	0.18 ± 0.04	1.64 ± 0.06	0.01 ± 0.16	0.28 ± 0.14	-0.33 ± 0.04
*102	2005	2	25	16	17	1.6 ± 0.2	0.3	12.77 ± 0.01	0.06	123.23 ± 0.02	-0.10	12.0		0.7	16	2.8	-2.83 ± 0.06	2.05 ± 0.05	0.79 ± 0.06	-0.91 ± 0.16	0.81 ± 0.20	-0.49 ± 0.04
103	2005	4	10	13	54	16.2 ± 0.5	-0.1	-1.78 ± 0.03	0.00	99.65 ± 0.04	-0.28	18.4 ± 1.6	-13.8	1.2	17	1.2	0.99 ± 0.18	-1.12 ± 0.11	0.13 ± 0.10	-0.28 ± 0.12	-0.48 ± 0.19	0.31 ± 0.06
104	2005	5	17	7	16	35.3 ± 0.6	-0.4	-8.33 ± 0.04	0.05	117.71 ± 0.06	0.07	12.0		0.5	16	0.9	0.53 ± 0.08	-0.42 ± 0.05	-0.11 ± 0.07	-0.67 ± 0.14	-0.15 ± 0.18	-0.28 ± 0.04
105	2005	6	5	12	32	31.3 ± 0.6	3.9	-7.07 ± 0.04	-0.34	155.37 ± 0.05	0.02	39.7 ± 2.2	5.6	0.6	16	1.5	1.46 ± 0.19	-0.99 ± 0.12	-0.47 ± 0.11	0.17 ± 0.10	-0.30 ± 0.09	0.66 ± 0.07
*106	2005	8	23	1	38	20.1 ± 0.2	3.0	-59.80 ± 0.01	-0.43	-26.68 ± 0.02	0.35	12.0		0.9	16	6.6	6.15 ± 0.11	-3.96 ± 0.12	-2.18 ± 0.11	3.84 ± 0.30	0.89 ± 0.31	-1.06 ± 0.09
*107	2005	8	31	1	24	54.9 ± 0.1	6.3	-59.48 ± 0.01	-0.12	-26.86 ± 0.02	0.24	12.0		1.4	17	2.1	2.12 ± 0.02	-1.33 ± 0.03	-0.79 ± 0.03	-1.09 ± 0.06	-0.68 ± 0.06	-0.08 ± 0.02
108	2005	9	22	19	51	57.8 ± 0.3	5.2	12.78 ± 0.02	0.36	40.54 ± 0.02	0.07	12.0		0.8	16	3.9	-3.67 ± 0.13	1.37 ± 0.10	2.30 ± 0.12	-0.56 ± 0.30	0.62 ± 0.31	-2.00 ± 0.09
109	2005	9	25	1	11	1.3 ± 0.3	2.6	12.57 ± 0.02	0.31	40.65 ± 0.02	0.14	12.0		0.7	16	3	-3.00 ± 0.10	0.89 ± 0.07	2.10 ± 0.10	-0.04 ± 0.22	-0.20 ± 0.24	-1.34 ± 0.07
110	2005	9	26	13	28	36.0 ± 0.5	2.7	12.91 ± 0.05	0.59	40.53 ± 0.03	0.07	12.0		0.8	16	5.3	-5.31 ± 0.35	0.53 ± 0.23	4.78 ± 0.28	1.03 ± 0.89	-0.13 ± 0.55	-1.06 ± 0.22
*111	2005	10	22	20	34	47.9 ± 0.2	6.0	-1.06 ± 0.01	-0.20	-91.31 ± 0.01	-0.36	12.0		1.3	17	1.9	1.52 ± 0.02	-1.05 ± 0.02	-0.47 ± 0.03	0.87 ± 0.05	-1.31 ± 0.06	-0.10 ± 0.02
*112	2006	1	1	7	12	8.8 ± 0.1	11.8	31.60 ± 0.01	0.21	140.17 ± 0.01	0.04	12.0		1.5	17	2.9	3.10 ± 0.04	-2.27 ± 0.04	-0.83 ± 0.04	-0.86 ± 0.09	-0.27 ± 0.10	-0.39 ± 0.03
113	2006	9	25	7	46	31.3 ± 0.1	0.6	-6.39 ± 0.01	-0.24	154.41 ± 0.01	0.05	48.1 ± 0.4	-13.1	1.3	17	1.6	1.93 ± 0.03	-1.17 ± 0.02	-0.76 ± 0.02	0.04 ± 0.02	-0.48 ± 0.02	0.15 ± 0.02
114	2007	7	15	11	24	23.4 ± 0.3	2.0	-2.68 ± 0.02	0.25	35.92 ± 0.02	-0.32	12.8 ± 0.9	2.8	1.0	16	7	-6.05 ± 0.39	5.33 ± 0.25	0.72 ± 0.28	0.98 ± 0.48	-3.07 ± 0.70	2.68 ± 0.17
115	2007	7	26	18	54	40.2 ± 0.4	3.0	-2.68 ± 0.02	0.00	35.90 ± 0.04	-0.11	12.0		0.8	16	4.2	-4.03 ± 0.22	3.10 ± 0.16	0.92 ± 0.23	-0.45 ± 0.45	-0.55 ± 0.61	1.84 ± 0.15
116	2007	9	27	20	47	24.2 ± 0.4	3.7	-21.55 ± 0.03	-0.36	169.19 ± 0.03	-0.07	21.5 ± 1.6	11.5	1.0	16	7.5	-5.85 ± 0.97	1.12 ± 0.59	4.72 ± 0.53	-4.31 ± 0.78	-0.04 ± 0.45	3.12 ± 0.25
117	2008	4	11	1	41	51.2 ± 0.4	3.7	16.00 ± 0.04	-0.13	144.78 ± 0.02	-0.31	12.0		0.6	16	1.7	-1.78 ± 0.08	0.31 ± 0.06	1.47 ± 0.07	-0.13 ± 0.26	0.49 ± 0.22	0.03 ± 0.06
118	2008	4	11	19	20	58.5 ± 0.4	1.8	16.19 ± 0.03	-0.05	144.74 ± 0.02	-0.47	12.0		0.7	16	3	-3.00 ± 0.11	0.19 ± 0.09	2.81 ± 0.10	0.41 ± 0.34	0.68 ± 0.28	-0.26 ± 0.09
119	2008	6	3	23	43	30.1 ± 0.5	3.5	-8.19 ± 0.03	-0.05	120.09 ± 0.07	-0.04	20.2 ± 1.6	10.2	0.8	16	3.4	3.16 ± 0.55	-3.22 ± 0.30	0.06 ± 0.35	-0.96 ± 0.38	-0.32 ± 0.57	-0.24 ± 0.17
*120	2008	6	12	13	10	14.7 ± 0.1	1.7	25.53 ± 0.01	0.07	141.18 ± 0.01	-0.07	12.0		1.1	17	1.1	1.25 ± 0.01	-0.55 ± 0.01	-0.70 ± 0.02	-0.10 ± 0.03	0.05 ± 0.04	-0.22 ± 0.01
*121	2008	11	18	12	46	3.8 ± 0.2	0.8	-18.76 ± 0.02	0.28	169.55 ± 0.02	0.08	12.0		0.9	16	3.5	-3.07 ± 0.10	1.57 ± 0.09	1.50 ± 0.08	1.86 ± 0.26	0.88 ± 0.29	-1.33 ± 0.07
*122	2009	2	17	3	30	58.8 ± 0.1	5.5	-30.54 ± 0.01	0.18	-178.58 ± 0.01	0.04	12.0		2.0	17	6.5	7.34 ± 0.05	-2.72 ± 0.05	-4.63 ± 0.05	-2.00 ± 0.15	-0.77 ± 0.14	1.21 ± 0.04
*123	2009	4	19	8	54	52.8 ± 0.3	6.2	14.66 ± 0.02	-0.16	144.23 ± 0.02	-0.33	12.0		0.7	16	3.1	-3.12 ± 0.11	0.95 ± 0.08	2.16 ± 0.10	-1.21 ± 0.33	0.58 ± 0.25	0.87 ± 0.07
*124	2009	5	26	0	49	42.9 ± 0.1	-4.2	-21.24 ± 0.01	-0.10	-175.62 ± 0.01	1.32	12.0		1.3	17	2	2.30 ± 0.02	-0.89 ± 0.02	-1.41 ± 0.02	-0.19 ± 0.06	-0.22 ± 0.06	0.42 ± 0.02

* shallow vertical-CLVD earthquake

Note: The last earthquake is also reported in the Surface Wave catalog (Category 1) - Table A3.

Table A2. Recalculated principal axes and best-double-couple parameters for 124 vertical-CLVD earthquakes in the Global CMT Catalog, 1976 - 2009.

No.	Scale Factor 10^{ex}	Principal Axes									M_0	Best Double Couple					
		T-axis			N-axis			P-axis				Plane 1			Plane 2		
		σ	δ	ε	σ	δ	ε	σ	δ	ε		φ_s	θ	λ	φ_s	θ	λ
1	17	3.37	72	301	-0.07	12	172	-3.30	14	79	3.3	153	33	68	358	60	104
2	18	1.37	65	244	-0.08	18	18	-1.30	17	114	1.3	229	32	125	9	64	70
*3	17	1.58	82	342	-0.64	2	83	-0.95	8	173	1.3	265	37	93	82	53	88
*4	17	1.93	68	120	-0.72	7	226	-1.21	21	319	1.6	61	24	106	223	67	83
5	17	3.81	76	66	0.18	14	251	-3.99	1	161	3.9	237	45	70	84	48	109
*6	17	2.53	88	293	-0.64	1	152	-1.89	1	62	2.2	151	44	88	334	46	92
7	16	6.07	74	191	0.27	15	358	-6.35	3	88	6.2	194	44	113	344	50	70
8	17	4.54	60	149	0.24	23	285	-4.79	19	23	4.7	146	33	135	275	67	65
9	17	5.10	75	189	0.41	8	310	-5.50	12	42	5.3	142	33	104	305	58	81
10	17	1.69	84	127	0.06	1	30	-1.76	6	300	1.7	30	39	89	211	51	91
11	18	1.23	1	55	-0.14	6	325	-1.08	84	156	1.2	151	44	-81	319	46	-99
12	18	1.53	26	211	0.12	10	116	-1.65	62	6	1.6	324	21	-60	112	72	-101
13	17	2.35	2	235	0.37	13	145	-2.71	77	333	2.5	338	45	-71	133	48	-108
*14	17	4.05	85	90	-1.29	4	239	-2.76	3	329	3.4	64	43	96	235	48	84
15	17	2.00	58	12	0.07	32	190	-2.07	1	281	2.0	39	52	132	163	54	49
16	16	4.55	78	176	1.50	5	291	-6.05	11	22	5.3	118	35	99	288	56	84
17	16	5.58	2	192	-0.08	0	282	-5.50	88	18	5.5	282	43	-90	103	47	-90
18	17	1.20	47	38	-0.15	41	200	-1.05	9	298	1.1	65	51	148	177	66	43
19	16	4.76	63	273	0.51	22	57	-5.27	14	153	5.0	271	37	129	45	63	65
20	17	1.20	65	277	-0.06	20	57	-1.14	15	152	1.2	268	35	126	46	63	68
21	17	1.29	12	275	-0.01	10	8	-1.28	74	135	1.3	353	34	-108	194	58	-78
22	16	7.31	65	168	0.85	2	74	-8.16	24	344	7.7	70	21	85	255	70	92
23	16	5.85	83	180	0.51	6	28	-6.36	3	298	6.1	21	42	81	214	49	98
24	17	0.85	13	5	0.04	17	99	-0.88	68	239	0.9	74	35	-120	289	60	-70
25	17	2.59	74	60	-0.12	6	173	-2.47	14	264	2.5	3	31	102	169	60	83
26	16	3.19	56	250	1.88	16	134	-5.08	29	35	4.1	88	22	41	318	76	107
27	17	1.18	65	106	-0.03	25	279	-1.16	3	11	1.2	125	48	125	258	53	58
28	17	5.77	16	237	0.72	20	141	-6.50	64	3	6.1	354	34	-53	131	64	-112
29	17	2.34	60	0	0.03	8	256	-2.37	28	162	2.4	231	18	64	78	74	98
*30	17	1.21	10	255	0.60	8	164	-1.82	77	36	1.5	355	35	-76	158	56	-100
31	16	2.74	75	284	0.28	8	45	-3.03	13	136	2.9	237	33	105	40	58	81
32	16	5.37	14	294	-0.20	33	34	-5.18	53	185	5.3	348	42	-145	230	67	-53
33	17	1.45	7	163	-0.15	43	259	-1.30	46	65	1.4	215	53	-148	105	65	-41
*34	17	0.84	80	110	-0.23	0	201	-0.60	10	292	0.7	22	35	90	201	55	90
35	16	7.64	72	295	-0.74	2	200	-6.91	18	109	7.3	197	27	86	21	63	92
36	17	0.78	8	325	0.28	29	231	-1.05	60	68	0.9	84	45	-47	211	59	-124
37	17	2.79	47	249	0.11	43	60	-2.89	4	154	2.8	280	55	146	31	62	40
*38	17	1.23	87	332	-0.30	3	130	-0.94	1	220	1.1	313	44	94	128	46	86
39	16	4.62	5	321	-0.79	26	53	-3.84	63	221	4.2	25	46	-127	253	55	-57
*40	16	2.02	8	219	0.96	3	128	-2.99	81	16	2.5	313	37	-84	126	53	-94
41	17	1.17	79	266	0.14	8	41	-1.31	7	132	1.2	231	38	102	35	53	81
42	16	4.20	72	272	-0.12	7	23	-4.08	17	115	4.1	215	29	104	19	62	82
43	17	0.88	77	36	-0.09	2	132	-0.79	13	223	0.8	315	32	93	131	58	88
44	16	5.78	79	9	1.32	4	120	-7.10	10	211	6.4	306	35	97	118	55	85
45	16	3.54	67	90	0.64	23	278	-4.17	3	187	3.9	254	47	58	117	52	120
46	17	0.85	82	114	0.04	2	220	-0.89	8	310	0.9	43	37	94	218	53	87
*47	17	4.64	82	101	-1.50	6	235	-3.14	6	326	3.9	63	39	99	231	51	82
*48	17	3.45	3	63	1.45	7	154	-4.90	83	311	4.2	146	43	-100	340	48	-81
49	17	1.16	0	27	0.05	11	297	-1.20	79	117	1.2	127	46	-75	286	46	-105
50	16	5.34	77	100	0.81	12	307	-6.15	6	216	5.7	293	40	72	137	52	105

* shallow vertical-CLVD earthquake

Table A2. (continued)

No.	Scale Factor 10^{ex}	Principal Axes									M_0	Best Double Couple					
		T-axis			N-axis			P-axis				Plane 1			Plane 2		
		σ	δ	ε	σ	δ	ε	σ	δ	ε		φ_1	θ	λ	φ_2	θ	λ
*51	17	2.14	73	115	-0.94	14	334	-1.18	10	241	1.7	314	37	67	163	57	106
52	16	3.78	13	141	0.96	32	42	-4.74	54	250	4.3	266	43	-38	26	66	-126
53	17	0.92	44	218	0.00	45	26	-0.93	6	122	0.9	250	56	149	358	65	38
54	17	2.47	75	7	0.19	15	203	-2.66	4	112	2.6	187	43	68	36	51	109
55	17	0.99	73	307	0.01	14	165	-0.99	10	72	1.0	145	37	67	354	57	107
56	16	2.11	23	273	-0.39	19	174	-1.72	59	49	1.9	37	28	-44	168	71	-111
57	16	1.82	68	113	0.36	20	266	-2.18	9	359	2.0	111	40	121	253	57	66
58	17	1.17	67	343	-0.03	13	105	-1.14	19	199	1.2	310	28	118	99	66	76
59	17	0.89	83	302	0.03	4	173	-0.93	5	82	0.9	168	40	84	356	50	95
*60	17	2.22	21	177	1.23	0	87	-3.44	69	356	2.8	267	24	-89	86	66	-90
61	16	1.44	5	307	0.15	2	217	-1.59	85	107	1.5	39	41	-87	216	50	-92
*62	17	3.09	81	181	-1.07	8	330	-2.02	5	60	2.6	159	41	102	323	50	79
63	16	3.93	65	10	-0.25	11	255	-3.69	22	161	3.8	230	25	62	80	68	102
64	17	3.01	36	68	0.97	14	168	-3.97	51	276	3.5	108	16	-152	350	83	-76
*65	16	4.99	29	326	2.82	8	61	-7.82	60	164	6.4	35	18	-117	243	74	-82
66	16	6.40	3	231	-2.07	11	140	-4.33	78	337	5.4	333	43	-73	130	49	-105
67	16	3.67	80	14	0.05	6	247	-3.73	8	156	3.7	238	37	80	72	53	98
68	16	6.00	3	45	-0.53	2	135	-5.48	86	257	5.7	133	42	-93	316	48	-87
69	16	3.95	12	263	0.03	12	170	-3.98	73	38	4.0	8	34	-69	163	58	-104
70	17	4.38	83	351	0.09	7	162	-4.46	1	252	4.4	349	44	100	155	47	80
*71	17	1.64	77	117	-0.62	9	344	-1.01	9	252	1.3	332	37	75	170	55	101
72	16	4.13	1	330	0.19	24	239	-4.31	66	62	4.2	82	49	-57	218	51	-122
73	16	3.01	78	107	0.56	8	334	-3.58	9	243	3.3	323	37	76	160	54	100
74	17	0.87	10	274	-0.08	10	182	-0.79	76	45	0.8	16	37	-72	175	55	-103
75	16	2.78	79	269	-0.06	0	360	-2.73	11	90	2.8	180	34	90	360	56	90
76	16	3.52	11	17	1.89	18	284	-5.41	69	136	4.5	129	38	-59	272	58	-112
77	16	6.77	70	264	-0.17	16	48	-6.60	11	141	6.7	251	37	118	37	58	71
78	16	5.69	25	111	-1.77	19	12	-3.92	57	248	4.8	237	26	-42	6	73	-110
79	16	1.13	72	48	-0.04	8	292	-1.10	16	200	1.1	278	29	73	117	62	99
80	16	2.97	79	295	0.32	8	155	-3.29	7	64	3.1	145	39	77	342	52	100
81	17	1.19	6	53	0.07	1	144	-1.26	84	246	1.2	142	39	-92	325	51	-88
82	17	1.61	10	55	0.15	0	325	-1.77	80	234	1.7	145	35	-90	325	55	-90
83	16	2.84	70	295	0.51	13	63	-3.35	15	156	3.1	264	32	115	56	62	75
84	16	5.92	9	176	0.05	12	268	-5.96	75	52	5.9	252	38	-110	97	55	-75
85	16	4.82	7	181	0.24	15	273	-5.07	73	66	4.9	254	40	-113	104	54	-71
86	16	7.17	5	175	-0.17	9	266	-7.01	80	56	7.1	255	41	-103	93	50	-79
87	16	3.30	85	5	0.76	2	118	-4.06	5	208	3.7	300	40	93	116	50	87
88	16	4.08	2	155	0.34	6	245	-4.43	84	50	4.3	239	44	-99	71	47	-82
89	16	1.21	72	320	0.29	4	216	-1.50	17	125	1.4	208	28	81	39	62	95
90	16	3.21	79	172	-0.25	11	4	-2.96	2	273	3.1	352	44	74	194	48	105
91	16	3.49	73	6	-0.45	5	258	-3.03	16	166	3.3	248	29	79	81	61	96
92	17	1.70	72	337	-0.27	16	127	-1.42	9	219	1.6	327	39	116	116	56	71
93	16	3.02	78	271	0.22	12	76	-3.24	3	167	3.1	269	43	108	66	49	74
94	16	7.36	76	315	0.55	3	212	-7.92	13	121	7.6	207	32	84	34	58	94
95	16	1.49	32	294	-0.16	3	202	-1.33	58	107	1.4	36	13	-76	201	77	-93
96	16	2.49	85	35	0.16	5	202	-2.65	1	292	2.6	27	44	97	198	46	83
97	16	1.87	77	353	0.09	12	196	-1.95	5	105	1.9	182	41	71	26	51	106
*98	17	2.87	80	187	-0.95	7	321	-1.91	7	52	2.4	150	38	101	316	52	81
99	16	6.26	68	337	0.15	3	75	-6.41	22	166	6.3	261	23	97	73	67	87
100	16	1.10	3	157	-0.23	12	247	-0.87	78	52	1.0	234	43	-108	78	49	-74

* shallow vertical-CLVD earthquake

Table A2. (continued)

No.	Scale Factor 10^m	Principal Axes									M_0	Best Double Couple					
		T-axis			N-axis			P-axis				Plane 1			Plane 2		
		σ	δ	ε	σ	δ	ε	σ	δ	ε		φ_s	θ	λ	φ_s	θ	λ
101	16	1.73	4	258	0.11	2	348	-1.84	85	102	1.8	346	41	-93	170	49	-87
*102	16	2.46	12	202	0.67	6	293	-3.13	76	50	2.8	284	33	-102	117	58	-83
103	17	1.27	63	111	-0.06	26	279	-1.21	5	12	1.2	127	46	128	259	55	57
104	16	0.88	63	179	0.02	10	70	-0.89	25	335	0.9	44	22	63	253	71	100
105	16	1.51	82	77	-0.04	6	305	-1.47	6	215	1.5	298	39	81	130	51	97
*106	16	7.47	71	350	-1.74	3	250	-5.72	18	159	6.6	243	27	82	72	63	94
*107	17	2.55	71	145	-0.82	5	250	-1.73	18	341	2.1	80	27	101	247	63	84
108	16	3.98	6	231	-0.22	1	141	-3.76	84	43	3.9	322	39	-89	141	51	-91
109	16	2.97	1	57	0.03	3	147	-3.01	87	298	3.0	145	44	-94	330	46	-86
110	16	5.04	2	76	0.44	10	346	-5.49	80	178	5.3	176	44	-76	337	48	-103
*111	17	2.37	62	60	-0.89	12	308	-1.48	26	213	1.9	278	22	58	132	72	102
*112	17	3.25	81	161	-0.73	1	255	-2.52	9	345	2.9	76	36	91	255	54	89
113	17	2.01	80	89	-0.78	9	292	-1.23	4	201	1.6	281	42	76	119	49	102
114	16	6.57	2	154	0.95	24	64	-7.52	65	249	7.0	268	48	-56	43	52	-122
115	16	4.20	5	150	-0.11	4	60	-4.10	84	292	4.2	244	40	-84	57	50	-95
116	16	6.96	11	126	1.08	25	221	-8.05	62	13	7.5	187	40	-131	56	61	-61
117	16	1.54	8	271	0.32	4	180	-1.86	81	67	1.7	5	37	-84	177	53	-94
118	16	2.90	6	265	0.23	8	356	-3.14	80	138	3.0	346	39	-103	183	52	-80
119	16	3.33	80	149	0.06	4	265	-3.39	9	355	3.4	90	37	97	262	54	85
*120	17	1.26	86	207	-0.40	4	36	-0.85	1	306	1.1	32	45	85	219	46	95
*121	16	2.98	9	38	1.05	23	304	-4.02	65	147	3.5	153	42	-53	289	58	-118
*122	17	7.80	78	158	-2.59	12	333	-5.22	1	64	6.5	166	45	107	322	47	73
*123	16	2.61	1	118	0.94	18	208	-3.56	72	26	3.1	190	47	-115	45	48	-65
*124	17	2.33	85	135	-0.68	5	332	-1.64	2	241	2.0	326	44	83	156	47	97

* shallow vertical-CLVD earthquake

Note: The last earthquake is also reported in the Surface Wave catalog (Category 1) - Table A4.

Table A3. Centroid-moment-tensor solutions for 59 earthquakes from the Global CMT Project's Surface Wave catalog (Category 1), 1991 - 2009.

No.	Centroid Parameters														Half Drtn	Scale Factor 10^{ex}	M_0	Elements of Moment Tensor					
	Date			Time				Latitude		Longitude		Depth						M_{rr}	$M_{\theta\theta}$	$M_{\phi\phi}$	$M_{r\theta}$	$M_{r\phi}$	$M_{\theta\phi}$
	Y	M	D	h	m	sec	δt_0	l	$\delta\lambda_0$	ϕ	$\delta\phi_0$	h	δh_0										
1	1991	8	14	18	13	51.6 ± 0.3	-0.4	-13.56 ± 0.01	0.19	167.77 ± 0.02	-0.48	12.0			1.5	16	4.0	0.13 ± 0.16	1.41 ± 0.12	-1.54 ± 0.14	-0.16 ± 0.33	1.72 ± 0.35	3.31 ± 0.10
2	1992	3	21	9	48	6.1 ± 0.3	6.1	-15.30 ± 0.02	-0.05	-176.13 ± 0.01	0.12	12.0			1.5	16	4.6	-1.21 ± 0.16	2.12 ± 0.13	-0.91 ± 0.14	-0.70 ± 0.34	-1.57 ± 0.38	3.94 ± 0.11
3	1993	12	1	10	2	21.0 ± 0.9	-3.0	44.44 ± 0.04	-0.06	-130.13 ± 0.06	-0.63	12.0			1.1	16	0.9	0.06 ± 0.07	-0.64 ± 0.06	0.58 ± 0.05	-0.43 ± 0.16	0.14 ± 0.14	-0.53 ± 0.06
4	1995	2	1	23	13	9.4 ± 0.3	5.4	10.35 ± 0.01	-0.40	-103.91 ± 0.01	0.34	12.0			1.5	16	5.7	-0.10 ± 0.16	-2.11 ± 0.14	2.21 ± 0.17	2.71 ± 0.34	-1.68 ± 0.36	4.36 ± 0.11
*5	1995	2	17	17	45	42.7 ± 0.2	-1.4	-3.85 ± 0.01	-0.10	152.10 ± 0.01	-0.15	12.0			1.4	16	4.3	3.69 ± 0.09	-1.75 ± 0.07	-1.94 ± 0.08	0.94 ± 0.21	3.02 ± 0.20	0.73 ± 0.06
6	1995	10	6	17	9	28.5 ± 0.5	0.5	34.14 ± 0.02	-0.11	139.04 ± 0.02	0.29	12.0			1.2	16	1.2	-0.20 ± 0.07	-0.83 ± 0.05	1.03 ± 0.05	0.43 ± 0.14	-0.21 ± 0.13	-0.60 ± 0.04
7	1996	1	5	9	55	12.1 ± 0.2	0.1	-2.95 ± 0.01	-0.20	148.06 ± 0.02	-0.19	12.0			1.5	16	4.4	-0.79 ± 0.14	2.13 ± 0.10	-1.34 ± 0.14	1.53 ± 0.28	-0.23 ± 0.35	3.68 ± 0.09
*8	1996	2	15	1	11	43.0 ± 0.2	-1.0	-3.85 ± 0.02	-0.10	152.03 ± 0.02	0.28	12.0			1.5	16	4.6	4.27 ± 0.11	-2.12 ± 0.09	-2.15 ± 0.11	0.68 ± 0.35	3.05 ± 0.31	0.96 ± 0.07
9	1996	5	15	9	22	12.2 ± 0.5	12.2	14.80 ± 0.05	0.30	144.05 ± 0.04	-0.45	12.0			1.2	16	1.4	-1.32 ± 0.07	0.25 ± 0.05	1.07 ± 0.07	0.41 ± 0.27	0.23 ± 0.20	0.41 ± 0.06
*10	1996	7	27	13	6	38.6 ± 0.5	14.6	18.77 ± 0.04	-0.23	-155.18 ± 0.03	-0.18	12.0			1.4	16	2.8	2.97 ± 0.14	-1.22 ± 0.12	-1.74 ± 0.12	-0.24 ± 0.50	-0.92 ± 0.39	-0.80 ± 0.11
11	1997	3	2	9	55	34.5 ± 0.6	6.4	-36.17 ± 0.03	0.33	178.32 ± 0.06	-0.18	12.0			1.1	16	1.4	-0.84 ± 0.07	0.52 ± 0.07	0.32 ± 0.06	1.05 ± 0.15	-0.12 ± 0.20	0.58 ± 0.05
12	1997	4	17	14	17	29.1 ± 0.3	1.1	44.24 ± 0.02	-0.26	-129.97 ± 0.02	-0.47	12.0			1.2	16	1.9	-0.05 ± 0.08	-1.21 ± 0.08	1.26 ± 0.06	-0.64 ± 0.19	0.80 ± 0.17	-1.07 ± 0.06
13	1998	3	18	22	43	36.6 ± 0.2	0.6	-19.47 ± 0.02	0.03	-175.89 ± 0.01	-0.39	12.0			1.5	16	5.3	-2.41 ± 0.19	-3.03 ± 0.18	5.43 ± 0.13	-1.43 ± 0.47	0.82 ± 0.40	-2.45 ± 0.12
14	1998	8	12	3	26	39.2 ± 0.2	-0.8	-16.64 ± 0.03	1.11	-174.34 ± 0.01	0.41	12.0			1.2	16	2.1	-1.99 ± 0.09	-0.07 ± 0.09	2.06 ± 0.06	-0.53 ± 0.30	0.08 ± 0.22	0.37 ± 0.06
15	1998	10	7	23	59	0.2 ± 0.3	-3.8	42.33 ± 0.03	0.08	-127.11 ± 0.03	0.14	12.0			1.3	16	1.4	-1.47 ± 0.06	0.20 ± 0.05	1.26 ± 0.04	-0.19 ± 0.21	0.11 ± 0.15	0.36 ± 0.04
16	1998	10	20	6	54	49.9 ± 0.3	1.9	-15.08 ± 0.02	0.17	-174.87 ± 0.02	-0.12	12.8 ± 2.6	2.8		1.2	16	2.1	-0.63 ± 0.13	1.88 ± 0.14	-1.25 ± 0.09	-0.40 ± 0.22	0.05 ± 0.21	1.34 ± 0.09
17	1999	4	1	15	39	15.5 ± 0.3	11.5	-55.56 ± 0.01	0.19	-27.32 ± 0.02	0.43	12.0			1.7	16	7.3	0.22 ± 0.17	1.03 ± 0.16	-1.25 ± 0.13	5.91 ± 0.41	0.23 ± 0.34	4.16 ± 0.12
18	1999	9	2	9	1	6.5 ± 0.4	-5.5	9.11 ± 0.02	-0.64	-83.88 ± 0.03	-0.13	12.0			1.1	16	1.1	0.55 ± 0.06	-0.53 ± 0.04	-0.02 ± 0.05	0.80 ± 0.09	0.09 ± 0.12	0.46 ± 0.04
19	2000	6	26	3	12	19.3 ± 0.4	-4.7	41.80 ± 0.04	-0.45	-127.12 ± 0.03	-0.37	12.0			1.1	16	1.1	-0.82 ± 0.06	-0.29 ± 0.06	1.10 ± 0.04	-0.18 ± 0.18	-0.55 ± 0.13	-0.09 ± 0.04
*20	2000	7	7	11	22	4.3 ± 0.6	-3.7	34.15 ± 0.04	-0.10	139.47 ± 0.04	-0.28	12.0			1.1	15	5.1	-6.00 ± 0.29	2.70 ± 0.25	3.29 ± 0.25	0.25 ± 1.03	-1.84 ± 0.80	0.50 ± 0.21
*21	2000	7	9	13	40	15.3 ± 0.2	15.3	34.11 ± 0.01	-0.14	139.56 ± 0.02	-0.19	12.0			1.9	17	0.7	-0.81 ± 0.02	0.38 ± 0.01	0.43 ± 0.01	0.23 ± 0.04	0.05 ± 0.04	0.18 ± 0.01
*22	2000	7	11	15	37	31.5 ± 0.2	-4.5	34.10 ± 0.01	-0.15	139.59 ± 0.01	-0.16	12.0			1.2	17	1.1	-1.28 ± 0.02	0.55 ± 0.01	0.73 ± 0.02	0.26 ± 0.04	-0.14 ± 0.04	0.30 ± 0.01
*23	2000	7	12	4	6	60.0 ± 0.2	-4.0	34.13 ± 0.01	-0.12	139.57 ± 0.01	-0.18	12.0			1.0	17	0.8	-0.88 ± 0.01	0.39 ± 0.01	0.48 ± 0.01	0.20 ± 0.04	-0.12 ± 0.04	0.20 ± 0.01
*24	2000	7	12	18	45	55.6 ± 0.2	-4.4	34.12 ± 0.01	-0.38	139.58 ± 0.01	0.08	12.0			1.2	17	1.1	-1.26 ± 0.02	0.54 ± 0.02	0.72 ± 0.02	0.30 ± 0.04	-0.10 ± 0.05	0.31 ± 0.02
*25	2000	7	13	17	12	29.8 ± 0.1	-2.2	34.10 ± 0.01	-0.15	139.60 ± 0.01	0.35	12.0			1.5	17	2.5	-2.73 ± 0.03	1.24 ± 0.03	1.49 ± 0.03	0.59 ± 0.07	-0.30 ± 0.08	0.72 ± 0.03
*26	2000	7	15	14	34	46.4 ± 0.2	-1.6	34.14 ± 0.01	-0.11	139.57 ± 0.01	-0.18	12.0			1.2	17	1.1	-1.29 ± 0.02	0.60 ± 0.02	0.70 ± 0.02	0.35 ± 0.05	-0.06 ± 0.05	0.28 ± 0.02
*27	2000	7	20	8	24	17.4 ± 0.2	1.4	34.11 ± 0.01	-0.14	139.58 ± 0.01	-0.17	12.0			1.1	17	1.0	-1.08 ± 0.02	0.48 ± 0.02	0.60 ± 0.02	0.22 ± 0.04	-0.21 ± 0.04	0.27 ± 0.01
*28	2000	7	21	0	27	51.4 ± 0.2	-0.6	34.16 ± 0.01	-0.09	139.49 ± 0.01	-0.26	12.0			1.0	17	0.8	-0.90 ± 0.02	0.40 ± 0.02	0.50 ± 0.02	0.31 ± 0.04	0.05 ± 0.04	0.20 ± 0.01
*29	2000	7	23	16	36	44.5 ± 0.2	-3.5	34.13 ± 0.01	-0.12	139.55 ± 0.01	-0.20	12.0			1.0	17	0.9	-0.96 ± 0.02	0.44 ± 0.01	0.52 ± 0.01	0.25 ± 0.04	0.00 ± 0.04	0.27 ± 0.01
*30	2000	7	24	19	55	37.3 ± 0.2	1.4	34.11 ± 0.01	-0.14	139.55 ± 0.01	-0.20	12.0			1.1	17	1.1	-1.19 ± 0.02	0.50 ± 0.01	0.69 ± 0.02	0.29 ± 0.04	-0.24 ± 0.04	0.33 ± 0.01
*31	2000	7	25	20	10	28.0 ± 0.1	-4.0	34.14 ± 0.01	-0.11	139.55 ± 0.01	-0.20	12.0			1.0	17	0.7	-0.82 ± 0.01	0.37 ± 0.01	0.46 ± 0.01	0.24 ± 0.03	-0.14 ± 0.03	0.18 ± 0.01
*32	2000	7	27	7	22	50.4 ± 0.1	-5.6	34.13 ± 0.01	-0.37	139.59 ± 0.01	0.09	12.0			1.2	17	1.5	-1.64 ± 0.02	0.71 ± 0.02	0.93 ± 0.02	0.43 ± 0.05	-0.27 ± 0.05	0.44 ± 0.02
*33	2000	7	28	7	7	39.3 ± 0.1	-4.7	34.10 ± 0.01	-0.15	139.58 ± 0.01	0.33	12.0			1.2	17	1.4	-1.45 ± 0.02	0.62 ± 0.02	0.82 ± 0.02	0.42 ± 0.05	-0.33 ± 0.05	0.38 ± 0.02
*34	2000	7	29	7	51	38.8 ± 0.1	2.8	34.12 ± 0.01	-0.13	139.57 ± 0.01	-0.18	12.0			1.4	17	2.2	-2.40 ± 0.03	1.11 ± 0.03	1.29 ± 0.03	0.67 ± 0.07	-0.29 ± 0.07	0.64 ± 0.02
*35	2000	7	30	13	36	33.5 ± 0.2	1.5	34.17 ± 0.02	-0.08	139.59 ± 0.02	-0.16	12.0			2.3	17	1.9	-2.05 ± 0.05	0.96 ± 0.04	1.08 ± 0.04	0.46 ± 0.16	-0.57 ± 0.17	0.45 ± 0.04
*36	2000	8	3	19	16	42.1 ± 0.2	2.1	34.14 ± 0.01	-0.11	139.52 ± 0.01	-0.23	12.0			1.3	17	1.9	-2.04 ± 0.04	0.88 ± 0.03	1.16 ± 0.03	0.60 ± 0.09	0.01 ± 0.10	0.53 ± 0.03
*37	2000	8	6	0	23	22.7 ± 0.1	2.7	34.13 ± 0.01	-0.12	139.53 ± 0.01	-0.22	12.0			1.4	17	2.4	-2.57 ± 0.04	1.12 ± 0.03	1.45 ± 0.03	0.72 ± 0.08	-0.09 ± 0.09	0.70 ± 0.03
*38	2000	8	17	19	7	44.2 ± 0.2	0.2	34.14 ± 0.01	-0.11	139.57 ± 0.01	-0.18	12.0			1.2	17	1.4	-1.57 ± 0.02	0.72 ± 0.02	0.85 ± 0.02	0.40 ± 0.06	-0.15 ± 0.07	0.38 ± 0.02
*39	2000	8	18	9	9	16.3 ± 0.2	4.3	34.30 ± 0.02	0.05	139.40 ± 0.02	0.15	12.0			1.4	16	2.3	-2.19 ± 0.06	1.19 ± 0.05	1.01 ± 0.05	1.35 ± 0.14	0.02 ± 0.15	0.46 ± 0.04
40	2001	10	5	10	49	5.5 ± 0.3	1.5	14.11 ± 0.03	-0.14	40.61 ± 0.04	0.36	12.0			1.1	16	1.1	-0.87 ± 0.05	0.35 ± 0.04	0.52 ± 0.06	0.23 ± 0.12	0.54 ± 0.18	-0.55 ± 0.04
41	2001	11	25	5	30	28.1 ± 0.4	4.1	12.06 ± 0.04	-0.19	41.67 ± 0.06	-0.08	12.0			1.1	15	5.9	-5.95 ± 0.41	4.92 ± 0.30	1.04 ± 0.52	0.72 ± 1.48	-0.78 ± 1.39	-1.94 ± 0.28
*42	2002	1	20	23	45	31.6 ± 0.2	-4.4	-1.42 ± 0.01	0.33	29.13 ± 0.02	-0.12	12.0			1.7	16	6.2	-6.98 ± 0.14	4.09 ± 0.12	2.90 ± 0.14	-1.13 ± 0.45	-0.21 ± 0.40	1.60 ± 0.12
*43	2002	8	16	21	30	47.5 ± 0.4	7.5	-20.28 ± 0.04	-0.03	-175.99 ± 0.03	-0.24	12.0			1.2	16	1.5	-1.53 ± 0.08	0.46 ± 0.10	1.07 ± 0.06	0.41 ± 0.24	-0.49 ± 0.23	0.48 ± 0.05
44	2002	10	23	23	36	41.6 ± 0.7	9.6	25.16 ± 0.03	-0.09	123.84 ± 0.04	0.09	12.0			1.1	16	1.0	-0.97 ± 0.05	0.91 ± 0.04	0.06 ± 0.04	-0.08 ± 0.11	0.21 ± 0.14	0.09 ± 0.04
45	2002	12	9	4	31	57.4 ± 0.2	5.4	44.20 ± 0.01	-0.30	-129.68 ± 0.01	-0.18	14.4 ± 1.1	4.4		1.4	16	4.9	0.04 ± 0.12	-4.01 ± 0.12	3.97 ± 0.11	-0.93 ± 0.21	0.44 ± 0.18	-2.68 ± 0.10
46	2003	1	31	20	28	50.8 ± 0.4	10.8	-18.79 ± 0.02	0.46	-175.77 ± 0.02	-0.52	12.0			1.3	16	2.8	-0.17 ± 0.13	-1.03 ± 0.13	1.21 ± 0.10	-0.91 ± 0.30	-0.23 ± 0.24	-2.38 ± 0.07
47	2003	7	2	16	4	54.5 ± 0.4	-1.5	10.24 ± 0.02	-0.51	-104.23 ± 0.02	0.02	12.0			1.2	16	1.5	-0.09 ± 0.06	-0.45 ± 0.05	0.55 ± 0.06	0.54 ± 0.13	-0.65 ± 0.14	1.16 ± 0.04
48	2004	1	26	5	31	14.9 ± 0.4	2.9	-9.21 ± 0.02	0.29	157.24 ± 0.02	-0.26	18.8 ± 2.4	8.8		1.2	16	1.6	0.17 ± 0.14	-0.51 ± 0.09	0.34 ± 0.09	-0.82 ± 0.20	0.42 ± 0.15	1.31 ± 0.09
49	2004	6	9	4	33	27.4 ± 0.3	-0.6	-37.24 ± 0.02	0.01	77.84 ± 0.02	-0.41	12.0			1.3	16	2.1	-0.50 ± 0.12	-1.23 ± 0.08	1.73 ± 0.09	-0.52 ± 0.20	0.57 ± 0.23	-1.28 ± 0.09
50	2004	10	22	11	22	13.3 ± 0.5	-2.7	-14.62 ± 0.03	0.13	-173.40 ± 0.02	-0.15	12.0			1.1	16	1.1	-0.42 ± 0.07	0.31 ± 0.08	0.11 ± 0.05	-0.30 ± 0.14	0.56 ± 0.13	0.85 ± 0.04

* shallow vertical-CLVD earthquake

Table A3. (continued)

No.	Centroid Parameters													Half Drtn	Scale Factor 10^{ex}	M_0	Elements of Moment Tensor					
	Date			Time				Latitude		Longitude		Depth										
	Y	M	D	h	m	sec	δt_0	l	$\delta\lambda_0$	ϕ	$\delta\phi_0$	h	δh_0				M_{rr}	$M_{\theta\theta}$	$M_{\phi\phi}$	$M_{r\theta}$	$M_{r\phi}$	$M_{\theta\phi}$
51	2005	6	24	6	29	59.7 ± 0.4	-0.3	43.04 ± 0.03	0.29	-126.62 ± 0.03	0.13	12.0		1.1	15	6.3	-6.42 ± 0.27	1.33 ± 0.26	5.09 ± 0.23	1.34 ± 0.96	1.06 ± 0.77	1.79 ± 0.20
52	2005	9	24	16	35	30.8 ± 0.4	2.8	12.69 ± 0.04	-0.06	40.46 ± 0.03	-0.29	12.0		1.1	16	1.2	-1.04 ± 0.06	0.12 ± 0.05	0.92 ± 0.06	-0.48 ± 0.14	0.26 ± 0.15	-0.38 ± 0.04
53	2005	9	25	6	37	15.0 ± 0.5	-5.0	12.60 ± 0.04	-0.15	40.47 ± 0.03	-0.28	14.1 ± 2.0	4.1	1.1	16	1.2	-1.24 ± 0.20	0.22 ± 0.10	1.02 ± 0.13	-0.15 ± 0.13	0.06 ± 0.15	-0.40 ± 0.05
54	2006	9	17	2	25	31.5 ± 0.6	-4.5	43.43 ± 0.02	0.18	-127.53 ± 0.04	-0.28	17.7 ± 1.6	7.7	1.1	16	0.9	-0.10 ± 0.06	-0.66 ± 0.05	0.76 ± 0.05	-0.13 ± 0.08	-0.02 ± 0.08	-0.56 ± 0.03
55	2008	3	19	13	14	58.2 ± 0.3	-5.8	-15.93 ± 0.02	-0.18	-174.54 ± 0.01	0.21	12.0		1.2	16	1.7	-0.12 ± 0.08	-0.41 ± 0.09	0.53 ± 0.07	0.27 ± 0.17	0.25 ± 0.18	-1.60 ± 0.05
56	2008	4	14	1	43	20.4 ± 0.3	0.4	15.99 ± 0.03	-0.26	144.76 ± 0.02	0.01	12.0		1.2	16	1.7	-1.66 ± 0.06	0.09 ± 0.05	1.57 ± 0.06	-0.31 ± 0.18	0.30 ± 0.17	0.10 ± 0.05
57	2008	4	17	3	36	11.9 ± 0.4	3.9	15.81 ± 0.05	0.06	144.61 ± 0.03	-0.14	12.9 ± 1.8	2.9	1.1	16	0.9	-0.89 ± 0.12	0.10 ± 0.06	0.79 ± 0.08	0.10 ± 0.12	0.39 ± 0.15	-0.06 ± 0.04
58	2008	4	22	4	6	56.7 ± 0.5	0.6	42.89 ± 0.04	-0.36	-126.60 ± 0.04	0.15	12.0		1.1	15	6.3	-6.12 ± 0.30	1.80 ± 0.29	4.32 ± 0.25	-1.29 ± 1.08	-2.68 ± 0.92	1.45 ± 0.23
*59	2009	5	26	0	49	42.9 ± 0.1	-4.2	-21.24 ± 0.01	-0.10	-175.62 ± 0.01	1.32	12.0		1.3	17	2.0	2.30 ± 0.02	-0.89 ± 0.02	-1.41 ± 0.02	-0.19 ± 0.06	-0.22 ± 0.06	0.42 ± 0.02

* shallow vertical-CLVD earthquake

Note: The last earthquake is also reported in the Surface Wave catalog (Category 1) - Table A1.

Table A4. Principal axes and best-double-couple parameters for 59 earthquakes from the Global CMT Project's Surface Wave catalog (Category 1), 1991 - 2009.

No.	Scale Factor 10^{ex}	Principal Axes									M_0	Best Double Couple					
		T-axis			N-axis			P-axis				Plane 1			Plane 2		
		σ	δ	ε	σ	δ	ε	σ	δ	ε		φ_s	θ	λ	φ_s	θ	λ
1	16	3.75	14	324	0.48	66	202	-4.23	20	59	4.0	101	66	-4	192	86	-156
2	16	5.17	13	144	-1.23	66	23	-3.94	20	239	4.6	280	66	-5	12	85	-156
3	16	0.88	20	245	0.08	61	113	-0.96	20	343	0.9	24	61	0	294	90	151
4	16	4.92	0	302	1.51	63	32	-6.42	27	212	5.7	350	71	-160	254	71	-20
*5	16	5.20	64	292	-1.88	13	173	-3.31	21	77	4.3	144	26	59	358	68	104
6	16	1.28	13	72	-0.13	65	313	-1.15	21	167	1.2	208	65	-6	300	84	-155
7	16	4.72	12	329	-0.71	68	91	-4.01	18	235	4.4	13	68	-176	281	86	-22
*8	16	5.61	67	289	-1.96	15	160	-3.65	17	65	4.6	132	31	59	347	64	107
9	16	1.29	8	295	0.14	11	26	-1.43	77	167	1.4	12	38	-107	214	54	-77
*10	16	3.14	79	96	-0.67	5	213	-2.46	9	304	2.8	40	36	98	210	55	84
11	16	1.31	22	332	0.19	23	72	-1.50	57	203	1.4	26	31	-140	261	71	-65
12	16	2.10	25	247	-0.42	62	99	-1.68	13	343	1.9	28	63	9	294	82	153
13	16	6.25	8	254	-1.84	57	152	-4.42	32	349	5.3	27	62	-18	126	74	-151
14	16	2.12	0	100	0.01	15	190	-2.14	75	9	2.1	175	47	-111	24	47	-69
15	16	1.37	1	287	0.12	8	197	-1.50	82	25	1.4	25	44	-79	190	47	-101
16	16	2.42	7	160	-0.64	78	285	-1.78	10	69	2.1	205	78	-178	114	88	-12
17	16	7.76	36	334	-0.97	36	96	-6.79	34	216	7.3	4	36	178	95	89	54
18	16	1.06	55	331	0.02	24	100	-1.08	24	201	1.1	330	30	143	92	73	65
19	16	1.25	15	88	-0.24	15	182	-1.01	69	316	1.1	158	33	-118	11	61	-73
*20	15	3.82	9	112	2.54	6	21	-6.36	79	259	5.1	209	36	-80	17	55	-97
*21	17	0.61	8	314	0.25	7	45	-0.86	79	177	0.7	36	38	-102	230	53	-81
*22	17	0.96	1	308	0.38	10	38	-1.33	80	210	1.1	27	45	-104	227	47	-76
*23	17	0.65	1	310	0.28	11	40	-0.92	79	213	0.8	28	45	-106	230	47	-75
*24	17	0.96	3	308	0.36	10	39	-1.32	79	203	1.1	28	43	-105	228	49	-76
*25	17	2.10	2	311	0.75	10	41	-2.85	79	211	2.5	30	44	-105	231	48	-76
*26	17	0.94	5	313	0.42	10	43	-1.36	79	196	1.1	32	41	-105	231	51	-77
*27	17	0.81	1	128	0.33	12	38	-1.14	78	222	1.0	230	45	-73	26	47	-106
*28	17	0.69	9	312	0.28	9	43	-0.97	77	179	0.8	31	37	-106	230	54	-79
*29	17	0.77	6	313	0.23	8	44	-1.00	80	190	0.9	34	40	-103	231	51	-79
*30	17	0.94	0	127	0.34	14	36	-1.28	76	218	1.1	230	46	-71	23	47	-109
*31	17	0.60	2	309	0.29	14	40	-0.89	76	212	0.7	26	45	-110	232	48	-72
*32	17	1.28	1	308	0.48	13	39	-1.76	77	214	1.5	25	45	-109	231	48	-72
*33	17	1.11	0	127	0.48	15	37	-1.59	75	218	1.4	232	47	-69	23	47	-111
*34	17	1.86	3	313	0.71	12	43	-2.56	77	208	2.2	30	43	-108	234	49	-74
*35	17	1.48	2	129	0.75	14	39	-2.24	75	229	1.9	234	44	-69	26	49	-109
*36	17	1.61	6	310	0.56	10	41	-2.16	78	188	1.9	29	40	-105	229	52	-78
*37	17	2.04	5	310	0.68	10	41	-2.72	78	196	2.4	29	41	-106	230	51	-76
*38	17	1.18	3	312	0.48	11	42	-1.66	78	206	1.4	30	43	-106	232	49	-75
*39	16	1.89	16	332	0.79	10	65	-2.67	70	186	2.3	46	30	-111	251	62	-78
40	16	1.03	9	234	0.14	26	328	-1.17	63	126	1.1	296	42	-130	165	59	-60
41	15	5.80	5	23	0.27	4	113	-6.06	84	243	5.9	109	40	-96	297	50	-85
*42	16	5.29	5	146	1.81	3	236	-7.09	84	357	6.2	233	40	-95	59	50	-86
*43	16	1.35	5	116	0.38	17	25	-1.73	72	222	1.5	224	43	-65	11	52	-112
44	16	0.92	2	174	0.09	12	265	-1.01	78	76	1.0	253	44	-107	95	48	-74
45	16	4.89	8	252	0.06	78	120	-4.94	9	344	4.9	28	78	0	118	90	-168
46	16	2.75	6	237	0.09	70	129	-2.84	19	329	2.8	11	73	-9	104	81	-162
47	16	1.36	12	120	0.28	59	9	-1.64	28	216	1.5	255	62	-12	350	79	-151
48	16	1.32	9	129	0.55	64	239	-1.86	24	35	1.6	174	66	-169	80	80	-24
49	16	2.39	14	249	-0.61	70	115	-1.78	14	342	2.1	25	70	0	115	90	-160
50	16	1.09	7	316	0.08	49	218	-1.17	40	51	1.1	86	58	-26	190	68	-145

* shallow vertical-CLVD earthquake

Table A4. (continued)

No.	Scale Factor 10^{ex}	Principal Axes									M_0	Best Double Couple					
		T-axis			N-axis			P-axis				Plane 1			Plane 2		
		σ	δ	ε	σ	δ	ε	σ	δ	ε		φ_s	θ	λ	φ_s	θ	λ
51	15	5.98	7	293	0.71	6	24	-6.69	81	156	6.3	16	39	-100	209	52	-82
52	16	1.16	11	245	0.06	15	152	-1.22	71	10	1.2	354	36	-63	142	58	-108
53	16	1.19	3	247	0.07	5	157	-1.26	84	4	1.2	343	43	-82	152	48	-97
54	16	0.95	1	251	-0.08	81	154	-0.87	9	341	0.9	26	83	-6	116	84	-173
55	16	1.73	1	233	-0.04	77	329	-1.69	13	143	1.7	279	80	-171	187	82	-10
56	16	1.60	5	273	0.14	10	182	-1.74	79	29	1.7	14	41	-75	174	51	-103
57	16	0.88	12	267	0.11	6	359	-0.99	76	116	0.9	349	33	-102	183	58	-82
58	15	5.73	14	115	1.14	0	205	-6.87	76	296	6.3	204	31	-91	25	59	-90
*59	17	2.33	85	135	-0.68	5	332	-1.64	2	241	2.0	326	44	83	156	47	97

* shallow vertical-CLVD earthquake

Note: The last earthquake is also reported in the Surface Wave catalog (Category 1) - Table A2.

Table A5. Centroid-moment-tensor solutions for 131 earthquakes from the Global CMT Project's Surface Wave catalog (Category 2), 1991 - 2009.

No.	Centroid Parameters														Half Drtn	Scale Factor 10^{ex}	M_0	Elements of Moment Tensor					
	Date			Time				Latitude		Longitude		Depth						M_{rr}	$M_{\theta\theta}$	$M_{\phi\phi}$	$M_{r\theta}$	$M_{r\phi}$	$M_{\theta\phi}$
	Y	M	D	h	m	sec	δt_0	l	$\delta\lambda_0$	ϕ	$\delta\phi_0$	h	δh_0										
1	1991	1	25	5	3	23.7 ± 0.3	3.7	-15.95 ± 0.02	-0.20	-172.49 ± 0.02	0.26	19.3 ± 0.7	9.3	0.9	16	6.0	5.23 ± 0.25	-0.06 ± 0.14	-5.18 ± 0.18	0.60 ± 0.25	2.87 ± 0.28	-0.77 ± 0.11
2	1991	3	30	5	43	50.9 ± 0.2	-1.1	-15.88 ± 0.02	-0.13	-174.72 ± 0.02	0.03	12.0		0.9	16	6.5	-1.93 ± 0.30	-2.18 ± 0.24	4.11 ± 0.21	-0.43 ± 0.56	1.47 ± 0.60	-5.49 ± 0.20
3	1991	8	21	21	1	11.4 ± 0.8	7.4	1.30 ± 0.03	0.05	-90.53 ± 0.05	0.22	12.0		0.6	16	2.5	-0.48 ± 0.20	0.81 ± 0.14	-0.32 ± 0.19	-0.27 ± 0.43	1.48 ± 0.40	-1.82 ± 0.12
*4	1991	9	6	5	40	54.6 ± 0.2	-1.4	-3.85 ± 0.01	-0.10	152.03 ± 0.02	-0.22	12.0		0.8	16	4.1	3.30 ± 0.11	-1.61 ± 0.08	-1.68 ± 0.11	0.71 ± 0.25	3.07 ± 0.21	0.74 ± 0.07
5	1991	9	24	1	32	43.3 ± 0.3	3.3	-37.66 ± 0.02	0.09	77.91 ± 0.02	0.66	12.0		0.7	16	2.7	-0.16 ± 0.17	-1.56 ± 0.16	1.72 ± 0.16	-0.09 ± 0.38	-0.08 ± 0.34	-2.08 ± 0.12
6	1991	10	4	11	43	37.4 ± 0.3	1.4	-16.74 ± 0.01	-0.24	168.22 ± 0.02	-0.28	12.0		0.6	16	1.7	-0.23 ± 0.08	-0.56 ± 0.07	0.78 ± 0.07	0.00 ± 0.14	-0.35 ± 0.16	-1.53 ± 0.05
7	1991	10	23	2	33	5.7 ± 0.2	1.7	-19.39 ± 0.02	0.36	-176.12 ± 0.01	-0.37	12.0		0.8	16	4.4	-1.19 ± 0.14	-2.87 ± 0.13	4.06 ± 0.11	-0.98 ± 0.36	0.50 ± 0.28	-2.43 ± 0.11
8	1992	2	11	15	31	41.6 ± 0.7	5.6	15.24 ± 0.06	0.74	144.52 ± 0.03	0.02	13.1 ± 1.8	3.1	0.5	16	1.1	-1.07 ± 0.15	0.05 ± 0.07	1.03 ± 0.10	0.36 ± 0.12	-0.23 ± 0.11	-0.10 ± 0.04
9	1992	3	6	19	12	10.4 ± 0.4	10.4	1.15 ± 0.02	0.40	-85.29 ± 0.03	0.46	12.0		0.7	16	2.4	-0.06 ± 0.13	0.76 ± 0.10	-0.69 ± 0.13	0.17 ± 0.34	0.92 ± 0.29	2.10 ± 0.09
10	1992	3	26	7	17	27.3 ± 0.3	7.3	-10.39 ± 0.02	-0.14	166.43 ± 0.02	0.18	12.0		0.7	16	2.9	-1.18 ± 0.12	1.20 ± 0.10	-0.03 ± 0.10	-0.20 ± 0.30	1.27 ± 0.25	-2.34 ± 0.09
11	1992	4	29	16	1	5.7 ± 0.4	1.7	21.89 ± 0.03	0.14	143.14 ± 0.03	-0.11	12.0		0.6	16	2.0	-2.01 ± 0.09	0.74 ± 0.06	1.28 ± 0.07	0.07 ± 0.21	0.73 ± 0.22	-0.73 ± 0.06
12	1992	7	27	16	55	30.8 ± 0.4	-5.2	-18.56 ± 0.03	-0.06	-175.29 ± 0.02	0.21	12.0		0.8	16	4.0	0.45 ± 0.15	-0.83 ± 0.12	0.38 ± 0.09	1.69 ± 0.19	3.50 ± 0.18	-0.64 ± 0.07
13	1992	9	21	22	49	54.2 ± 0.4	10.2	-15.08 ± 0.02	0.42	-175.09 ± 0.02	-0.59	13.7 ± 2.0	3.7	0.8	16	3.4	-0.70 ± 0.16	2.06 ± 0.14	-1.36 ± 0.13	1.05 ± 0.30	-0.21 ± 0.23	2.70 ± 0.14
14	1992	10	28	14	7	5.1 ± 0.4	1.1	-29.21 ± 0.03	-0.21	-176.60 ± 0.03	0.40	19.9 ± 1.3	9.9	0.8	16	3.5	2.90 ± 0.26	-0.84 ± 0.17	-2.06 ± 0.16	0.40 ± 0.21	2.30 ± 0.18	-0.51 ± 0.08
15	1992	11	3	17	55	45.2 ± 0.4	-6.8	-14.87 ± 0.03	-0.12	-173.81 ± 0.02	-0.06	12.0		0.6	16	1.6	-0.31 ± 0.12	0.03 ± 0.11	0.28 ± 0.10	-0.43 ± 0.20	-0.14 ± 0.23	1.49 ± 0.07
16	1992	11	6	9	3	1.6 ± 0.3	-2.4	-14.79 ± 0.03	-0.04	-176.04 ± 0.02	-0.29	12.0		0.7	16	2.7	-2.68 ± 0.10	1.57 ± 0.10	1.11 ± 0.09	-0.05 ± 0.28	-0.54 ± 0.27	1.24 ± 0.07
17	1993	2	10	17	57	3.0 ± 0.5	7.0	23.52 ± 0.03	-0.23	123.62 ± 0.03	-0.13	12.0		0.5	16	1.1	0.38 ± 0.05	-0.44 ± 0.04	0.06 ± 0.04	0.62 ± 0.07	0.74 ± 0.09	-0.32 ± 0.03
18	1993	2	22	23	49	33.8 ± 0.6	-2.2	16.16 ± 0.05	-0.09	144.82 ± 0.03	0.07	12.0		0.6	16	1.3	-1.37 ± 0.07	0.09 ± 0.05	1.28 ± 0.06	0.04 ± 0.16	0.12 ± 0.17	-0.17 ± 0.06
19	1993	2	23	0	17	57.0 ± 0.5	5.0	16.12 ± 0.04	0.37	144.76 ± 0.03	0.01	12.0		0.5	16	1.1	-1.07 ± 0.05	0.08 ± 0.04	0.99 ± 0.05	0.09 ± 0.13	0.30 ± 0.12	0.01 ± 0.04
20	1993	5	13	6	6	24.7 ± 0.3	-7.3	-15.73 ± 0.02	-0.48	-174.55 ± 0.02	0.20	12.0		0.6	16	2.2	-0.43 ± 0.16	-0.62 ± 0.14	1.05 ± 0.13	-0.46 ± 0.29	-0.39 ± 0.27	-1.90 ± 0.10
21	1993	6	19	10	32	1.7 ± 0.4	1.7	-14.81 ± 0.03	0.19	-173.14 ± 0.02	-0.14	12.0		0.6	16	1.5	0.59 ± 0.09	0.48 ± 0.08	-1.07 ± 0.06	0.47 ± 0.17	0.85 ± 0.15	0.77 ± 0.05
22	1993	7	13	22	54	24.8 ± 0.2	0.8	-2.99 ± 0.01	0.26	148.12 ± 0.02	0.87	12.0		0.7	16	2.6	-0.41 ± 0.12	1.30 ± 0.08	-0.89 ± 0.13	0.24 ± 0.23	-0.43 ± 0.26	2.28 ± 0.07
23	1993	8	20	22	57	40.7 ± 0.3	-3.3	-15.03 ± 0.03	-0.03	-172.94 ± 0.01	0.06	12.0		0.8	16	3.7	-0.26 ± 0.17	1.86 ± 0.15	-1.61 ± 0.12	1.47 ± 0.30	2.40 ± 0.30	1.81 ± 0.10
24	1993	9	24	1	22	56.7 ± 0.3	0.7	15.18 ± 0.03	-0.07	144.50 ± 0.02	-0.25	12.0		0.7	16	3.4	-3.43 ± 0.12	0.19 ± 0.08	3.25 ± 0.12	-0.24 ± 0.29	-0.10 ± 0.26	0.13 ± 0.08
25	1993	10	30	18	46	2.2 ± 0.4	10.2	-19.31 ± 0.04	0.44	-176.11 ± 0.02	-0.36	12.0		0.9	16	4.1	-1.71 ± 0.41	-1.99 ± 0.34	3.70 ± 0.31	-0.38 ± 0.93	-0.48 ± 0.75	-2.84 ± 0.24
26	1993	12	30	7	31	46.6 ± 0.6	2.6	10.23 ± 0.03	-0.27	-103.88 ± 0.03	0.62	12.0		0.6	16	1.8	0.28 ± 0.10	-0.75 ± 0.07	0.47 ± 0.11	-0.86 ± 0.22	-0.10 ± 0.21	1.41 ± 0.06
*27	1994	1	25	23	15	1.9 ± 0.2	-2.1	-3.82 ± 0.01	-0.07	152.05 ± 0.02	-0.20	12.0		0.8	16	3.4	3.46 ± 0.09	-1.82 ± 0.07	-1.64 ± 0.09	0.48 ± 0.23	2.03 ± 0.20	0.57 ± 0.05
28	1994	1	26	4	19	34.2 ± 0.3	6.2	-15.16 ± 0.02	0.09	-176.01 ± 0.01	-0.26	12.0		0.7	16	2.0	-0.14 ± 0.11	1.34 ± 0.11	-1.19 ± 0.08	0.43 ± 0.24	-0.14 ± 0.20	1.51 ± 0.08
29	1994	2	7	21	18	15.5 ± 0.4	-0.5	-14.87 ± 0.05	0.13	-173.28 ± 0.02	-0.28	12.7 ± 3.8	2.7	0.6	16	1.4	0.23 ± 0.19	0.89 ± 0.12	-1.12 ± 0.14	-0.58 ± 0.33	-0.03 ± 0.21	0.74 ± 0.08
30	1994	3	6	12	35	18.3 ± 0.4	-1.7	-15.11 ± 0.04	0.14	-174.21 ± 0.02	0.04	12.0		0.5	16	1.2	-0.23 ± 0.08	0.39 ± 0.08	-0.15 ± 0.06	-0.45 ± 0.14	0.23 ± 0.21	1.01 ± 0.04
31	1994	3	6	13	47	23.2 ± 0.3	3.2	-15.22 ± 0.03	0.03	-174.19 ± 0.01	0.06	12.0		0.5	16	1.2	-0.16 ± 0.07	0.58 ± 0.06	-0.42 ± 0.05	-0.47 ± 0.11	-0.16 ± 0.16	0.97 ± 0.04
32	1994	3	7	13	26	36.8 ± 0.2	-3.2	-15.10 ± 0.02	-0.35	-174.20 ± 0.01	-0.45	12.0		0.8	16	4.2	-0.27 ± 0.13	-0.45 ± 0.12	0.72 ± 0.10	-0.24 ± 0.26	1.04 ± 0.27	3.99 ± 0.08
*33	1994	3	19	21	49	42.9 ± 0.4	-1.1	41.67 ± 0.03	-0.58	-127.06 ± 0.03	-0.31	12.0		0.6	16	1.5	-1.25 ± 0.06	0.10 ± 0.05	1.14 ± 0.05	-1.01 ± 0.17	-0.28 ± 0.13	-0.05 ± 0.04
34	1994	3	25	8	3	47.7 ± 0.4	3.7	-15.14 ± 0.04	0.11	-174.44 ± 0.02	0.31	12.0		0.6	16	1.6	-0.01 ± 0.15	0.02 ± 0.15	-0.01 ± 0.12	-0.46 ± 0.25	-0.05 ± 0.32	1.54 ± 0.07
35	1994	3	30	21	50	23.8 ± 0.4	7.8	-15.22 ± 0.02	0.53	-174.84 ± 0.02	-0.09	12.0		0.8	16	4.8	-1.46 ± 0.17	3.13 ± 0.16	-1.67 ± 0.14	0.73 ± 0.35	0.78 ± 0.34	4.01 ± 0.12
36	1994	5	25	2	3	2.3 ± 0.4	-1.7	22.90 ± 0.03	0.15	142.39 ± 0.03	0.14	12.0		0.6	16	1.3	-1.16 ± 0.07	0.40 ± 0.05	0.76 ± 0.06	-0.34 ± 0.15	0.24 ± 0.15	-0.61 ± 0.04
37	1994	6	14	2	35	40.5 ± 0.4	-11.5	-15.44 ± 0.03	-0.69	-173.43 ± 0.03	-0.18	12.0		0.8	16	2.7	2.01 ± 0.11	-1.50 ± 0.12	-0.51 ± 0.09	-2.00 ± 0.21	0.35 ± 0.27	-0.05 ± 0.06
38	1994	8	11	5	14	19.4 ± 0.2	-4.6	-15.05 ± 0.02	-0.30	-174.24 ± 0.01	0.01	12.0		0.6	16	2.1	-0.29 ± 0.10	0.47 ± 0.11	-0.17 ± 0.08	0.17 ± 0.17	0.07 ± 0.18	2.06 ± 0.06
*39	1994	11	8	13	7	56.8 ± 0.4	4.8	-15.91 ± 0.03	0.59	-173.97 ± 0.03	-0.47	12.0		0.6	16	2.3	-2.16 ± 0.12	1.47 ± 0.13	0.69 ± 0.07	1.06 ± 0.23	1.01 ± 0.28	0.15 ± 0.07
40	1994	12	5	0	50	20.8 ± 0.3	4.8	-15.22 ± 0.02	0.03	167.56 ± 0.03	-0.19	12.0		0.7	16	2.4	2.29 ± 0.10	-2.05 ± 0.08	-0.23 ± 0.07	0.20 ± 0.18	-0.97 ± 0.29	-0.57 ± 0.06
41	1994	12	9	16	14	7.4 ± 0.3	-8.6	-15.16 ± 0.02	0.09	167.59 ± 0.03	-0.16	12.0		0.6	16	1.2	1.01 ± 0.05	-0.62 ± 0.04	-0.39 ± 0.04	-0.57 ± 0.10	-0.46 ± 0.13	-0.48 ± 0.03
*42	1995	1	10	17	44	0.1 ± 0.3	0.1	-14.24 ± 0.02	0.01	-169.03 ± 0.02	-0.28	12.0		0.7	16	2.5	-2.16 ± 0.09	1.14 ± 0.09	1.02 ± 0.06	-1.35 ± 0.20	1.07 ± 0.22	-0.38 ± 0.05
*43	1995	1	10	23	49	26.3 ± 0.3	-1.7	-14.25 ± 0.03	0.00	-168.97 ± 0.03	-0.22	12.0		0.7	16	2.0	-2.30 ± 0.08	1.19 ± 0.10	1.11 ± 0.07	-0.53 ± 0.26	0.57 ± 0.28	-0.28 ± 0.05
*44	1995	1	11	18	16	5.9 ± 0.3	-2.1	-14.18 ± 0.03	-0.43	-169.00 ± 0.03	-0.25	12.0		0.7	16	1.9	-1.90 ± 0.08	0.87 ± 0.09	1.03 ± 0.06	-0.54 ± 0.22	1.05 ± 0.26	-0.15 ± 0.05
45	1995	9	5	21	21	24.2 ± 0.3	-3.8	15.32 ± 0.02	0.07	144.47 ± 0.02	0.22	12.0		0.6	16	1.5	-1.52 ± 0.05	0.06 ± 0.03	1.46 ± 0.04	-0.07 ± 0.11	0.04 ± 0.09	-0.13 ± 0.03
*46	1995	9	9	15	53	17.4 ± 0.2	-2.6	-16.59 ± 0.03	-0.34	-174.38 ± 0.02	-0.13	12.0		0.6	16	1.8	-1.90 ± 0.07	0.34 ± 0.07	1.56 ± 0.04	-0.65 ± 0.25	0.11 ± 0.17	-0.06 ± 0.05
47	1995	11	28	13	19	51.9 ± 0.3	-0.1	-25.77 ± 0.03	0.48	-177.20 ± 0.02	-0.45	12.0		0.8	16	3.3	3.36 ± 0.12	-0.48 ± 0.11	-2.87 ± 0.09	-0.84 ± 0.39	0.53 ± 0.31	0.66 ± 0.08
48	1997	2	23	3	41	17.0 ± 0.3	5.0	-19.29 ± 0.02	0.46	-176.08 ± 0.02	-0.33	13.6 ± 2.1	3.6	0.7	16	2.3	-0.91 ± 0.22	-0.69 ± 0.14	1.60 ± 0.16	-0.25 ± 0.26	-0.81 ± 0.23	-1.75 ± 0.11
49	1997	3	10	2	55	41.5 ± 0.3	5.5	11.97 ± 0.01	0.22	43.27 ± 0.02	0.02	12.0		0.7	16	2.8	-1.11 ± 0.15	2.63 ± 0.10	-1.52 ± 0.13	0.28 ± 0.25	1.29 ± 0.29	-0.97 ± 0.09
50	1997	9	10	11	35	35.5 ± 0.5	7.5	24.81 ± 0.03	0.56	123.09 ± 0.03	-0.66	22.8 ± 1.1	12.8	0.6	16	1.4	-1.25 ± 0.12	1.20 ± 0.09	0.06 ± 0.06	0.57 ± 0.08	-0.13 ± 0.08	0.45 ± 0.04

* shallow vertical-CLVD earthquake

Table A5. (continued)

No.	Centroid Parameters													Half Drtn	Scale Factor 10^{ex}	M_0	Elements of Moment Tensor					
	Date			Time				Latitude		Longitude		Depth										
	Y	M	D	h	m	sec	δt_0	l	$\delta\lambda_0$	ϕ	$\delta\phi_0$	h	δh_0				M_{rr}	$M_{\theta\theta}$	$M_{\phi\phi}$	$M_{r\theta}$	$M_{r\phi}$	$M_{\theta\phi}$
51	1997	11	7	15	23	50.0 ± 0.5	-9.9	23.71 ± 0.03	-0.54	123.63 ± 0.03	-0.12	23.3 ± 1.4	13.3	0.5	16	1.1	0.85 ± 0.14	-0.60 ± 0.08	-0.25 ± 0.08	0.33 ± 0.06	0.52 ± 0.07	-0.49 ± 0.04
52	1998	10	8	0	7	16.5 ± 0.4	-3.5	42.25 ± 0.05	0.00	-127.13 ± 0.04	-0.38	12.0		0.4	15	6.4	-6.62 ± 0.35	1.23 ± 0.36	5.40 ± 0.30	-1.40 ± 1.43	0.17 ± 1.00	1.50 ± 0.25
53	1998	11	10	5	47	27.5 ± 0.4	-0.5	-15.00 ± 0.02	-0.50	-173.23 ± 0.02	0.27	12.0		0.7	16	2.4	-0.89 ± 0.10	1.04 ± 0.08	-0.15 ± 0.08	-1.73 ± 0.15	1.44 ± 0.16	0.32 ± 0.06
54	1999	11	23	21	46	5.7 ± 0.4	-2.3	-9.04 ± 0.02	-0.29	-108.66 ± 0.03	-0.41	12.0		0.6	16	1.8	-0.40 ± 0.10	0.57 ± 0.08	-0.17 ± 0.10	0.44 ± 0.21	-0.81 ± 0.20	1.43 ± 0.07
55	1999	11	28	12	40	3.8 ± 0.3	11.8	-14.81 ± 0.04	0.44	-173.82 ± 0.02	-0.07	12.0		0.6	16	1.2	-1.29 ± 0.07	0.36 ± 0.07	0.93 ± 0.04	0.01 ± 0.16	0.08 ± 0.15	0.43 ± 0.03
*56	2000	7	10	17	11	52.0 ± 0.1	0.0	34.09 ± 0.01	-0.16	139.55 ± 0.01	-0.20	12.0		1.3	17	1.7	-1.90 ± 0.03	0.82 ± 0.03	1.08 ± 0.03	0.42 ± 0.06	-0.17 ± 0.07	0.49 ± 0.02
*57	2000	7	16	1	37	55.0 ± 0.2	-5.0	34.12 ± 0.01	-0.13	139.59 ± 0.01	-0.16	12.0		1.0	17	0.8	-0.94 ± 0.02	0.41 ± 0.01	0.53 ± 0.01	0.22 ± 0.04	-0.11 ± 0.04	0.22 ± 0.01
*58	2000	7	16	17	11	51.3 ± 0.3	7.3	34.12 ± 0.02	0.37	139.55 ± 0.02	-0.20	12.0		1.0	16	6.7	-7.54 ± 0.17	3.31 ± 0.15	4.23 ± 0.15	1.86 ± 0.44	0.16 ± 0.43	1.66 ± 0.13
*59	2000	7	17	8	26	41.3 ± 0.2	1.3	34.10 ± 0.01	-0.15	139.58 ± 0.01	-0.17	12.0		1.0	17	0.8	-0.93 ± 0.01	0.41 ± 0.01	0.52 ± 0.01	0.19 ± 0.04	-0.13 ± 0.04	0.23 ± 0.01
*60	2000	7	17	21	35	45.4 ± 0.2	1.4	34.10 ± 0.01	-0.15	139.60 ± 0.01	-0.15	12.0		1.1	17	0.9	-0.98 ± 0.02	0.43 ± 0.01	0.55 ± 0.02	0.28 ± 0.04	-0.09 ± 0.04	0.23 ± 0.01
*61	2000	7	18	20	32	29.5 ± 0.2	-2.5	34.13 ± 0.01	-0.12	139.59 ± 0.01	0.34	12.0		1.2	17	1.4	-1.61 ± 0.03	0.76 ± 0.02	0.85 ± 0.03	0.31 ± 0.06	-0.15 ± 0.06	0.40 ± 0.02
*62	2000	7	19	16	15	40.0 ± 0.2	-4.1	34.10 ± 0.01	-0.15	139.51 ± 0.02	-0.24	12.0		0.9	16	5.4	-6.10 ± 0.13	2.68 ± 0.12	3.42 ± 0.12	1.59 ± 0.33	-0.06 ± 0.34	1.28 ± 0.10
*63	2000	7	21	15	7	21.3 ± 0.2	-6.7	34.09 ± 0.01	-0.16	139.53 ± 0.01	-0.22	12.0		1.0	16	6.5	-7.43 ± 0.13	3.38 ± 0.12	4.05 ± 0.12	1.27 ± 0.33	-0.11 ± 0.33	1.68 ± 0.10
*64	2000	7	22	5	1	23.9 ± 0.2	-4.1	34.14 ± 0.01	-0.11	139.53 ± 0.01	-0.22	12.0		1.1	17	0.9	-0.97 ± 0.02	0.44 ± 0.02	0.53 ± 0.02	0.35 ± 0.04	0.04 ± 0.04	0.21 ± 0.01
*65	2000	7	22	17	20	43.9 ± 0.2	-4.1	34.10 ± 0.01	-0.15	139.52 ± 0.02	-0.23	12.0		0.9	16	4.3	-4.96 ± 0.10	2.40 ± 0.09	2.56 ± 0.09	0.88 ± 0.25	0.26 ± 0.24	1.04 ± 0.09
*66	2000	7	24	5	25	20.0 ± 0.2	0.0	34.10 ± 0.01	-0.15	139.53 ± 0.01	-0.22	12.0		1.0	16	6.9	-7.56 ± 0.14	3.61 ± 0.13	3.94 ± 0.13	1.16 ± 0.36	-1.49 ± 0.36	2.04 ± 0.11
*67	2000	7	25	9	55	32.1 ± 0.2	-3.9	34.09 ± 0.01	-0.16	139.58 ± 0.01	0.33	12.0		0.9	16	5.4	-6.09 ± 0.10	2.72 ± 0.09	3.37 ± 0.10	0.96 ± 0.25	-0.94 ± 0.28	1.49 ± 0.08
*68	2000	7	26	3	57	54.9 ± 0.2	-5.1	34.12 ± 0.01	-0.38	139.56 ± 0.02	0.06	12.0		0.9	16	5.2	-5.88 ± 0.11	2.80 ± 0.10	3.07 ± 0.11	1.50 ± 0.26	-0.59 ± 0.29	1.31 ± 0.09
*69	2000	7	26	13	29	43.8 ± 0.1	-0.2	34.11 ± 0.01	-0.14	139.55 ± 0.01	-0.20	12.0		1.1	17	1.0	-1.06 ± 0.01	0.47 ± 0.01	0.59 ± 0.01	0.27 ± 0.04	-0.20 ± 0.04	0.27 ± 0.01
*70	2000	7	31	22	45	0.9 ± 0.3	-3.1	34.18 ± 0.02	-0.32	139.54 ± 0.02	0.04	12.0		1.3	17	1.7	-1.85 ± 0.05	0.73 ± 0.04	1.12 ± 0.04	0.51 ± 0.10	-0.13 ± 0.10	0.45 ± 0.04
*71	2000	8	2	6	15	35.8 ± 0.1	-0.2	34.09 ± 0.01	-0.16	139.58 ± 0.01	-0.17	12.0		1.6	17	3.0	-3.29 ± 0.03	1.49 ± 0.03	1.80 ± 0.04	0.59 ± 0.08	-0.40 ± 0.08	0.98 ± 0.03
*72	2000	8	4	16	11	13.6 ± 0.1	1.6	34.11 ± 0.01	-0.14	139.57 ± 0.01	-0.18	12.0		1.2	17	1.4	-1.52 ± 0.02	0.66 ± 0.02	0.86 ± 0.02	0.29 ± 0.04	-0.25 ± 0.05	0.41 ± 0.01
*73	2000	8	8	0	3	29.3 ± 0.2	1.3	34.13 ± 0.01	-0.12	139.51 ± 0.01	-0.24	12.0		0.9	16	5.5	-6.11 ± 0.10	2.69 ± 0.09	3.43 ± 0.09	1.69 ± 0.23	-0.35 ± 0.26	1.42 ± 0.08
*74	2000	8	8	17	11	58.6 ± 0.1	-1.4	34.10 ± 0.01	-0.15	139.60 ± 0.01	-0.15	12.0		1.3	17	1.5	-1.65 ± 0.02	0.72 ± 0.02	0.93 ± 0.02	0.31 ± 0.05	-0.19 ± 0.05	0.45 ± 0.02
*75	2000	8	10	22	2	47.4 ± 0.1	-0.6	34.11 ± 0.01	-0.14	139.59 ± 0.01	-0.16	12.0		1.5	17	2.5	-2.76 ± 0.03	1.20 ± 0.03	1.56 ± 0.03	0.63 ± 0.08	-0.33 ± 0.08	0.77 ± 0.03
*76	2000	8	13	6	40	21.4 ± 0.1	-2.6	34.12 ± 0.01	-0.13	139.60 ± 0.01	-0.15	12.0		1.3	17	1.9	-2.01 ± 0.03	0.90 ± 0.03	1.11 ± 0.03	0.49 ± 0.07	-0.24 ± 0.07	0.56 ± 0.02
*77	2000	8	16	0	7	29.2 ± 0.2	1.2	34.10 ± 0.01	-0.15	139.60 ± 0.01	-0.15	12.0		1.1	17	0.9	-0.99 ± 0.02	0.43 ± 0.01	0.56 ± 0.01	0.14 ± 0.04	-0.17 ± 0.04	0.26 ± 0.01
*78	2000	8	16	15	57	6.7 ± 0.1	-5.3	34.10 ± 0.01	-0.15	139.58 ± 0.01	-0.17	12.0		1.1	17	1.0	-1.09 ± 0.01	0.46 ± 0.01	0.63 ± 0.02	0.25 ± 0.03	-0.05 ± 0.04	0.27 ± 0.01
79	2000	8	16	16	17	11.1 ± 0.4	-0.9	33.63 ± 0.02	-0.87	139.83 ± 0.03	0.33	12.0		1.1	16	1.1	-1.00 ± 0.05	0.59 ± 0.04	0.40 ± 0.04	-0.25 ± 0.09	-0.35 ± 0.10	0.51 ± 0.03
80	2000	9	23	21	26	45.1 ± 0.4	5.1	33.73 ± 0.02	-0.02	139.78 ± 0.03	0.53	13.6 ± 1.8	3.6	0.5	15	8.8	5.21 ± 0.77	-2.29 ± 0.40	-2.92 ± 0.47	5.17 ± 0.84	5.30 ± 0.89	-1.55 ± 0.18
81	2001	12	24	8	56	18.5 ± 0.4	2.5	12.12 ± 0.03	0.37	41.66 ± 0.05	-0.09	12.0		0.5	15	7.5	-6.96 ± 0.44	5.54 ± 0.32	1.42 ± 0.52	1.26 ± 1.34	-1.68 ± 1.28	-3.36 ± 0.31
82	2002	1	1	21	2	44.2 ± 0.3	4.2	-5.38 ± 0.02	0.12	146.64 ± 0.03	-0.86	12.0		0.6	16	2.2	-1.57 ± 0.10	0.61 ± 0.08	0.95 ± 0.09	1.78 ± 0.17	0.49 ± 0.19	-0.41 ± 0.05
83	2002	10	26	2	32	3.9 ± 0.4	3.9	-55.44 ± 0.05	0.31	-29.71 ± 0.04	-0.46	12.0		0.6	16	1.0	-1.01 ± 0.06	0.12 ± 0.05	0.89 ± 0.04	0.24 ± 0.17	-0.25 ± 0.13	-0.06 ± 0.04
84	2003	1	17	1	6	33.0 ± 0.3	9.0	23.50 ± 0.02	-0.25	123.64 ± 0.02	-0.11	22.9 ± 1.1	12.9	0.8	16	2.9	1.80 ± 0.18	-1.55 ± 0.11	-0.25 ± 0.09	1.23 ± 0.11	1.62 ± 0.12	-1.30 ± 0.06
*85	2003	4	5	7	13	45.5 ± 0.3	9.5	38.65 ± 0.04	-0.10	15.19 ± 0.05	-0.56	12.0		0.4	15	3.8	4.37 ± 0.15	-2.51 ± 0.14	-1.86 ± 0.15	0.82 ± 0.69	0.26 ± 0.72	-0.71 ± 0.12
86	2003	4	19	4	3	6.8 ± 0.4	-5.2	23.61 ± 0.02	-0.64	123.70 ± 0.02	-0.05	22.4 ± 1.7	12.4	0.5	16	1.1	0.69 ± 0.13	-0.48 ± 0.07	-0.21 ± 0.07	0.49 ± 0.06	0.64 ± 0.08	-0.57 ± 0.04
87	2004	1	4	12	35	26.4 ± 0.3	-1.6	11.94 ± 0.02	-0.31	43.16 ± 0.05	0.91	14.9 ± 2.1	4.9	0.5	15	6.2	-4.70 ± 1.08	5.88 ± 0.66	-1.18 ± 0.62	2.44 ± 0.60	1.70 ± 0.99	-0.97 ± 0.32
88	2004	12	30	4	28	15.9 ± 0.2	-0.1	-3.40 ± 0.01	0.10	144.12 ± 0.02	-0.38	13.1 ± 1.0	3.1	0.9	16	5.3	3.36 ± 0.27	-4.31 ± 0.18	0.95 ± 0.17	-3.20 ± 0.37	-0.50 ± 0.33	1.64 ± 0.10
89	2005	1	4	3	26	24.2 ± 0.2	0.2	-14.80 ± 0.03	-0.05	-176.03 ± 0.02	-0.28	12.0		0.7	16	2.2	-2.18 ± 0.08	0.87 ± 0.08	1.31 ± 0.07	-0.63 ± 0.25	-0.10 ± 0.21	0.97 ± 0.05
90	2005	1	8	21	35	2.2 ± 0.2	-1.8	-14.57 ± 0.03	0.18	-175.90 ± 0.02	-0.15	12.0		0.7	16	2.6	-2.62 ± 0.08	1.26 ± 0.09	1.37 ± 0.07	0.38 ± 0.28	-0.06 ± 0.27	1.11 ± 0.07
91	2005	6	16	1	47	43.1 ± 0.3	-0.9	-14.69 ± 0.02	0.06	-173.55 ± 0.01	-0.30	12.0		0.6	16	1.6	-0.75 ± 0.09	-0.29 ± 0.08	1.04 ± 0.07	-0.11 ± 0.16	0.70 ± 0.17	1.22 ± 0.05
92	2005	9	25	10	49	5.9 ± 0.4	-6.1	12.59 ± 0.03	-0.16	40.54 ± 0.03	-0.21	12.0		0.5	16	1.2	-1.15 ± 0.06	0.25 ± 0.05	0.91 ± 0.07	0.00 ± 0.13	-0.06 ± 0.17	-0.48 ± 0.04
93	2005	10	19	18	49	3.2 ± 0.2	7.2	-16.83 ± 0.01	-0.08	168.40 ± 0.01	-0.35	12.0		0.6	16	1.9	0.75 ± 0.08	0.18 ± 0.07	-0.93 ± 0.06	0.59 ± 0.14	0.79 ± 0.15	-1.69 ± 0.05
94	2005	11	24	0	23	19.6 ± 0.4	-8.4	-14.50 ± 0.03	-0.25	-173.77 ± 0.02	-0.02	12.0		0.9	16	2.2	-2.17 ± 0.11	0.64 ± 0.11	1.53 ± 0.08	0.42 ± 0.25	-0.21 ± 0.25	0.95 ± 0.07
95	2006	3	1	21	9	6.1 ± 0.4	2.1	-22.98 ± 0.02	-0.23	171.46 ± 0.03	0.21	13.2 ± 1.4	3.2	0.6	16	1.5	1.35 ± 0.15	-1.32 ± 0.10	-0.03 ± 0.07	0.70 ± 0.14	0.16 ± 0.11	0.25 ± 0.04
96	2006	3	2	13	6	25.2 ± 0.3	1.2	-15.26 ± 0.02	-0.01	-175.57 ± 0.01	0.18	14.0 ± 2.1	4.0	0.6	16	1.4	-0.47 ± 0.11	-0.31 ± 0.07	0.79 ± 0.08	-0.18 ± 0.11	-0.02 ± 0.11	1.26 ± 0.07
97	2006	3	18	14	34	50.6 ± 0.3	-5.4	-15.27 ± 0.02	-0.27	-175.20 ± 0.02	-0.20	12.0		0.6	16	2.0	-0.26 ± 0.09	0.98 ± 0.08	-0.72 ± 0.07	-0.63 ± 0.17	-0.84 ± 0.18	1.47 ± 0.06
98	2006	3	21	11	32	5.1 ± 0.3	5.1	-15.07 ± 0.02	0.18	-174.96 ± 0.01	-0.21	12.0		0.6	16	1.7	-0.71 ± 0.08	1.16 ± 0.07	-0.44 ± 0.06	0.13 ± 0.15	0.38 ± 0.14	1.36 ± 0.05
99	2006	3	22	17	40	27.5 ± 0.4	-4.5	-37.33 ± 0.03	-0.08	78.15 ± 0.03	-0.10	12.0		0.5	15	7.8	-1.56 ± 0.53	-5.22 ± 0.46	6.79 ± 0.41	3.75 ± 0.90	1.46 ± 1.06	2.72 ± 0.43
100	2006	3	23	12	24	18.6 ± 0.3	2.6	-37.24 ± 0.02	0.01	78.17 ± 0.03	-0.08	12.0		0.5	16	1.0	0.04 ± 0.07	-0.92 ± 0.05	0.88 ± 0.06	-0.28 ± 0.13	0.37 ± 0.13	-0.05 ± 0.05

* shallow vertical-CLVD earthquake

Table A5. (continued)

No.	Centroid Parameters														Half Drtn	Scale Factor 10^{nx}	M_0	Elements of Moment Tensor					
	Date			Time				Latitude		Longitude		Depth						M_{rr}	$M_{\theta\theta}$	$M_{\phi\phi}$	$M_{r\theta}$	$M_{r\phi}$	$M_{\theta\phi}$
	Y	M	D	h	m	sec	δt_0	l	$\delta\lambda_0$	ϕ	$\delta\phi_0$	h	δh_0										
101	2006	4	5	16	1	28.4 ± 0.2	0.4	-37.23 ± 0.03	0.02	78.27 ± 0.04	0.02	12.0			0.6	16	1.9	-1.64 ± 0.08	0.78 ± 0.07	0.86 ± 0.07	-1.11 ± 0.23	0.33 ± 0.20	-0.64 ± 0.05
102	2006	4	28	20	52	20.9 ± 0.3	4.8	-14.93 ± 0.02	0.32	-174.10 ± 0.02	0.15	15.1 ± 1.8	5.1		0.6	16	1.5	-0.07 ± 0.09	-0.05 ± 0.07	0.12 ± 0.06	-0.46 ± 0.18	0.44 ± 0.19	1.35 ± 0.07
103	2006	6	5	18	2	40.3 ± 0.2	8.3	0.99 ± 0.01	0.49	-85.35 ± 0.01	0.15	15.1 ± 1.0	5.1		0.8	16	3.6	-0.66 ± 0.12	1.57 ± 0.11	-0.91 ± 0.11	-0.18 ± 0.25	0.40 ± 0.28	3.38 ± 0.09
104	2006	7	3	19	49	43.0 ± 0.2	7.1	-15.09 ± 0.02	0.16	-174.37 ± 0.01	-0.12	12.0			0.7	16	2.3	0.13 ± 0.09	1.14 ± 0.08	-1.27 ± 0.07	-0.16 ± 0.18	0.13 ± 0.19	1.99 ± 0.06
105	2006	7	6	8	46	26.9 ± 0.2	2.9	-5.55 ± 0.01	0.20	150.83 ± 0.02	0.08	16.2 ± 0.8	6.2		0.7	16	2.5	-2.32 ± 0.16	2.10 ± 0.10	0.22 ± 0.09	0.49 ± 0.15	0.67 ± 0.23	0.65 ± 0.05
106	2006	7	15	5	14	10.7 ± 0.4	2.7	-5.57 ± 0.02	0.18	150.84 ± 0.02	-0.41	15.8 ± 2.1	5.8		0.5	16	1.0	-0.15 ± 0.11	0.92 ± 0.08	-0.77 ± 0.07	-0.03 ± 0.12	-0.21 ± 0.15	-0.46 ± 0.05
107	2006	8	11	18	1	41.1 ± 0.3	-2.9	-19.51 ± 0.03	-0.26	-175.79 ± 0.02	-0.04	12.0			0.6	16	1.7	-0.66 ± 0.12	-1.09 ± 0.09	1.75 ± 0.08	-0.56 ± 0.22	0.08 ± 0.21	-0.66 ± 0.07
108	2006	8	11	18	7	38.8 ± 0.2	2.8	-19.53 ± 0.02	0.22	-175.85 ± 0.01	-0.10	12.0			0.8	16	3.6	-0.75 ± 0.13	-2.07 ± 0.10	2.81 ± 0.10	-1.30 ± 0.28	-0.27 ± 0.25	-2.14 ± 0.08
*109	2006	8	17	5	37	21.2 ± 0.4	1.2	-1.47		-78.44		12.0			0.5	15	5.3	-5.82 ± 0.36	4.55 ± 0.25	1.27 ± 0.37	0.08 ± 0.57	-1.00 ± 0.65	-0.43 ± 0.24
110	2006	9	22	10	16	54.0 ± 0.3	-2.0	-20.75 ± 0.02	0.00	-175.81 ± 0.01	-0.06	12.0			0.6	16	1.6	-0.69 ± 0.09	-0.87 ± 0.07	1.56 ± 0.06	-0.46 ± 0.18	-0.35 ± 0.13	-0.66 ± 0.06
111	2006	10	8	5	8	43.5 ± 0.3	3.5	-9.10 ± 0.01	-0.35	-108.28 ± 0.02	-0.53	14.2 ± 2.1	4.2		0.6	16	1.4	-0.36 ± 0.09	0.82 ± 0.08	-0.46 ± 0.06	0.02 ± 0.10	-0.34 ± 0.11	1.16 ± 0.06
112	2006	11	3	0	21	5.5 ± 0.3	1.5	-14.70 ± 0.04	0.05	-175.94 ± 0.03	-0.19	12.0			0.6	16	2.0	-2.09 ± 0.08	0.98 ± 0.08	1.11 ± 0.07	0.52 ± 0.29	-0.10 ± 0.25	0.75 ± 0.06
113	2006	11	14	9	11	43.5 ± 0.4	-8.5	21.86 ± 0.03	0.11	143.12 ± 0.02	0.37	13.6 ± 1.2	3.6		0.5	16	1.2	-1.29 ± 0.14	0.29 ± 0.07	1.00 ± 0.08	0.20 ± 0.10	-0.02 ± 0.08	-0.29 ± 0.03
114	2006	11	15	2	42	46.5 ± 0.3	6.6	23.55 ± 0.02	-0.20	123.67 ± 0.02	-0.08	23.2 ± 1.2	13.2		0.7	16	2.2	1.40 ± 0.17	-1.10 ± 0.10	-0.30 ± 0.09	0.79 ± 0.09	1.15 ± 0.11	-1.09 ± 0.06
115	2006	12	13	10	15	38.8 ± 0.3	2.8	11.14 ± 0.02	-0.11	124.68 ± 0.04	-0.07	12.0			0.5	16	0.8	-0.70 ± 0.05	0.89 ± 0.03	-0.19 ± 0.05	0.09 ± 0.10	0.11 ± 0.13	0.11 ± 0.03
116	2007	4	3	12	29	40.1 ± 0.4	4.1	-8.07 ± 0.02	-0.32	155.81 ± 0.05	-0.44	12.0			1.0	16	3.7	-3.88 ± 0.20	3.35 ± 0.16	0.53 ± 0.19	0.19 ± 0.53	0.52 ± 0.70	0.17 ± 0.15
117	2007	8	6	18	57	13.0 ± 0.4	1.0	-26.15 ± 0.02	0.10	-177.68 ± 0.02	-0.43	15.7 ± 2.0	5.7		0.7	16	2.0	-0.69 ± 0.15	0.30 ± 0.10	0.39 ± 0.11	0.72 ± 0.25	-0.67 ± 0.27	1.59 ± 0.08
118	2008	1	31	7	8	59.4 ± 0.3	3.4	-19.76 ± 0.02	0.24	169.87 ± 0.03	-0.13	12.0			0.6	16	1.6	-1.23 ± 0.07	0.48 ± 0.07	0.74 ± 0.06	0.45 ± 0.17	0.77 ± 0.18	-0.85 ± 0.05
119	2008	2	11	23	20	30.6 ± 0.2	6.6	-15.34 ± 0.02	0.16	-174.75 ± 0.01	-0.25	12.0			0.7	16	2.2	-0.80 ± 0.09	0.39 ± 0.09	0.41 ± 0.07	0.36 ± 0.17	0.79 ± 0.19	2.00 ± 0.06
120	2008	2	28	8	1	58.6 ± 0.3	-1.4	-37.17 ± 0.04	0.08	78.25 ± 0.04	0.00	12.0			0.6	16	2.1	-1.74 ± 0.10	0.87 ± 0.09	0.87 ± 0.09	-1.19 ± 0.32	0.31 ± 0.27	-0.75 ± 0.06
*121	2008	4	11	0	46	13.3 ± 0.4	5.3	16.09 ± 0.04	-0.16	144.69 ± 0.02	-0.06	12.0			0.5	16	1.2	-1.14 ± 0.07	0.14 ± 0.05	1.00 ± 0.05	0.55 ± 0.17	0.11 ± 0.13	-0.14 ± 0.04
122	2008	4	25	18	44	0.3 ± 0.3	0.3	-15.25 ± 0.02	0.50	-174.97 ± 0.01	-0.22	19.2 ± 1.7	9.2		0.8	16	2.5	-0.30 ± 0.16	-0.03 ± 0.13	0.34 ± 0.10	0.75 ± 0.19	0.79 ± 0.19	2.29 ± 0.11
*123	2008	7	22	8	45	22.4 ± 0.2	2.4	-17.36 ± 0.02	-0.61	167.52 ± 0.02	-0.23	12.0			0.8	16	2.7	2.55 ± 0.10	-0.67 ± 0.09	-1.87 ± 0.07	0.73 ± 0.22	-1.45 ± 0.23	0.19 ± 0.06
124	2009	3	7	9	41	0.5 ± 0.2	-11.5	-15.53 ± 0.01	-0.78	-174.94 ± 0.01	-0.19	12.0			1.3	16	2.3	-0.01 ± 0.10	2.14 ± 0.08	-2.13 ± 0.07	-0.44 ± 0.18	-0.69 ± 0.16	0.04 ± 0.07
125	2009	3	10	20	32	32.7 ± 0.6	0.7	10.22 ± 0.03	-0.53	-104.12 ± 0.03	0.13	12.0			1.2	16	1.5	-0.26 ± 0.08	-0.53 ± 0.06	0.80 ± 0.07	0.37 ± 0.15	-0.60 ± 0.17	1.10 ± 0.05
126	2009	4	17	11	8	49.8 ± 0.4	9.8	14.67 ± 0.04	-0.08	144.02 ± 0.05	-0.73	12.0			1.1	15	5.8	-5.06 ± 0.45	2.89 ± 0.32	2.17 ± 0.44	-0.49 ± 1.29	2.09 ± 1.19	3.18 ± 0.30
127	2009	8	2	16	40	18.7 ± 0.7	-5.3	14.28 ± 0.04	0.03	-93.00 ± 0.06	-0.75	14.9 ± 1.7	4.9		1.1	16	0.9	0.93 ± 0.15	-0.79 ± 0.09	-0.14 ± 0.08	0.00 ± 0.09	0.12 ± 0.12	0.16 ± 0.04
128	2009	9	28	18	49	33.3 ± 0.3	5.3	27.78 ± 0.02	-0.47	127.79 ± 0.03	-0.46	12.0			1.2	16	1.0	-0.65 ± 0.06	0.85 ± 0.04	-0.20 ± 0.05	0.09 ± 0.09	-0.47 ± 0.11	0.45 ± 0.03
129	2009	10	1	17	39	36.1 ± 0.2	8.1	-15.26 ± 0.02	-0.01	-175.80 ± 0.01	-0.05	12.0			1.2	16	2.2	-0.26 ± 0.08	1.61 ± 0.08	-1.35 ± 0.06	-0.10 ± 0.16	-0.15 ± 0.17	1.68 ± 0.05
130	2009	10	3	14	2	14.5 ± 0.3	-1.5	-14.75 ± 0.05	0.00	-176.02 ± 0.03	-0.27	12.0			1.2	16	1.5	-1.56 ± 0.07	0.64 ± 0.08	0.92 ± 0.06	0.15 ± 0.30	-0.33 ± 0.19	0.58 ± 0.05
131	2009	12	23	0	26	5.6 ± 0.6	21.6	10.44 ± 0.02	0.69	-103.67 ± 0.03	0.58	12.0			1.2	16	1.2	0.27 ± 0.08	-1.15 ± 0.06	0.88 ± 0.06	-0.01 ± 0.14	0.35 ± 0.12	0.49 ± 0.05

* shallow vertical-CLVD earthquake

Table A6. Principal axes and best-double-couple parameters for 131 earthquakes from the Global CMT Project's Surface Wave catalog (Category 2), 1991 - 2009.

No.	Scale Factor 10^{nn}	Principal Axes									M_0	Best Double Couple					
		T-axis			N-axis			P-axis				Plane 1			Plane 2		
		σ	δ	ε	σ	δ	ε	σ	δ	ε		φ_s	θ	λ	φ_s	θ	λ
1	16	5.99	75	285	0.05	1	189	-6.05	15	99	6.0	187	30	87	10	60	92
2	16	7.53	9	240	-2.12	79	25	-5.40	6	149	6.5	284	79	178	15	88	11
3	16	2.58	21	222	-0.24	49	339	-2.34	33	117	2.5	263	50	-171	167	83	-40
*4	16	4.91	63	289	-1.66	13	171	-3.23	23	75	4.1	140	25	57	356	69	104
5	16	2.73	1	64	-0.16	87	167	-2.57	3	334	2.7	109	88	-178	19	88	-2
6	16	1.83	8	57	-0.24	78	191	-1.59	8	326	1.7	102	78	-180	12	90	-12
7	16	4.93	7	252	-1.05	72	139	-3.87	17	344	4.4	27	73	-7	119	83	-163
8	16	1.08	7	82	0.12	15	350	-1.19	74	198	1.1	188	40	-67	339	54	-108
9	16	2.44	15	322	-0.06	67	191	-2.38	16	57	2.4	100	67	-1	190	89	-157
10	16	3.21	12	220	-0.71	50	325	-2.50	37	120	2.9	267	55	-160	165	74	-37
11	16	1.87	8	238	0.32	11	329	-2.18	76	110	2.0	315	38	-107	157	54	-77
12	16	4.04	47	284	-0.07	13	28	-3.97	41	129	4.0	283	13	166	27	87	77
13	16	3.70	11	332	-0.64	70	93	-3.06	17	239	3.4	16	70	-175	285	86	-20
14	16	3.81	69	277	-0.68	3	15	-3.13	21	106	3.5	202	24	98	14	66	86
15	16	1.73	11	133	-0.34	74	265	-1.38	12	41	1.6	177	74	-179	87	89	-16
16	16	2.63	4	140	0.13	8	49	-2.76	81	258	2.7	238	41	-78	42	50	-100
17	16	1.04	54	292	0.10	15	44	-1.14	31	144	1.1	274	19	142	41	78	75
18	16	1.31	2	262	0.07	2	352	-1.38	87	125	1.3	350	43	-93	174	48	-87
19	16	1.03	8	271	0.09	4	2	-1.12	81	117	1.1	357	37	-96	185	53	-85
20	16	2.29	2	57	-0.22	70	152	-2.08	20	326	2.2	104	75	-167	10	77	-16
21	16	1.52	43	326	0.06	42	180	-1.58	17	73	1.5	120	46	22	14	74	134
22	16	2.73	0	148	-0.29	76	56	-2.44	14	238	2.6	282	80	-9	14	81	-170
23	16	4.00	31	328	-0.51	41	207	-3.50	34	81	3.7	113	41	-3	205	88	-131
24	16	3.26	1	92	0.20	4	183	-3.45	86	348	3.4	179	44	-95	6	46	-85
25	16	4.89	3	68	-1.55	71	166	-3.34	18	337	4.1	114	75	-169	21	79	-15
26	16	1.65	24	128	0.24	59	267	-1.89	18	30	1.8	168	60	175	260	86	30
*27	16	4.24	70	287	-1.67	15	154	-2.56	14	60	3.4	130	33	63	342	61	107
28	16	2.09	8	336	-0.14	77	105	-1.95	10	244	2.0	20	77	-179	290	89	-13
29	16	1.41	26	163	-0.03	63	328	-1.38	6	70	1.4	204	68	165	300	76	23
30	16	1.20	9	145	-0.04	61	252	-1.16	27	50	1.2	190	64	-167	95	78	-26
31	16	1.33	18	149	-0.30	70	304	-1.02	8	57	1.2	192	71	173	284	83	19
32	16	4.26	8	310	-0.16	75	189	-4.09	13	42	4.2	85	75	-3	176	87	-165
*33	16	1.18	9	96	0.63	27	190	-1.81	62	349	1.5	158	43	-131	28	59	-59
34	16	1.63	13	136	-0.04	73	275	-1.59	11	44	1.6	180	73	179	270	89	17
35	16	5.55	8	330	-1.57	79	193	-3.99	8	61	4.8	106	79	0	16	90	169
36	16	1.28	9	232	-0.04	6	141	-1.24	79	20	1.3	329	36	-80	137	54	-97
37	16	2.95	65	193	-0.54	4	95	-2.41	25	3	2.7	85	21	79	276	70	94
38	16	2.24	4	319	-0.30	86	112	-1.94	2	229	2.1	4	86	179	94	89	4
*39	16	1.92	19	337	0.79	9	244	-2.71	69	130	2.3	82	28	-71	240	64	-100
40	16	2.65	70	77	-0.43	20	253	-2.21	1	343	2.4	93	47	118	235	49	63
41	16	1.25	72	140	-0.01	0	231	-1.23	18	321	1.2	52	27	91	231	63	90
*42	16	2.15	22	220	0.70	1	129	-2.85	68	38	2.5	311	23	-89	129	67	-91
*43	16	1.59	11	222	0.87	1	312	-2.45	79	48	2.0	311	34	-92	133	56	-89
*44	16	1.53	19	241	0.78	1	331	-2.31	71	63	1.9	330	26	-91	151	64	-89
45	16	1.47	1	265	0.05	2	175	-1.52	87	16	1.5	357	44	-87	172	46	-93
*46	16	1.57	3	266	0.51	15	175	-2.08	75	6	1.8	11	44	-69	162	49	-110
47	16	3.56	78	197	-0.43	10	343	-3.12	6	74	3.3	175	39	105	335	52	78
48	16	2.65	10	63	-0.65	57	168	-2.00	31	327	2.3	109	61	-164	11	76	-30
49	16	2.84	0	193	-0.07	52	283	-2.78	38	102	2.8	244	64	-151	141	64	-29
50	16	1.45	11	343	-0.03	13	75	-1.41	73	214	1.4	58	36	-112	264	57	-75

* shallow vertical-CLVD earthquake

Table A6. (continued)

No.	Scale Factor 10^{nn}	Principal Axes									M_0	Best Double Couple					
		T-axis			N-axis			P-axis				Plane 1			Plane 2		
		σ	δ	ε	σ	δ	ε	σ	δ	ε		φ_1	θ	λ	φ_1	θ	λ
51	16	1.07	70	284	0.04	12	48	-1.11	16	142	1.1	249	30	114	42	62	77
52	15	5.89	1	108	1.00	10	198	-6.88	80	11	6.4	188	45	-105	28	47	-76
53	16	2.17	34	197	0.52	17	299	-2.69	51	51	2.4	238	19	-153	121	81	-73
54	16	1.69	4	141	0.16	57	44	-1.85	32	234	1.8	272	64	-21	12	71	-153
55	16	1.16	2	298	0.13	1	208	-1.29	88	80	1.2	30	43	-88	207	47	-92
*56	17	1.46	2	309	0.52	10	39	-1.98	80	207	1.7	28	44	-105	228	48	-76
*57	17	0.70	2	308	0.28	11	38	-0.98	79	210	0.8	27	45	-106	229	48	-75
*58	16	5.62	6	309	2.23	8	40	-7.85	80	183	6.7	31	40	-102	226	51	-80
*59	17	0.70	1	309	0.27	11	39	-0.98	79	215	0.8	28	45	-105	229	47	-75
*60	17	0.74	4	310	0.31	12	41	-1.05	78	203	0.9	27	43	-108	231	50	-74
*61	17	1.21	2	313	0.46	9	43	-1.67	81	210	1.4	34	44	-103	232	48	-78
*62	16	4.47	5	309	1.92	9	40	-6.39	80	189	5.4	30	41	-104	228	51	-79
*63	16	5.47	3	310	2.12	6	41	-7.59	83	192	6.5	34	42	-99	226	49	-82
*64	17	0.74	9	313	0.31	10	45	-1.05	77	181	0.9	32	37	-106	232	55	-78
*65	16	3.60	5	314	1.47	4	44	-5.07	83	171	4.3	40	40	-96	228	50	-85
*66	16	5.83	1	132	2.09	11	42	-7.93	79	229	6.9	233	45	-74	32	47	-105
*67	16	4.57	1	129	1.75	10	38	-6.32	80	223	5.4	228	45	-76	29	47	-103
*68	16	4.29	3	314	1.90	11	45	-6.20	79	206	5.2	33	43	-106	234	49	-76
*69	17	0.81	0	309	0.33	14	39	-1.14	76	217	1.0	26	46	-109	232	47	-71
*70	17	1.43	3	305	0.54	12	36	-1.96	78	199	1.7	23	43	-107	226	49	-75
*71	17	2.63	1	311	0.78	10	41	-3.41	80	216	3.0	31	45	-104	230	47	-76
*72	17	1.19	0	128	0.41	11	38	-1.60	79	220	1.4	229	46	-74	27	47	-106
*73	16	4.59	4	310	1.88	11	41	-6.46	78	198	5.5	29	42	-106	230	50	-76
*74	17	1.29	1	309	0.42	10	39	-1.71	80	214	1.5	29	45	-104	228	47	-76
*75	17	2.18	2	309	0.72	11	40	-2.90	79	211	2.5	28	44	-106	230	48	-75
*76	17	1.58	2	311	0.54	12	41	-2.12	78	210	1.9	29	44	-107	232	48	-74
*77	17	0.77	2	127	0.26	10	37	-1.03	80	227	0.9	227	44	-76	28	48	-103
*78	17	0.83	3	308	0.31	9	38	-1.14	80	198	1.0	28	42	-104	227	49	-77
79	16	1.11	11	139	-0.01	5	48	-1.09	77	293	1.1	236	34	-80	44	57	-97
80	15	9.29	61	316	-1.04	2	223	-8.25	29	132	8.8	218	16	84	43	74	92
81	15	7.67	8	30	-0.36	7	121	-7.32	80	253	7.5	112	38	-101	306	53	-81
82	16	1.64	27	13	1.04	14	276	-2.68	59	161	2.2	134	22	-49	271	73	-105
83	16	0.93	8	84	0.16	10	352	-1.09	77	213	1.0	185	38	-74	345	54	-102
84	16	2.75	63	286	0.36	15	48	-3.11	22	144	2.9	259	27	124	42	68	74
*85	15	4.47	83	346	-1.41	2	238	-3.06	6	148	3.8	236	39	87	60	51	93
86	16	1.05	65	290	0.20	11	44	-1.25	22	138	1.1	248	25	116	40	68	78
87	15	6.46	12	5	-0.49	22	270	-5.97	65	121	6.2	120	38	-53	257	60	-116
88	16	4.81	63	143	0.94	19	276	-5.75	18	12	5.3	130	31	128	267	66	69
89	16	2.14	6	130	0.17	10	221	-2.31	78	8	2.2	209	40	-106	49	52	-77
90	16	2.44	2	314	0.24	6	44	-2.67	83	203	2.6	37	43	-99	230	48	-81
91	16	1.88	12	299	-0.50	48	195	-1.39	39	39	1.6	71	53	-22	174	72	-141
92	16	1.16	1	62	-0.01	2	152	-1.15	88	291	1.2	151	44	-92	334	46	-88
93	16	1.41	2	35	1.05	73	298	-2.45	17	126	1.9	169	76	-11	262	80	-166
94	16	2.14	1	303	0.13	12	33	-2.27	78	209	2.2	21	46	-106	224	47	-74
95	16	1.55	74	331	-0.03	9	96	-1.52	13	188	1.5	291	33	108	90	59	79
96	16	1.62	3	123	-0.45	78	229	-1.17	11	33	1.4	169	80	-174	78	84	-10
97	16	2.21	22	148	-0.50	61	13	-1.71	19	245	2.0	287	61	2	196	88	151
98	16	1.97	7	330	-0.63	65	226	-1.34	24	63	1.7	104	68	-13	198	78	-158
99	15	7.94	14	286	-0.20	56	38	-7.73	30	187	7.8	330	58	-168	234	80	-32
100	16	1.03	22	265	-0.04	63	124	-1.00	16	1	1.0	44	63	5	312	86	153

* shallow vertical-CLVD earthquake

Table A6. (continued)

No.	Scale Factor 10^{m}	Principal Axes									M_0	Best Double Couple					
		T-axis			N-axis			P-axis				Plane 1			Plane 2		
		σ	δ	ε	σ	δ	ε	σ	δ	ε		φ_1	θ	λ	φ_2	θ	λ
101	16	1.77	17	220	0.30	11	127	-2.07	69	5	1.9	328	29	-66	121	63	-103
102	16	1.39	0	313	0.20	67	222	-1.59	23	43	1.5	86	74	-16	180	74	-163
103	16	3.93	1	325	-0.59	81	229	-3.34	9	55	3.6	100	83	-6	190	84	-173
104	16	2.26	2	151	0.14	85	265	-2.41	4	61	2.3	196	86	-178	106	88	-4
105	16	2.40	8	341	0.11	11	249	-2.51	76	108	2.5	83	38	-72	242	54	-103
106	16	1.04	1	14	-0.10	75	108	-0.94	15	284	1.0	60	79	-170	328	80	-12
107	16	1.91	5	257	-0.36	58	159	-1.56	31	350	1.7	29	65	-20	127	72	-154
108	16	3.63	3	249	-0.13	64	153	-3.50	26	340	3.6	22	70	-17	117	74	-159
*109	15	4.61	1	8	1.35	8	98	-5.96	82	269	5.3	90	44	-101	285	47	-79
110	16	1.75	6	77	-0.32	53	174	-1.43	36	343	1.6	126	61	-157	24	70	-31
111	16	1.52	5	149	-0.27	70	45	-1.25	19	241	1.4	283	73	-10	16	80	-163
112	16	1.82	4	314	0.38	10	45	-2.19	79	202	2.0	33	42	-105	233	50	-77
113	16	1.11	2	70	0.20	7	340	-1.31	83	177	1.2	167	43	-80	333	48	-99
114	16	2.00	65	282	0.33	15	46	-2.33	20	141	2.2	255	28	122	40	66	74
115	16	0.91	4	354	-0.18	11	263	-0.73	79	102	0.8	95	43	-74	254	49	-104
116	16	3.37	2	356	0.58	6	266	-3.94	83	101	3.7	93	44	-81	260	47	-99
117	16	1.94	1	314	0.06	53	45	-2.00	37	224	2.0	6	64	-152	263	65	-29
118	16	1.51	7	233	0.22	29	327	-1.74	60	130	1.6	294	45	-133	167	58	-55
119	16	2.60	14	314	-0.88	64	194	-1.72	22	49	2.2	90	65	-6	183	84	-154
120	16	1.94	17	219	0.26	12	125	-2.20	69	1	2.1	327	30	-65	119	63	-104
*121	16	1.02	1	262	0.33	21	352	-1.35	69	170	1.2	332	48	-119	191	49	-62
122	16	2.83	19	313	-0.68	71	132	-2.15	0	223	2.5	356	76	166	89	77	14
*123	16	3.10	71	58	-0.69	5	164	-2.40	18	256	2.7	355	28	102	161	63	84
124	16	2.23	12	178	0.11	69	54	-2.34	17	271	2.3	314	70	-4	45	87	-160
125	16	1.49	12	117	-0.02	60	6	-1.47	28	213	1.5	252	62	-12	347	79	-151
126	15	5.83	6	317	0.01	20	225	-5.84	69	62	5.8	67	43	-60	209	54	-115
127	16	0.94	84	276	-0.11	6	104	-0.83	1	13	0.9	97	44	81	290	46	99
128	16	1.02	3	159	-0.01	37	67	-1.01	53	253	1.0	281	53	-42	39	58	-135
129	16	2.38	3	156	-0.26	85	19	-2.11	3	246	2.2	291	86	0	201	90	176
130	16	1.39	3	127	0.24	10	37	-1.63	79	235	1.5	228	43	-75	28	49	-103
131	16	1.13	22	282	0.14	68	112	-1.27	3	13	1.2	60	72	13	326	77	162

* shallow vertical-CLVD earthquake

Table A7. Centroid-moment-tensor solutions for 86 shallow vertical-CLVD earthquakes located near recently active volcanoes.

No.	Centroid Parameters													Half Drtn	Scale Factor 10^{ex}	M_o	Elements of Moment Tensor					
	Date			Time				Latitude		Longitude		Depth										
	Y	M	D	h	m	sec	δt_0	l	$\delta\lambda_0$	ϕ	$\delta\phi_0$	h				M_{rr}	$M_{\theta\theta}$	$M_{\phi\phi}$	$M_{r\theta}$	$M_{r\phi}$	$M_{\theta\phi}$
1	1978	5	16	7	35	49.1 ± 0.3	2.1	40.99 ± 0.02	0.00	141.44 ± 0.03	0.18	12.0	1.2	17	1.3	1.53 ± 0.04	-0.90 ± 0.04	-0.63 ± 0.04	0.35 ± 0.11	0.11 ± 0.11	-0.02 ± 0.04
2	1978	9	9	6	1	7.6 ± 0.3	0.7	-56.34 ± 0.02	-0.03	-27.31 ± 0.04	0.35	12.0	1.3	17	1.6	1.48 ± 0.05	-0.87 ± 0.04	-0.62 ± 0.05	-0.59 ± 0.11	-0.92 ± 0.11	-0.05 ± 0.04
3	1979	10	1	12	23	51.2 ± 0.2	2.6	-21.29 ± 0.01	-0.21	-175.66 ± 0.01	0.05	12.0	1.4	17	2.2	2.53 ± 0.04	-0.91 ± 0.05	-1.62 ± 0.04	0.03 ± 0.11	0.12 ± 0.10	0.52 ± 0.03
4	1984	6	13	2	29	29.8 ± 0.2	5.2	31.57 ± 0.01	0.09	139.97 ± 0.02	-0.11	12.0	1.6	17	3.4	4.01 ± 0.09	-2.38 ± 0.07	-1.63 ± 0.10	-0.06 ± 0.19	-0.50 ± 0.22	-0.64 ± 0.07
5	1990	5	15	15	21	31.1 ± 0.6	2.3	-2.96 ± 0.04	0.00	35.80 ± 0.02	-0.05	12.0	1.3	17	1.5	-1.67 ± 0.05	0.56 ± 0.04	1.11 ± 0.06	-0.46 ± 0.16	0.43 ± 0.14	-0.09 ± 0.04
6	1991	9	6	5	40	54.6 ± 0.2	-1.4	-3.85 ± 0.01	-0.10	152.03 ± 0.02	-0.22	12.0	0.8	16	4.1	3.30 ± 0.11	-1.61 ± 0.08	-1.68 ± 0.11	0.71 ± 0.25	3.07 ± 0.21	0.74 ± 0.07
7	1992	8	20	18	31	39.9 ± 0.2	5.2	25.43 ± 0.02	-0.05	141.13 ± 0.02	-0.20	12.0	1.0	17	0.7	0.79 ± 0.02	-0.28 ± 0.01	-0.51 ± 0.02	-0.09 ± 0.04	-0.24 ± 0.05	-0.11 ± 0.01
8	1994	1	16	10	18	41.5 ± 0.1	2.9	-20.62 ± 0.01	0.00	-175.20 ± 0.01	0.31	12.0	1.1	17	1.1	1.23 ± 0.02	-0.67 ± 0.02	-0.56 ± 0.02	0.07 ± 0.04	0.03 ± 0.05	0.32 ± 0.01
9	1994	1	25	23	15	1.9 ± 0.2	-2.1	-3.82 ± 0.01	-0.07	152.05 ± 0.02	-0.20	12.0	0.8	16	3.4	3.46 ± 0.09	-1.82 ± 0.07	-1.64 ± 0.09	0.48 ± 0.23	2.03 ± 0.20	0.57 ± 0.05
10	1994	3	19	21	49	42.9 ± 0.4	-1.1	41.67 ± 0.03	-0.58	-127.06 ± 0.03	-0.31	12.0	0.6	16	1.5	-1.25 ± 0.06	0.10 ± 0.05	1.14 ± 0.05	-1.01 ± 0.17	-0.28 ± 0.13	-0.05 ± 0.04
11	1994	11	8	13	7	56.8 ± 0.4	4.8	-15.91 ± 0.03	0.59	-173.97 ± 0.03	-0.47	12.0	0.6	16	2.3	-2.16 ± 0.12	1.47 ± 0.13	0.69 ± 0.07	1.06 ± 0.23	1.01 ± 0.28	0.15 ± 0.07
12	1995	1	10	13	43	35.8 ± 0.0	1.9	-14.30		-168.83		12.0	0.9	16	2.5	-2.87 ± 0.10	1.51 ± 0.11	1.36 ± 0.07	-0.70 ± 0.20	0.26 ± 0.17	-0.48 ± 0.06
13	1995	1	10	17	44	0.1 ± 0.3	0.1	-14.24 ± 0.02	0.01	-169.03 ± 0.02	-0.28	12.0	0.7	16	2.5	-2.16 ± 0.09	1.14 ± 0.09	1.02 ± 0.06	-1.35 ± 0.20	1.07 ± 0.22	-0.38 ± 0.05
14	1995	1	10	23	49	26.3 ± 0.3	-1.7	-14.25 ± 0.03	0.00	-168.97 ± 0.03	-0.22	12.0	0.7	16	2.0	-2.30 ± 0.08	1.19 ± 0.10	1.11 ± 0.07	-0.53 ± 0.26	0.57 ± 0.28	-0.28 ± 0.05
15	1995	1	11	18	16	5.9 ± 0.3	-2.1	-14.18 ± 0.03	-0.43	-169.00 ± 0.03	-0.25	12.0	0.7	16	1.9	-1.90 ± 0.08	0.87 ± 0.09	1.03 ± 0.06	-0.54 ± 0.22	1.05 ± 0.26	-0.15 ± 0.05
16	1995	2	17	17	45	42.7 ± 0.2	-1.4	-3.85 ± 0.01	-0.10	152.10 ± 0.01	-0.15	12.0	1.4	16	4.3	3.69 ± 0.09	-1.75 ± 0.07	-1.94 ± 0.08	0.94 ± 0.21	3.02 ± 0.20	0.73 ± 0.06
17	1995	9	9	15	53	17.4 ± 0.2	-2.6	-16.59 ± 0.03	-0.34	-174.38 ± 0.02	-0.13	12.0	0.6	16	1.8	-1.90 ± 0.07	0.34 ± 0.07	1.56 ± 0.04	-0.65 ± 0.25	0.11 ± 0.17	-0.06 ± 0.05
18	1996	2	15	1	11	43.0 ± 0.2	-1.0	-3.85 ± 0.02	-0.10	152.03 ± 0.02	0.28	12.0	1.5	16	4.6	4.27 ± 0.11	-2.12 ± 0.09	-2.15 ± 0.11	0.68 ± 0.35	3.05 ± 0.31	0.96 ± 0.07
19	1996	7	27	13	6	38.6 ± 0.5	14.6	18.77 ± 0.04	-0.23	-155.18 ± 0.03	-0.18	12.0	1.4	16	2.8	2.97 ± 0.14	-1.22 ± 0.12	-1.74 ± 0.12	-0.24 ± 0.50	-0.92 ± 0.39	-0.80 ± 0.11
20	1996	9	4	18	16	7.7 ± 0.1	5.8	31.51 ± 0.01	-0.05	139.99 ± 0.01	0.06	12.0	1.7	17	3.9	4.49 ± 0.04	-2.61 ± 0.04	-1.88 ± 0.05	-0.31 ± 0.10	-0.96 ± 0.10	-0.73 ± 0.04
21	1996	9	9	4	34	21.9 ± 0.1	1.4	30.44 ± 0.01	0.01	130.95 ± 0.01	0.22	12.0	1.7	17	4.2	-4.79 ± 0.04	1.81 ± 0.04	2.98 ± 0.04	-0.49 ± 0.10	-0.69 ± 0.10	-0.85 ± 0.03
22	1997	9	5	3	23	17.0 ± 0.1	2.6	-56.41 ± 0.01	-0.15	-27.47 ± 0.01	0.35	12.0	1.3	17	1.7	1.86 ± 0.02	-0.95 ± 0.02	-0.89 ± 0.02	-0.34 ± 0.05	-0.83 ± 0.05	0.20 ± 0.02
23	1999	6	29	5	50	9.2 ± 0.1	0.3	-9.59 ± 0.01	-0.12	147.97 ± 0.01	0.12	12.0	1.6	17	2.8	-2.72 ± 0.03	1.50 ± 0.03	1.23 ± 0.03	-1.88 ± 0.08	-0.13 ± 0.07	0.01 ± 0.03
24	1999	8	7	6	17	30.5 ± 0.1	1.6	-21.24 ± 0.01	-0.15	-175.61 ± 0.01	0.45	12.0	1.4	17	2.6	2.97 ± 0.03	-1.19 ± 0.03	-1.78 ± 0.03	-0.71 ± 0.07	0.08 ± 0.07	0.40 ± 0.02
25	1999	12	4	8	46	57.7 ± 0.2	0.9	51.56 ± 0.02	0.09	-178.29 ± 0.02	0.13	12.0	0.8	16	6.4	-4.64 ± 0.13	1.50 ± 0.13	3.14 ± 0.09	5.20 ± 0.29	1.77 ± 0.29	0.07 ± 0.09
26	2000	7	7	11	22	4.3 ± 0.6	-3.7	34.15 ± 0.04	-0.10	139.47 ± 0.04	-0.28	12.0	1.1	15	5.1	-6.00 ± 0.29	2.70 ± 0.25	3.29 ± 0.25	0.25 ± 1.03	-1.84 ± 0.80	0.50 ± 0.21
27	2000	7	9	13	40	15.3 ± 0.2	15.3	34.11 ± 0.01	-0.14	139.56 ± 0.02	-0.19	12.0	1.9	17	0.7	-0.81 ± 0.02	0.38 ± 0.01	0.43 ± 0.01	0.23 ± 0.04	0.05 ± 0.04	0.18 ± 0.01
28	2000	7	10	17	11	52.0 ± 0.1	0.0	34.09 ± 0.01	-0.16	139.55 ± 0.01	-0.20	12.0	1.3	17	1.7	-1.90 ± 0.03	0.82 ± 0.03	1.08 ± 0.03	0.42 ± 0.06	-0.17 ± 0.07	0.49 ± 0.02
29	2000	7	11	15	37	31.5 ± 0.2	-4.5	34.10 ± 0.01	-0.15	139.59 ± 0.01	-0.16	12.0	1.2	17	1.1	-1.28 ± 0.02	0.55 ± 0.01	0.73 ± 0.02	0.26 ± 0.04	-0.14 ± 0.04	0.30 ± 0.01
30	2000	7	12	4	6	60.0 ± 0.2	-4.0	34.13 ± 0.01	-0.12	139.57 ± 0.01	-0.18	12.0	1.0	17	0.8	-0.88 ± 0.01	0.39 ± 0.01	0.48 ± 0.01	0.20 ± 0.04	-0.12 ± 0.04	0.20 ± 0.01
31	2000	7	12	18	45	55.6 ± 0.2	-4.4	34.12 ± 0.01	-0.38	139.58 ± 0.01	0.08	12.0	1.2	17	1.1	-1.26 ± 0.02	0.54 ± 0.02	0.72 ± 0.02	0.30 ± 0.04	-0.10 ± 0.05	0.31 ± 0.02
32	2000	7	13	17	12	29.8 ± 0.1	-2.2	34.10 ± 0.01	-0.15	139.60 ± 0.01	0.35	12.0	1.5	17	2.5	-2.73 ± 0.03	1.24 ± 0.03	1.49 ± 0.03	0.59 ± 0.07	-0.30 ± 0.08	0.72 ± 0.03
33	2000	7	15	14	34	46.4 ± 0.2	-1.6	34.14 ± 0.01	-0.11	139.57 ± 0.01	-0.18	12.0	1.2	17	1.1	-1.29 ± 0.02	0.60 ± 0.02	0.70 ± 0.02	0.35 ± 0.05	-0.06 ± 0.05	0.28 ± 0.02
34	2000	7	16	1	37	55.0 ± 0.2	-5.0	34.12 ± 0.01	-0.13	139.59 ± 0.01	-0.16	12.0	1.0	17	0.8	-0.94 ± 0.02	0.41 ± 0.01	0.53 ± 0.01	0.22 ± 0.04	-0.11 ± 0.04	0.22 ± 0.01
35	2000	7	16	17	11	51.3 ± 0.3	7.3	34.12 ± 0.02	0.37	139.55 ± 0.02	-0.20	12.0	1.0	16	6.7	-7.54 ± 0.17	3.31 ± 0.15	4.23 ± 0.15	1.86 ± 0.44	0.16 ± 0.43	1.66 ± 0.13
36	2000	7	17	8	26	41.3 ± 0.2	1.3	34.10 ± 0.01	-0.15	139.58 ± 0.01	-0.17	12.0	1.0	17	0.8	-0.93 ± 0.01	0.41 ± 0.01	0.52 ± 0.01	0.19 ± 0.04	-0.13 ± 0.04	0.23 ± 0.01
37	2000	7	17	21	35	45.4 ± 0.2	1.4	34.10 ± 0.01	-0.15	139.60 ± 0.01	-0.15	12.0	1.1	17	0.9	-0.98 ± 0.02	0.43 ± 0.01	0.55 ± 0.02	0.28 ± 0.04	-0.09 ± 0.04	0.23 ± 0.01
38	2000	7	18	20	32	29.5 ± 0.2	-2.5	34.13 ± 0.01	-0.12	139.59 ± 0.01	0.34	12.0	1.2	17	1.4	-1.61 ± 0.03	0.76 ± 0.02	0.85 ± 0.03	0.31 ± 0.06	-0.15 ± 0.06	0.40 ± 0.02
39	2000	7	19	16	15	40.0 ± 0.2	-4.1	34.10 ± 0.01	-0.15	139.51 ± 0.02	-0.24	12.0	0.9	16	5.4	-6.10 ± 0.13	2.68 ± 0.12	3.42 ± 0.12	1.59 ± 0.33	-0.06 ± 0.34	1.28 ± 0.10
40	2000	7	20	8	24	17.4 ± 0.2	1.4	34.11 ± 0.01	-0.14	139.58 ± 0.01	-0.17	12.0	1.1	17	1.0	-1.08 ± 0.02	0.48 ± 0.02	0.60 ± 0.02	0.22 ± 0.04	-0.21 ± 0.04	0.27 ± 0.01
41	2000	7	21	0	27	51.4 ± 0.2	-0.6	34.16 ± 0.01	-0.09	139.49 ± 0.01	-0.26	12.0	1.0	17	0.8	-0.90 ± 0.02	0.40 ± 0.02	0.50 ± 0.02	0.31 ± 0.04	0.05 ± 0.04	0.20 ± 0.01
42	2000	7	21	15	7	21.3 ± 0.2	-6.7	34.09 ± 0.01	-0.16	139.53 ± 0.01	-0.22	12.0	1.0	16	6.5	-7.43 ± 0.13	3.38 ± 0.12	4.05 ± 0.12	1.27 ± 0.33	-0.11 ± 0.33	1.68 ± 0.10
43	2000	7	22	5	1	23.9 ± 0.2	-4.1	34.14 ± 0.01	-0.11	139.53 ± 0.01	-0.22	12.0	1.1	17	0.9	-0.97 ± 0.02	0.44 ± 0.02	0.53 ± 0.02	0.35 ± 0.04	0.04 ± 0.04	0.21 ± 0.01
44	2000	7	22	17	20	43.9 ± 0.2	-4.1	34.10 ± 0.01	-0.15	139.52 ± 0.02	-0.23	12.0	0.9	16	4.3	-4.96 ± 0.10	2.40 ± 0.09	2.56 ± 0.09	0.88 ± 0.25	0.26 ± 0.24	1.04 ± 0.09
45	2000	7	23	16	36	44.5 ± 0.2	-3.5	34.13 ± 0.01	-0.12	139.55 ± 0.01	-0.20	12.0	1.0	17	0.9	-0.96 ± 0.02	0.44 ± 0.01	0.52 ± 0.01	0.25 ± 0.04	0.00 ± 0.04	0.27 ± 0.01
46	2000	7	24	5	25	20.0 ± 0.2	0.0	34.10 ± 0.01	-0.15	139.53 ± 0.01	-0.22	12.0	1.0	16	6.9	-7.56 ± 0.14	3.61 ± 0.13	3.94 ± 0.13	1.16 ± 0.36	-1.49 ± 0.36	2.04 ± 0.11
47	2000	7	24	19	55	37.3 ± 0.2	1.4	34.11 ± 0.01	-0.14	139.55 ± 0.01	-0.20	12.0	1.1	17	1.1	-1.19 ± 0.02	0.50 ± 0.01	0.69 ± 0.02	0.29 ± 0.04	-0.24 ± 0.04	0.33 ± 0.01
48	2000	7	25	9	55	32.1 ± 0.2	-3.9	34.09 ± 0.01	-0.16	139.58 ± 0.01	0.33	12.0	0.9	16	5.4	-6.09 ± 0.10	2.72 ± 0.09	3.37 ± 0.10	0.96 ± 0.25	-0.94 ± 0.28	1.49 ± 0.08
49	2000	7	25	20	10	28.0 ± 0.1	-4.0	34.14 ± 0.01	-0.11	139.55 ± 0.01	-0.20	12.0	1.0	17	0.7	-0.82 ± 0.01	0.37 ± 0.01	0.46 ± 0.01	0.24 ± 0.03	-0.14 ± 0.03	0.18 ± 0.01
50	2000	7	26	3	57	54.9 ± 0.2	-5.1	34.12 ± 0.01	-0.38	139.56 ± 0.02	0.06	12.0	0.9	16	5.2	-5.88 ± 0.11	2.80 ± 0.10	3.07 ± 0.11	1.50 ± 0.26	-0.59 ± 0.29	1.31 ± 0.09

Note: All earthquakes are shallow with centroid depths fixed to 12 km.

Table A7. (continued)

No.	Centroid Parameters												Half Drtn	Scale Factor 10^{ex}	M_0	Elements of Moment Tensor					
	Date			Time				Latitude		Longitude		Depth									
	Y	M	D	h	m	sec	δt_0	l	$\delta\lambda_0$	ϕ	$\delta\phi_0$	h				M_{rr}	$M_{\theta\theta}$	$M_{\phi\phi}$	$M_{r\theta}$	$M_{r\phi}$	$M_{\theta\phi}$
51	2000	7	26	13	29	43.8 ± 0.1	-0.2	34.11 ± 0.01	-0.14	139.55 ± 0.01	-0.20	12.0	1.1	17	1.0	-1.06 ± 0.01	0.47 ± 0.01	0.59 ± 0.01	0.27 ± 0.04	-0.20 ± 0.04	0.27 ± 0.01
52	2000	7	27	7	22	50.4 ± 0.1	-5.6	34.13 ± 0.01	-0.37	139.59 ± 0.01	0.09	12.0	1.2	17	1.5	-1.64 ± 0.02	0.71 ± 0.02	0.93 ± 0.02	0.43 ± 0.05	-0.27 ± 0.05	0.44 ± 0.02
53	2000	7	28	7	7	39.3 ± 0.1	-4.7	34.10 ± 0.01	-0.15	139.58 ± 0.01	0.33	12.0	1.2	17	1.4	-1.45 ± 0.02	0.62 ± 0.02	0.82 ± 0.02	0.42 ± 0.05	-0.33 ± 0.05	0.38 ± 0.02
54	2000	7	29	7	51	38.8 ± 0.1	2.8	34.12 ± 0.01	-0.13	139.57 ± 0.01	-0.18	12.0	1.4	17	2.2	-2.40 ± 0.03	1.11 ± 0.03	1.29 ± 0.03	0.67 ± 0.07	-0.29 ± 0.07	0.64 ± 0.02
55	2000	7	30	13	36	33.5 ± 0.2	1.5	34.17 ± 0.02	-0.08	139.59 ± 0.02	-0.16	12.0	2.3	17	1.9	-2.05 ± 0.05	0.96 ± 0.04	1.08 ± 0.04	0.46 ± 0.16	-0.57 ± 0.17	0.45 ± 0.04
56	2000	7	31	22	45	0.9 ± 0.3	-3.1	34.18 ± 0.02	-0.32	139.54 ± 0.02	0.04	12.0	1.3	17	1.7	-1.85 ± 0.05	0.73 ± 0.04	1.12 ± 0.04	0.51 ± 0.10	-0.13 ± 0.10	0.45 ± 0.04
57	2000	8	2	6	15	35.8 ± 0.1	-0.2	34.09 ± 0.01	-0.16	139.58 ± 0.01	-0.17	12.0	1.6	17	3.0	-3.29 ± 0.03	1.49 ± 0.03	1.80 ± 0.04	0.59 ± 0.08	-0.40 ± 0.08	0.98 ± 0.03
58	2000	8	3	19	16	42.1 ± 0.2	2.1	34.14 ± 0.01	-0.11	139.52 ± 0.01	-0.23	12.0	1.3	17	1.9	-2.04 ± 0.04	0.88 ± 0.03	1.16 ± 0.03	0.60 ± 0.09	0.01 ± 0.10	0.53 ± 0.03
59	2000	8	4	16	11	13.6 ± 0.1	1.6	34.11 ± 0.01	-0.14	139.57 ± 0.01	-0.18	12.0	1.2	17	1.4	-1.52 ± 0.02	0.66 ± 0.02	0.86 ± 0.02	0.29 ± 0.04	-0.25 ± 0.05	0.41 ± 0.01
60	2000	8	6	0	23	22.7 ± 0.1	2.7	34.13 ± 0.01	-0.12	139.53 ± 0.01	-0.22	12.0	1.4	17	2.4	-2.57 ± 0.04	1.12 ± 0.03	1.45 ± 0.03	0.72 ± 0.08	-0.09 ± 0.09	0.70 ± 0.03
61	2000	8	8	0	3	29.3 ± 0.2	1.3	34.13 ± 0.01	-0.12	139.51 ± 0.01	-0.24	12.0	0.9	16	5.5	-6.11 ± 0.10	2.69 ± 0.09	3.43 ± 0.09	1.69 ± 0.23	-0.35 ± 0.26	1.42 ± 0.08
62	2000	8	8	17	11	58.6 ± 0.1	-1.4	34.10 ± 0.01	-0.15	139.60 ± 0.01	-0.15	12.0	1.3	17	1.5	-1.65 ± 0.02	0.72 ± 0.02	0.93 ± 0.02	0.31 ± 0.05	-0.19 ± 0.05	0.45 ± 0.02
63	2000	8	10	22	2	47.4 ± 0.1	-0.6	34.11 ± 0.01	-0.14	139.59 ± 0.01	-0.16	12.0	1.5	17	2.5	-2.76 ± 0.03	1.20 ± 0.03	1.56 ± 0.03	0.63 ± 0.08	-0.33 ± 0.08	0.77 ± 0.03
64	2000	8	13	6	40	21.4 ± 0.1	-2.6	34.12 ± 0.01	-0.13	139.60 ± 0.01	-0.15	12.0	1.3	17	1.9	-2.01 ± 0.03	0.90 ± 0.03	1.11 ± 0.03	0.49 ± 0.07	-0.24 ± 0.07	0.56 ± 0.02
65	2000	8	16	0	7	29.2 ± 0.2	1.2	34.10 ± 0.01	-0.15	139.60 ± 0.01	-0.15	12.0	1.1	17	0.9	-0.99 ± 0.02	0.43 ± 0.01	0.56 ± 0.01	0.14 ± 0.04	-0.17 ± 0.04	0.26 ± 0.01
66	2000	8	16	15	57	6.7 ± 0.1	-5.3	34.10 ± 0.01	-0.15	139.58 ± 0.01	-0.17	12.0	1.1	17	1.0	-1.09 ± 0.01	0.46 ± 0.01	0.63 ± 0.02	0.25 ± 0.03	-0.05 ± 0.04	0.27 ± 0.01
67	2000	8	17	19	7	44.2 ± 0.2	0.2	34.14 ± 0.01	-0.11	139.57 ± 0.01	-0.18	12.0	1.2	17	1.4	-1.57 ± 0.02	0.72 ± 0.02	0.85 ± 0.02	0.40 ± 0.06	-0.15 ± 0.07	0.38 ± 0.02
68	2000	8	18	9	9	16.3 ± 0.2	4.3	34.30 ± 0.02	0.05	139.40 ± 0.02	0.15	12.0	1.4	16	2.3	-2.19 ± 0.06	1.19 ± 0.05	1.01 ± 0.05	1.35 ± 0.14	0.02 ± 0.15	0.46 ± 0.04
69	2001	1	18	20	17	17.4 ± 0.1	3.0	-56.31 ± 0.01	-0.10	-27.43 ± 0.02	0.07	12.0	1.2	17	1.3	1.52 ± 0.02	-0.64 ± 0.02	-0.88 ± 0.02	-0.20 ± 0.06	-0.49 ± 0.06	0.16 ± 0.02
70	2002	1	20	23	45	31.6 ± 0.2	-4.4	-1.42 ± 0.01	0.33	29.13 ± 0.02	-0.12	12.0	1.7	16	6.2	-6.98 ± 0.14	4.09 ± 0.12	2.90 ± 0.14	-1.13 ± 0.45	-0.21 ± 0.40	1.60 ± 0.12
71	2002	8	16	21	30	47.5 ± 0.4	7.5	-20.28 ± 0.04	-0.03	-175.99 ± 0.03	-0.24	12.0	1.2	16	1.5	-1.53 ± 0.08	0.46 ± 0.10	1.07 ± 0.06	0.41 ± 0.24	-0.49 ± 0.23	0.48 ± 0.05
72	2003	4	5	7	13	45.5 ± 0.3	9.5	38.65 ± 0.04	-0.10	15.19 ± 0.05	-0.56	12.0	0.4	15	3.8	4.37 ± 0.15	-2.51 ± 0.14	-1.86 ± 0.15	0.82 ± 0.69	0.26 ± 0.72	-0.71 ± 0.12
73	2004	11	10	10	35	38.0 ± 0.1	4.0	-21.26 ± 0.01	-0.07	-175.62 ± 0.01	0.48	12.0	1.4	17	2.4	2.74 ± 0.03	-1.20 ± 0.03	-1.54 ± 0.03	-0.71 ± 0.07	0.17 ± 0.07	0.44 ± 0.02
74	2005	2	25	16	17	1.6 ± 0.2	0.3	12.77 ± 0.01	0.06	123.23 ± 0.02	-0.10	12.0	0.7	16	2.8	-2.83 ± 0.06	2.05 ± 0.05	0.79 ± 0.06	-0.91 ± 0.16	0.81 ± 0.20	-0.49 ± 0.04
75	2005	8	23	1	38	20.1 ± 0.2	3.0	-59.80 ± 0.01	-0.43	-26.68 ± 0.02	0.35	12.0	0.9	16	6.6	6.15 ± 0.11	-3.96 ± 0.12	-2.18 ± 0.11	3.84 ± 0.30	0.89 ± 0.31	-1.06 ± 0.09
76	2005	8	31	1	24	54.9 ± 0.1	6.3	-59.48 ± 0.01	-0.12	-26.86 ± 0.02	0.24	12.0	1.4	17	2.1	2.12 ± 0.02	-1.33 ± 0.03	-0.79 ± 0.03	-1.09 ± 0.06	-0.68 ± 0.06	-0.08 ± 0.02
77	2005	10	22	20	34	47.9 ± 0.2	6.0	-1.06 ± 0.01	-0.20	-91.31 ± 0.01	-0.36	12.0	1.3	17	1.9	1.52 ± 0.02	-1.05 ± 0.02	-0.47 ± 0.03	0.87 ± 0.05	-1.31 ± 0.06	-0.10 ± 0.02
78	2006	1	1	7	12	8.8 ± 0.1	11.8	31.60 ± 0.01	0.21	140.17 ± 0.01	0.04	12.0	1.5	17	2.9	3.10 ± 0.04	-2.27 ± 0.04	-0.83 ± 0.04	-0.86 ± 0.09	-0.27 ± 0.10	-0.39 ± 0.03
79	2006	8	17	5	37	21.2 ± 0.4	1.2	-1.47		-78.44		12.0	0.5	15	5.3	-5.82 ± 0.36	4.55 ± 0.25	1.27 ± 0.37	0.08 ± 0.57	-1.00 ± 0.65	-0.43 ± 0.24
80	2008	4	11	0	46	13.3 ± 0.4	5.3	16.09 ± 0.04	-0.16	144.69 ± 0.02	-0.06	12.0	0.5	16	1.2	-1.14 ± 0.07	0.14 ± 0.05	1.00 ± 0.05	0.55 ± 0.17	0.11 ± 0.13	-0.14 ± 0.04
81	2008	6	12	13	10	14.7 ± 0.1	1.7	25.53 ± 0.01	0.07	141.18 ± 0.01	-0.07	12.0	1.1	17	1.1	1.25 ± 0.01	-0.55 ± 0.01	-0.70 ± 0.02	-0.10 ± 0.03	0.05 ± 0.04	-0.22 ± 0.01
82	2008	7	22	8	45	22.4 ± 0.2	2.4	-17.36 ± 0.02	-0.61	167.52 ± 0.02	-0.23	12.0	0.8	16	2.7	2.55 ± 0.10	-0.67 ± 0.09	-1.87 ± 0.07	0.73 ± 0.22	-1.45 ± 0.23	0.19 ± 0.06
83	2008	11	18	12	46	3.8 ± 0.2	0.8	-18.76 ± 0.02	0.28	169.55 ± 0.02	0.08	12.0	0.9	16	3.5	-3.07 ± 0.10	1.57 ± 0.09	1.50 ± 0.08	1.86 ± 0.26	0.88 ± 0.29	-1.33 ± 0.07
84	2009	2	17	3	30	58.8 ± 0.1	5.5	-30.54 ± 0.01	0.18	-178.58 ± 0.01	0.04	12.0	2.0	17	6.5	7.34 ± 0.05	-2.72 ± 0.05	-4.63 ± 0.05	-2.00 ± 0.15	-0.77 ± 0.14	1.21 ± 0.04
85	2009	4	19	8	54	52.8 ± 0.3	6.2	14.66 ± 0.02	-0.16	144.23 ± 0.02	-0.33	12.0	0.7	16	3.1	-3.12 ± 0.11	0.95 ± 0.08	2.16 ± 0.10	-1.21 ± 0.33	0.58 ± 0.25	0.87 ± 0.07
86	2009	5	26	0	49	42.9 ± 0.1	-4.2	-21.24 ± 0.01	-0.10	-175.62 ± 0.01	1.32	12.0	1.3	17	2.0	2.30 ± 0.02	-0.89 ± 0.02	-1.41 ± 0.02	-0.19 ± 0.06	-0.22 ± 0.06	0.42 ± 0.02

Note: All earthquakes are shallow with centroid depths fixed to 12 km.

Table A8. Principal axes and best-double-couple parameters for 86 shallow vertical-CLVD earthquakes located near recently active volcanoes.

No.	Scale Factor 10^{exp}	Principal Axes									M_0	Best Double Couple					
		T-axis			N-axis			P-axis				Plane 1			Plane 2		
		σ	δ	ε	σ	δ	ε	σ	δ	ε		φ_s	θ	λ	φ_s	θ	λ
1	17	1.58	82	342	-0.64	2	83	-0.95	8	173	1.3	265	37	93	82	53	88
2	17	1.93	68	120	-0.72	7	226	-1.21	21	319	1.6	61	24	106	223	67	83
3	17	2.53	88	293	-0.64	1	152	-1.89	1	62	2.2	151	44	88	334	46	92
4	17	4.05	85	90	-1.29	4	239	-2.76	3	329	3.4	64	43	96	235	48	84
5	17	1.21	10	255	0.60	8	164	-1.82	77	36	1.5	355	35	-76	158	56	-100
6	16	4.91	63	289	-1.66	13	171	-3.23	23	75	4.1	140	25	57	356	69	104
7	17	0.84	80	110	-0.23	0	201	-0.60	10	292	0.7	22	35	90	201	55	90
8	17	1.23	87	332	-0.30	3	130	-0.94	1	220	1.1	313	44	94	128	46	86
9	16	4.24	70	287	-1.67	15	154	-2.56	14	60	3.4	130	33	63	342	61	107
10	16	1.18	9	96	0.63	27	190	-1.81	62	349	1.5	158	43	-131	28	59	-59
11	16	1.92	19	337	0.79	9	244	-2.71	69	130	2.3	82	28	-71	240	64	-100
12	16	2.02	8	219	0.96	3	128	-2.99	81	16	2.5	313	37	-84	126	53	-94
13	16	2.15	22	220	0.70	1	129	-2.85	68	38	2.5	311	23	-89	129	67	-91
14	16	1.59	11	222	0.87	1	312	-2.45	79	48	2.0	311	34	-92	133	56	-89
15	16	1.53	19	241	0.78	1	331	-2.31	71	63	1.9	330	26	-91	151	64	-89
16	16	5.20	64	292	-1.88	13	173	-3.31	21	77	4.3	144	26	59	358	68	104
17	16	1.57	3	266	0.51	15	175	-2.08	75	6	1.8	11	44	-69	162	49	-110
18	16	5.61	67	289	-1.96	15	160	-3.65	17	65	4.6	132	31	59	347	64	107
19	16	3.14	79	96	-0.67	5	213	-2.46	9	304	2.8	40	36	98	210	55	84
20	17	4.64	82	101	-1.50	6	235	-3.14	6	326	3.9	63	39	99	231	51	82
21	17	3.45	3	63	1.45	7	154	-4.90	83	311	4.2	146	43	-100	340	48	-81
22	17	2.14	73	115	-0.94	14	334	-1.18	10	241	1.7	314	37	67	163	57	106
23	17	2.22	21	177	1.23	0	87	-3.44	69	356	2.8	267	24	-89	86	66	-90
24	17	3.09	81	181	-1.07	8	330	-2.02	5	60	2.6	159	41	102	323	50	79
25	16	4.99	29	326	2.82	8	61	-7.82	60	164	6.4	35	18	-117	243	74	-82
26	15	3.82	9	112	2.54	6	21	-6.36	79	259	5.1	209	36	-80	17	55	-97
27	17	0.61	8	314	0.25	7	45	-0.86	79	177	0.7	36	38	-102	230	53	-81
28	17	1.46	2	309	0.52	10	39	-1.98	80	207	1.7	28	44	-105	228	48	-76
29	17	0.96	1	308	0.38	10	38	-1.33	80	210	1.1	27	45	-104	227	47	-76
30	17	0.65	1	310	0.28	11	40	-0.92	79	213	0.8	28	45	-106	230	47	-75
31	17	0.96	3	308	0.36	10	39	-1.32	79	203	1.1	28	43	-105	228	49	-76
32	17	2.10	2	311	0.75	10	41	-2.85	79	211	2.5	30	44	-105	231	48	-76
33	17	0.94	5	313	0.42	10	43	-1.36	79	196	1.1	32	41	-105	231	51	-77
34	17	0.70	2	308	0.28	11	38	-0.98	79	210	0.8	27	45	-106	229	48	-75
35	16	5.62	6	309	2.23	8	40	-7.85	80	183	6.7	31	40	-102	226	51	-80
36	17	0.70	1	309	0.27	11	39	-0.98	79	215	0.8	28	45	-105	229	47	-75
37	17	0.74	4	310	0.31	12	41	-1.05	78	203	0.9	27	43	-108	231	50	-74
38	17	1.21	2	313	0.46	9	43	-1.67	81	210	1.4	34	44	-103	232	48	-78
39	16	4.47	5	309	1.92	9	40	-6.39	80	189	5.4	30	41	-104	228	51	-79
40	17	0.81	1	128	0.33	12	38	-1.14	78	222	1.0	230	45	-73	26	47	-106
41	17	0.69	9	312	0.28	9	43	-0.97	77	179	0.8	31	37	-106	230	54	-79
42	16	5.47	3	310	2.12	6	41	-7.59	83	192	6.5	34	42	-99	226	49	-82
43	17	0.74	9	313	0.31	10	45	-1.05	77	181	0.9	32	37	-106	232	55	-78
44	16	3.60	5	314	1.47	4	44	-5.07	83	171	4.3	40	40	-96	228	50	-85
45	17	0.77	6	313	0.23	8	44	-1.00	80	190	0.9	34	40	-103	231	51	-79
46	16	5.83	1	132	2.09	11	42	-7.93	79	229	6.9	233	45	-74	32	47	-105
47	17	0.94	0	127	0.34	14	36	-1.28	76	218	1.1	230	46	-71	23	47	-109
48	16	4.57	1	129	1.75	10	38	-6.32	80	223	5.4	228	45	-76	29	47	-103
49	17	0.60	2	309	0.29	14	40	-0.89	76	212	0.7	26	45	-110	232	48	-72
50	16	4.29	3	314	1.90	11	45	-6.20	79	206	5.2	33	43	-106	234	49	-76

Note: All earthquakes are shallow with centroid depths fixed to 12 km.

Table A8. (continued)

No.	Scale Factor 10^{ex}	Principal Axes									M_0	Best Double Couple					
		T-axis			N-axis			P-axis				Plane 1			Plane 2		
		σ	δ	ε	σ	δ	ε	σ	δ	ε		φ_s	θ	λ	φ_s	θ	λ
51	17	0.81	0	309	0.33	14	39	-1.14	76	217	1.0	26	46	-109	232	47	-71
52	17	1.28	1	308	0.48	13	39	-1.76	77	214	1.5	25	45	-109	231	48	-72
53	17	1.11	0	127	0.48	15	37	-1.59	75	218	1.4	232	47	-69	23	47	-111
54	17	1.86	3	313	0.71	12	43	-2.56	77	208	2.2	30	43	-108	234	49	-74
55	17	1.48	2	129	0.75	14	39	-2.24	75	229	1.9	234	44	-69	26	49	-109
56	17	1.43	3	305	0.54	12	36	-1.96	78	199	1.7	23	43	-107	226	49	-75
57	17	2.63	1	311	0.78	10	41	-3.41	80	216	3.0	31	45	-104	230	47	-76
58	17	1.61	6	310	0.56	10	41	-2.16	78	188	1.9	29	40	-105	229	52	-78
59	17	1.19	0	128	0.41	11	38	-1.60	79	220	1.4	229	46	-74	27	47	-106
60	17	2.04	5	310	0.68	10	41	-2.72	78	196	2.4	29	41	-106	230	51	-76
61	16	4.59	4	310	1.88	11	41	-6.46	78	198	5.5	29	42	-106	230	50	-76
62	17	1.29	1	309	0.42	10	39	-1.71	80	214	1.5	29	45	-104	228	47	-76
63	17	2.18	2	309	0.72	11	40	-2.90	79	211	2.5	28	44	-106	230	48	-75
64	17	1.58	2	311	0.54	12	41	-2.12	78	210	1.9	29	44	-107	232	48	-74
65	17	0.77	2	127	0.26	10	37	-1.03	80	227	0.9	227	44	-76	28	48	-103
66	17	0.83	3	308	0.31	9	38	-1.14	80	198	1.0	28	42	-104	227	49	-77
67	17	1.18	3	312	0.48	11	42	-1.66	78	206	1.4	30	43	-106	232	49	-75
68	16	1.89	16	332	0.79	10	65	-2.67	70	186	2.3	46	30	-111	251	62	-78
69	17	1.64	77	117	-0.62	9	344	-1.01	9	252	1.3	332	37	75	170	55	101
70	16	5.29	5	146	1.81	3	236	-7.09	84	357	6.2	233	40	-95	59	50	-86
71	16	1.35	5	116	0.38	17	25	-1.73	72	222	1.5	224	43	-65	11	52	-112
72	15	4.47	83	346	-1.41	2	238	-3.06	6	148	3.8	236	39	87	60	51	93
73	17	2.87	80	187	-0.95	7	321	-1.91	7	52	2.4	150	38	101	316	52	81
74	16	2.46	12	202	0.67	6	293	-3.13	76	50	2.8	284	33	-102	117	58	-83
75	16	7.47	71	350	-1.74	3	250	-5.72	18	159	6.6	243	27	82	72	63	94
76	17	2.55	71	145	-0.82	5	250	-1.73	18	341	2.1	80	27	101	247	63	84
77	17	2.37	62	60	-0.89	12	308	-1.48	26	213	1.9	278	22	58	132	72	102
78	17	3.25	81	161	-0.73	1	255	-2.52	9	345	2.9	76	36	91	255	54	89
79	15	4.61	1	8	1.35	8	98	-5.96	82	269	5.3	90	44	-101	285	47	-79
80	16	1.02	1	262	0.33	21	352	-1.35	69	170	1.2	332	48	-119	191	49	-62
81	17	1.26	86	207	-0.40	4	36	-0.85	1	306	1.1	32	45	85	219	46	95
82	16	3.10	71	58	-0.69	5	164	-2.40	18	256	2.7	355	28	102	161	63	84
83	16	2.98	9	38	1.05	23	304	-4.02	65	147	3.5	153	42	-53	289	58	-118
84	17	7.80	78	158	-2.59	12	333	-5.22	1	64	6.5	166	45	107	322	47	73
85	16	2.61	1	118	0.94	18	208	-3.56	72	26	3.1	190	47	-115	45	48	-65
86	17	2.33	85	135	-0.68	5	332	-1.64	2	241	2.0	326	44	83	156	47	97

Note: All earthquakes are shallow with centroid depths fixed to 12 km.

Appendix B

Earthquake source parameters for the 2010 western Gulf of Aden rifting episode

This is the final accepted manuscript for work that has been published as:
Shuler, A. & Nettles, M. 2012. Earthquake source parameters for the 2010 western Gulf of Aden rifting episode, *Geophys. J. Int.*, **190**, 1111-1122, doi:10.1111/j.1365-246X.2012.05529.x.

Abstract

On November 14, 2010, an intense swarm of earthquakes began in the western Gulf of Aden. Within a 48-hour period, 82 earthquakes with magnitudes between 4.5 and 5.5 were reported along an ~80-km-long segment of the east-west trending Aden Ridge, making this swarm one of the largest ever observed in an extensional oceanic setting. In this study, we calculate centroid-moment-tensor solutions for 110 earthquakes that occurred between November 2010 and April 2011. Over eighty percent of the cumulative seismic moment was due to earthquakes that occurred within one week of the onset of the swarm. We find that this sequence has a *b*-value of ~1.6 and is dominated by normal-faulting earthquakes that, early in the swarm, migrate westwards with time. These earthquakes are located in rhombic basins along a section of the ridge that was previously characterized by low levels of seismicity and a lack of recent volcanism on the seafloor. Body-wave modeling demonstrates that the events occur in the top 2 to 3 km of the crust. Nodal planes of the normal-faulting earthquakes are consistent with previously mapped faults in the axial valley. A small number of strike-slip earthquakes observed between two basins near 44°E, where the axial valley changes orientation, depth and width, likely indicate the presence of an incipient transform fault and the early stages of ridge-transform segmentation. The direction of extension accommodated by the earthquakes is intermediate between the rift-orthogonal and the direction of relative motion between the Arabian and

Somalian plates, consistent with the oblique style of rifting occurring along the slow-spreading Aden Ridge. The 2010 swarm shares many characteristics with dike-induced rifting episodes from both oceanic and continental settings. We conclude that the 2010 swarm represents the seismic component of an undersea magmatic rifting episode along the nascent Aden Ridge, and attribute the large size of the earthquakes to the combined effects of the slow spreading rate, relatively thick crust and recent quiescence. We estimate that the rifting episode was caused by dike intrusions that propagated laterally for 12 to 18 hours, accommodating ~1-14 m of opening or ~85-800 years of spreading along this section of the ridge. Our findings demonstrate the westward propagation of active seafloor spreading into this section of the western Gulf of Aden and illustrate that deformation at the onset of seafloor spreading may be accommodated by discrete episodes of faulting and magmatism. A comparison with similar sequences on land suggests that the 2010 episode may be only the first of several dike-induced rifting episodes to occur in the western Gulf of Aden.

B1. Introduction

The Gulf of Aden is a young ocean basin that stretches from the Afar depression in East Africa to the Carlsberg Ridge in the Indian Ocean (Figure B1). Here, northeastward motion of the Arabian plate relative to the Somalian plate is accommodated by oblique spreading on a system of approximately east-west trending rift zones (Bosworth *et al.* 2005; Manighetti *et al.* 1997; Cochran *et al.* 1981; Courtillot 1980). Beginning in mid-November 2010, the western Gulf of Aden between 43.75° and 44.5°E experienced an intense swarm of earthquakes. Within a 48-hour period, 24 earthquakes with magnitudes between 5.0 and 5.5, and 58 earthquakes with magnitudes between 4.5 and 5.0, were reported in this area. The magnitudes of these

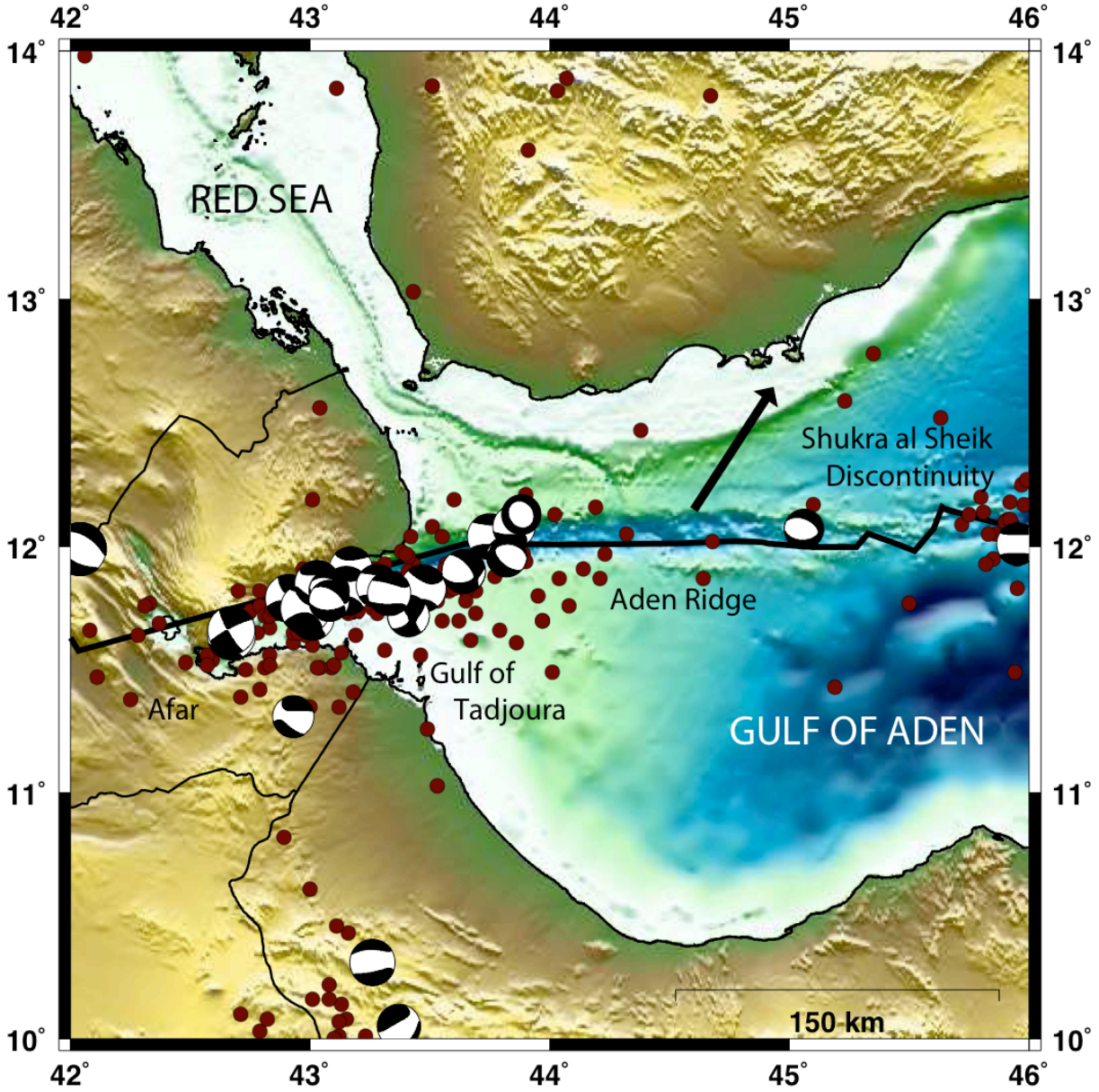

Figure B1. Map of the western Gulf of Aden and surroundings. The Carlsberg Ridge lies east of the Shukra al Sheik discontinuity, outside the frame of the figure. Maroon dots mark the locations of earthquakes in the NEIC catalog (1973-2010). Focal mechanisms are from the Global CMT catalog (1976-2010). All seismic data plotted covers the entire period of the catalogs prior to the start of the earthquake swarm. Plate boundary information is from Bird (2003). The plate motion vector for the Arabian plate relative to the Somalian plate (1.6 cm/yr at N34°E) is from MORVEL (DeMets *et al.* 2010). Topography and bathymetry is plotted from the GEBCO_08 Grid, version 20100927, http://www.gebco.net.

earthquakes, as well as the large number of earthquakes in a short time, make this swarm one of the largest ever observed in an extensional oceanic setting. Teleseismically detected earthquakes continued to occur for several months after the onset of the swarm, although at a much lower rate. The earthquake sequence occurred on a tectonically complex section of the Aden Ridge, crossing structural and mechanical boundaries (Dauteuil *et al.* 2001; Hébert *et al.* 2001). In this chapter, we use data from the Global Seismographic Network to estimate source parameters for 110 earthquakes in the sequence in order to characterize the swarm and better constrain the tectonics of this nascent spreading center. Comparison with seismic and volcanic activity in other regions suggests the swarm represents the seismic component of an undersea rifting episode, the first documented in this area.

B2. Tectonic Background

The impingement of the Afar mantle plume on the base of the African lithosphere ~31 Ma triggered continental rifting in the Gulf of Aden (Baker *et al.* 1996; Hoffmann *et al.* 1997; Rochette *et al.* 1997; Ukstins *et al.* 2002; Bosworth *et al.* 2005). This event, combined with regional extension due to subduction of Africa beneath Eurasia (Malkin & Shemenda 1991; Courtillot *et al.* 1999; Jolivet & Faccenna 2000; Bellahsen *et al.* 2003; Bosworth *et al.* 2005) resulted in the initiation of seafloor spreading in the eastern Gulf of Aden. Extension propagated westwards over time, reaching the Shukra al Sheik discontinuity, and the eastern edge of the Afar plume, approximately 10 Ma (Bosworth *et al.* 2005). Rifting stalled there, and propagated into the central and western Gulf of Aden only within the last 2-3 Ma (Cochran 1981; Bosworth *et al.* 2005). Gravity and magnetic data have indicated that the western boundary of active seafloor spreading is currently at approximately 44°E (Hébert *et al.* 2001). East of the Shukra al

Sheik discontinuity, the crust is oceanic with a mean thickness of 6 km, and extension is accommodated by faulting and oceanic accretion along a well-developed ridge-transform system (Dauteuil *et al.* 2001). In the area of the 2010 earthquake swarm, however, the crustal thickness ranges from 6 to 13 km, and although an axial trough is present, ridge-transform segmentation is poorly developed (Dauteuil *et al.* 2001). This section of the Aden Ridge is part of a ~130 km-long transition between oceanic lithosphere in the east and stretched continental lithosphere in the west (Dauteuil *et al.* 2001; Hébert *et al.* 2001).

The Aden Ridge spreads at a rate of 1.6 cm/yr in the direction N34°E (DeMets *et al.* 2010; Figure B1). The spreading direction is oblique to the rift axis, which trends N90°E between the Shukra al Sheik discontinuity and ~44°E longitude, and N70°E as it approaches the Gulf of Tadjoura. East of 44°E the axial valley is between 1000 and 1500 m deep and has a mean width of 20 km. Acoustic reflectivity surveys have shown that this portion of the ridge consists of overlapping rhombic basins oriented N120°E (Manighetti *et al.* 1997; Dauteuil *et al.* 2001). The axial valley is bounded by east-west trending normal faults while the center of the valley contains left-stepping en echelon faults oriented N100-120°E that accommodate both extension and right-lateral strike-slip motion (Manighetti *et al.* 1997; Dauteuil *et al.* 2001). West of 44°E, the axial valley changes orientation, deepens to 1650 meters and narrows to a width of 10-15 km. There the ridge is composed of several basins containing linear to sigmoidal normal faults striking N80°-N120°E (Tamsett & Searle 1988; Taylor *et al.* 1994; Tuckwell *et al.* 1996; Dauteuil *et al.* 2001). Backscatter images from a 1995 cruise showed no recent lava flows or volcanic cones between 43.3° and 44.3°E (Dauteuil *et al.* 2001).

B3. Seismic Overview

The section of the Aden Ridge that ruptured during the 2010 swarm was previously characterized by low levels of seismicity (Figure B1). Prior to 2010, the area between 43.9°E and 45°E had not ruptured in a M5+ earthquake in at least the last 38 years, the era of modern seismic instrumentation and the time-span covered by the catalogs of the USGS National Earthquake Information Center (NEIC, 1973-present) and Global Centroid Moment Tensor Project (GCMT, 1976-present, Dziewonski *et al.* 1981; Ekström *et al.* 2005). This contrasts with other sections of the ridge, including the Gulf of Tadjoura near the Afar triple junction and the Sheba Ridge east of the Shukra al Sheik discontinuity, where moderate-sized earthquakes occur frequently.

The 2010 western Gulf of Aden earthquake sequence was preceded by an M_W 4.5 earthquake on 13 November at 18:26 GMT. The main part of the sequence began 12 hours later on 14 November at 06:32 with an M_W 5.4 earthquake. Over the next 48 hours, 82 earthquakes with magnitudes 4.5 and greater were located by the NEIC and/or by the Global CMT Project using surface waves (Ekström 2006; see Figure B2). The number of moderate-sized earthquakes in this sequence is extraordinary, and is comparable to the number of similarly sized earthquakes expected in the aftershock sequence of an M_W 7-8 main shock (Shcherbakov & Turcotte 2004; Shcherbakov *et al.* 2005), even though the largest earthquake was only M_W 5.5. Seventy percent of the cumulative seismic moment of the swarm is due to earthquakes occurring the first day, and 83% to earthquakes occurring the first week (Figure B3). Earthquakes were detected in the area through August 2011, although they occurred at a much lower rate than during the swarm.

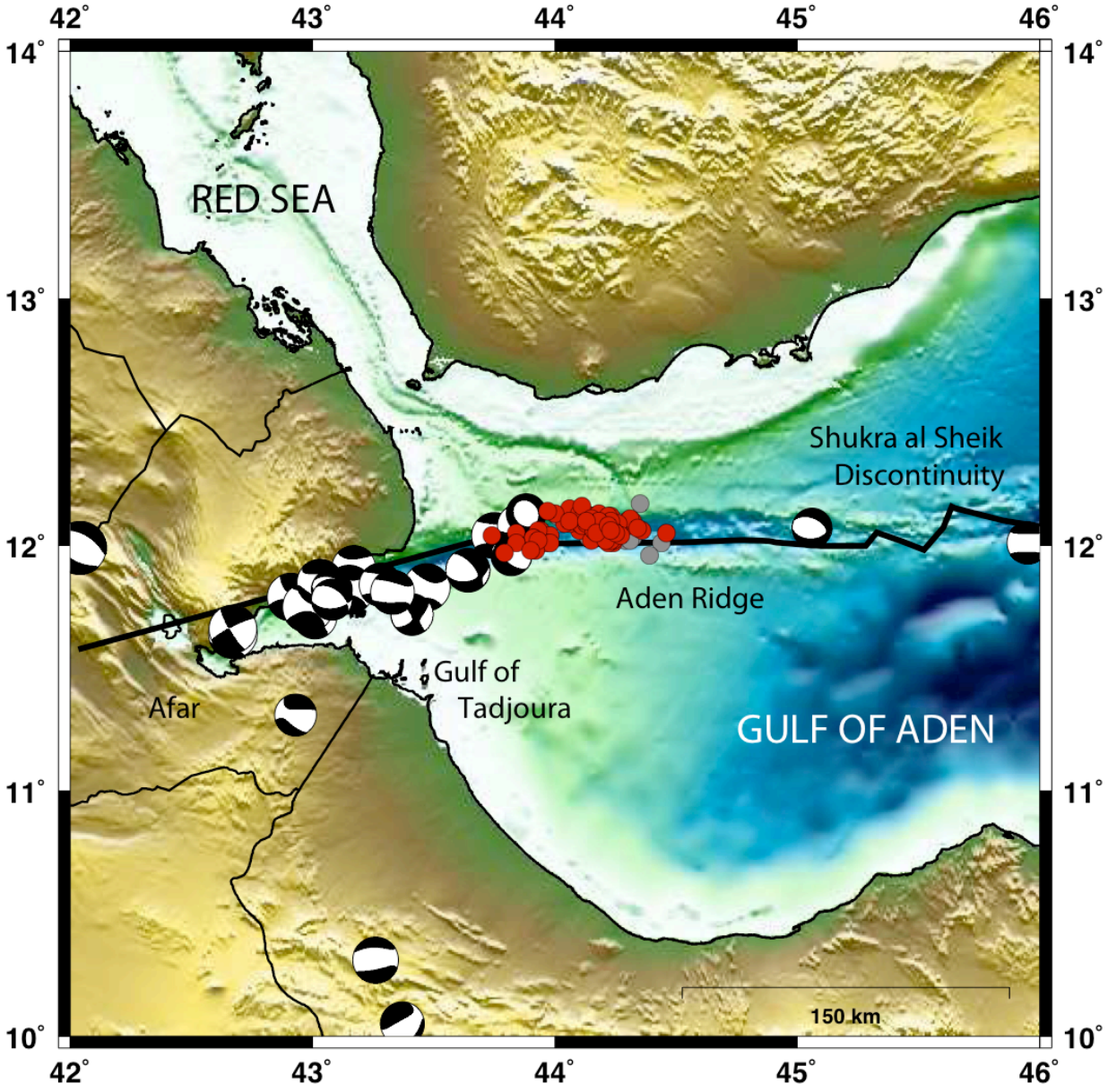

Figure B2. Centroid locations for 110 earthquakes analyzed in this study (November 2010-April 2011). Red dots denote earthquakes with well-constrained locations while grey dots denote earthquakes with less-well-constrained locations. Focal mechanisms, plate boundary information, bathymetry and topography are as in Figure B1.

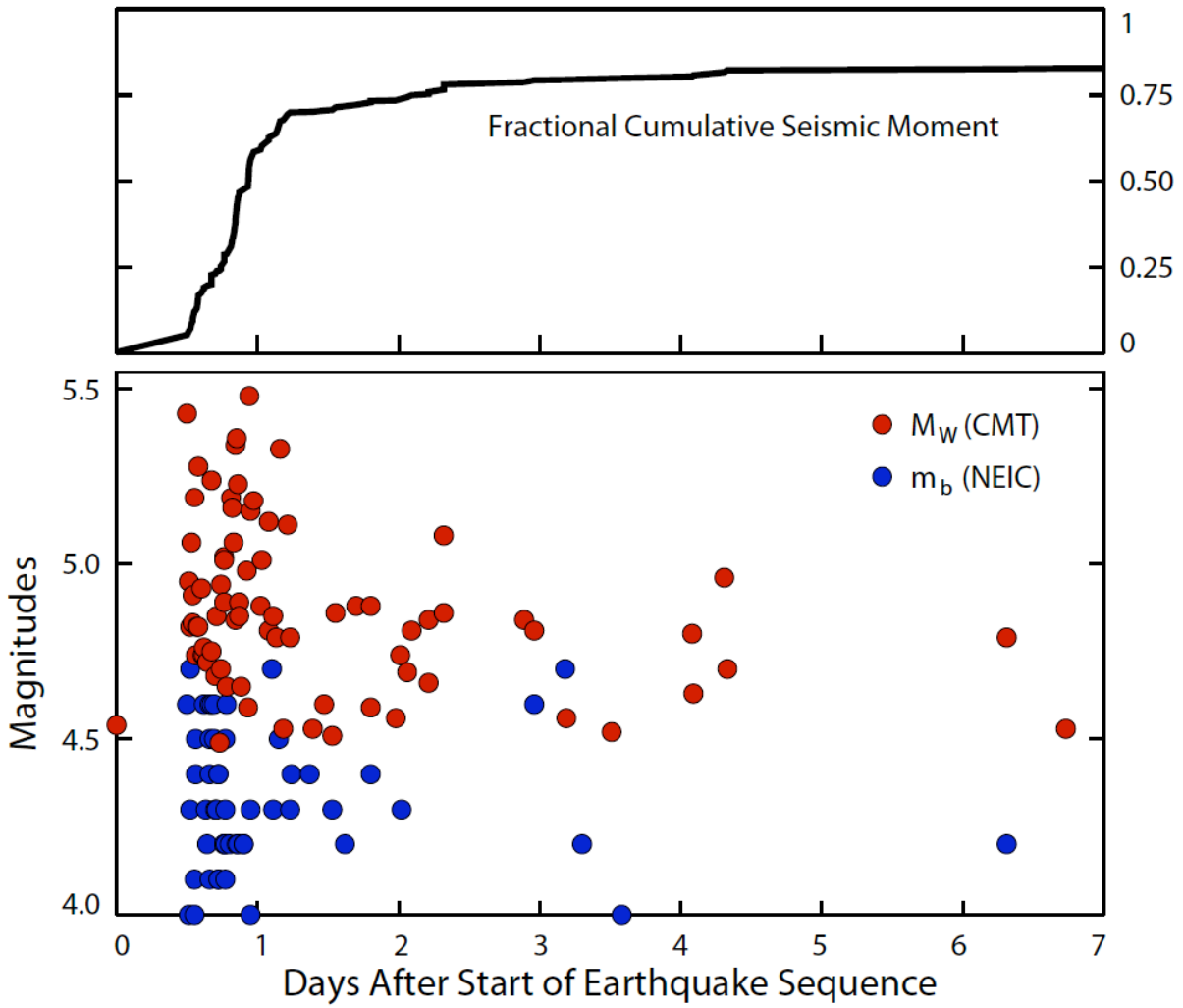

Figure B3. Top: Fractional cumulative seismic moment during the first week of the 2010 Gulf of Aden earthquake sequence. The cumulative seismic moment is estimated by summing the scalar moments for earthquakes analyzed in this study. The cumulative seismic moment through April 2011 is 3.5×10^{18} Nm, which is equivalent to a single M_W 6.3 earthquake.

Bottom: Times and magnitudes of earthquakes. Red dots show moment magnitudes for earthquakes analyzed in this study. Blue dots show times and magnitudes for additional earthquakes reported by the USGS NEIC; these are not included in the moment sum.

B4. Data and Methods

We use data from the IRIS-USGS Global Seismographic Network (GSN), Geoscope, GEOFON, MEDNET and the Canadian Regional Seismic Network to calculate centroid moment tensors, locations and times for earthquakes in the western Gulf of Aden between November 2010 and April 2011, the first six months after the start of the swarm. We calculate centroid-moment-tensor solutions generally following the standard GCMT approach for earthquakes with $M_W <$ 5.5 (Dziewonski *et al.* 1981; Arvidsson & Ekström 1998; Ekström *et al.* 2005), which incorporates long-period body waves filtered from 40-150 s and intermediate-period surface waves filtered from 50-150 s. Solutions for the smallest earthquakes are constrained primarily by surface-wave data, and in this case, we adjust the filter to shorter periods (40-100 or 35-75 s) on a case-by-case basis to increase the signal-to-noise ratio. Data from 30-100 stations are used for each solution, with the nearest station being FURI-IU, located ~675 km away near Addis Ababa, Ethiopia.

Because all of the earthquakes in the western Gulf of Aden swarm are shallow, their depths cannot be resolved well with the long-period seismic data used in standard GCMT analysis. Likewise, depth estimates could not easily be read from depth phases because the direct and reflected teleseismic P waves for shallow normal-faulting earthquakes typically have opposite polarity and occur very close together in time. To obtain accurate estimates of focal depth, we model the broadband teleseismic body waves of the largest earthquakes of the sequence ($M_W \geq$ 5.2) using the method of Ekström (1989). We perform an inversion of P and SH waveforms for focal mechanism, focal depth and moment-rate function. For this analysis, we deconvolve the instrument response to obtain broadband displacement records filtered from 1-100 s period.

Synthetic seismograms are calculated using ray theory and the Preliminary Reference Earth Model (PREM; Dziewonski & Anderson 1981). Reflections and conversions near the source are modeled using a layer-matrix method for a regional velocity model. We use the CRUST2.0 velocity model for the Red Sea (Y0 – thinned continental crust with 1.0 km thick sediment layer; Bassin *et al.* 2000), adding a 1.25 km thick water layer on top to match local bathymetry. The CMT estimate of the point-source moment tensor is included as a soft constraint in the inversion to ensure that focal mechanisms calculated from the broadband data are compatible with the long-period data used in CMT analysis.

B5. Results

We are able to obtain CMT solutions for 110 earthquakes of the western Gulf of Aden sequence and broadband body-wave estimates of depth for four of the larger events. These results are summarized in Figures B4-B7, and source parameters are provided in Tables B1, C1 and C2 (see Appendix C), and in electronic format on our web site (www.globalcmt.org). Below, we examine the source parameters retrieved in the context of known geology, and, in Section B6, consider implications of the sequence in light of the tectonic setting and ongoing evolution of the Gulf of Aden.

B5.1. Centroid-Moment-Tensor Solutions

We attempted to analyze all 198 earthquakes with initial magnitudes of 4.0 or larger as reported by the NEIC and/or the GCMT Project, and were able to obtain CMT solutions for 110 earthquakes with magnitudes $4.5 \leq M_W \leq 5.5$. (Figure B3). Solutions for the 25 largest earthquakes, those with $M_W \geq 5.0$, have been adopted as the preferred solutions of the Global

CMT catalog, which has a minimum magnitude threshold of M~5. We consider both these and our additional 85 solutions for smaller events here. Focal mechanisms are presented in Figure B4. The solutions are generally robust and well constrained. In the figures and tables, we identify 18 earthquakes as having less well-constrained focal mechanisms. This designation is given to events with the smallest number of usable data, which is due to small magnitude and/or the presence of large amplitude waveforms from other earthquakes. Nonetheless, focal mechanisms for the least well-constrained earthquakes are consistent with those of the best-constrained events (Figures B4 and B6), and we do not distinguish between them in the discussion below.

Although we report complete deviatoric moment tensors for the western Gulf of Aden earthquakes in Table C1, we plot only the double-couple components of the focal mechanisms in Figure B4 because we are unable to constrain the non-double-couple component well using the existing data. This is due to the fact that there are few close stations, and many of the earthquakes are near the magnitude threshold of GCMT analysis. The largest normal-faulting earthquakes have small non-double-couple components, and are consistent with rupture on planar faults. Larger non-double-couple components are retrieved for the least well-constrained earthquakes and earthquakes with strike-slip focal mechanisms, but for these events we find that double-couple moment tensors fit the data nearly as well as the full solutions. The strikes and dips of the nodal planes for the two types of solutions are nearly identical.

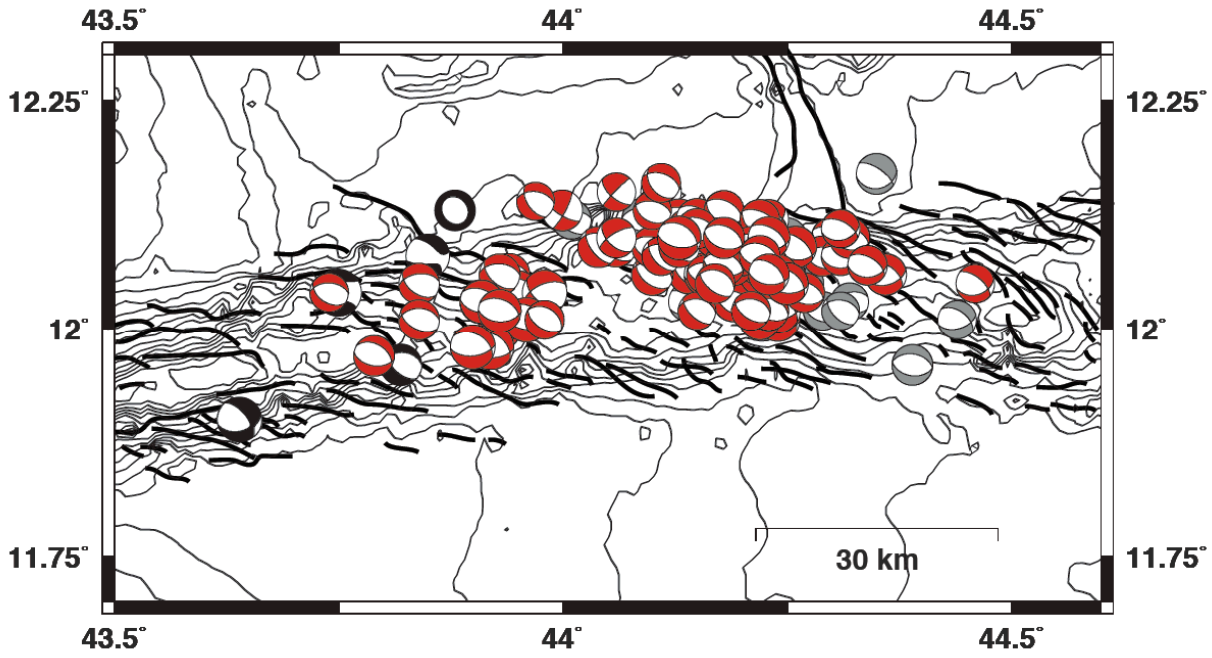

Figure B4. Focal mechanisms for the western Gulf of Aden. Black focal mechanisms are pre-swarm earthquakes from the Global CMT catalog. Focal mechanisms for the sequence that began on November 13, 2010 are plotted in red and grey, with only the double-couple component shown. The best-constrained focal mechanisms are plotted in red, and the less well-constrained focal mechanisms are plotted in grey. Black lines show fault traces from Dauteuil *et al.* (2001). Bathymetry from GEBCO is plotted in 100-meter contours.

The standard errors for the latitude and longitude components of the centroid locations are between three and five kilometers on average (Table C1). Due to uneven station distributions, the presence of noise and unmodeled structural heterogeneity (Nakanishi & Kanamori 1982; Smith & Ekström 1997; Hjörleifsdóttir & Ekström 2010), we believe that the actual errors are likely to be larger. The good correspondence between the centroid locations and the axial valley, however, suggest that absolute location errors are typically less than 20 km. Because the distances between individual earthquakes in the sequence are small, and because we use a similar station distribution for each CMT solution, the relative location errors are expected to be smaller, approximately 5-10 km.

The western Gulf of Aden swarm is dominated by normal-faulting earthquakes located in the axial valley between 43.75° and 44.5°E (Figure B4). These earthquakes have WNW-ESE striking nodal planes that are oriented N109°E on average, or ~75° from the direction of relative plate motion (DeMets *et al.* 2010). The rotation of the nodal planes with respect to the spreading-orthogonal direction is consistent with fault populations at other oblique rifts around the world (Taylor *et al.* 1994; Tuckwell *et al.* 1996). The normal-faulting earthquakes have dip angles that are close to 45°, with the average dip angles of the shallow and steep nodal planes being 42° and 51°, respectively. For these events, there is excellent agreement between the distribution of retrieved strike angles of the nodal planes and observed fault orientations measured using acoustic reflectivity data (Dauteuil *et al.* 2001). Though the vast majority of the earthquakes show normal faulting, a small fraction of the earthquakes have strike-slip focal mechanisms with NE-SW and NW-SE striking nodal planes, consistent with the extension direction.

The western Gulf of Aden earthquakes are clustered in both space and time. Spatially, the centroid locations are divided into two elongated groups, which are offset from one another by 10-15 kilometers (Figure B4). These groups correspond to mapped basins inside the axial valley, east and west of 44°E (Dauteuil *et al.* 2001). While normal-faulting earthquakes are distributed throughout the basins, strike-slip earthquakes are predominantly located near the offset between two of the basins near 44°E. At the beginning of the sequence, the basins east of 44°E were active, producing four of the ten largest earthquakes observed during the entire sequence within the first six hours. Beginning at 12:49 on November 14, activity shifted to the western basin for approximately ten hours and produced the remaining six of the ten largest earthquakes. From November 15 onwards, seismicity continued at a lower rate and was concentrated east of 44°E.

We do not find any evidence for uniform migration of the centroids with time. However, we do observe a westward propagation of the onset of seismicity for the first 12 hours of the swarm, as shown in Figure B5. We find that seismicity migrated at a rate no higher than ~1.1 m/s, which is consistent with earthquake swarms from Iceland and Afar (Brandsdóttir & Einarsson 1979; Belachew et al. 2011).

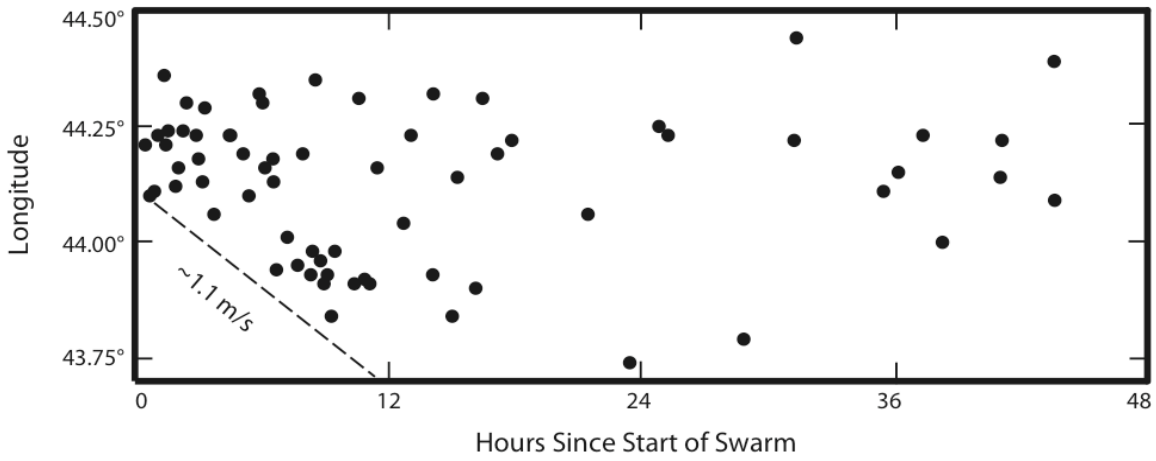

Figure B5. Spatial and temporal distribution of earthquakes for the first 48 hours of the swarm. Earthquakes are plotted as black circles at the longitude of their centroid locations. The time plotted in this figure is relative to the start of the swarm, 14 November at 06:32 GMT. For reference, a propagation rate of 1.1 m/s is indicated by the dashed line. This is a maximum estimate for the propagation rate of the onset of seismicity.

The principal axes of the moment tensor provide information about the strain accommodated by fault movements (McKenzie 1969; Townend 2006). The tension axes indicate the direction of maximum extension during an earthquake. Tension axes are close to horizontal for both normal-faulting and strike-slip earthquakes in the western Gulf of Aden sequence, and the azimuths of the tension axes we determine are plotted in Figure B6. For normal-faulting earthquakes, the average azimuth of the tension axes is N19°E, which is intermediate between the spreading direction from global plate motion vectors, N34°E (DeMets *et al.* 2010), and the normal to the ridge trend in this area, N20°W-N0°E. These observations are consistent with earthquake focal

mechanisms at other oblique rifts around the world (Fournier & Petit 2007), as well as with the orientations of normal-fault structures observed in analog models of oblique rifting (Withjack & Jamison 1986; Tron & Brun 1991; Clifton *et al.* 2000). The tension axes of the strike-slip earthquakes near 44°E are rotated counter-clockwise relative to those of the normal-faulting earthquakes, as expected for a left-stepping transform fault connecting two ridge segments. The full deviatoric moment tensors for these earthquakes are also consistent with composite focal mechanisms resulting from earthquakes with subevents on both ridge and transform segments with this left-stepping geometry (Frohlich 1994). The strike-slip earthquakes likely indicate that the offset between basins near 44°E is a transfer zone (Dauteuil & Brun 1993; Bellahsen *et al.* 2006; Autin *et al.* 2010), in the process of developing into a transform fault, as has already occurred east of the Shukra al Sheik discontinuity.

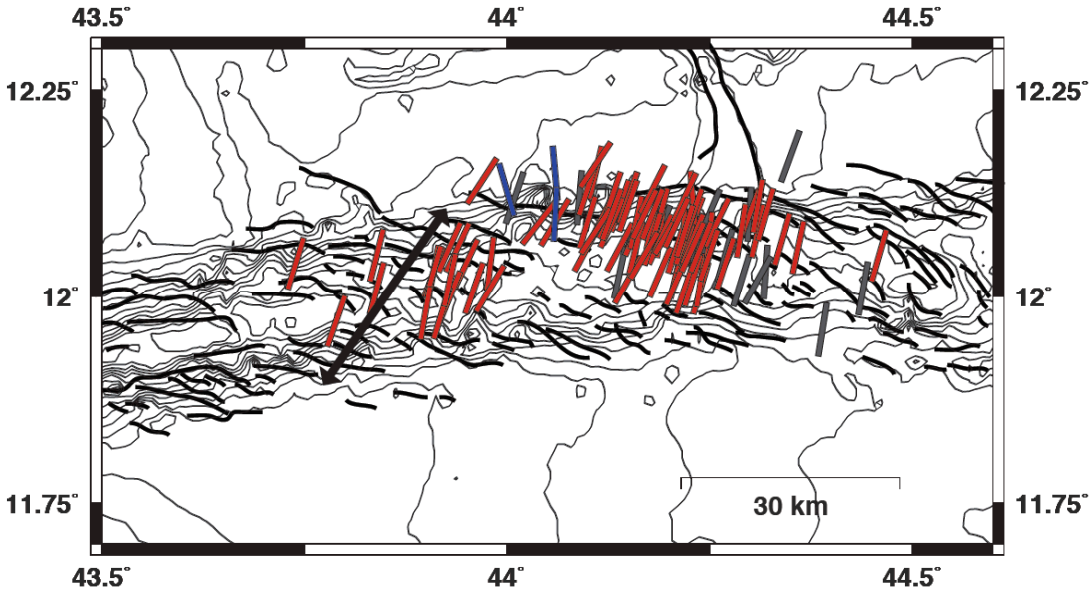

Figure B6. Azimuths of tension axes for the western Gulf of Aden earthquakes. Tension axes are plotted at the centroid locations, and are drawn in blue for earthquakes with large strike-slip components, and red or grey for the best-constrained and less well-constrained normal-faulting earthquakes. The double-headed black arrow shows the spreading direction from the global plate motion model MORVEL (DeMets *et al.* 2010). Black lines show fault traces from Dauteuil *et al.* (2001). Bathymetry from GEBCO is plotted in 100-meter contours. Tension axes are plotted in chronological order, and a single, early strike-slip event at 12.09ºN, 44.2ºE is obscured by later normal-faulting events.

B5.2. Teleseismic Body Wave Modeling

We are able to model the teleseismic body waves of four earthquakes, all occurring on November 14, 2010. The first of these earthquakes occurred east of 44°E, while the remaining earthquakes are located in the western basin. Although the focal depth estimates depend on the particular choice of crustal model, we find that, for reasonable choices of sediment thickness ranging from 0-1 km, the waveforms can be fit well and the differences between focal depth estimates are well within the 1 to 2 km uncertainty associated with the Ekström (1989) method. An example of the waveform fits achieved is shown in Figure B7. In Table B1, we present focal depths that were calculated using a velocity model that includes a 1.25-km layer of water and a 1-km layer of sediments. This model was chosen to account for the fact that the sediment thickness in the western Gulf of Aden ranges from essentially zero near the ridge axis to 2 km outside the rift (Khanbari 2000 as cited in Hébert *et al.* 2001). The focal depths we retrieve are shallow, ranging from 1.6 to 2.6 km below the seafloor. If we use a sediment thickness of zero km, the focal depth estimates range from 1.4 to 2.4 km below the seafloor. These depth estimates are consistent with other earthquakes from mid-ocean ridges with similar spreading rates (Huang & Solomon, 1988). For M_W 5.5 normal-faulting earthquakes, empirical scaling relationships estimate the down-dip fault width to be ~5 km (Wells & Coppersmith 1994), so it is likely that some of the earthquakes in this sequence ruptured the surface of the seafloor. If indeed 1 km of sediments is present, our depth estimates suggest that the earthquakes occurred only ~0.5-1.5 km into the crystalline crust. Such shallow depth estimates suggest either the earthquakes had unusually high stress drops, unlikely if the earthquakes occurred on pre-existing faults, or that seismogenic rupture continued into the sediment layer.

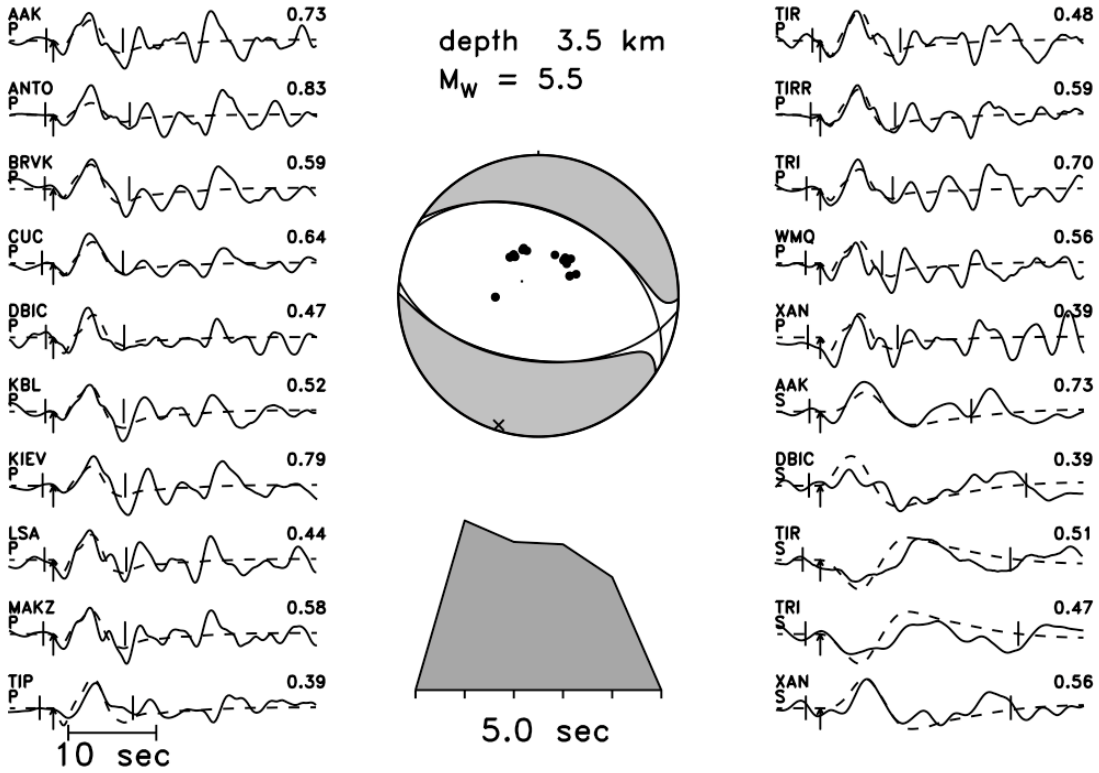

Figure B7. Focal-depth analysis for the M_W 5.5 earthquake on November 14, 2010 at 17:02 GMT. Solid lines are broadband teleseismic P and SH waveforms, and dashed lines are synthetic seismograms. Brackets across the waveforms show the portions of the seismograms that were used in the inversion, and arrows indicate the picked first arrivals. The station names and maximum amplitude (in microns) are printed for each waveform. The focal mechanism and moment-rate function determined by the body-wave inversion are plotted in the center of the figure. Solid black lines on the focal mechanism show nodal planes for the double-couple part of the moment tensor. Black dots on the focal mechanism show where the plotted waveforms exited the focal sphere. The focal depth of the earthquake is 3.5 km below the sea surface, or 2.3 km below the seafloor.

Earthquake Date and Time	M_W	Depth (km)
11/14/10 06:32	5.4	1.6
11/14/10 13:50	5.2	2.6
11/14/10 17:02	5.5	2.3
11/14/10 22:22	5.3	1.8

Table B1. Focal depth estimates determined by broadband analysis. The depths are relative to the seafloor.

B6. Discussion

The western Gulf of Aden earthquake sequence occurred beneath more than a kilometer of water in one of the most dangerous shipping routes in the world (Smith *et al.* 2011). Thus, there are no independent observations of the deformation that took place during this episode, either from satellite interferometry or from ship-based surveys. However, the character of the seismic activity is similar to dike-induced earthquake sequences observed in both continental and oceanic settings, and we infer that this sequence is the seismic component of a magmatic rifting episode. We base this interpretation on the swarm-like nature of the sequence, and the dominance of normal-faulting earthquakes clustered around the ridge axis. With this interpretation, we estimate the duration of the diking event and the amount of opening that took place along this section of the ridge. We use published analog models to interpret our observations in the context of the evolution of the Gulf of Aden and other oblique rifts around the world.

B6.1. Comparison to Other Dike-Induced Rifting Episodes

During rifting episodes along mid-ocean ridges and magma-rich segments of continental rifts, both dikes and faults accommodate plate boundary separation. As dikes propagate laterally though the crust, they trigger slip on faults located above and ahead of the intrusions (Rubin & Pollard 1988; Rubin 1992; Rubin & Gillard 1998). After propagation ceases, earthquakes continue to occur on pre-existing faults close to failure due to changes in Coulomb stress caused by the dike injection and related faulting and thermal stressing, although these earthquakes are generally fewer in number (Toda *et al.* 2002; Ayele *et al.* 2009; Kulpinski *et al.* 2009; Ebinger *et al.* 2010). Dike-induced rifting episodes in both continental and oceanic settings are characterized by earthquake sequences that have neither a single large mainshock nor a decrease

in magnitude with time (Abdallah *et al.* 1979; Brandsdóttir & Einarsson 1979; Tolstoy *et al.* 2001; Wright *et al.* 2006; Rowland *et al.* 2007; Ayele *et al.* 2009; Keir *et al.* 2009; Ebinger *et al.* 2008, 2010; Riedel & Schlindwein 2010). Such swarms have elevated *b* values, which are typically attributed to high thermal gradients and the presence or migration of magmatic and/or hydrothermal fluids (Brandsdóttir & Einarsson 1979; King 1983; Hill *et al.* 1990; Wiemer & McNutt 1997; Wiemer *et al.* 1998; Toda *et al.* 2002; Farrell *et al.* 2009).

For the western Gulf of Aden sequence, we estimated the *b*-value by examining the frequency-magnitude distribution. The magnitude of completeness (M_c) was defined as the magnitude below which the data depart from a linear trend by more than one standard deviation (Zúñiga & Wyss 1995). Using the maximum likelihood approach (Utsu 1965; Aki 1965; Bender 1983; Wiemer 2001) with a M_c of M_W 4.8 and calculating the uncertainty by bootstrapping, we estimate the *b*-value for the western Gulf of Aden sequence to be 1.6 +/- 0.18, which is significantly higher than the global average value of ~1.0 (Frohlich & Davis 1993). The estimate of *b*-value remains well above 1.0 for choices of M_c larger than 4.8.

Although there is some debate over whether particular earthquake swarms on mid-ocean ridges are due to episodes of tectonic extension or magmatism (Bergman & Solomon 1990), dike-induced earthquake swarms have now been observed directly on many mid-ocean ridges. Along fast and intermediate-spreading mid-ocean ridges, dike intrusions produce short-lived swarms of $M_W \leq 4.0$ earthquakes that are observed primarily by ocean-bottom seismometers (Fox *et al.* 1995; Tolstoy *et al.* 2006; Dziak *et al.* 1995, 2007, 2009), while larger, teleseismically-detected swarms of dike-induced earthquakes are generally only located on slow and ultra-slow spreading

ridges such as the Mid-Atlantic Ridge and the Gakkel Ridge (Müller & Jokat 2000; Tolstoy *et al.* 2001; Dziak *et al.* 2004; Riedel & Schlindwein 2010; Schlindwein & Riedel 2010; Korger & Schlindwein 2011). For normal-faulting earthquakes along mid-ocean ridges, an inverse relationship between maximum earthquake size and spreading rate has been observed, and is attributed to thermal limitations on the depth of the seismogenic zone (Soloman & Burr 1979; Huang & Solomon 1988; Bird *et al.* 2009).

The mid-ocean ridge swarm that is most similar to the swarm investigated in this study is the 1999 Gakkel Ridge swarm, which lasted nine months and produced 20 normal-faulting earthquakes with $M_W \geq 5.0$ (Müller & Jokat 2000; Tolstoy *et al.* 2001; Ekström *et al.* 2003; Riedel & Schlindwein 2010). In that case, sonar images and bathymetric data suggest that the swarm was associated with a volcanic eruption on the seafloor (Edwards *et al.* 2001). As at the Gakkel Ridge, the large magnitudes of the earthquakes in this study can likely be attributed in part to the slow spreading rate in the western Gulf of Aden.

The regional crustal structure and tectonic history of the western Gulf of Aden may also help explain the large magnitudes of the earthquakes. The area of the earthquake swarm has thick crust, which is transitional from oceanic to continental (Dauteuil *et al.* 2001; Hébert *et al.* 2001), and thicker sections of brittle crust can support larger earthquakes (Rubin 1990). Large earthquakes have also been associated with dikes that are the first to intrude host rift zones after long periods of quiescence (Rubin & Gillard 1998). Based on the seismic history and on the seafloor observations of Dauteuil *et al.* (2001), this rifting episode is the first in the western Gulf

of Aden in a minimum of several decades, and may represent westward propagation of active seafloor spreading into a new section of the Aden Ridge.

This interpretation of rift propagation is consistent with the fact that the earthquake swarm that most closely resembles the western Gulf of Aden sequence, continental or oceanic, occurred on an incipient mid-ocean ridge in neighboring Afar. The September 2005 diking episode in Afar was characterized by hundreds of teleseismically-detected, shallow earthquakes located in a 120-km-long by 25-km-wide area of the Dabbahu segment of the Red Sea rift over a period of three weeks. These earthquakes were predominantly normal faulting and 17 had $M_W \geq 5.0$ (Ebinger *et al.* 2008, 2010; Ayele *et al.* 2009). Like the western Gulf of Aden sequence, the largest magnitude earthquake in the 2005 Afar rifting episode was M_W 5.5 and the cumulative seismic moment was equivalent to a single M_W 6.3 earthquake (Ebinger *et al.* 2008; Grandin *et al.* 2009). InSAR studies confirm that a magma volume of 1.5-2.5 km^3 was injected along a 65-km-long shallow dike during the 2005 Afar rifting episode (Wright *et al.* 2006; Grandin *et al.* 2009).

Because the western Gulf of Aden sequence has elevated *b*-value and is dominated by shallow, normal-faulting earthquakes that migrate over time, closely resembling well-documented dike-induced earthquake sequences in both oceanic and continental settings, we conclude that this swarm represents the seismic component of a magmatic rifting episode along the nascent Aden Ridge. The large size of the earthquakes is likely due to the combined effects of the slow spreading rate, relatively thick crust, and recent quiescence.

B6.2. Rifting Episode Duration and Opening Estimates

The similarities between the earthquakes in this study and those associated with the well-documented Afar rifting episodes enable us to make a rough estimate of the duration of the dike intrusion, as well as the amount of opening that took place during the 2010 rifting episode. Belachew *et al.* (2011) performed a detailed analysis of local seismic data from nine dike intrusions in Afar, and concluded that the largest earthquakes in each sequence were caused by faulting and graben formation above laterally propagating dike intrusions. Based on cumulative seismic moment curves, they conclude that the vast majority of seismic moment is accumulated during the dike propagation phase, after which seismicity decreases significantly, and the slope of the cumulative seismic moment curve flattens. Interpreting our cumulative seismic moment curve (Figure B3) in the same way, we estimate that the main dike intrusion in the western Gulf of Aden propagated for less than 18 hours. This result is consistent with our observation that seismicity migrated westwards for approximately 12 hours during the beginning of the swarm. Combining these results, we conclude that the dike propagation phase during the 2010 western Gulf of Aden rifting episode likely lasted between 12 and 18 hours. This is shorter than the dike propagation phase for the 2005 rifting episode in Afar, which lasted several days (Ayele *et al.* 2009).

Using our CMT solutions, and assuming that all extension occurs on planar normal faults, we estimate the amount of spreading accommodated by the earthquakes using the following expression:

$$\sum M_0 = \mu L h d / (\sin(\theta)\cos(\theta)), \quad \text{(B1)}$$

modified from Solomon *et al.* (1988). Here, $\sum M_0$ is the cumulative seismic moment of the normal-faulting earthquakes, μ is the shear modulus, h is the thickness of the seismogenic layer, θ is the dip of the fault planes, L is the total along-axis length of the ridge segments that slipped in the earthquakes, and d is the total amount of horizontal opening. We use values of 3.0×10^{10} N/m^2 for μ, and 10 km for h (Dauteuil *et al.* 2001), and calculate the remaining parameters from the CMT solutions. $\sum M_0$ is 3.4×10^{18} Nm, and we estimate L from the distance between the easternmost and westernmost earthquake centroids, finding a value of 80 km. We use 51° for θ, which is the average dip angle for the steeply dipping nodal planes. Because all of the retrieved nodal-plane dips are close to this value, the result depends little on the details of this choice. Solving for the horizontal displacement, we obtain a value of $d \approx 7$ cm, which is equivalent to ~4 years of spreading assuming that opening occurs solely by seismogenic extension of the brittle lithosphere at a rate of 1.63 cm/yr, the full spreading rate predicted by MORVEL for 12°N, 44°E (DeMets *et al.* 2010). If instead we constrain h to be 5 km, the down-dip width for the largest earthquakes based on our depth and scalar moment estimates and scaling relationships of Wells & Coppersmith (1994), the estimate of horizontal opening is twice as large, $d \approx 14$ cm, which is equivalent to ~8 years of spreading.

However, the amount of opening that occurred during the western Gulf of Aden rifting episode is likely to be much higher. Along slow-spreading mid-ocean ridges, earthquakes account for no more than 10-20% of plate separation (Solomon *et al.* 1988). Rifting episodes in continental settings are also generally dominated by aseismic deformation. In Iceland, the Asal Rift and Afar, field measurements of fault offsets from rifting episodes are much larger than the amount of slip required to generate the observed earthquake swarms (Brandsdóttir & Einarsson 1979;

Doubré & Peltzer 2007; Rowland *et al.* 2007). Additional aseismic opening may occur due to the volume change associated with the dike intrusion. The discrepancy between seismogenic and total opening can also be demonstrated by comparing the cumulative seismic moment to estimates of the combined geodetic moment, which accounts for dip slip on normal faults and volume change due to magma intrusions. For the September 2005 rifting episode in Afar, the geodetic moment was at least an order of magnitude larger than the cumulative seismic moment (Wright *et al.* 2006; Grandin *et al.* 2009). Belachew *et al.* (2011) compared the seismic and geodetic moments for nine rifting episodes in Afar between 2006 and 2009, and found that earthquakes accounted for only ~0.1-3.5% of the total deformation. Following Solomon et al. (1988) and Belachew *et al.* (2011), if we assume that 1-5% of the total deformation was accommodated by earthquakes, we estimate that this discrete rifting episode may have accommodated ~1-14 m of opening, or ~85-800 years of spreading, in this section of the western Gulf of Aden.

B6.3. Evolution of the Western Gulf of Aden

The Gulf of Aden is a transtensional setting where rift formation occurs due to oblique divergence. The relative amounts of extension and shear, and therefore the faulting patterns that are produced along a given section of the rift, depend on the obliquity angle, α, which is the angle between the rift trend (N70-90°E) and the direction of relative plate motion (N34°E, DeMets *et al.* 2010). The obliquity angle in the western Gulf of Aden varies between ~35° and 55° in the area of the recent earthquake swarm, with the highest value of α being found east of 44°E where the rift trends east-west. For similar values of α, analog models show that oblique rifting produces en echelon arrays of normal faults in the axial valley (Withjack & Jamison 1986;

Tron & Brun 1991; Dauteuil & Brun 1993; McClay & White 1995; Clifton *et al.* 2000; Mart & Dauteuil 2000; Clifton & Schlische 2001; Corti *et al.* 2001, 2003; Agostini *et al.* 2009; Autin *et al.* 2010). In the models, these normal faults strike in a direction intermediate between rift-parallel and perpendicular to the spreading direction (Withjack & Jamison 1986; Clifton *et al.* 2000; Corti *et al.* 2001, 2003; Autin *et al.* 2010). The orientations of the nodal planes from our CMT solutions support these results. For normal faulting earthquakes, the average strike angle of the nodal planes is N109°E, which is intermediate between N70-90°E and N124°E. Analytical models demonstrate that these fault patterns arise because the combination of extension and shear in oblique rifts results in the principal extensional strain being oriented approximately halfway between the normal to the rift trend and the spreading direction (Withjack & Jamison 1986). The strain pattern we find in the western Gulf of Aden provides observational validation of this explanation. The mean orientation of the tension axes we observe in the swarm is N19°E, intermediate between north-south and the direction of relative plate motion, N34°E.

Overall, there is excellent agreement between the results of our seismic analysis and models of oblique rifting, which allows us to remark on the both the current and future states of the rift system in the western Gulf of Aden. Recent scaled analog models by Autin *et al.* (2010) suggest that the oblique rifting in the Gulf of Aden was not initiated on a pre-existing weak zone, so that the structures that develop are not influenced by previous geometry. Their work, as well as other analog models (Clifton & Schlische 2001; Agostini *et al.* 2009), indicate that the western Gulf of Aden is in the late stages of oblique rifting, where deformation is largely controlled by slip on pre-existing fault segments. The similarities between the orientations of faults mapped prior to the earthquake swarm (Dauteuil *et al.* 2001) and the nodal planes of the normal-faulting

earthquakes supports the interpretation that the 2010 swarm occurred on pre-existing faults in the axial valley. Based on the analog models, we expect that further extension will result in additional slip and lengthening of optimally oriented en echelon normal faults (Clifton *et al.* 2000; Clifton & Schlische 2001; Agostini *et al.* 2009). In addition, we expect that some of the transfer zones between individual basins may evolve towards transform faults (Dauteuil & Brun 1993; Bellahsen *et al.* 2006; Autin *et al.* 2010), and segmentation of the ridge will increase as seafloor spreading develops in the western Gulf of Aden. The occurrence of strike-slip earthquakes in the 2010 swarm, near a step-over between basins and a change in ridge orientation at 44°E, may indicate the presence of an incipient transform fault.

In analog models of oblique rifts, normal faults in the axial valley control the emplacement of magmatic intrusions and define the locations of ocean accretion centers (Clifton & Schlische 2001; Agostini *et al.* 2009; Autin *et al.* 2010). This progression has already been documented within basins east of the recent swarm, where seafloor spreading is more developed and there are linear chains of volcanoes oriented N110°-120°E (Tamsett & Searle 1988; Dauteuil *et al.* 2001). Prior to 2010, the section of the rift where the swarm is located was characterized by low levels of seismicity and a lack of recent volcanism, and gravity and magnetic surveys indicated that seafloor spreading had not yet been initiated (Dauteuil *et al.* 2001; Hébert *et al.* 2001). We believe that the earthquakes in the 2010 swarm are the seismic component of a dike-induced rifting episode, which provides evidence for westward propagation of seafloor spreading into this area. As in Afar, this swarm confirms that deformation at the onset of seafloor spreading is achieved by intense episodes of dike intrusion and faulting. For now it is unknown whether this rifting episode will consist of a single diking episode, like in the Asal Rift in 1978 (Abdallah *et*

al. 1979), or whether additional dike intrusion episodes will follow as in Afar and Iceland. If the latter, we expect additional dike intrusions to become progressively more effusive, leading to eruptions on the seafloor (Buck *et al.* 2006; Hamlin *et al.* 2010).

B7. Conclusions

In the western Gulf of Aden, the east-west trending boundary between the Arabian and Somalian plates is transitioning from a continental rift to a mid-ocean ridge. Until recently, the section of the nascent Aden Ridge near 44ºE was characterized by low levels of seismicity and a lack of recent volcanism on the seafloor, and has been believed to lie west of the boundary of active seafloor spreading. However, our analysis of a swarm of moderate to large earthquakes that began on November 14, 2010 in this area indicates that the early stages of seafloor spreading have now propagated into this section of the rift. The swarm closely resembles dike-induced earthquake swarms from both continental and oceanic settings, and was likely triggered by the lateral propagation of a shallow dike intrusion. Though the sequence was dominated by shallow, normal-faulting earthquakes, we also find evidence for an incipient transform fault and the early stages of rift-transform segmentation. The direction of extension accommodated by the normal-faulting earthquakes of the sequence is intermediate between the rift-orthogonal and the spreading direction predicted by global plate motion vectors, validating analog and analytical models of oblique rifting. Our findings indicate that deformation at the onset of seafloor spreading is achieved by discrete episodes of faulting and magmatism.

References

Abdallah, A., Courtillot, V., Kasser, M., Le Dain, A.-Y., Lépine, J.-C., Robineau, B., Ruegg, J.-C., Tapponnier, P., & Tarantola, A., 1979. Relevance of Afar seismicity and volcanism to the mechanics of accreting plate boundaries, *Nature*, **282**, 17-23.

Agostini, A., Corti, G., Zeoli, A. & Mulugeta, G., 2009. Evolution, pattern, and partitioning of deformation during oblique continental rifting: Inferences from lithospheric-scale centrifuge models, *Geochem. Geophys. Geosys.*, **10**, doi:10.1029/2009GC002676.

Aki, K., 1965. Maximum likelihood estimate of *b* in the formula *log N = a-bM* and its confidence limits. *Bull. Earthq. Res. Inst. Univ. Tokyo*, **43**, 237-239.

Arvidsson, R. & Ekström, G., 1998. Global CMT analysis of moderate earthquakes, $M_W \geq 4.5$, using intermediate-period surface waves, *Bull. Seism. Soc. Am.*, **88**, 1003-1013.

Autin, J., Bellahsen, N., Husson, L., Beslier, M.-O., Leroy, S., & d'Acremont, E., 2010. Analog models of oblique rifting in a cold lithosphere, *Tectonics*, **29**, doi:10.1029/2010TC002671.

Ayele, A., Keir, D., Ebinger, C., Wright, T. J., Stuart, G. W., Buck, W. R., Jacques, E., Ogubazghi, G., & Sholan, J., 2009. September 2005 mega-dike emplacement in the Manda-Harraro nascent oceanic rift (Afar depression), *Geophys. Res. Lett.*, **36**, doi:10.1029/2009GL039605.

Baker, J., Snee, L., & Menzies, M., 1996. A brief Oligocene period of flood volcanism in Yemen: Implications for the duration and rate of continental flood volcanism at the Afro-Arabian triple junction, *Earth Planet. Sci. Lett.*, **138**, 39-55, doi:10.1016/0012-821X(95)00229-6.

Bassin, C., Laske, G., & Masters, G., 2000. The Current Limits of Resolution for Surface Wave Tomography in North America, *Eos Trans. AGU*, **81**(48), Fall. Meet. Suppl., Abstract T31B-1820.

Belachew, M., Ebinger, C., Coté, D., Keir, D., Rowland, J. V., Hammond, J. O. S., & Ayele, A., 2011. Comparison of dike intrusions in an incipient seafloor-spreading segment in Afar, Ethiopia: Seismicity perspectives, *J. Geophys. Res.*, **116**, doi:10.1029/2010JB007908.

Bellahsen, N., Faccenna, C., Funicello, F., Daniel, J.-M., & Jolivet, L., 2003. Why did Arabia separate from Africa?: insights from 3-D laboratory experiments, *Earth Planet. Sci. Lett.*, **216**, 365-381.

Bellahsen, N., Fournier, M., d'Acremont, E., Leroy, S., & Daniel, J. M., 2006. Fault reactivation and rift localization: Northeastern Gulf of Aden margin, *Tectonics*, **25**, doi:10.1029/2004TC001626.

Bender, B., 1983. Maximum likelihood estimation of b values for magnitude grouped data. *Bull. Seism. Soc. Am*., **73**, 831-851.

Bergman, E. A. & Solomon, S. C., 1990. Earthquake Swarms on the Mid-Atlantic Ridge: Products of Magmatism or Extensional Tectonics?, *J. Geophys. Res*., **95**, 4943-4965.

Bird, P., 2003. An updated digital model of plate boundaries. *Geochem. Geophys. Geosys.*, **4**, doi:10.1029/2001GC000252.

Bird, P., Kagan, Y. Y., Jackson, D. D., Schoenberg, F. P., & Werner, M. J., 2009. Linear and Nonlinear Relations between Relative Plate Velocity and Seismicity, *Bull. Seism. Soc. Am.*, **99**, 3097-3113, doi:10.1785/0120090082.

Bosworth, W., Huchon, P., & McClay, K., 2005. The Red Sea and Gulf of Aden Basins, *J. African Earth Sci*., **43**, 334-378.

Brandsdóttir, B., & Einarsson, P., 1979. Seismic activity associated with the September 1977 deflation of the Krafla central volcano in northeastern Iceland, *J. Volcanol. Geotherm. Res*., **6**, 197-212.

Buck, W. R., Einarsson, P., & Brandsdóttir, B., 2006. Tectonic stress and magma chamber size as controls on dike propagation: Constraints from the 1975-1984 Krafla rifting episode, *J. Geophys. Res*., **111**, doi:10.1029/2005JB003879.

Clifton, A. E. & Schlische, R. W., 2001. Nucleation, growth, and linkage of faults in oblique rift zones: Results from experimental clay models and implications for maximum fault size, *Geology*, **29**, 455-458.

Clifton, A. E., Schlische, R. W., Withjack, M. O., & Ackermann, R. V., 2000. Influence of rift obliquity on fault-population systematics: results of experimental clay models, *J. Struct. Geol*., **22**, 1491-1509.

Cochran, J. R., 1981. The Gulf of Aden: Structure and Evolution of a Young Ocean Basin and Continental Margin, *J. Geophys. Res*., **86**, 263-287.

Corti, G., Bonini, M., Innocenti, F., Manetti, P., & Mulugeta, G., 2001. Centrifuge models simulating magma emplacement during oblique rifting, *J. Geodyn*., **31**, 557-576.

Corti, G., Bonini, M., Conticelli, S., Innocenti, F., Manetti, P., Sokoutis, D., 2003. Analog modeling of continental extension: a review focused on the relations between the patterns of deformation and the presence of magma, *Earth Sci. Rev*., **63**, 169-247.

Courtillot, V. E., 1980. Opening of the Gulf of Aden and Afar by progressive tearing. *Phys. Earth Planet. Inter*., **21**, 343-350.

Courtillot, V., Jaupart, C., Manighetti, I., Tapponnier, P., & Besse, J., 1999. On causal links between flood basalts and continental breakup, *Earth Planet. Sci. Lett*., **166**, 177-195.

Dauteuil, O., & Brun, J.-P., 1993. Oblique rifting in a slow-spreading ridge, *Nature***, 361**, 145-148.

Dauteuil, O., Huchon, P., Quemeneur, F., & Souriot, T., 2001. Propagation of an oblique spreading center: the western Gulf of Aden, *Tectonophysics*, **332**, 423-442.

DeMets, C., Gordon, R. G., & Argus, D. F., 2010. Geologically current plate motions, *Geophys. J. Int.,* **181**, doi:10.1111/j.1365-246X.2009.04491.x.

Doubré, C., & Peltzer, G., 2007. Fluid-controlled faulting process in the Asal rift, Djibouti, from 8 yr of radar interferometry observations, *Geology*, **35**, doi:10.1130/G23022A.1.

Dziak, R. P., Fox, C. G., & Schreiner, A. E., 1995. The June-July 1993 seismo-acoustic event at CoAxial segment, Juan de Fuca Ridge: Evidence for a lateral dike injection, *Geophys. Res. Lett*., **22**, doi:10.1029/94GL01857.

Dziak, R., Smith, D., Bohnenstiehl, D., Fox, C., Desbruyeres, D., Matsumoto, H., Tolstoy, M., & Fornari, D., 2004. Evidence of a recent magma dike intrusion at the slow-spreading Lucky Strike segment, Mid-Atlantic Ridge, *J. Geophys. Res*., **109**, doi:10.1029/2004JB003141.

Dziak, R. P., Bohnenstiehl, D. R., Cowen, J. P., Baker, E. T., Rubin, K. H., Haxel, J. H., & Fowler, M. J., 2007. Rapid dike emplacement leads to eruptions and hydrothermal plume release during seafloor spreading events, *Geology*, **35**, doi:10.1130/G23476A.1.

Dziak, R. P., Bohnenstiehl, D. R., Matsumoto, H., Fowler, M. J., Haxel, J. H., Tolstoy, M., & Waldhauser, F., 2009. January 2006 seafloor-spreading event at 9˚50'N, East Pacific Rise: Ridge dike intrusion and transform fault interactions from regional hydroacoustic data. *Geochem. Geophys. Geosyst*., **10**, doi:10.1029/2009GC002388.

Dziewonski, A. M., & Anderson, 1981. Preliminary Reference Earth Model, *Phys. Earth Planet. Inter.*, **25**, 297-356.

Dziewonski, A. M., Chou, T.-A., & J. H. Woodhouse, 1981. Determination of Earthquake Source Parameters from Waveform Data for Studies of Global and Regional Seismicity, *J. Geophys. Res*., **86**, 2825-2852.

Ebinger, C. J., Keir, D., Ayele, A., Calais, E., Wright, T. J., Belachew, M., Hammond, J. O. S., Campbell, E., & Buck, W. R., 2008. Capturing magma intrusion and faulting processes during continental rupture: seismicity of the Dabbahu (Afar) rift, *Geophys. J. Int*., **174**, doi:10.1111/j.1365-246X.2008.03877.x.

Ebinger, C., Ayele, A., Keir, D., Rowland, J., Yirgu, G., Wright, T., Belachew, M., & Hamling, I., 2010. Length and Timescales of Rift Faulting and Magma Intrusion: The Afar Rifting Cycle from 2005 to Present, *Annu. Rev. Earth Planet. Sci*., **38**, doi:10.1146/annurev-earth-040809-152333.

Edwards, M. H., Kurras, G. J., Tolstoy, M., Bohnenstiehl, D. R., Coackley, B. J., Cochran, J. R., 2001. Evidence of recent volcanic activity on the ultraslow-spreading Gakkel Ridge, *Nature*, **409**, 808-812.

Ekström, G., 1989. A very broad band inversion method for the recovery of earthquake source parameters, *Tectonophysics*, **166**, 73-100.

Ekström, G., 2006. Global Detection and Location of Seismic Sources by Using Surface Waves, *Bull. Seism. Soc. Am*., **96**, doi:10.1785/0120050175.

Ekström, G., Dziewonski, A. M., Maternovskaya, N. N., & Nettles, M., 2003. Global seismicity of 2001: centroid-moment tensor solutions for 961 earthquakes, *Phys. Earth Planet. Inter.*, **136**, 165-185.

Ekström, G., Dziewonski, A. M., Maternovskaya, N. N., & Nettles, M., 2005. Global seismicity of 2003: centroid-moment-tensor solutions for 1087 earthquakes, *Phys. Earth Planet. Inter*., **148**, 327-351.

Farrell, J., Husen, S., & Smith, R. B., 2009. Earthquake swam and b-value characterization of the Yellowstone volcano-tectonic system, J. Volcanol. Geotherm. Res., **188**, 260-276.

Fournier, M., & Petit, C., 2007. Oblique rifting at oceanic ridges: Relationship between spreading and stretching directions from earthquake focal mechanisms, *J. Struct. Geol*., **29**, 201-208.

Fox, C., Radford, W. E., Dziak, R., Lau, T.-K., Matsumoto, H., & Schreiner, A. E., 1995. Acoustic detection of a seafloor spreading episode on the Juan de Fuca ridge using military hydrophone arrays, *Geophys. Res. Lett*., **22**, doi:10.1029/94GL02059.

Frohlich, C., 1994. Earthquakes with Non-Double-Couple Mechanisms, *Science*, **264**, 804-807.

Frohlich, C., & Davis, S. D., 1993. Teleseismic b values; Or, Much Ado About 1.0, *J. Geophys. Res*., **98**, 631-644.

Grandin, R., Socquet, A., Binet, R., Klinger, Y., Jacques, E., de Chabalier, J.-B., King, G. C. P., Lasserre, C., Tait, S., Tapponnier, P., Delorme, A., & Pinzuti, P., 2009. September 2005 Manda Hararo-Dabbahu rifting event, Afar (Ethiopia): Constraints provided by geodetic data, *J. Geophys. Res*., **114**, doi:10.1029/2008JB005843.

Hamling, I. J., Wright, T. J., Calais, E., Bennati, L., & Lewi, E., 2010. Stress transfer between thirteen successive dyke intrusions in Ethiopia, *Nature Geosci*., **3**, doi:10.1038/NGEO967.

Hébert, H., Deplus, C., Huchon, P., Khanbari, K., & Audin, L., 2001. Lithospheric structure of a nascent spreading ridge inferred from gravity data: The western Gulf of Aden, *J. Geophys. Res*., **106**, 26,345-26,363.

Hill, D. P., Ellsworth, W. L., Johnston, M. J. S., Langbein, J. O., Oppenheimer, D. H., Pitt, A. M., Reasenberg, P. A., Sorey, M. L., & McNutt, S. R., 1990. The 1989 earthquake swarm beneath Mammoth Mountain, California: An initial look at the 4 May through 30 September activity, *Bull. Seism. Soc. Am.*, **80**, 325-339.

Hjörleifsdóttir, V., & Ekström, G., 2010. Effects of three-dimensional Earth structure on CMT earthquake parameters. *Phys. Earth Planet. Inter*., **179**, 178-190, doi:10.1016/j.pepi.2009.11.003.

Hoffman, C., Courtillot, V., Féraud, G., Rochette, P., Yirgu, G., Ketefo, E., & Pik, R., 1997. Timing of the Ethiopian flood basalt event and implications for plume birth and global change, *Nature*, **389**, 838-841, doi:10.1038/39853.

Huang, P. Y., & Solomon, S. C., 1988. Centroid Depth of Mid-Ocean Ridge Earthquakes: Dependence on Spreading Rate, *J. Geophys. Res*., **93**, 13,445-13,477.

Jolivet, L., & Faccenna, C., 2000. Mediterranean extension and the Africa-Eurasia collision, *Tectonics*, **19**, 1095-1106, doi:10.1029/2000TC900018.

Keir, D., Hamling, I. J., Ayele, A., Calais, C., Ebinger, C., Wright, T. J., Jacques, E., Mohamed, K., Hammond, J. O. S., Belachew, M., Baker, E., Rowland, J. V., Lewi, E., & Bennati, L., 2009. Evidence for focused magma accretion at segment centers from lateral dike injections captured beneath the Red Sea rift in Afar, *Geology*, **37**, doi:10.1130/G25147A.1.

Khanbari, K., 2000. *Propagation d'un rift océanique: le Golfe d'Aden*, Thèse de Doctorat, Univ. Paris Sud, Paris, France.

King, G., 1983. The Accomodation of Large Strains in the Upper Lithosphere of the Earth and Other Solids by Self-similar Fault Systems: the Geometrical Origin of b-Value, *Pure App. Geophys*., **121**, 761-815.

Korger, E. I. M., & Schlindwein, V., 2011. Performance of localization algorithms for teleseismic mid-ocean ridge earthquakes: the 1999 Gakkel Ridge earthquake swarm and its geological interpretation, *Geophys. J. Int*., **188**, 613-625, doi:10.1111/j.1365-246X.2011.05282.x.

Kulpinski, K , Coté, D. M., Ebinger, C. J., Keir, D., & Ayele, A., 2009. Testing models of dike intrusion during rifting episodes: The role of heating in triggering earthquakes in Afar, *Eos Trans. AGU*, **9**(52), Fall Meet. Suppl., Abstract T31B-1820.

Malkin, B. V., & Shemenda, A. I., 1991. Mechanism of rifting: Considerations based on results of physical modeling and on geological and geophysical data, *Tectonophysics*, **199**, 193-210, doi:10.1016/0040-1951(91)90170-O.

Manighetti, I., Tapponnier, P., Courtillot, V., Gruszow, S., & Gillot, P.-Y., 1997. Propagation of rifting along the Arabia-Somalia plate boundary: The Gulfs of Aden and Tadjoura, *J. Geophys. Res*., **102**, 2681-2710.

Mart, Y., & Dauteuil, O., 2000. Analog experiments of propagation of oblique rifts, *Tectonophysics*, **316**, 121-132.

McClay, K. R., & White, M. J., 1995. Analog modeling of orthogonal and oblique rifting, *Mar. Petro. Geol*., **12**, 137-151.

McKenzie, D. P., 1969. The relation between fault plane solutions for earthquakes and the directions of the principal stress, *Bull. Seism. Soc. Am*., **59**, 591-601.

Müller, C. & Jokat, W., 2000. Seismic Evidence for Volcanic Activity Discovered in Central Arctic, *EOS, Trans. AGU*, **81**, 265-269.

Nakanishi, I., & Kanamori, H., 1982. Effects of lateral heterogeneity and source process time on the linear moment tensor inversion of long-period Rayleigh-waves. *Bull. Seismol. Soc. Am.*, **72**, 2063-2080.

Riedel, C., & Schlindwein, V., 2010. Did the 1999 earthquake swarm on Gakkel Ridge open a volcanic conduit? A detailed teleseismic data analysis, *J. Seismol*., **14**, 505-522.

Rochette, P., Tamrat, E., Féraud, G., Pik, R., Courtillot, V., Kefeto, E., Coulon, C., Hoffmann, C., Vandamme, D., & Yirgu, G. (1997), Magnetostratigraphy and timing of the Oligocene Ethiopian traps, *Earth Planet Sci. Lett*., **14**, 497-510.

Rowland, J. V., Baker, E., Ebinger, C. J., Keir, D., Kidane, T., Biggs, J., Hayward, N., & Wright, T. J., 2007. Fault growth at a nascent slow-spreading ridge: 2005 Dabbahu rifting episode, Afar, *Geophys. J. Int*., **171**, 1226-1246.

Rubin, A. M., 1990. A comparison of rift-zone tectonics in Iceland and Hawaii, *Bull. Volcanol*., **52**, 302-319.

Rubin, A. M., 1992. Dike-induced Faulting and Graben Subsidence in Volcanic Rift Zones, *J. Geophys. Res.,* **97**, 1839-1858.

Rubin, A. M. & Pollard, D. D., 1988. Dike-induced faulting in rift zones of Iceland and Afar, *Geology*, **16**, 413-417.

Rubin, A. M. & Gillard, D., 1998. Dike-induced earthquakes: Theoretical considerations, *J. Geophys. Res.*, **103**, 10,017-10,030.

Schlindwein, V., & Riedel, C., 2010. Location and source mechanism of sound signals at Gakkel ridge, Arctic Ocean: Submarine Strombolian activity in the 1999-2001 volcanic episode, *Geochem. Geophys. Geosys.*, **11**, doi:10.1029/2009GC002706.

Shcherbakov, R. & Turcotte, D., 2004. A Modified Form of Båth's Law. *Bull. Seism. Soc. Am.*, **94**, 5, 1968-1975.

Shcherbakov, R., Turcotte, D., & Rundle, J., 2005. Aftershock Statistics, *Pure Appl. Geophys.*, **162**, 1051-1076, doi:10.1007/s00024-004-2661-8.

Smith, G., & Ekström, G., 1997. Interpretation of earthquake epicenter and CMT centroid locations, in terms of rupture length and direction. *Phys. Earth Planet. Inter.*, **102**, 123-132.

Smith, S. R., Bourassa, M. A., & Long, M., 2011. Pirate Attacks Affect Indian Ocean Climate Research, *Eos, Trans. AGU*, **92**, 225-226.

Solomon, S. C. & Burr, N. C., 1979. The relationship of source parameters of ridge-crest and transform earthquakes to the thermal structure of oceanic lithosphere, *Tectonophysics*, **55**, 107-126.

Solomon, S. C., Huang, P. Y., & Meinke, L., 1988. The seismic moment budget of slowly spreading ridges, *Nature*, **334**, 58-60.

Tamsett, D., & Searle, R. C., 1988. Structure and Development of the Midocean Ridge Plate Boundary in the Gulf of Aden: Evidence from GLORIA Side Scan Sonar, *J. Geophys. Res.*, **93**, 3157-3178.

Taylor, B., Crook, K., & Sinton, J., 1994. Extensional transform zones and oblique spreading centers, *J. Geophys. Res.*, **99**, 19,707-19,718.

Toda, S., Stein, R. S., & Sagiya, T., 2002. Evidence from the AD 2000 Izu islands earthquake swarm that stressing rate governs seismicity, *Nature*, **419**, 58-61.

Tolstoy, M., Bohnenstiehl, D. R., Edwards, M. H. & Kurras, G. J., 2001. Seismic character of volcanic activity at the ultraslow-spreading Gakkel Ridge, *Geology*, **29**, 1139-1142.

Tolstoy, M., Cowen, J. P., Baker, E. T., Fornari, D. J., Rubin, K. H., Shank, T. M., Waldhauser, F., Bohnenstiehl, D. R., Forsyth, D. W., Holmes, R. C., Love, B., Perfit, M. R., Weekly,

R. T., Soule, S. A., & Glazer, B., 2006. A Sea-Floor Spreading Event Captured by Seismometers, *Science*, **314**, 1920-1922.

Townend, J., 2006. What do Faults Feel? Observational Constraints on the Stresses Acting on Seismogenic Faults, in *Earthquakes: Radiated Energy and the Physics of Faulting*, pp. 313-327, eds. Abercrombie, R., McGarr, A., Di Toro, G., & Kanamori, H., AGU Geophys. Monograph Series, Washington D.C.

Tron, V. & Brun, J.-P., 1991. Experiments on oblique rifting in brittle-ductile systems, *Tectonophysics*, **188**, 71-84.

Tuckwell, G. W., Bull, J. M., & Sanderson, D. J., 1996. Models of fracture orientation at oblique spreading centers, *J. Geolog. Soc. London*, **153**, 185-189.

Ukstins, I. A., Renne, P. R., Wolfenden, E., Baker, J., Ayalew, D., & Menzies, M., 2002. Matching conjugate volcanic rifted margins: 40Ar/39Ar chronostratigraphy of the pre- and syn-rift bimodal flood volcanism in Ethiopia and Yemen, *Earth Planet. Sci. Lett.*, **198**, 289-306, doi:10.1016/S0012-821X(02)00525-3.

Utsu, T., 1965. A method for determining the value of *b* in a formula *log N = a-bM* showing the magnitude frequency for earthquakes. *Geophys. Bull. Hokkaido Univ.*, **13**, 99-103.

Wells, D. L., & Coppersmith, K. J., 1994. New Empirical Relationships among Magnitude, Rupture Length, Rupture Width, Rupture Area, and Surface Displacement, *Bull. Seism. Soc. Am.*, **84**, 974-1002.

Wiemer, S., 2001. A Software Package to Analyze Seismicity: ZMAP, *Seism. Res. Lett.*, **72**, 374-383.

Wiemer, S., & McNutt, S. R., 1997. Variations in the frequency-magnitude distribution with depth in two volcanic areas: Mount St. Helens, Washington, and Mt. Spurr, Alaska, *Geophys. Res. Lett.*, **24**, 189-192.

Wiemer, S., McNutt, S. R., & Wyss, M., 1998. Temporal and three-dimensional spatial analyses of the frequency-magnitude distribution near Long Valley Caldera, California, *Geophys. J. Int.*, **134**, 409-421.

Withjack, M. O., & Jamison, W. R., 1986. Deformation produced by oblique rifting, *Tectonophysics*, **126**, 99-124.

Wright, T. J., Ebinger, C., Biggs, J., Ayele, A., Yirgu, G., Keir, D., & Stork, A., 2006. Magma-maintained rift segmentation at continental rupture in the 2005 Afar dyking episode, *Nature*, **442**, doi:10.1038/nature04978.

Zúñiga, R., & Wyss, M., 1995. Inadvertent Changes in Magnitude Reported in Earthquake Catalogs: Their Evaluation through *b*-Value Estimates, *Bull. Seism. Soc. Am.*, **85**, 1858-1866.

Appendix C

This appendix contains Supplementary Information for Appendix B. These data tables have been published as Supporting Information for Shuler and Nettles (2012), and are reprinted with permission.

Shuler, A. & Nettles, M. 2012. Earthquake source parameters for the 2010 western Gulf of Aden rifting episode, *Geophys. J. Int.*, **190**, 1111-1122, doi:10.1111/j.1365-246X.2012.05529.x.

Table C1: Centroid-moment-tensor solutions for 110 earthquakes occurring in the western Gulf of Aden from 2010 November to 2011 April. The number in the first column is the event number for each earthquake. An asterisk next to the event number indicates that the earthquake is less-well constrained (see text). The event number is followed by the year, month, day and origin time of the earthquake. The origin time listed is that of the centroid solution, where δt_0 indicates the time shift (in seconds) with respect to the time reported by the NEIC in its Preliminary Determination of Epicenters (PDE) or the Global CMT Project's Surface Wave Catalog.

The hypocentral coordinates are for the centroid location, and $\delta\lambda_0$ and $\delta\phi_0$ indicate the perturbations in latitude and longitude obtained with respect to the original epicenter. Because all of the earthquakes are shallow, their centroid depths were constrained by the inversion to be 12 kilometers, so no standard error in depth is given.

The half duration (*Half Drtn*) of the earthquake is a fixed parameter in the inversion, estimated from the scalar moment using an empirical relationship. The moment-rate function is modeled as a triangle.

The scale factor (10^{ex}) is the number by which the scalar seismic moment and moment-tensor elements must be multiplied to obtain a result in Nm. The entries in the table represent the exponent (ex) values. The scalar moment (M_0) is defined as $M_0 = (\sigma_{max} - \sigma_{min})/2$, where σ_{max} and σ_{min} are the maximum and minimum eigenvalues of the moment tensor.

The elements of the moment tensor are given in the standard spherical coordinate system (Gilbert & Dziewonski 1975). In Cartesian coordinates, $M_{rr} = M_{zz}$, $M_{\theta\theta} = M_{xx}$, $M_{\phi\phi} = M_{yy}$, $M_{r\theta} = M_{xz}$, $M_{r\phi} = -M_{yz}$, and $M_{\theta\phi} = -M_{xy}$ (see Aki & Richards 2002). The CMT solutions are constrained to have no isotropic component, so that $M_{rr} + M_{\theta\theta} + M_{\phi\phi} = 0$. In some cases, the elements of $M_{r\theta}$ and $M_{r\phi}$ are also constrained to zero because of the instability of the solution. In these cases, the corresponding values and standard errors are omitted in the table. Each element of the moment tensor is followed by its estimated standard error.

Table C2: Moment tensors expressed in principal-axis system and best-double-couple parameters. As in Table S1, the number in the first column is the event number, and an asterisk next to the event number indicates that the solution is less-well constrained. The scale factor (10^{ex}) is the number by which the scalar seismic moment and eigenvalues must be multiplied to obtain a result in Nm. Each principal axis is described by an eigenvalue, plunge and azimuth. The scalar moment (M_0) is repeated from Table S1. The strike, dip, and rake for the nodal planes of the best-double-couple mechanism are listed, following the convention of Aki & Richards (2002).

References:

Aki, K. & Richards, P. G., 2002. *Quantitative Seismology*, 2nd edn, University Science Books, Sausalito, California.

Gilbert, F., Dziewonski, A. M., 1975. An application of normal mode theory to the retrieval of structural parameters and source mechanisms from seismic spectra. *Philos. Trans. R. Soc., Lond. Ser. A*, **278**, 187-269.

Table C1. Centroid-moment-tensor solutions for 110 earthquakes occurring in the Western Gulf of Aden, 11/2010-4/2011.

	Centroid Parameters													Half	Scale		Elements of Moment Tensor					
No.	Date			Time			Latitude		Longitude		Depth**			Drtn	Factor	M_0						
	Y	M	D	h	m	sec	δt_0	λ	$\delta\lambda_0$	ϕ	$\delta\phi_0$	h			10^{ex}		M_{rr}	$M_{\theta\theta}$	$M_{\phi\phi}$	$M_{r\theta}$	$M_{r\phi}$	$M_{\theta\phi}$
1	2010	11	13	18	26	55.9 ± 0.5	0.2	12.06 ± 0.04	0.24	44.14 ± 0.06	0.18	12.0	0.5	16	0.8	-0.71 ± 0.07	0.61 ± 0.04	0.10 ± 0.06	-0.13 ± 0.15	0.32 ± 0.21	-0.30 ± 0.05
2	2010	11	14	6	32	28.4 ± 0.1	0.4	12.03 ± 0.01	0.05	44.21 ± 0.01	0.25	12.0	1.9	17	1.8	-1.57 ± 0.03	1.65 ± 0.03	-0.07 ± 0.03	-0.49 ± 0.07	-0.28 ± 0.08	-0.47 ± 0.03
3	2010	11	14	6	46	9.2 ± 0.3	0.8	12.06 ± 0.02	0.16	44.10 ± 0.04	0.05	12.0	1.0	16	3.3	-3.27 ± 0.15	2.56 ± 0.11	0.71 ± 0.15	-0.04 ± 0.42	0.91 ± 0.66	-1.23 ± 0.11
4	2010	11	14	6	58	21.5 ± 0.5	1.2	12.15 ± 0.04	0.47	44.11 ± 0.07	-0.01	12.0	1.0	16	2.1	-1.64 ± 0.15	1.51 ± 0.11	0.13 ± 0.16	0.98 ± 0.41	0.93 ± 0.56	-0.60 ± 0.11
5	2010	11	14	7	8	32.8 ± 0.3	0.6	12.03 ± 0.02	0.23	44.23 ± 0.03	0.28	12.0	1.1	16	4.9	-4.69 ± 0.21	4.70 ± 0.15	-0.02 ± 0.19	-0.14 ± 0.52	-0.33 ± 0.75	-1.31 ± 0.15
6	2010	11	14	7	27	35.7 ± 0.4	1.7	12.06 ± 0.02	0.14	44.36 ± 0.05	0.39	12.0	1.2	16	2.9	-2.40 ± 0.17	2.66 ± 0.12	-0.25 ± 0.18	0.05 ± 0.43	-1.29 ± 0.62	-0.56 ± 0.13
7	2010	11	14	7	31	17.0 ± 0.4	-3.0	12.06 ± 0.03	-0.19	44.21 ± 0.06	-0.04	12.0	1.3	16	2.2	-1.94 ± 0.18	1.93 ± 0.11	0.01 ± 0.16	0.16 ± 0.36	0.91 ± 0.59	-0.66 ± 0.11
8	2010	11	14	7	38	34.3 ± 0.2	1.1	12.01 ± 0.01	0.08	44.24 ± 0.02	0.25	12.0	1.2	17	0.8	-0.72 ± 0.02	0.69 ± 0.02	0.03 ± 0.02	-0.20 ± 0.05	-0.12 ± 0.07	-0.22 ± 0.02
9	2010	11	14	8	0	3.8 ± 0.5	9.3	12.10 ± 0.04	0.20	44.12 ± 0.07	-0.01	12.0	1.0	16	1.6	-1.62 ± 0.13	1.24 ± 0.09	0.37 ± 0.13	-0.02 ± 0.38	0.44 ± 0.52	-0.50 ± 0.09
10	2010	11	14	8	8	40.0 ± 0.3	0.5	12.08 ± 0.02	0.30	44.16 ± 0.05	0.17	12.0	1.0	16	2.2	-1.87 ± 0.12	1.57 ± 0.09	0.30 ± 0.11	0.50 ± 0.28	1.09 ± 0.44	-0.71 ± 0.08
11	2010	11	14	8	21	21.5 ± 0.2	-0.2	12.02 ± 0.01	-0.01	44.24 ± 0.02	0.28	12.0	1.3	17	1.0	-0.92 ± 0.02	0.93 ± 0.02	-0.01 ± 0.02	-0.34 ± 0.05	-0.30 ± 0.07	-0.21 ± 0.02
12	2010	11	14	8	30	19.9 ± 0.4	-2.3	12.10 ± 0.03	0.17	44.30 ± 0.06	0.27	12.0	1.0	16	2.1	-2.07 ± 0.15	1.84 ± 0.10	0.23 ± 0.15	0.37 ± 0.39	-0.26 ± 0.57	-0.71 ± 0.11
13	2010	11	14	8	59	21.4 ± 0.3	1.4	12.07 ± 0.02	-0.18	44.23 ± 0.04	-0.02	12.0	1.3	16	3.1	-2.99 ± 0.12	2.55 ± 0.09	0.44 ± 0.11	0.82 ± 0.31	-0.90 ± 0.48	-0.68 ± 0.09
14	2010	11	14	9	5	55.5 ± 0.4	-1.7	12.09 ± 0.02	0.29	44.18 ± 0.05	0.14	12.0	1.0	16	1.6	-0.60 ± 0.12	1.42 ± 0.07	-0.82 ± 0.10	0.19 ± 0.25	1.00 ± 0.36	0.18 ± 0.10
15	2010	11	14	9	17	51.0 ± 0.4	-0.1	12.10 ± 0.04	0.19	44.13 ± 0.05	0.14	12.0	1.2	16	1.6	-1.59 ± 0.11	1.22 ± 0.08	0.37 ± 0.12	-0.20 ± 0.35	0.59 ± 0.39	-0.53 ± 0.08
16	2010	11	14	9	23	25.8 ± 0.4	-0.9	12.08 ± 0.03	0.07	44.29 ± 0.06	0.29	12.0	1.1	16	1.8	-1.74 ± 0.12	1.52 ± 0.08	0.22 ± 0.14	0.40 ± 0.37	0.48 ± 0.44	-0.27 ± 0.08
17	2010	11	14	9	49	23.5 ± 0.4	-0.1	12.09 ± 0.03	0.15	44.06 ± 0.05	0.22	12.0	1.0	16	1.5	-1.46 ± 0.10	1.09 ± 0.06	0.37 ± 0.09	0.06 ± 0.25	0.29 ± 0.37	-0.64 ± 0.07
*18	2010	11	14	10	34	25.7 ± 0.8	-0.8	12.04 ± 0.04	0.19	44.23 ± 0.06	0.13	12.0	1.1	16	1.7	-1.69 ± 0.20	1.64 ± 0.15	0.05 ± 0.18			-0.36 ± 0.16
19	2010	11	14	10	37	43.6 ± 0.2	-3.8	12.07 ± 0.01	0.13	44.23 ± 0.02	0.26	12.0	1.3	17	0.9	-0.91 ± 0.02	0.86 ± 0.01	0.04 ± 0.02	0.00 ± 0.06	-0.11 ± 0.09	-0.23 ± 0.01
20	2010	11	14	11	14	12.7 ± 0.4	0.2	12.03 ± 0.04	0.25	44.19 ± 0.06	0.17	12.0	1.0	16	1.3	-1.41 ± 0.09	1.07 ± 0.07	0.34 ± 0.10	0.09 ± 0.31	0.27 ± 0.40	-0.37 ± 0.07
21	2010	11	14	11	30	16.1 ± 0.3	-2.1	12.09 ± 0.02	-0.01	44.10 ± 0.05	0.15	12.0	1.2	16	2.4	-2.29 ± 0.12	2.16 ± 0.08	0.13 ± 0.11	0.43 ± 0.29	0.01 ± 0.50	-0.69 ± 0.09
*22	2010	11	14	12	0	43.9 ± 0.7	-3.1	12.03 ± 0.05	0.22	44.32 ± 0.12	0.33	12.0	1.0	15	7.0	-6.71 ± 0.83	5.77 ± 0.48	0.95 ± 0.90	0.31 ± 2.06	3.54 ± 3.78	-0.35 ± 0.65
*23	2010	11	14	12	10	11.7 ± 0.4	-2.3	12.10 ± 0.02	0.27	44.30 ± 0.03	0.42	12.0	1.0	16	1.4	-1.50 ± 0.10	1.35 ± 0.06	0.15 ± 0.09			-0.08 ± 0.07
24	2010	11	14	12	17	15.1 ± 0.2	-0.7	12.09 ± 0.02	0.26	44.16 ± 0.03	0.31	12.0	1.1	16	3.2	-3.23 ± 0.11	2.89 ± 0.08	0.34 ± 0.11	-0.32 ± 0.30	-0.72 ± 0.38	-0.57 ± 0.08
25	2010	11	14	12	39	5.0 ± 0.2	9.7	12.09 ± 0.01	0.36	44.18 ± 0.03	0.24	12.0	1.1	16	4.2	-4.23 ± 0.13	3.88 ± 0.10	0.34 ± 0.12	-0.17 ± 0.39	-0.82 ± 0.60	-0.78 ± 0.10
26	2010	11	14	12	41	47.4 ± 0.4	-1.2	12.12 ± 0.02	0.16	44.13 ± 0.05	0.23	12.0	1.0	16	2.7	-2.83 ± 0.13	2.35 ± 0.10	0.48 ± 0.12	-0.18 ± 0.39	0.37 ± 0.57	-0.72 ± 0.11
27	2010	11	14	12	49	57.4 ± 0.2	1.3	12.06 ± 0.01	0.20	43.94 ± 0.03	0.18	12.0	1.1	16	4.1	-3.77 ± 0.14	3.40 ± 0.10	0.37 ± 0.13	0.06 ± 0.35	1.12 ± 0.56	-1.70 ± 0.10
*28	2010	11	14	13	19	53.3 ± 0.4	1.3	12.12 ± 0.03	-0.13	44.01 ± 0.05	-0.24	12.0	1.1	16	1.2	-1.01 ± 0.07	0.81 ± 0.05	0.20 ± 0.06	0.39 ± 0.17	0.67 ± 0.23	-0.32 ± 0.05
29	2010	11	14	13	50	5.4 ± 0.2	1.9	12.04 ± 0.01	0.11	43.95 ± 0.02	0.01	12.0	1.3	17	0.8	-0.65 ± 0.02	0.65 ± 0.01	0.00 ± 0.02	-0.20 ± 0.05	0.10 ± 0.06	-0.38 ± 0.02
30	2010	11	14	14	4	37.5 ± 0.2	6.7	12.08 ± 0.01	0.11	44.19 ± 0.02	0.26	12.0	1.3	16	6.9	-6.56 ± 0.18	6.10 ± 0.14	0.46 ± 0.17	-1.28 ± 0.49	-2.42 ± 0.66	-0.92 ± 0.13
31	2010	11	14	14	27	42.0 ± 0.3	-0.6	12.00 ± 0.02	0.22	43.93 ± 0.03	0.26	12.0	1.2	16	4.9	-4.18 ± 0.22	4.23 ± 0.16	-0.06 ± 0.22	-1.56 ± 0.52	0.64 ± 0.67	-2.09 ± 0.16
32	2010	11	14	14	33	20.0 ± 0.2	0.8	12.04 ± 0.01	0.09	43.98 ± 0.02	0.17	12.0	1.7	17	1.3	-0.85 ± 0.04	1.43 ± 0.02	-0.59 ± 0.03	0.18 ± 0.09	0.33 ± 0.12	-0.26 ± 0.03
*33	2010	11	14	14	41	46.8 ± 0.4	-2.1	12.17 ± 0.03	0.21	44.35 ± 0.07	0.48	12.0	1.0	16	2.3	-1.70 ± 0.15	1.57 ± 0.10	0.13 ± 0.16	1.09 ± 0.42	-1.26 ± 0.56	-0.18 ± 0.12
34	2010	11	14	14	55	27.4 ± 0.1	1.6	12.01 ± 0.01	-0.03	43.96 ± 0.02	0.16	12.0	1.4	17	1.4	-1.18 ± 0.03	1.18 ± 0.02	0.00 ± 0.03	-0.44 ± 0.07	-0.12 ± 0.09	-0.52 ± 0.02
35	2010	11	14	15	6	30.9 ± 0.2	0.3	12.03 ± 0.01	0.12	43.91 ± 0.02	0.27	12.0	1.7	17	0.9	-0.82 ± 0.02	0.79 ± 0.02	0.03 ± 0.02	-0.17 ± 0.06	0.08 ± 0.10	-0.32 ± 0.02
36	2010	11	14	15	15	5.7 ± 0.3	-0.4	12.06 ± 0.02	-0.04	43.93 ± 0.04	0.18	12.0	1.1	16	2.7	-2.39 ± 0.14	2.19 ± 0.09	0.20 ± 0.12	0.18 ± 0.31	0.95 ± 0.50	-1.02 ± 0.09
37	2010	11	14	15	27	13.2 ± 0.3	0.1	12.05 ± 0.02	0.29	43.84 ± 0.04	0.13	12.0	1.0	16	2.4	-2.03 ± 0.11	2.18 ± 0.07	-0.15 ± 0.10	0.30 ± 0.25	0.86 ± 0.42	-0.66 ± 0.08
38	2010	11	14	15	37	1.8 ± 0.4	1.8	12.01 ± 0.03	0.13	43.98 ± 0.05	0.21	12.0	1.1	16	1.2	-1.17 ± 0.08	0.84 ± 0.06	0.33 ± 0.07	-0.26 ± 0.21	0.16 ± 0.28	-0.50 ± 0.06
39	2010	11	14	16	33	18.8 ± 0.2	0.5	12.03 ± 0.01	0.14	43.91 ± 0.03	0.25	12.0	1.1	16	3.7	-3.50 ± 0.11	3.29 ± 0.08	0.22 ± 0.10	-0.92 ± 0.29	-0.73 ± 0.42	-0.75 ± 0.09
40	2010	11	14	16	46	13.7 ± 0.5	-0.7	12.08 ± 0.03	0.27	44.31 ± 0.08	0.37	12.0	1.0	16	1.0	-0.92 ± 0.08	0.85 ± 0.05	0.08 ± 0.07	0.24 ± 0.21	-0.27 ± 0.30	-0.14 ± 0.06

* Indicates less-well-constrained event (see text).

** All depths fixed to 12.0 kilometers

Table C1 (continued)

No.	Centroid Parameters: Date Y	M	D	Time h	m	sec	δt_0	Latitude λ	$\delta\lambda_0$	Longitude ϕ	$\delta\phi_0$	Depth** h	Half Drtn	Scale Factor 10^{ex}	M_0	Elements of Moment Tensor: M_{rr}	$M_{\theta\theta}$	$M_{\phi\phi}$	$M_{r\theta}$	$M_{r\phi}$	$M_{\theta\phi}$
41	2010	11	14	17	2	54.8 ± 0.2	7.1	11.98 ± 0.01	0.12	43.92 ± 0.02	0.20	12.0	1.9	17	2.1	-1.86 ± 0.05	1.88 ± 0.04	-0.03 ± 0.05	-0.41 ± 0.12	-0.33 ± 0.15	-0.69 ± 0.04
42	2010	11	14	17	17	8.0 ± 0.2	0.2	12.03 ± 0.01	0.16	43.91 ± 0.02	0.17	12.0	1.0	16	6.6	-6.33 ± 0.17	5.93 ± 0.13	0.40 ± 0.16	-0.84 ± 0.49	-1.16 ± 0.68	-1.85 ± 0.12
43	2010	11	14	17	39	29.1 ± 0.2	11.6	12.06 ± 0.01	0.20	44.16 ± 0.02	0.18	12.0	1.2	17	0.7	-0.71 ± 0.02	0.67 ± 0.01	0.04 ± 0.02	-0.07 ± 0.04	-0.24 ± 0.05	-0.11 ± 0.01
44	2010	11	14	18	54	28.4 ± 0.3	-0.3	12.09 ± 0.02	0.08	44.04 ± 0.03	0.02	12.0	1.1	16	2.7	-2.37 ± 0.10	1.65 ± 0.07	0.72 ± 0.09	-0.23 ± 0.24	1.57 ± 0.36	-0.76 ± 0.08
45	2010	11	14	19	15	44.4 ± 0.2	-0.4	12.07 ± 0.01	0.09	44.23 ± 0.02	0.31	12.0	1.3	16	4.1	-3.60 ± 0.12	3.49 ± 0.09	0.11 ± 0.12	-0.61 ± 0.29	-1.80 ± 0.40	-1.00 ± 0.09
46	2010	11	14	20	18	3.0 ± 0.2	-0.2	12.02 ± 0.01	0.10	43.93 ± 0.02	0.31	12.0	1.2	16	6.0	-5.69 ± 0.17	5.79 ± 0.11	-0.10 ± 0.15	-0.55 ± 0.39	-0.84 ± 0.65	-1.32 ± 0.11
47	2010	11	14	20	19	45.4 ± 0.5	-1.1	12.10 ± 0.03	0.26	44.32 ± 0.07	0.24	12.0	1.2	16	2.1	-2.20 ± 0.17	1.80 ± 0.11	0.39 ± 0.15	0.26 ± 0.42	-0.20 ± 0.61	-0.43 ± 0.11
48	2010	11	14	21	14	45.1 ± 0.2	0.3	12.01 ± 0.01	0.25	43.84 ± 0.03	0.11	12.0	1.2	16	2.4	-2.19 ± 0.10	2.30 ± 0.06	-0.11 ± 0.10	-0.24 ± 0.22	0.56 ± 0.36	-0.64 ± 0.07
49	2010	11	14	21	29	6.2 ± 0.3	0.7	12.11 ± 0.02	0.30	44.14 ± 0.04	0.20	12.0	1.1	16	2.0	-2.01 ± 0.09	1.70 ± 0.06	0.32 ± 0.08	-0.10 ± 0.25	-0.10 ± 0.34	-0.56 ± 0.06
50	2010	11	14	22	22	31.2 ± 0.1	1.1	11.98 ± 0.01	0.07	43.90 ± 0.01	0.32	12.0	1.5	17	1.3	-1.11 ± 0.02	1.11 ± 0.02	0.00 ± 0.02	-0.42 ± 0.05	-0.33 ± 0.07	-0.26 ± 0.02
51	2010	11	14	22	41	49.4 ± 0.5	-2.6	12.11 ± 0.03	-0.14	44.31 ± 0.10	0.56	12.0	1.1	16	0.8	-0.70 ± 0.07	0.69 ± 0.04	0.01 ± 0.07	0.20 ± 0.19	-0.35 ± 0.32	-0.06 ± 0.06
52	2010	11	14	23	25	35.4 ± 0.2	0.6	12.10 ± 0.01	-0.02	44.19 ± 0.02	0.18	12.0	1.2	16	5.9	-5.55 ± 0.13	4.97 ± 0.10	0.58 ± 0.12	-0.31 ± 0.32	-2.45 ± 0.43	-1.18 ± 0.10
53	2010	11	15	0	6	8.0 ± 0.4	1.9	12.09 ± 0.02	0.18	44.22 ± 0.05	0.40	12.0	1.1	16	2.0	-1.81 ± 0.12	1.87 ± 0.07	-0.06 ± 0.12	0.41 ± 0.24	-0.54 ± 0.42	0.09 ± 0.09
54	2010	11	15	3	44	3.8 ± 0.4	-1.4	12.15 ± 0.02	0.16	44.06 ± 0.03	0.38	12.0	1.0	16	0.8	-0.27 ± 0.06	0.85 ± 0.04	-0.58 ± 0.05	0.29 ± 0.12	0.16 ± 0.15	0.10 ± 0.04
55	2010	11	15	5	44	51.0 ± 0.4	3.0	12.04 ± 0.03	-0.21	43.74 ± 0.06	-0.01	12.0	1.1	16	1.0	-0.98 ± 0.08	0.86 ± 0.05	0.12 ± 0.09	0.12 ± 0.20	0.28 ± 0.27	-0.26 ± 0.06
56	2010	11	15	7	9	6.3 ± 0.5	-1.0	12.07 ± 0.04	0.13	44.25 ± 0.08	0.37	12.0	1.0	16	0.7	-0.76 ± 0.06	0.61 ± 0.04	0.15 ± 0.06	-0.17 ± 0.21	-0.19 ± 0.29	-0.07 ± 0.04
57	2010	11	15	7	36	8.6 ± 0.3	1.7	12.09 ± 0.02	0.16	44.23 ± 0.03	0.23	12.0	1.3	16	2.5	-2.48 ± 0.09	2.10 ± 0.07	0.39 ± 0.09	-0.10 ± 0.23	-0.47 ± 0.35	-0.77 ± 0.06
58	2010	11	15	11	12	21.7 ± 0.2	2.0	11.97 ± 0.01	0.20	43.79 ± 0.03	0.32	12.0	1.0	16	2.6	-2.24 ± 0.10	2.47 ± 0.07	-0.22 ± 0.10	-0.44 ± 0.20	-0.18 ± 0.37	-1.11 ± 0.07
59	2010	11	15	13	37	48.9 ± 0.3	-0.9	12.06 ± 0.02	0.05	44.22 ± 0.03	0.27	12.0	1.0	16	2.6	-2.42 ± 0.10	2.06 ± 0.07	0.36 ± 0.10	-1.04 ± 0.27	-0.26 ± 0.31	-0.75 ± 0.07
*60	2010	11	15	13	44	54.2 ± 0.5	1.3	12.01 ± 0.04	0.25	44.44 ± 0.08	0.53	12.0	1.0	16	1.0	-0.81 ± 0.08	0.78 ± 0.06	0.03 ± 0.08	-0.13 ± 0.22	-0.62 ± 0.33	-0.14 ± 0.07
61	2010	11	15	17	54	2.7 ± 0.4	-2.6	12.08 ± 0.04	0.13	44.11 ± 0.05	0.17	12.0	1.0	16	0.9	-0.86 ± 0.06	0.59 ± 0.04	0.27 ± 0.06	0.02 ± 0.18	0.49 ± 0.19	-0.20 ± 0.04
62	2010	11	15	18	37	1.8 ± 0.3	-0.6	12.12 ± 0.02	0.30	44.15 ± 0.05	0.21	12.0	1.1	16	1.6	-1.63 ± 0.08	1.38 ± 0.06	0.25 ± 0.08	0.19 ± 0.22	-0.26 ± 0.33	-0.47 ± 0.06
63	2010	11	15	19	48	5.0 ± 0.3	-1.8	12.12 ± 0.02	0.25	44.23 ± 0.05	0.39	12.0	1.0	16	1.4	-0.97 ± 0.08	1.38 ± 0.05	-0.42 ± 0.08	0.13 ± 0.16	-0.54 ± 0.30	0.18 ± 0.05
64	2010	11	15	20	44	7.5 ± 0.3	-0.1	12.13 ± 0.01	0.15	44.00 ± 0.02	0.18	12.0	1.1	16	2.0	-0.54 ± 0.09	1.79 ± 0.06	-1.25 ± 0.09	1.18 ± 0.20	0.39 ± 0.22	0.94 ± 0.07
*65	2010	11	15	23	29	29.5 ± 0.5	-0.3	12.03 ± 0.03	0.26	44.14 ± 0.07	0.31	12.0	1.0	16	1.2	-0.84 ± 0.08	0.93 ± 0.05	-0.09 ± 0.08	0.30 ± 0.18	-0.86 ± 0.33	-0.01 ± 0.07
66	2010	11	15	23	35	29.2 ± 0.3	0.0	12.07 ± 0.02	0.18	44.22 ± 0.04	0.23	12.0	1.1	16	2.3	-2.32 ± 0.09	1.98 ± 0.07	0.34 ± 0.08	-0.19 ± 0.29	0.08 ± 0.43	-0.66 ± 0.07
*67	2010	11	16	2	5	18.3 ± 0.8	-2.7	11.96 ± 0.03	-0.04	44.39 ± 0.05	0.43	12.0	1.1	16	2.4	-2.61 ± 0.28	2.22 ± 0.19	0.39 ± 0.28			-0.29 ± 0.23
*68	2010	11	16	2	7	1.0 ± 0.4	5.7	12.12 ± 0.02	0.17	44.09 ± 0.02	0.13	12.0	1.4	16	5.2	-6.00 ± 0.28	4.43 ± 0.18	1.57 ± 0.28			-0.26 ± 0.22
69	2010	11	16	15	51	27.8 ± 0.2	0.7	12.07 ± 0.02	0.04	44.19 ± 0.03	0.19	12.0	1.2	16	2.3	-2.34 ± 0.09	1.84 ± 0.06	0.51 ± 0.09	-0.21 ± 0.22	-0.24 ± 0.33	-0.82 ± 0.06
70	2010	11	16	17	37	24.1 ± 0.3	0.8	12.01 ± 0.02	0.10	44.22 ± 0.05	0.18	12.0	1.0	16	2.1	-2.00 ± 0.09	1.69 ± 0.06	0.31 ± 0.10	-0.56 ± 0.26	0.46 ± 0.44	-0.49 ± 0.07
*71	2010	11	16	22	58	34.6 ± 0.4	-0.6	12.09 ± 0.03	0.30	44.16 ± 0.08	0.18	12.0	1.1	16	0.9	-0.82 ± 0.06	0.67 ± 0.04	0.14 ± 0.06	0.19 ± 0.16	0.33 ± 0.31	-0.24 ± 0.05
72	2010	11	17	6	36	12.5 ± 0.5	4.5	12.02 ± 0.04	-0.23	44.15 ± 0.06	-0.60	12.0	1.1	15	7.6	-6.86 ± 0.54	5.41 ± 0.37	1.45 ± 0.54	-1.21 ± 1.58	3.93 ± 1.94	-1.95 ± 0.38
73	2010	11	17	20	28	27.4 ± 0.3	-2.4	12.09 ± 0.02	0.16	44.13 ± 0.04	0.01	12.0	1.1	16	2.0	-1.79 ± 0.09	1.45 ± 0.06	0.33 ± 0.09	0.05 ± 0.25	1.16 ± 0.29	-0.45 ± 0.06
74	2010	11	17	20	45	36.6 ± 0.4	-0.5	12.08 ± 0.03	0.09	44.20 ± 0.05	0.26	12.0	1.0	16	1.1	-1.09 ± 0.07	0.79 ± 0.05	0.30 ± 0.08	0.20 ± 0.21	0.22 ± 0.25	-0.46 ± 0.05
75	2010	11	18	1	56	52.7 ± 0.2	-1.0	12.12 ± 0.01	0.11	44.15 ± 0.02	0.16	12.0	1.0	16	3.5	-3.46 ± 0.10	2.89 ± 0.08	0.57 ± 0.10	-0.43 ± 0.28	-0.98 ± 0.36	-0.95 ± 0.08
76	2010	11	18	2	25	51.3 ± 0.3	-0.1	12.13 ± 0.03	0.21	44.18 ± 0.04	0.23	12.0	1.1	16	1.4	-1.44 ± 0.08	1.10 ± 0.05	0.34 ± 0.07	0.24 ± 0.22	-0.07 ± 0.26	-0.51 ± 0.06
77	2010	11	20	1	55	22.9 ± 0.3	-4.8	12.09 ± 0.02	0.26	44.21 ± 0.03	0.19	12.0	1.0	16	1.9	-2.00 ± 0.08	1.61 ± 0.06	0.39 ± 0.08	0.04 ± 0.20	-0.12 ± 0.28	-0.64 ± 0.06
78	2010	11	20	11	53	55.3 ± 0.5	-1.9	12.13 ± 0.04	0.12	44.10 ± 0.07	0.18	12.0	1.0	16	0.8	-0.79 ± 0.06	0.65 ± 0.04	0.14 ± 0.07	0.17 ± 0.21	0.10 ± 0.22	-0.20 ± 0.05
79	2010	11	20	23	38	35.1 ± 0.2	0.1	12.09 ± 0.02	0.16	44.26 ± 0.03	0.29	12.0	1.1	16	3.1	-3.04 ± 0.10	2.43 ± 0.08	0.61 ± 0.10	0.39 ± 0.27	-1.05 ± 0.38	-0.99 ± 0.08
*80	2010	11	21	16	46	18.1 ± 0.5	2.1	12.04 ± 0.02	-0.21	44.27 ± 0.04	0.52	12.0	1.1	16	0.7	-0.81 ± 0.06	0.57 ± 0.04	0.24 ± 0.06			-0.20 ± 0.05

* Indicates less-well-constrained event (see text).

** All depths fixed to 12.0 kilometers

Table C1 (continued)

No.	Centroid Parameters: Date Y	M	D	Time h	m	sec ±	δt_0	Latitude λ ±	$\delta\lambda_0$	Longitude ϕ ±	$\delta\phi_0$	Depth** h	Half Drtn	Scale Factor 10^{ex}	M_0	Elements of Moment Tensor: M_{rr} ±	$M_{\theta\theta}$ ±	$M_{\phi\phi}$ ±	$M_{r\theta}$ ±	$M_{r\phi}$ ±	$M_{\theta\phi}$ ±
*81	2010	11	21	22	12	25.8 ± 0.5	0.9	12.05 ± 0.02	0.53	44.25 ± 0.04	0.20	12.0	1.1	16	0.8	-0.85 ± 0.07	0.66 ± 0.04	0.18 ± 0.08			-0.18 ± 0.06
82	2010	11	21	22	26	12.1 ± 0.4	-2.3	12.02 ± 0.03	0.00	44.23 ± 0.05	0.09	12.0	1.2	16	1.4	-1.33 ± 0.07	1.13 ± 0.05	0.20 ± 0.07	-0.39 ± 0.22	0.25 ± 0.25	-0.29 ± 0.05
83	2010	11	22	22	3	20.1 ± 0.4	-1.3	12.06 ± 0.03	0.25	44.16 ± 0.05	0.36	12.0	1.0	16	1.2	-1.14 ± 0.08	1.08 ± 0.05	0.06 ± 0.08	-0.17 ± 0.21	0.09 ± 0.25	-0.26 ± 0.05
84	2010	11	23	14	31	34.9 ± 0.3	-1.5	12.10 ± 0.02	0.18	44.06 ± 0.04	0.37	12.0	1.0	16	1.5	-0.63 ± 0.09	1.47 ± 0.06	-0.84 ± 0.09	0.40 ± 0.17	0.74 ± 0.30	-0.24 ± 0.07
*85	2010	11	23	20	50	6.1 ± 0.4	-1.9	12.05 ± 0.02	-0.20	44.27 ± 0.04	0.52	12.0	1.1	16	0.8	-0.83 ± 0.07	0.70 ± 0.04	0.13 ± 0.07			-0.18 ± 0.05
86	2010	11	24	13	36	18.0 ± 0.4	-0.6	12.07 ± 0.03	0.10	44.34 ± 0.05	0.30	12.0	1.0	16	1.3	-1.26 ± 0.08	1.15 ± 0.06	0.10 ± 0.08	0.26 ± 0.21	-0.50 ± 0.28	-0.26 ± 0.06
87	2010	11	24	19	9	8.4 ± 0.4	-1.7	12.02 ± 0.03	0.10	44.21 ± 0.05	0.20	12.0	1.0	16	1.1	-1.08 ± 0.07	0.90 ± 0.05	0.18 ± 0.07	-0.23 ± 0.20	0.40 ± 0.24	-0.29 ± 0.05
88	2010	11	25	7	11	6.3 ± 0.3	0.6	12.07 ± 0.02	0.29	44.23 ± 0.05	0.18	12.0	1.0	16	1.3	-1.28 ± 0.07	1.11 ± 0.05	0.17 ± 0.07	-0.02 ± 0.19	-0.06 ± 0.29	-0.46 ± 0.05
89	2010	11	25	13	43	57.3 ± 0.3	-0.2	12.12 ± 0.03	0.15	44.22 ± 0.04	0.24	12.0	1.0	16	1.5	-1.38 ± 0.07	1.09 ± 0.05	0.28 ± 0.07	0.56 ± 0.20	-0.23 ± 0.26	-0.51 ± 0.06
90	2010	11	25	22	41	17.4 ± 0.3	0.9	12.10 ± 0.03	0.23	44.17 ± 0.04	0.13	12.0	1.1	16	1.5	-1.54 ± 0.07	1.14 ± 0.05	0.40 ± 0.07	0.27 ± 0.22	-0.27 ± 0.30	-0.44 ± 0.06
91	2010	11	28	5	19	47.3 ± 0.5	3.3	12.14 ± 0.03	-0.36	43.97 ± 0.05	-0.53	12.0	1.1	15	7.5	-6.19 ± 0.61	4.85 ± 0.36	1.35 ± 0.56	1.25 ± 1.25	3.37 ± 1.64	-3.51 ± 0.36
*92	2010	11	29	4	1	43.3 ± 0.5	7.3	12.08 ± 0.03	-0.17	44.19 ± 0.04	0.44	12.0	1.1	15	6.3	-6.22 ± 0.55	5.49 ± 0.39	0.74 ± 0.58			-2.21 ± 0.46
93	2010	11	30	9	34	20.8 ± 0.4	-0.7	12.09 ± 0.03	0.14	44.21 ± 0.05	0.24	12.0	1.0	16	2.5	-2.56 ± 0.17	2.09 ± 0.11	0.47 ± 0.17	-0.11 ± 0.39	-0.03 ± 0.58	-0.96 ± 0.13
94	2010	12	5	1	7	29.0 ± 0.3	-0.4	12.16 ± 0.03	0.14	44.11 ± 0.04	0.14	12.0	1.0	16	1.1	-1.03 ± 0.06	0.68 ± 0.04	0.34 ± 0.07	0.27 ± 0.17	0.23 ± 0.18	-0.46 ± 0.04
95	2010	12	6	11	34	46.8 ± 0.3	0.5	12.04 ± 0.03	0.15	44.27 ± 0.05	0.24	12.0	1.0	16	1.4	-1.50 ± 0.07	1.21 ± 0.05	0.29 ± 0.08	0.08 ± 0.25	-0.04 ± 0.39	-0.34 ± 0.06
*96	2010	12	6	12	18	17.9 ± 0.4	9.9	12.02 ± 0.02	0.27	44.29 ± 0.03	-0.46	12.0	1.1	16	1.0	-1.02 ± 0.07	0.84 ± 0.05	0.18 ± 0.08			-0.23 ± 0.05
*97	2010	12	6	12	44	24.3 ± 0.4	8.3	12.05 ± 0.02	0.30	44.24 ± 0.03	-0.01	12.0	1.2	16	0.9	-0.99 ± 0.07	0.77 ± 0.05	0.22 ± 0.07			-0.30 ± 0.05
98	2010	12	6	12	55	5.3 ± 0.4	-0.7	12.05 ± 0.03	0.12	44.46 ± 0.06	0.36	12.0	1.1	16	0.9	-0.68 ± 0.06	0.78 ± 0.04	-0.09 ± 0.07	0.18 ± 0.20	-0.56 ± 0.25	-0.15 ± 0.05
99	2010	12	11	14	2	17.6 ± 0.4	0.2	12.06 ± 0.03	0.15	44.24 ± 0.05	0.24	12.0	1.0	16	1.8	-1.90 ± 0.12	1.47 ± 0.08	0.43 ± 0.13	-0.23 ± 0.32	-0.04 ± 0.37	-0.51 ± 0.07
100	2010	12	11	14	6	26.1 ± 0.2	0.6	12.10 ± 0.02	0.17	44.23 ± 0.03	0.25	12.0	1.1	16	4.2	-4.04 ± 0.13	3.54 ± 0.09	0.51 ± 0.13	0.08 ± 0.39	-1.33 ± 0.48	-1.12 ± 0.09
101	2010	12	19	19	24	35.3 ± 0.2	-0.6	12.07 ± 0.01	0.04	44.18 ± 0.03	0.17	12.0	1.0	16	2.8	-2.84 ± 0.09	2.54 ± 0.06	0.30 ± 0.09	-0.42 ± 0.21	-0.09 ± 0.33	-0.75 ± 0.07
102	2010	12	31	18	9	31.5 ± 0.3	-0.5	12.11 ± 0.02	0.24	44.15 ± 0.04	0.15	12.0	1.1	16	1.7	-1.77 ± 0.08	1.53 ± 0.05	0.24 ± 0.08	0.02 ± 0.22	0.09 ± 0.31	-0.49 ± 0.06
103	2010	12	31	22	4	42.9 ± 0.3	-1.4	12.10 ± 0.02	0.22	44.18 ± 0.03	0.12	12.0	1.1	16	2.7	-2.80 ± 0.11	2.28 ± 0.08	0.52 ± 0.10	-0.27 ± 0.29	-0.15 ± 0.42	-0.84 ± 0.08
104	2011	1	10	2	29	57.1 ± 0.2	-0.5	12.10 ± 0.01	0.06	44.13 ± 0.02	0.14	12.0	1.2	16	6.6	-6.42 ± 0.16	5.21 ± 0.12	1.21 ± 0.16	-2.00 ± 0.41	-1.18 ± 0.53	-1.95 ± 0.12
105	2011	1	30	2	28	41.8 ± 0.2	-2.5	12.05 ± 0.01	0.03	44.25 ± 0.02	0.18	12.0	1.3	16	4.3	-4.13 ± 0.11	3.47 ± 0.08	0.66 ± 0.11	-1.26 ± 0.27	-0.89 ± 0.38	-1.26 ± 0.09
106	2011	2	1	11	24	30.7 ± 0.4	-1.3	12.05 ± 0.03	0.27	44.17 ± 0.05	0.21	12.0	1.1	16	1.5	-1.44 ± 0.07	1.04 ± 0.05	0.40 ± 0.08	-0.39 ± 0.20	0.61 ± 0.29	-0.40 ± 0.05
*107	2011	2	3	2	42	32.1 ± 0.6	0.1	12.02 ± 0.04	-0.48	44.31 ± 0.07	0.81	12.0	1.1	15	7.5	-6.97 ± 0.61	5.35 ± 0.37	1.61 ± 0.65	-0.03 ± 1.72	3.46 ± 1.98	-2.35 ± 0.40
108	2011	3	30	1	42	47.7 ± 0.3	-1.5	12.08 ± 0.02	0.09	44.22 ± 0.03	0.16	12.0	1.2	16	2.5	-2.56 ± 0.09	2.14 ± 0.06	0.42 ± 0.10	-0.41 ± 0.24	-0.16 ± 0.31	-0.60 ± 0.06
109	2011	4	19	9	7	59.6 ± 0.4	-5.3	12.06 ± 0.02	0.00	44.23 ± 0.04	0.26	12.0	1.2	16	2.4	-2.28 ± 0.11	1.83 ± 0.09	0.46 ± 0.14	-0.42 ± 0.28	-0.81 ± 0.46	-0.78 ± 0.08
*110	2011	4	19	9	37	52.8 ± 0.4	-3.4	12.10 ± 0.02	0.09	44.25 ± 0.03	0.13	12.0	1.1	16	1.8	-1.79 ± 0.10	1.55 ± 0.08	0.24 ± 0.12			-0.67 ± 0.07

* Indicates less-well-constrained event (see text).

** All depths fixed to 12.0 kilometers

Table C2. Principal axes and best-double-couple parameters.

No.	Scale Factor 10^{nn}	Principal Axes									M_0	Best Double Couple					
		T-axis			N-axis			P-axis				Plane 1			Plane 2		
		σ	δ	ξ	σ	δ	ξ	σ	δ	ξ		φ_c	θ	λ	φ_c	θ	λ
1	16	0.79	10	208	0.03	16	300	-0.82	71	86	0.8	279	38	-117	131	57	-71
2	17	1.82	7	193	-0.10	14	101	-1.72	74	309	1.8	299	40	-68	90	54	-108
3	16	3.21	4	208	0.28	12	298	-3.48	77	100	3.3	284	42	-109	129	50	-74
4	16	1.86	12	13	0.51	26	277	-2.37	61	126	2.1	132	40	-47	262	62	-120
5	16	5.04	0	195	-0.33	5	104	-4.72	85	288	4.9	289	45	-83	100	45	-96
6	16	2.78	3	12	0.24	25	104	-3.01	64	275	2.9	78	47	-126	304	53	-58
7	16	2.14	2	198	0.19	23	289	-2.33	67	104	2.2	266	48	-122	129	51	-60
8	17	0.78	6	196	0.00	13	104	-0.78	76	311	0.8	300	40	-70	94	53	-106
9	16	1.48	4	206	0.23	12	296	-1.72	78	98	1.6	283	42	-108	127	50	-74
10	16	1.89	0	24	0.57	26	294	-2.46	64	114	2.2	138	50	-55	270	51	-125
11	17	1.02	9	189	0.07	19	96	-1.08	69	303	1.0	300	40	-60	83	56	-113
12	16	2.15	6	21	-0.03	3	111	-2.12	83	229	2.1	107	39	-95	294	51	-86
13	16	2.94	10	19	0.34	9	111	-3.28	76	242	3.1	97	36	-106	297	56	-79
14	16	1.48	9	352	0.24	47	252	-1.72	42	90	1.6	122	54	-26	228	69	-141
15	16	1.54	8	208	0.22	13	300	-1.76	75	86	1.6	283	38	-111	129	55	-74
16	16	1.60	5	9	0.31	15	278	-1.91	74	119	1.8	115	42	-68	266	52	-109
17	16	1.47	2	211	0.05	10	301	-1.52	79	111	1.5	290	44	-105	131	48	-76
*18	16	1.72	0	192	-0.03	0	102	-1.69	90	180	1.7	282	45	-90	102	45	-90
19	17	0.92	1	15	-0.01	7	105	-0.92	83	277	0.9	98	44	-99	291	46	-81
20	16	1.22	1	203	0.24	10	293	-1.46	80	110	1.3	283	45	-104	122	46	-76
21	16	2.41	5	17	-0.07	3	287	-2.33	84	162	2.4	111	40	-85	284	50	-94
*22	15	5.80	0	4	2.32	21	274	-8.11	69	95	7.0	114	49	-61	254	49	-119
*23	16	1.36	0	184	0.14	0	94	-1.50	90	180	1.4	274	45	-90	94	45	-90
24	16	3.02	2	192	0.39	12	101	-3.40	78	289	3.2	294	45	-73	90	48	-106
25	16	4.05	0	12	0.33	10	102	-4.38	80	282	4.2	92	46	-105	292	46	-75
26	16	2.61	3	199	0.26	5	289	-2.87	84	79	2.7	284	42	-98	114	48	-83
27	16	4.18	3	205	-0.10	16	296	-4.09	74	104	4.1	279	44	-113	129	50	-69
*28	16	0.96	4	19	0.46	27	287	-1.42	62	118	1.2	136	47	-51	266	55	-124
29	17	0.86	8	205	-0.17	1	295	-0.68	81	32	0.8	293	37	-92	116	53	-89
30	16	6.31	4	187	1.17	18	96	-7.48	71	290	6.9	296	44	-63	81	52	-113
31	16	5.38	10	202	-0.91	0	292	-4.48	80	22	4.9	292	35	-90	112	55	-90
32	17	1.47	3	7	-0.37	35	274	-1.10	54	101	1.3	128	52	-43	248	58	-133
*33	16	2.08	21	20	0.46	17	116	-2.54	63	242	2.3	82	28	-127	303	68	-72
34	17	1.43	8	199	-0.14	13	108	-1.29	74	320	1.4	304	39	-69	98	54	-106
35	17	0.93	6	200	-0.08	1	290	-0.84	84	29	0.9	289	39	-92	111	51	-89
36	16	2.63	3	204	0.12	20	295	-2.75	69	107	2.7	274	46	-119	132	51	-63
37	16	2.36	1	14	0.07	23	284	-2.42	67	107	2.4	126	49	-58	263	50	-121
38	16	1.19	7	211	0.02	0	301	-1.21	83	32	1.2	301	38	-90	121	52	-90
39	16	3.54	6	191	0.26	13	100	-3.79	75	306	3.7	296	41	-70	90	52	-107
40	16	0.92	9	13	0.10	11	104	-1.01	76	245	1.0	89	37	-108	292	55	-76

* Indicates less-well-constrained event (see text).

Table C2 (continued)

No.	Scale Factor 10^{n*}	Principal Axes									M_0	Best Double Couple					
		T-axis			N-axis			P-axis				Plane 1			Plane 2		
		σ	δ	ξ	σ	δ	ξ	σ	δ	ξ		φ_s	θ	λ	φ_s	θ	λ
41	17	2.13	4	197	-0.14	14	106	-1.99	75	304	2.1	302	43	-69	94	51	-108
42	16	6.51	2	196	0.12	12	106	-6.63	78	297	6.6	298	44	-73	95	48	-106
43	17	0.69	1	189	0.10	17	99	-0.79	73	283	0.7	296	46	-66	83	49	-113
44	16	2.32	14	218	0.71	18	313	-3.03	67	93	2.7	285	35	-123	143	61	-69
45	16	3.76	1	195	0.68	24	104	-4.44	66	287	4.1	307	49	-57	83	51	-122
46	16	6.08	2	192	-0.23	10	102	-5.86	80	292	6.0	292	44	-76	93	48	-103
47	16	1.94	4	16	0.28	3	106	-2.23	85	229	2.1	103	41	-94	288	49	-86
48	16	2.49	5	195	-0.16	13	286	-2.33	76	86	2.4	271	42	-110	117	51	-73
49	16	1.90	1	199	0.13	3	109	-2.02	87	304	2.0	293	44	-85	106	46	-95
50	17	1.22	9	190	0.07	18	97	-1.30	70	304	1.3	300	40	-61	84	56	-112
51	16	0.74	10	10	0.12	20	103	-0.86	68	254	0.8	77	39	-122	296	58	-66
52	16	5.28	2	15	1.17	20	106	-6.45	70	280	5.9	86	47	-118	303	50	-64
53	16	1.92	6	359	0.09	16	91	-2.01	73	248	2.0	72	41	-114	283	53	-70
54	16	0.93	14	355	-0.28	62	237	-0.65	24	91	0.8	131	63	-7	224	84	-153
55	16	0.94	1	17	0.12	15	287	-1.07	75	110	1.0	122	46	-69	272	48	-111
56	16	0.64	6	186	0.18	12	94	-0.82	76	302	0.7	289	40	-71	85	52	-105
57	16	2.40	1	21	0.17	10	111	-2.57	80	286	2.5	101	45	-104	301	47	-76
58	16	2.89	4	199	-0.56	10	109	-2.32	79	310	2.6	300	42	-74	100	50	-104
59	16	2.51	10	198	0.20	12	106	-2.71	74	329	2.6	302	36	-70	98	56	-104
*60	16	0.80	1	190	0.35	29	99	-1.15	61	281	1.0	306	51	-52	75	52	-127
61	16	0.72	9	213	0.32	19	306	-1.04	69	99	0.9	282	39	-120	139	57	-67
62	16	1.57	5	20	0.10	6	111	-1.67	82	252	1.6	104	41	-99	296	50	-82
63	16	1.40	2	355	-0.09	32	86	-1.32	58	262	1.4	56	51	-133	292	55	-50
64	16	2.56	22	344	-1.03	67	180	-1.52	6	76	2.0	122	70	12	28	79	160
*65	16	1.01	14	12	0.42	29	110	-1.43	57	259	1.2	68	40	-139	305	65	-57
66	16	2.22	3	199	0.11	0	289	-2.33	87	25	2.3	289	42	-90	110	48	-90
*67	16	2.27	0	189	0.34	0	99	-2.61	90	180	2.4	279	45	-90	99	45	-90
*68	16	4.45	0	185	1.55	0	95	-6.00	90	180	5.2	275	45	-90	95	45	-90
69	16	2.23	1	205	0.16	7	115	-2.38	83	304	2.3	302	44	-80	108	47	-100
70	16	1.96	10	199	0.19	6	290	-2.15	78	52	2.1	281	36	-101	115	55	-82
*71	16	0.77	3	19	0.19	20	288	-0.96	70	116	0.9	129	46	-61	271	51	-117
72	15	6.78	12	209	1.66	17	303	-8.44	69	85	7.6	277	36	-120	133	59	-70
73	16	1.65	7	205	0.65	23	298	-2.32	66	99	2.0	271	43	-125	135	56	-62
74	16	1.07	1	30	0.10	14	300	-1.16	76	127	1.1	134	45	-71	287	48	-109
75	16	3.23	1	199	0.52	15	109	-3.75	75	292	3.5	304	46	-69	95	48	-111
76	16	1.38	5	27	0.09	2	296	-1.46	85	189	1.4	118	40	-87	295	50	-92
77	16	1.88	1	23	0.12	3	113	-2.01	87	269	1.9	110	44	-94	296	46	-86
78	16	0.73	5	18	0.10	9	287	-0.83	79	136	0.8	118	41	-76	280	51	-102
79	16	2.97	8	26	0.36	12	118	-3.32	75	265	3.1	102	39	-110	307	54	-75
*80	16	0.67	0	205	0.14	0	115	-0.81	90	180	0.7	295	45	-90	115	45	-90

* Indicates less-well-constrained event (see text).

Table C2 (continued)

No.	Scale Factor 10^{n*}	Principal Axes									M_0	Best Double Couple					
		T-axis			N-axis			P-axis				Plane 1			Plane 2		
		σ	δ	ξ	σ	δ	ξ	σ	δ	ξ		φ_1	θ	λ	φ_2	θ	λ
*81	16	0.72	0	198	0.12	0	108	-0.85	90	180	0.8	288	45	-90	108	45	-90
82	16	1.29	10	197	0.13	5	288	-1.42	79	43	1.4	281	36	-98	111	55	-84
83	16	1.16	5	194	0.00	3	284	-1.16	85	42	1.2	281	40	-94	106	50	-87
84	16	1.55	10	3	0.00	47	262	-1.55	41	101	1.5	133	54	-25	238	70	-142
*85	16	0.75	0	196	0.08	0	106	-0.83	90	180	0.8	286	45	-90	106	45	-90
86	16	1.27	9	16	0.16	15	108	-1.43	72	257	1.3	89	39	-115	299	55	-71
87	16	1.06	10	203	0.14	12	295	-1.21	74	76	1.1	278	37	-111	123	56	-75
88	16	1.30	0	22	-0.02	3	112	-1.28	87	290	1.3	109	45	-94	295	45	-86
89	16	1.47	12	25	0.04	1	295	-1.51	78	198	1.5	117	33	-87	294	57	-92
90	16	1.39	7	26	0.20	4	116	-1.59	82	236	1.5	111	38	-97	299	52	-85
91	15	7.07	3	213	0.91	26	305	-7.96	64	116	7.5	278	47	-127	146	54	-57
*92	15	6.36	0	201	-0.13	0	111	-6.22	90	180	6.3	291	45	-90	111	45	-90
93	16	2.53	1	205	0.03	2	115	-2.56	88	326	2.5	296	44	-88	113	46	-92
94	16	1.01	3	34	0.13	16	303	-1.13	73	133	1.1	140	45	-66	289	50	-112
95	16	1.32	2	18	0.18	0	108	-1.50	88	210	1.4	108	43	-91	288	47	-89
*96	16	0.91	0	197	0.11	0	107	-1.02	90	180	1.0	287	45	-90	107	45	-90
*97	16	0.90	0	204	0.09	0	114	-0.99	90	180	0.9	294	45	-90	114	45	-90
98	16	0.86	12	16	0.16	28	112	-1.02	59	265	0.9	75	41	-135	308	62	-58
99	16	1.69	3	202	0.23	3	112	-1.92	85	337	1.8	295	42	-85	109	48	-94
100	16	3.94	4	19	0.47	15	110	-4.41	74	276	4.2	94	43	-112	303	51	-70
101	16	2.79	4	197	0.09	4	106	-2.88	84	330	2.8	291	41	-84	103	49	-95
102	16	1.70	0	199	0.08	3	289	-1.78	87	104	1.7	286	45	-94	111	45	-86
103	16	2.63	2	202	0.20	4	112	-2.83	85	317	2.7	296	43	-83	107	47	-96
104	16	6.17	7	200	0.86	14	108	-7.03	75	316	6.6	305	40	-69	98	53	-107
105	16	4.05	6	199	0.51	15	107	-4.56	74	311	4.3	305	41	-67	96	53	-109
106	16	1.37	13	210	0.28	10	302	-1.65	73	70	1.5	286	33	-109	129	59	-78
*107	15	6.68	7	209	1.55	19	302	-8.24	70	99	7.5	279	41	-119	136	55	-67
108	16	2.35	4	197	0.26	6	106	-2.61	83	323	2.5	293	41	-82	102	49	-97
109	16	2.19	1	204	0.41	19	114	-2.59	71	296	2.4	312	47	-64	96	49	-115
*110	16	1.84	0	203	-0.04	0	113	-1.79	90	180	1.8	293	45	-90	113	45	-90

* Indicates less-well-constrained event (see text).